Mitochondrial morphology and motility in retinal ganglion cells

Thesis submitted for the degree of Doctor of Philosophy

Cardiff University

May 2021

Shanshan Sun

School of Optometry and Vision Sciences

Cardiff University

Contents

Acknowledgements

I would like to thank my supervisors Prof Marcela Votruba, Prof Frank Sengpiel and Dr Irina Erchova for their continuous support and guidance throughout my PhD study. I would like to also thank Sharon Seto for all her help with basic training and technique guidance. Thank you to Nick White for all his tutorials on fluorescence and confocal microscopy. Thank you to Dr Malgorzata Rozanowska and Dr Kathy Beirne for all their help through lab works and PhD study. I would like to thank Carmine Varricchio for his help with measurement of mitochondrial bioenergetics. Thanks Dr Hayley Dingsdale from School of Bioscience for her kind and patient help on RGCs cell culture. Thank you to Dr Anthony Hayes form Biosi-imaging hub for his tutorial on LSM880 Airyscan confocal microscope, IMARIS software and suggestions on data analysis. Thank you to the people from 2.11 who have helped to create an enjoyable working environment.

Abbreviations

ADOA	Autosomal Dominant Optic Atrophy
ATP	Adenosine-5’-triphosphate
DMEM	Dulbecco’s modified Eagle’s medium
DRP1	Dynamin-related protein 1
LHON	Leber Hereditary Optic Neuropathy
MEFs	Mouse embryonic fibroblasts
MPP	Mitochondrial processing peptidase
MQC	Mitochondrial quality control
mtDNA	Mitochondrial deoxyribonucleic acid
OCT	Optical Coherence Tomography
OPA1	optic atrophy 1
OMM	Outer mitochondrial membrane
PBS	Phosphate-buffered saline
RGC	Retinal ganglion cells
ROS	Reactive oxygen species
siRNA	Small interfering RNA
ION	Inherited optic neuropathy

IMM	Inner mitochondrial membrane
IMS	Intermembrane space
PD	Parkinson’s disease
AD	Alzheimer’s disease
FCCP	Carbonyl cyanide-p-trifluoromethoxyphenylhydrazone
OCR	Oxygen consumption rate
GCL	Ganglion cell layer
IPL	Inner plexiform layer
INL	Inner nuclear layer
ONL	Outer nuclear layer
OPL	Outer plexiform layer
ON	Optic nerve
PSD95	postsynaptic density protein 95
RXRγ	Retinoid X receptor gamma
CAR	Cone arrestin
GFAP	Glial fibrillary acidic protein
GS	Glutamine synthetase
hiPSCs	Human induced pluripotent stem cells
PGC-1α	Peroxisome proliferator-activated receptor gamma coactivator 1-alpha

List of Figures

cristae junctions to control the widening or constriction of cristae. The loss of OPA1 will cause excessively widened and dysfunctional cristae, and release of pro-apoptotic proteins including cytochrome c. OMM: outer mitochondrial membrane; IMM: inner mitochondrial membrane. (Diagram summarised from Baker et al. 2019).

Figure 1.7 Transmission electron micrographs of optic nerve taken from B6;C3-*Opa1*^{Q285STOP} mutant mouse model of ADOA. (A, C, E) control groups; (B, D, F) Opa1$^{+/-}$ groups. The optic nerves appear comparable at 6 months old between genotypes (A, B); however, show evidence of anomalies in the optic nerve such as whirls of myelin (black arrows) by 9 months old (C, D), which continued to 18 months old (F). Scale bar = 2 μm (Image from Davies et al. 2007, copyright license #4927970479995).

Figure 3.1 Principle of mitochondrial bioenergetics measurement. (A) Diagram of oxygen consumption rate (OCR) assay. (B) Targets of each compound injected during assay in the electron transport chain. In the electron transport chain, the electrons are transferred from complex I or II to complex III and IV and release energy/H^+ at the same time. Complex I, III and IV use the energy to pump H^+ to mitochondrial intermembrane space (MIS). So there is a electrochemical gradient established and the H^+ can flow down the gradient through complex V (ATP synthase) to produce ATP. Oligomycin is an ATP synthase inhibitor, used to clarify the proportion of ATP-linked respiration in the basal respiration. FCCP is an uncoupling agent to collapse the proton gradient to claim Maximal respiration and reserve capacity. A mixture injection of rotenone and antimycin A can shut down the whole mitochondrial respiration.

Figure 3.2 Identification of primary retinal ganglion cells (RGCs) isolated by two-step immunopanning after two days in culture. (A) Phase-contrast image showing the

characteristic morphology of RGCs. (B) Immunofluorescent staining with Hoechst 33342 (blue), Thy1.2 (green), RBPMS (red) and merged image. Scale bar = 50 μm.

Figure 3.3 Representative confocal images of mitochondrial movements from WT and *Opa1*$^{+/-}$ RGC cultures. Mitochondria were stained by MitoTracker®Red CMXRos and captured under a Zeiss LSM 880 confocal microscope and Zen Zeiss software under the MtRed filter with a 63X oil magnification lens (Carl Zeiss, UK), scale bar = 20 μm.

Figure 3.4 No significant change was found in mitochondrial length over time, as measured during 10-minute time-lapse imaging by confocal microscopy in WT and *Opa1*$^{+/-}$ cultures. Mitochondria were stained by the specific mitochondrial vital dye, MitoTracker®Red CMXRos and captured using a Zeiss LSM 880 confocal microscope by time-lapse imaging with 5-second intervals for 10 minutes. The length of mitochondria was measured manually by FIJI software at frames 1, 30, 60, 90 and 120 (0 min, 2.5 min, 5 min, 7.5 min and 10 min) in WT (A; n=665 mitochondria) and *Opa1*$^{+/-}$ (B; n=698 mitochondria) cultures respectively. All the results are from 3 independent cultures, data shown as mean ± SD, N=3.

Figure 3.5 Opa1 deficiency decreases the length of mitochondria in vitro. The length of mitochondria was measured manually by FIJI software at frames 1, 30, 60, 90 and 120 (0 min, 2.5 min, 5 min, 7.5 min and 10 min). Statistically significant shorter mitochondria were observed in *Opa1*$^{+/-}$ cultures. (A) The length of mitochondria measured at frame 1 (0 min). n=130 mitochondria in WT group; n=140 mitochondria in *Opa1*$^{+/-}$ group. (B) The length of mitochondria measured at frame 30 (2.5 min). n=133 mitochondria in WT group; n=137 mitochondria in *Opa1*$^{+/-}$ group. (C) The length of mitochondria measured at frame 60 (5 min). n=130 mitochondria in WT group; n=143 mitochondria in *Opa1*$^{+/-}$ group. (D) The length of mitochondria measured at frame 90 (7.5 min). n=136 mitochondria in WT group; n=141 mitochondria in *Opa1*$^{+/-}$

group. (E) The length of mitochondria measured at frame 120 (10 min). n=136 mitochondria in WT group; n=137 mitochondria in *Opa1*$^{+/-}$ group. Data analysed from 3 independent cultures. Data shown as mean ± SD, N=3. *p < 0.05 vs WT.

Figure 3.6 Representative kymographs from WT and *Opa1*$^{+/-}$ RGC cultures, n=9 neurites in each condition from 3 independent cultures. Scale bar = 20 μm. All kymographs are presented in the Appendix III Figure S31.

Figure 3.7 Opa1 deficiency increases mitochondrial motility. (A, B) Distribution of the mitochondrial population classified as stationary and motile; n=9 neurites in both WT and *Opa1*$^{+/-}$ RGC cultures from 3 independent cultures. (C) Fluttering population within stationary mitochondria was defined as the number of mitochondria classified as stationary but which fluttered within a small distance (moving directions changed, maximum moving distance > 2 μm); n=9 neurites in WT and *Opa1*$^{+/-}$ RGC cultures from 3 independent cultures. (D) Contact rate calculated as the number of contacts between mitochondria per minute divided by the total number of mitochondria, n=9 neurites in WT and *Opa1*$^{+/-}$ RGC cultures from 3 independent cultures. Data shown as mean ± SD, N=3. *p < 0.05, **p < 0.01 vs WT.

Figure 3.8 Opa1 deficiency increases the velocity of mitochondrial movement. No significant difference was found in mitochondrial length from RGC neurites between wild-type and *Opa1*$^{+/-}$ RGCs. (A) Velocities of mitochondria calculated from WT and *Opa1*$^{+/-}$ RGC neurites calculated from kymographs; n=147 mitochondria in WT group, n=267 mitochondria in *Opa1*$^{+/-}$ group from 3 independent cultures (N=3). (B) Each mitochondrial length of the moving mitochondria from WT and *Opa1*$^{+/-}$ RGC neurites in (A) was measured by FIJI software. Data shown as mean ± SD, N=3. *p <0.05 vs WT.

Figure 3.9 Distribution of mitochondrial velocity and length in WT RGCs. No significant difference was found in mitochondrial velocity with the increase of mitochondrial length in WT RGCs. (A) Distribution of mitochondrial velocity according to their length, n=147 mitochondrial from 3 independent cultures. Red line framed area=greatest mitochondrial concentration (based on the heatmap result from (B)). (B) Heatmap of distribution of mitochondrial velocity and length. Red line framed area=greatest mitochondrial concentration (percentage of distributed mitochondria in each square > 10%). (C) Mitochondria distributed by velocity with different ranges of length (<2 μm, 2-3 μm and >3 μm); n=53 mitochondria with length <2 μm; n=54 mitochondria with length between 2 and 3 μm; n=40 with length >3 μm from 3 independent cultures (N=3). Data shown as mean ± SD. Supplementary histograms characterizing the detailed distribution of mitochondrial velocity and length from WT RGCs have been added in Appendix III Figure S34.

Figure 3.10 Distribution of mitochondrial velocity and length in *Opa1*$^{+/-}$ RGCs. No significant difference was found in mitochondrial velocity with the increase of mitochondrial length in *Opa1*$^{+/-}$ RGCs. (A) Distribution of mitochondrial velocity based on their length, n=267 mitochondrial from 3 independent cultures. Red line framed area=greatest mitochondrial concentration (based on the heatmap result from (B)). (B) Heatmap of distribution of mitochondrial velocity and length. Red line framed area=greatest mitochondrial concentration (percentage of distributed mitochondria in each square>10%). (C) Mitochondria distributed by velocity with different ranges of length (<2 μm, 2-3 μm and >3 μm); n=186 mitochondria with length <2 μm; n=62 mitochondria with length between 2 and 3 μm; n=19 with length >3 μm from 3 independent cultures (N=3). Data shown as mean ± SD. Supplementary histograms characterizing the detailed distribution of mitochondrial velocity and length from *Opa1*$^{+/-}$ RGCs have been added in Appendix III Figure S34.

Figure 3.11 Comparative analysis of mitochondrial bioenergetics between wild-type

and *Opa1*$^{+/-}$ mouse primary retinal ganglion cells. Cells were measured on the 3rd in vitro. (A) OCR profile plot. Oxygen consumption rate (OCR) was recorded by Seahorse Extracellular Flux Analyzer at baseline and after the sequential injections of oligomycin (1 μM), FCCP (2.5 μM), and a mixture of rotenone and antimycin (1 μM). (B) Basal respiration, (C) ATP-linked respiration, (D) maximal respiration, (E) spare respiratory capacity was calculated. Data are shown as the mean ± SEM of three independent experiments, each with five replicates. *$p < 0.05$ vs wild-type group.

Figure 4.1 *In vitro* hypertension model setup.

Figure 4.2 Representative confocal images of mitochondrial movements from control (CT) and hypertension cultures. RGC cultures were imaged after 10 days' culture and mitochondria were stained by MitoTracker®Red CMXRos and captured under a Zeiss LSM 880 confocal microscope and Zen Zeiss software under the MtRed filter with a 63X oil magnification lens (Carl Zeiss, UK), scale bar = 20 μm.

Figure 4.3 No significant difference was found in the mitochondrial length during 10-minute time-lapse imaging by confocal microscopy in control (CT) and hypertension cultures. The mitochondria were stained by the specific mitochondrial vital dye, MitoTracker®Red CMXRos and captured using a Zeiss LSM 880 confocal microscope by time-lapse imaging with 5-second intervals for 10 minutes. The length of mitochondria was measured manually by FIJI software at frames 1, 30, 60, 90 and 120 (0 min, 2.5 min, 5 min, 7.5 min and 10 min) in CT (A; n=778 mitochondria) and hypertension (B; n=755 mitochondria) cultures respectively. All the results are from 3 independent cultures, data shown as mean ± SD, N=3.

Figure 4.4 Hypertensive stress decreases the length of mitochondria in vitro. The length of mitochondria was measured manually by FIJI software at frames 1, 30, 60,

90 and 120 (0 min, 2.5 min, 5 min, 7.5 min and 10 min). Statistically significant shorter mitochondria were observed in hypertension cultures. (A) The length of mitochondria was measured at frame 1 (0 min). n=153 mitochondria in CT group; n=149 mitochondria in hypertension group. (B) The length of mitochondria was measured at frame 30 (2.5 min). n=165 mitochondria in CT group; n=148 mitochondria in hypertension group. (C) The length of mitochondria was measured at frame 60 (5 min). n=158 mitochondria in CT group; n=154 mitochondria in hypertension group. (D) The length of mitochondria was measured at frame 90 (7.5 min). n=153 mitochondria in CT group; n=151 mitochondria in hypertension group. (E) The length of mitochondria was measured at frame 120 (10 min). n=149 mitochondria in CT group; n=153 mitochondria in hypertension group. Data analysed from 3 independent cultures. Data shown as mean ± SD, N=3. *p <0.05, **p <0.01 vs CT.

Figure 4.5 Representative kymographs from control (CT) and hypertension RGC cultures, n=9 neurites in both conditions from 3 independent cultures. Scale bar = 20 μm. All kymographs are presented in Appendix Figure S41.

Figure 4.6 Hypertensive stress increases mitochondrial motility, but not contact rate. (A, B) Distribution of the mitochondrial population classified as stationary and motile; n=9 neurites in control (CT) and hypertension groups from 3 independent cultures. (C) The fluttering population within stationary mitochondria was defined as the mitochondria that had stationary status but fluttered within a small distance (moving directions changed, maximum moving distance > 2 μm); n=9 neurites in control and hypertension groups from 3 independent cultures. (D) The contact rate was calculated as the number of contacts between mitochondria per minute divided by the total number of mitochondria, n=9 neurites in in control and hypertension groups from 3 independent cultures. Data shown as mean ± SD, N=3. *p <0.05 vs CT.

Figure 4.7 No apparent difference in the velocity of mitochondrial movement caused by hypertensive stress. (A) Velocities of mitochondria calculated from control (CT) and hypertension groups calculated from kymographs; n=137 mitochondria in CT group, n=195 mitochondria in hypertension group from 3 independent cultures (N=3). No significant difference was found in mitochondrial length from RGC neurites between control and hypertension groups. (B) Each mitochondrial length of the moving mitochondria from control and hypertension cultures in (A) was measured by FIJI software. Data shown as mean ± SD, N=3.

Figure 4.8 Distribution of mitochondrial velocity and length in control RGCs. No significant difference was found on mitochondrial velocity with the increase of mitochondrial length in RGCs under normal condition. (A) Distribution of mitochondrial velocity according to their length, n=137 mitochondrial from 3 independent cultures. Red line framed area=greatest mitochondrial concentration (based on the heatmap result from (B)). (B) Heatmap of distribution of mitochondrial velocity and length. Red line framed area=greatest mitochondrial concentration (percentage of distributed mitochondria in each square>10%). (C) Mitochondria distributed by velocity with different ranges of length (<2 μm, 2-3 μm and >3 μm); n=24 mitochondria with length <2 μm; n=66 mitochondria with length between 2 and 3 μm; n=47 with length >3 μm from 3 independent cultures (N=3). Data shown as mean ± SD. The supplementary histograms characterized the detailed distribution of mitochondrial velocity and length from control RGCs has been added in Appendix Figure S44.

Figure 4.9 Distribution of mitochondrial velocity and length in RGCs under hypertensive stress. No significant difference was found on mitochondrial velocity with the increase of mitochondrial length in RGCs under hypertensive stress. (A) Distribution of mitochondrial velocity based on their length, n=195 mitochondrial from 3 independent cultures. Red line framed area=greatest mitochondrial concentration (based on the heatmap result from (B)). (B) Heatmap of distribution of mitochondrial

velocity and length. Red line framed area=greatest mitochondrial concentration (percentage of distributed mitochondria in each square>10%). (C) Mitochondria distributed by velocity with different ranges of length (<2 μm, 2-3 μm and >3 μm); n=74 mitochondria with length <2 μm; n=73 mitochondria with length between 2 and 3 μm; n=48 with length >3 μm from 3 independent cultures (N=3). Data shown as mean ± SD. The supplementary histograms characterized the detailed distribution of mitochondrial velocity and length from RGCs under hypertensive stress has been added in Appendix Figure S44.

Figure 5.1 Figure 5.1 Representative confocal images of mitochondrial movements from control and nicotinamide-treated (50 μM, 100 μM, 500 μM and 1 mM) groups. Mitochondria were stained by MitoTracker®Red CMXRos and captured under a Zeiss LSM 880 confocal microscope and Zen Zeiss software under the MtRed filter with a 63X oil magnification lens (Carl Zeiss, UK), scale bar = 20 μm.

Figure 5.2 The length of mitochondria was increased in 1 mM nicotinamide-treated RGCs at 0 min, 7.5 min and 10 min compared to the control. The length of mitochondria was stained by specific mitochondrial vital dye, MitoTracker®Red CMXRos and captured using a Zeiss LSM 880 confocal microscope by time-lapse imaging with 5-seconds' interval for 10 minutes. The length of mitochondria were measured manually by FIJI software at frames 1, 30, 60, 90 and 120 (0 min, 2.5 min, 5 min, 7.5 min and 10 min). (A) The length of mitochondria was measured at frame 1 (0 min). n=127 mitochondria in control group; n=171 mitochondria in 50 μM nicotinamide-treated group; n=209 mitochondria in 100 μM nicotinamide-treated group; n=159 mitochondria in 500 μM nicotinamide-treated group; n=203 mitochondria in 1 mM nicotinamide-treated group. (B) The length of mitochondria was measured at frame 30 (2.5 min). n=127 mitochondria in control group; n=161 mitochondria in 50 μM nicotinamide-treated group; n=219 mitochondria in 100 μM nicotinamide-treated group; n=174 mitochondria in 500 μM nicotinamide-treated group; n=193 mitochondria in 1 mM

nicotinamide-treated group. (C) The length of mitochondria was measured at frame 60 (5 min). n=137 mitochondria in control group; n=154 mitochondria in 50 μM nicotinamide-treated group; n=212 mitochondria in 100 μM nicotinamide-treated group; n=167 mitochondria in 500 μM nicotinamide-treated group; n=194 mitochondria in 1 mM nicotinamide-treated group. (D) The length of mitochondria was measured at frame 90 (7.5 min). n=137 mitochondria in control group; n=160 mitochondria in 50 μM nicotinamide-treated group; n=202 mitochondria in 100 μM nicotinamide-treated group; n=174 mitochondria in 500 μM nicotinamide-treated group; n=197 mitochondria in 1 mM nicotinamide-treated group. (E) The length of mitochondria was measured at frame 120 (10 min). n=137 mitochondria in control group; n=158 mitochondria in 50 μM nicotinamide-treated group; n=193 mitochondria in 100 μM nicotinamide-treated group; n=168 mitochondria in 500 μM nicotinamide-treated group; n=186 mitochondria in 1 mM nicotinamide-treated group. Data shown as mean ± SD, N=3.

Figure 5.3 Nicotinamide treatment increases mitochondrial coverage in RGC neurites in vitro observed at 0 min, 2.5 min and 7.5 min. The mitochondrial coverage in the neurite was calculated as the percentage of total mitochondrial length along the neurite divided by the length of neurite, n=9 neurites from each of control and nicotinamide-treated groups from 3 independent cultures. The mitochondrial coverage in the neurite was statistically increased by nicotinamide at concentrations of 100μM and 1mM at timepoints 0 min, 2.5 min and 7.5 min compared to the control group. No significant difference was found on the mitochondrial coverage of neurite during the 10-minute time-lapse imaging through confocal microscope in each of control and nicotinamide-treated groups (see Appendix V Figure S53). (A, B, C, D, E) The percentage of mitochondrial coverage of neurite calculated from 9 neurites in control and nicotinamide-treated cultures at frames 1, 30, 60, 90 and 120 (0 min, 2.5 min, 5 min, 7.5 min and 10 min). Data shown as mean ± SD, N=3. *p <0.05, **p <0.01 vs control.

Figure 5.4 Representative Kymographs from control and nicotinamide-treated groups

(50 μM, 100, 500, 1 mM), n=9 neurites treated with each concentration from 3 independent cultures. All kymographs has been presented in the Appendix V Figure S51.

Figure 5.5 Nicotinamide treatment increases mitochondrial motility. (A, B) Distribution of the mitochondrion population classified as stationary and motile; n=9 neurites in each condition from 3 independent cultures. (C) Fluttering population within stationary mitochondria was defined as the mitochondria classified as stationary status but fluttered within a small distance (moving directions changed, maximum moving distance > 2 μm); n=9 neurites in each condition from 3 independent cultures. (D) Contact rate calculated as the number of contacts between mitochondria per minute divided by the total number of mitochondria, n=9 neurites in each condition from 3 independent cultures. Data shown as mean ± SD, N=3. *p <0.05, **p <0.01 vs control.

Figure 5.6 Nicotinamide treatment increases the velocity of mitochondrial movement. No significant difference was found on mitochondrial length between control and nicotinamide-treated groups. (A) Velocities of mitochondria calculated from control and nicotinamide treated groups; n=52 mitochondria in control group, n=356 mitochondria in 50 μM nicotinamide-treated group, n=249 mitochondria in 100 μM nicotinamide-treated group, n=324 mitochondria in 500 μM nicotinamide-treated group, n=292 mitochondria in 1 mM nicotinamide-treated group from 3 independent cultures (N=3). (B) Each mitochondrial length of the moving mitochondria from each conditions in (A) was measured by FIJI software. Data shown as mean ± SD, N=3. *p <0.05, **p <0.01, ***p <0.001 vs control.

Figure 5.7 Distribution of mitochondrial velocity and length in control RGCs. No significant difference was found on mitochondrial velocity with the increase of mitochondrial length in control RGCs. (A) Distribution of mitochondrial velocity

according to their length, n=52 mitochondrial from 3 independent cultures. Red line framed area=highly concentrated area of mitochondrial distribution (based on the data from (B)). (B) Heatmap of distribution of mitochondrial velocity and length. Red line framed area = mitochondrial distribution >10% in each square. (C) Mitochondria distributed by velocity with different ranges of length (<2 μm, 2-3 μm and >3 μm); n=10 mitochondria with length <2 μm; n=23 mitochondria with length between 2 and 3 μm; n=19 with length >3 μm from 3 independent cultures (N=3). Data shown as mean ± SD. The supplementary histograms characterized the detailed distribution of mitochondrial velocity and length from control RGCs has been added in Appendix V Figure S54.

Figure 5.8 Distribution of mitochondrial velocity and length in 50 μM nicotinamide-treated RGCs. No significant difference was found on mitochondrial velocity with the increase of mitochondrial length in 50 μM nicotinamide-treated RGCs. (A) Distribution of mitochondrial velocity according to their length, n=356 mitochondrial from 3 independent cultures. Red line framed area=highly concentrated area of mitochondrial distribution (based on the data from (B)). (B) Heatmap of distribution of mitochondrial velocity and length. Red line framed area = mitochondrial distribution >10% in each square. (C) Mitochondria distributed by velocity with different ranges of length (<2 μm, 2-3 μm and >3 μm); n=63 mitochondria with length <2 μm; n=154 mitochondria with length between 2 and 3 μm; n=139 with length >3 μm from 3 independent cultures (N=3). Data shown as mean ± SD. The supplementary histograms characterized the detailed distribution of mitochondrial velocity and length from 50 μM nicotinamide-treated RGCs has been added in Appendix V Figure S54.

Figure 5.9 Distribution of mitochondrial velocity and length in 100 μM nicotinamide-treated RGCs. No significant difference was found on mitochondrial velocity with the increase of mitochondrial length in 100 μM nicotinamide-treated RGCs. (A) Distribution of mitochondrial velocity according to their length, n=249 mitochondrial from 3

independent cultures. Red line framed area=highly concentrated area of mitochondrial distribution (based on the data from (B)). (B) Heatmap of distribution of mitochondrial velocity and length. Red line framed area = mitochondrial distribution >10% in each square. (C) Mitochondria distributed by velocity with different ranges of length (<2 μm, 2-3 μm and >3 μm); n=51 mitochondria with length <2 μm; n=111 mitochondria with length between 2 and 3 μm; n=87 with length >3 μm from 3 independent cultures (N=3). Data shown as mean ± SD. The supplementary histograms characterized the detailed distribution of mitochondrial velocity and length from 100 μM nicotinamide-treated RGCs has been added in Appendix V Figure S54.

Figure 5.10 Distribution of mitochondrial velocity and length in 500 μM nicotinamide-treated RGCs. No significant difference was found on mitochondrial velocity with the increase of mitochondrial length in 500 μM nicotinamide-treated RGCs. (A) Distribution of mitochondrial velocity according to their length, n=324 mitochondrial from 3 independent cultures. Red line framed area=highly concentrated area of mitochondrial distribution (based on the data from (B)). (B) Heatmap of distribution of mitochondrial velocity and length. Red line framed area = mitochondrial distribution >10% in each square. (C) Mitochondria distributed by velocity with different ranges of length (<2 μm, 2-3 μm and >3 μm); n=63 mitochondria with length <2 μm; n=134 mitochondria with length between 2 and 3 μm; n=127 with length >3 μm from 3 independent cultures (N=3). Data shown as mean ± SD. The supplementary histograms characterized the detailed distribution of mitochondrial velocity and length from 500 μM nicotinamide-treated RGCs has been added in Appendix V Figure S54.

Figure 5.11 Distribution of mitochondrial velocity and length in 1 mM nicotinamide-treated RGCs. No significant difference was found on mitochondrial velocity with the increase of mitochondrial length in 1 mM nicotinamide-treated RGCs. (A) Distribution of mitochondrial velocity according to their length, n=292 mitochondrial from 3 independent cultures. Red line framed area=highly concentrated area of mitochondrial

distribution (based on the data from (B)). (B) Heatmap of distribution of mitochondrial velocity and length. Red line framed area = mitochondrial distribution >10% in each square. (C) Mitochondria distributed by velocity with different ranges of length (<2 μm, 2-3 μm and >3 μm); n=52 mitochondria with length <2 μm; n=111 mitochondria with length between 2 and 3 μm; n=129 with length >3 μm from 3 independent cultures (N=3). Data shown as mean ± SD. The supplementary histograms characterized the detailed distribution of mitochondrial velocity and length from 1 mM nicotinamide-treated RGCs has been added in Appendix V Figure S54.

Figure 6.1 Primary cortical neurons were transfected with mito-Kikume-Green. Selected mitochondria were irradiated using a 405-nm laser line and mito-Kikume-Green was converted into mito-Kikume-Red. Fusion events can be observed when green and red fluorescent mitochondria merged as yellow (Cagalinec et al. 2016).

List of Tables

ganglion cells were identified by retrograde labelling and counted in a semi-automatic fashion (cells/mm^2, means ± SEM). Statistical significance calculated by unpaired *t*-test: *p < 0.05, **p < 0.01, ***p < 0.001 vs controls. (Table from Alavi et al. 2007, copyright licence #4927990329777).

Table 1.5 Examples of protocol for reprogramming somatic cells to iPSCs.

Table 1.6 Examples of protocol for differentiating hiPSCs to RGCs.

Table 2.1 The constitution of retinal ganglion cell (RGC) growth medium. The neurotrophic and growth factors were dissolved into prewarmed mixture of neuralbasal and DMEM medium, i.e. Insulin, sodium pyruvate, L-glutamine, forskolin, NS21 supplement, bran-derived neurotrophic factor (BDNF) and ciliary neurotrophic factor (CNF) etc.

Table 2.2 Major steps and time consumption of two-step immunopanning method. The retina was dissected out from the mouse eye and dissociated and triturated into cell suspension, followed by negative and positive panning process. The selected RGCs were then plated and cultured in the RGCs specific growth medium.

Table 2.3 Primary and secondary antibodies used for identifying retinal ganglion cells.

Summary

OPA1 is the key regulator for the mitochondrial fusion and fission balance and also plays an important role in the pathological process of ADOA, causing visual dysfunction and even systemic disabilities. Retinal ganglion cells (RGCs) are vulnerable to energy disturbances, preferentially affected in most ADOA patients. The precise role of mitochondrial dynamics in retinal ganglion cell health and progression of cell death remains unclear. Thus, in this thesis it is hypothesized that alterations in mitochondrial dynamics during the early asymptomatic stages of ADOA precede the neurodegeneration and consequent RGC death.

Utilising immunofluorescence, time-lapse imaging and measurement of oxygen consumption rates, it was found that Opa1 deficiency leads to significant fragmentation of mitochondrial morphology, activation of mitochondrial motility and impaired respiratory function in RGCs from the B6; C3-*Opa1*^{Q285STOP} mouse model. The increased motility of mitochondria is hypothesized to be a spontaneous compensatory response which promotes fusion activity and facilitates energy production. This result highlights the significant alterations in the intricate interplay between mitochondrial morphology, motility, and energy production in RGCs with Opa1 deficiency long before the onset of clinical symptoms of the pathology.

In order to explore and gain a better understanding of mitochondrial morphology and motility in RGCs under different conditions, hypertensive stress and drug administration were applied to RGCs *in vitro*. In the *in vitro* hypertension model, it was found that hypertensive stress caused shortened length of mitochondrial structures accompanied with increased mitochondrial motility. By applying nicotinamide directly into the RGC culture medium *in vitro* with different concentrations for 24 hours, it was found that nicotinamide increased the percentage of motile mitochondria in neurites of RGCs as well as the velocities of mitochondrial movement.

Chapter 1 Introduction

1.1 Autosomal dominant optic atrophy

Autosomal dominant optic atrophy (ADOA) or dominant optic atrophy (DOA), also called Kjer optic atrophy, was given it's eponymous name after the Danish ophthalmologist Dr Poul Kjer, who published a seminal aerticle in 1959 (Kjer 1959). ADOA is a neuro-ophthalmic condition characterized by a bilateral degeneration of the optic nerves, causing reduced visual acuity, sometimes leading to blindness beginning in childhood.

1.1.1 Epidemiology

ADOA is a common form of inherited optic neuropathy. The estimated prevalence is 1/10,000, but varies between 1/10,000 and 1/20,000 (Yu-Wai-Man et al. 2011b; Yu-Wai-Man et al. 2014). ADOA is inherited in an autosomal dominant manner, hence a heterozygous patient with ADOA has a 50% chance of passing on the disease to offspring, assuming his/her partner does not have the disease. ADOA has a high penetrance, around 70%, but this can be extremely variable depending on the family, mutation and diagnostic criteria. The clinical phenotype is also highly heterogenous, and varies both within and between families.

1.1.2 Clinical presentation

ADOA, was first described by Batten, and later by Kjer (Batten 1896; Kjer 1959). ADOA typically presents as a non-syndromic bilateral optic neuropathy which manifests during adolescence or early adult life, although ADOA typically begins in the first or second decade of life (Pilz et al. 2017). ADOA patients typically experience a slowly progressive, insidious, bilateral visual loss, which is irreversible with central or centrocaecal scotomas in the visual field and often accompanied by a tritanopic or mixed dyschromotopsia (Yu-Wai-Man et al. 2010a; Yu-Wai-Man et al. 2016). Since

ADOA typically has incomplete penetrance, the clinical presentation is heterogeneous and not all family-members who carry pathogenic mutations present with visual impairments (Cohn et al. 2007; Amati-Bonneau et al. 2009; Skidd et al. 2013; Barboni et al. 2014). Evidence also suggests that both genetic penetrance and environmental factors might exert crucial effects on the ADOA clinical phenotype (Amati-Bonneau et al. 2009). Few studies reveal any associated environmental factors implicated in ADOA. Chen et al. 2019 suggested that excessive ethanol consumption could be an isolated cause or risk factor, and reported that there may be greater peripheral neurological manifestations by comparing the vibration sensation between optic atrophy patients that consumed alcohol and those that did not (Chen et al. 2019).

Visual acuity usually remains better than 20/200. It has been revealed that one third of patients retain central visual acuity better than 20/60, while a half of patients only have central visual acuity between 20/60 and 20/200, and the remainder are worse than <20/200 (Yu-Wai-Man et al. 2010a; Skidd et al. 2013).

ADOA is caused by loss of retinal ganglion cells (RGCs) located in the inner retina, particularly (but not exclusively) in the papillomacular bundle (a collection of RGCs that carry information from the macula (central retina) to the optic nerve and on to the brain). The loss of RGCs in the papillomacular bundle can lead to the typical temporal pallor of the optic nerve head, centrocaecal scotoma, and reduced central acuity (Chun and Rizzo 2016). As shown in Figure 1.1, the eye fundus examination typically shows a bilateral and symmetrical pallor of the temporal side of the optic disc, suggesting the loss of projecting RGC fibres via the optic nerve to the brain. The optic disc pallor indicating the atrophic morphology of optic nerve, can be either diffuse involving the entire neuro-retinal rim, or present as a temporal wedge (Yu-Wai-Man et al. 2009b).

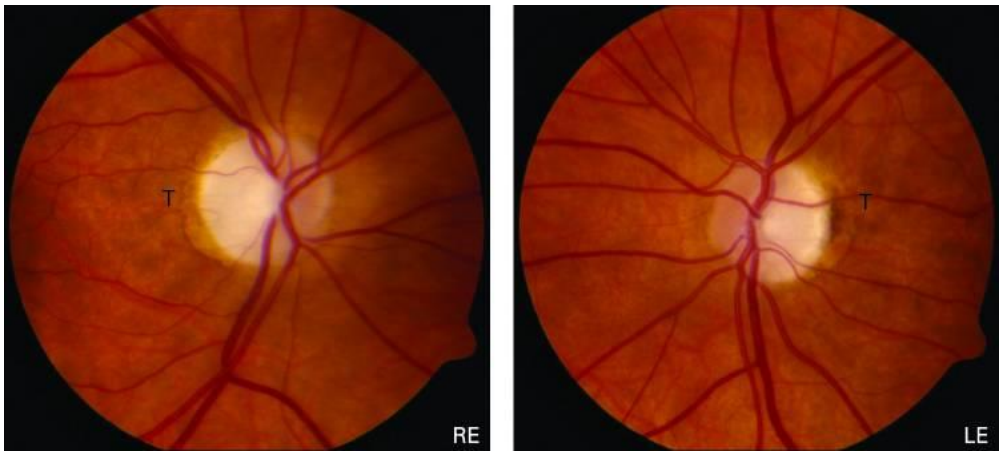

Figure 1.1 Eye fundus examination showing typical fundal appearance in ADOA patients with bilateral optic disc pallor more significant in the temporal quadrant (RE, right eye; LE, left eye; T, temporal quadrant). (Image from Yu-Wai-Man et al. 2009b).

RGC loss and atrophy of the optic nerve are also accompanied by thinning of the nerve fibre layer of the retina, which is one of the characteristic features revealed by high-resolution Optical Coherence Tomography (OCT). Yu-Wai-Man et al. 2011 performed OCT imaging on patients with molecularly confirmed OPA1 mutations compared to normal controls demonstrated a significant reduction in the mean peripapillary retinal nerve fibre layer (RNFL) thickness with the appearance that the temporal quadrant being more severely affected while the nasal quadrant relatively spared, which was consistent with the specific temporal disc pallor observed by the eye fundus examination, shown as Table 1.1. (Yu-Wai-Man et al. 2011a).

Quadrant	Mean RNFL thickness (SD) (μm)			
	OPA1 (N=80)	Controls (N=30)	Percentage decrease	P-value
Average	54.11(11.98)	98.77 (10.86)	45.2	<0.0001
Temporal	33.44 (8.31)	81.60 (14.31)	59.0	<0.0001
Inferior	61.84 (18.72)	122.70 (20.14)	49.6	<0.0001

Superior	71.00 (21.58)	122.00 (14.86)	41.8	<0.0001
Nasal	49.99 (12.76)	67.43 (17.59)	25.9	<0.0001

Table 1.1 Retinal nerve fibre layer (RNFL) thickness data for *OPA1* patients and normal controls. *OPA1* mutant patients had a statistically significant reduction in the mean peripapillary RNFL thickness compared to the control group by independent sample *t*-test analysis, $^{\#}p < 0.0001$ vs control group. The percentage decrease was greater in the temporal quadrant (59%), followed by the inferior (49.6%), superior (41.8%), and nasal (25.9%) quadrants. (Table 1.1 summarised from Yu-Wai-Man et al. 2011a).

Visual field analysis shows a centrocaecal scotoma, and sometimes a central or paracentral scotoma, while the peripheral field remains normal (Figure 1.2). Tritanopia may also be detected and is strong evidence of ADOA (Puomila et al. 2005). Of interest, even in severe cases of ADOA, the pupillary reflex and circadian rhythms are not affected, indicating the relative sparing of melanopsin RGCs during the course of ADOA (Bremner et al. 2001; La Morgia et al. 2010).

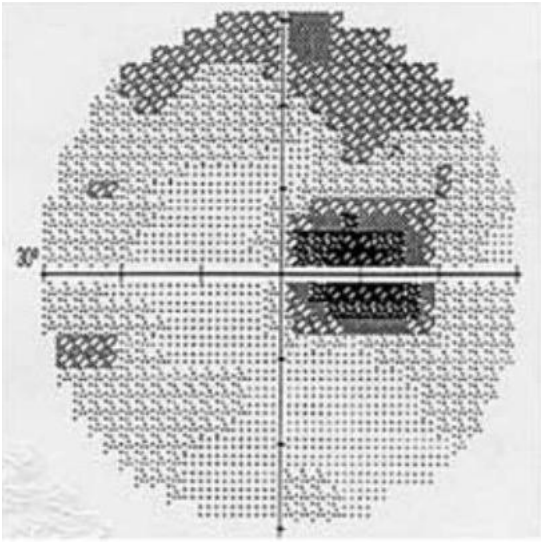

Figure 1.2 Right visual field of a patient with ADOA showing a centrocaecal scotoma. Image from (Aung et al. 2002).

It has been reported that almost 20% of OPA1 mutation carriers developed a ADOA plus phenotype associated with a broad range of extra-ocular symptoms, i.e. sensorineural deafness, ataxia, myopathy, peripheral neuropathy axonal sensory-motor polyneuropathy and chronic progressive external ophthalmoplegia (Hudson et al. 2008; Alavi and Fuhrmann 2013). This suggests different cell types in the body are differently affected by the *OPA1* mutation, whilst RGCs appear to be the most vulnerable.

1.1.3 Pathophysiology

ADOA is the most common autosomal inherited optic neuropathy (ION) and is inherited in an autosomal dominant mode of inheritance (Lenaers et al. 2012). ADOA is primarily associated with the mutation of *OPA1* gene, which is a nuclear gene located on chromosome 3q28-q29. Pathogenic mutations in the OPA1 gene are responsible for 65% to 90% of well-defined ADOA cases (Cohn et al. 2007; Almind et al. 2012). Ham et al. 2017 obtained both genetic and clinical information of 408 patients with confirmed *OPA1* mutations from published reports and illustrated the genotype-phenotype correlation of the various mutations in *OPA1* gene, 120 of whom showed extra-ocular manifestations (ADOA “plus”). They found that classic ADOA patients (without extra-ophthalmological manifestations) were more likely to have *OPA1* mutations in exons 27, 9, 8 and 17, whereas ADOA “plus” patients were more likely to have *OPA1* mutations in exons 14, 15 and 17. Deletions were the most common mutation seen in 40% of the cases in ADOA classic group, while missense mutations were the most common mutation seen in 68% of the individuals in ADOA “plus” group (Ham et al. 2019). It has also been demonstrated that most mutations above lead to incomplete transcription and a significant downregulation of *OPA1* when compared to the wild-type expression, named haplo-insufficiency, which results in cristae disorganization and mitochondrial aggregation supported by numerous evidence from cell lines and

animal models of ADOA (Marchbank et al. 2002; Zanna et al. 2008; Kushnareva et al. 2016). This means that the single remaining functional copy fails to express sufficient protein and results in an abnormal clinical phenotype in a diploid organism with only one functional copy of the gene (Chun and Rizzo 2016). Thus, haplo-insufficiency of OPA1 is the major pathogenic mechanism in ADOA.

OPA1 deficiency lead to a deficient mitochondrial fusion network and also cause disruption of mitochondrial cristae junctions and instability of the mitochondrial cristae structure as well as mitochondrial membrane network, which dramatically promotes the release of pro-apoptotic cytochrome c and finally results in mitochondrial pathway apoptosis and irreversible cell death (Zanna et al. 2008; Landes et al. 2010b; Alavi and Fuhrmann 2013). The mitochondrial fragmentation raises the production of reactive oxygen species (ROS) and destabilise the mitochondrial respiratory chain complexes, resulting in decreased ATP production and reduced cellular energetic metabolism, which accelerates the apoptosis of RGCs (Carelli et al. 2013).

	All patients	**ADOA classic**	**ADOA "plus"**
Mutation type			
Missense	31%	19%	68%
Nonsense	16%	17%	12%
Splicing defect	18%	20%	14%
Deletion	30%	40%	6%
Insertion	1%	2%	-
Duplication	1%	1%	-

Table 1.2 Description of mutations in ADOA patients. A significant difference is seen in the frequency of mutation types between ADOA classic and ADOA "plus"

groups by Fisher's exact test (p value < 0.001). Deletions were the most common mutation seen in the 40% of ADOA classic group, whereas missense mutations were the most frequent mutation seen in 68% of the ADOA "plus" patients (adapted from Ham et al. 2019).

1.2 Retinal ganglion cells (RGCs)

1.2.1 Definition

The retina is a sensory membrane which lines the inner surface of the posterior part of the eye. The vertebrate retina is composed of ten distinct layers, which comprise the inner limiting membrane, nerve fibre layer, ganglion cell layer, inner plexiform layer, inner nuclear layer, outer nuclear layer, external limiting membrane, layer of rods and cones and retinal pigment epithelium. Glial cells, retinal ganglion cells (RGC), amacrine cells, bipolar cells, horizontal cells and photoreceptors are the major cell types in the vertebrate retina. Each of the retinal cell types locates in specific retina layers and may be detected by specific antibodies (see Figure 1.3).

A retinal ganglion cell (RGC) is a type of neural cell and is located in the ganglion cell layer of the retina near the inner surface. There are about 0.7 to 1.5 million RGCs in one human retina (Watson 2014). RGCs set up synaptic contacts with bipolar cells and retinal amacrine cells to receive visual information. RGCs transmit visual information to several visual processing centres in the brain through their axons, i.e. thalamus, hypothalamus, and mesencephalon in the form of action potentials (Erskine and Herrera 2014). The impairment of RGCs is directly related to several optic nerve diseases such as autosomal dominant optic atrophy (ADOA), Leber's hereditary optic neuropathy (LHON), and glaucoma.

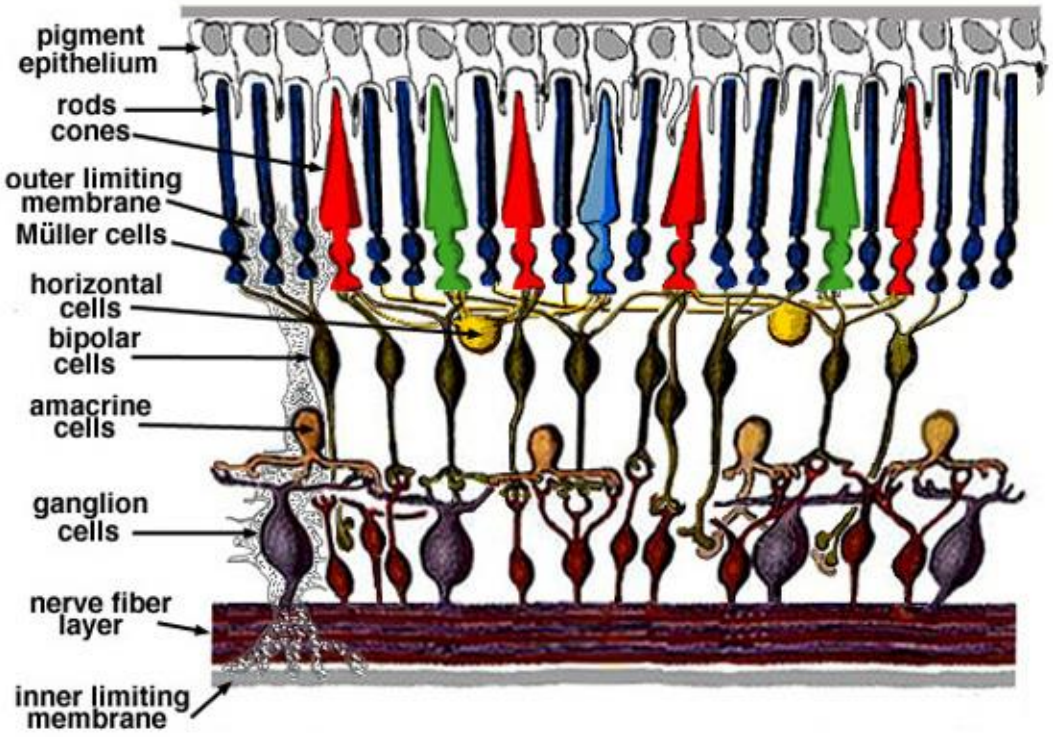

Figure 1.3 A diagram of the layers and cells in the retina. Source: http://webvision.med.utah.edu/; Kolb H, Fernandez E, Nelson R. The Organization of the Retina and Visual System (Online Book).

1.2.2 Vulnerability of RGCs

RGCs are preferentially involved in ADOA patients, and seemingly the only cell type in the retina among the 60 different neuronal cell types which suffer from ADOA mutations (Yu-Wai-Man et al. 2011b; Alavi and Fuhrmann 2013). The reason could be explained in part by the anatomy of RGCs and their axons. First of all, the mean diameter of the soma of the RGC is 20 μm and the estimated volume is 4000 μm^3, however the length of their axons that reach the nucleus of lateral geniculate is measured as 8 cm, which is 4000 times longer than the diameter of RGC soma, and the estimated volume of axons is 80,000 μm^3, equivalent to 20 times the soma volume (Lenaers et al. 2009). Additionally the retina is one of the highest oxygen and energy consuming tissues in the body, thus the retinal cells especially the RGCs and their axons have a tremendous high energy requirement to sustain the transmission of action potentials and are sensitive to disturbances in the supply of energy sources (Yu et al. 2014). Secondly, in humans RGC axons are in an unmyelinated state in the retinal nerve fibre layer in the retina, before they reach the optic papilla and on their way to enter the optic nerve, thus the axon is unmyelinated in the eye globe and become myelinated only after passing the lamina cribrosa. The RGC soma and axons in the eye are located in the central visual field and are exposed to the day light stress. Without the protection of myelination, the light can directly result in a permanent oxidative stress and pro-apoptotic stimulation (Lascaratos et al. 2007; Li and Osborne 2008; Osborne et al. 2008). Thirdly, the unmyelinated portion of the RGC axons requires a lot more energy to generate the action potential because of the lack of the saltatory conduction compared to the myelinated portion after the point of lamina cribrosa. Thus, the mitochondria are unevenly distributed along the RGC axons, which leads to a significant physiological shift at the lamina cribrosa –highly abundant and round within the unmyelinated region while considerable reduction in mitochondria abundance within the myelinated region (Wang et al. 2003; Barron et al. 2004). The accumulated mitochondria at the lamina cribrosa could cause uneven mitochondrial axoplasmic transport, and antero- and retro-grade flows of neurotrophic factors. It has been demonstrated that the specular structure

of lamina cribrosa with unevenly distributed mitochondria is a critical determinant of the degree of susceptibility to damage such as elevated intraocular pressure, in which the axonal transport could be obstructed within the nerve head at the lamina cribrosa (Quigley et al. 1981). The blockage of transportation will inhibit not only the energy supply, but also the neurotrophic factors such as brain-derived neurotrophic factors (BDNF), which can result in irreversible RGC loss (Quigley et al. 2000). Moreover, since the intraocular pressure surrounding the RGCs in the eye is always higher than the intracranial pressure surrounding the axons in the optic nerve and brain, and the pressure may fluctuate from time to time, the mitochondrial axoplasmic transport could also be influenced by these two different types of pressure and their fluctuation (Nusbaum et al. 2015; Wang et al. 2017). Thus, RGCs and their mitochondria are technically vulnerable to environmental stimuli based on their peculiar anatomy. Previous research has also indicated that OPA1 dysfunction could also lead to an increasing susceptibility to apoptosis and loss of axons in the optic nerve (Carelli et al. 2009).

Additionally, melanopsin-containing RGCs (mRGCs), a special subset of RGCs constituting only 1% of the RGCs population, were reported to be resistant to mitochondrial dysfunction and maintain the non-image-forming light driven functions (La Morgia et al. 2010; Perganta et al. 2013) independently from melanopsin expression (Gonzalez-Menendez et al. 2015). The large cellular size of mRGCs with a high cellular content of mitochondria might be the possible factors protecting mRGCs from mitochondrial dysfunctions (La Morgia et al. 2010; Georg et al. 2017).

1.3 Mitochondrial dynamics and life cycle

Mitochondria are power houses of the cell and critical for preserving cellular form and function with a properly organized and healthy network. The global dynamic mitochondrial network emerges from four major activities: mitochondrial fusion and fission, motility, mitophagy and biogenesis, with critical influences on each other, which builds up a delicate life circle. (Ito and

Di Polo 2017).

1.3.1 Mitochondrial fusion and fission balance

The retina is one of the highest metabolically active organs in the body, thus it is crucial to maintain a stable and high energy supply. Mitochondria are ancient organelles evolved from bacteria (Labbe et al. 2014). They play a role in the retina in order to meet the high energy consumption by generating ATP through efficient oxidative phosphorylation. Mitochondria are double membrane endosymbiotic organelles and are often referred to as the powerhouses of the cell, which are at the heart of eukaryotic cell metabolism (Nunnari and Suomalainen 2012). They are dynamic organelles that continuously undergo fission and fusion and move along the cytoskeleton to build up the mitochondrial network (Tagaya and Arasaki 2017) (see Figure 2). These dynamic processes provide a number of healthy mitochondria throughout the complex morphological structure of retinal ganglion cells and also allow the neurons to rapidly adapt to the rapid alterations of energy demand (Ito and Di Polo 2017). Mitochondrial fission and fusion are mediated by four dynamin-related GTPase which are responsible for the constant changes in the mitochondrial location, size and shape in response to physiological and pathological cues. In rodents, two different dynamin-related GTPase are involved in membrane fusion, since there are two mitochondrial membranes, the inner and outer membranes. Mitofusin 1 (MFN1) and MFN2 (the close homologue of MFN1) take charge of catalyzing the outer mitochondrial membrane (OMM). Mutations in *MFN2* gene were initially reported to be responsible for the rare neurodegenerative disease, Charcot-Marie-Tooth subtype 2A (CMT2A) (Verhoeven et al. 2006). Optic atrophy 1 (OPA1) is the dynamin-related protein mediating the fusion of inner mitochondrial membrane (IMM). Mitochondrial fusion will be severely impaired if any of these three GTPases are depleted (Chen et al. 2003; Song et al. 2007; Zhao et al. 2015). The OPA1 protein is likely to connect with the mitofusins to form protein complexes so as to integrate the fusion of inner and outer mitochondrial membrane (Cipolat et al. 2004).

In contrast, mitochondrial fission is mainly mediated by dynamin-related protein 1 (DRP1), which is also referred as Dynamin-1-like protein, and assembles on mitochondrial tubules mediating constriction and scission (Smirnova et al. 2001; Meyer et al. 2017). DRP1 protein is oligomerized and recruited by OMM-localized receptors to the OMM, i.e. mitochondrial fission factor (MFF), mitochondrial division 49/51 (MiD49/51), and in some cases mitochondrial fission 1 (FIS1). Evidence indicates that DRP1- dependent mitochondrial morphology changes might control the regulation mediated by MFNs and OPA1 (Saita et al. 2016). Specifically, MFF is the best-established receptor for DRP1 (Chan 2012). Knockdown of the *MFF* gene reduced the amount of recruited DRP1 to mitochondria (Otera et al. 2010), suggesting their close association with each other. In contrast, inhibition of FIS1 resulted in elongation of mitochondria but did not abrogate the recruitment of DRP1 to the mitochondrial surface (Lee et al. 2004). Thus some researchers have concluded that MFF may play a dominant role in mitochondrial fission in most mammalian cell types, while FIS1 may exert an important function in some specific cell types (Chan 2012). In Table 1.3, summarizes the essential proteins involved in the mitochondrial fusion and fission dynamic network.

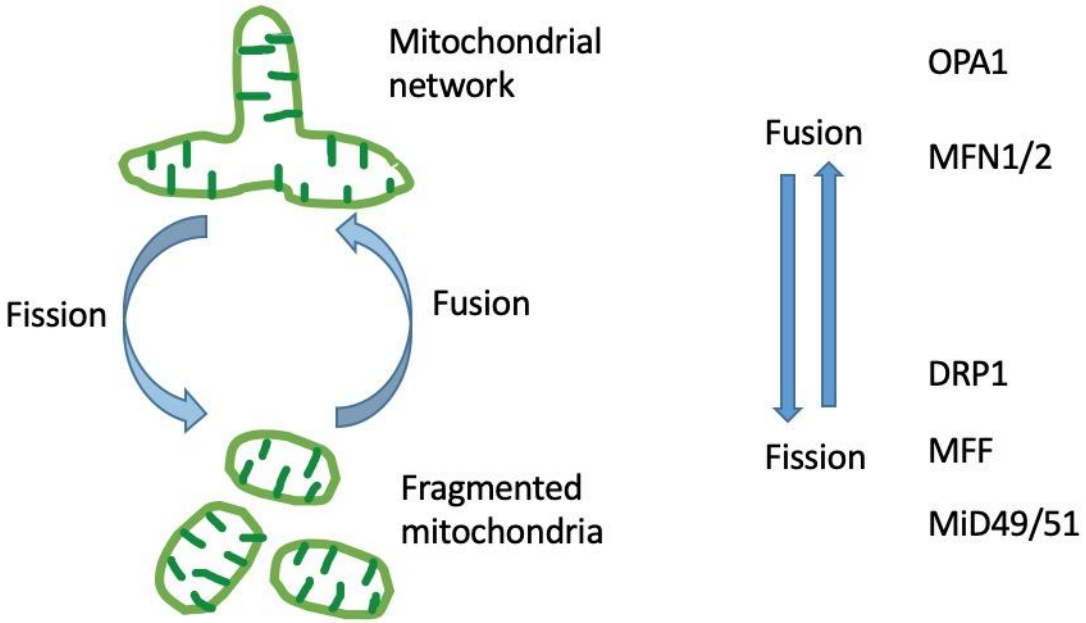

Figure 1.4 Proteins involved in mitochondrial fusion and fission dynamics. Mitochondrial fusion is mainly mediated by Mitofusin 1 (MFN1) and Mitofusin 2 (MFN2) located in the outer

mitochondrial membrane (OMM), and OPA1 located in the inner mitochondrial membrane (IMM). Mitochondrial fission is mainly mediated by dynamin-related protein 1 (DRP1), oligomerized and recruited by OMM-localized receptors, i.e. mitochondrial fission factor (MFF), mitochondrial division 49/51 (MiD49/51), and mitochondrial fission 1 (FIS1).

Fusion:

Protein	***Full name***	***Description***
MFN1	Mitofusin1	Essential for outer membrane fusion; *MFN2*: causative gene of neurodegenerative disorders-CMT2a. (Ainbinder et al. 2015; Ryu et al. 2015)
MFN2	Mitofusin2	
OPA1	Mitochondrial dynamin like GTPase	Mediation of inner membrane fusion; Involved in the formation of cristae structure. (Lenaers et al. 2009)

Fission:

Protein	***Full name***	***Description***
DRP1	Dynamin 1-like	Localized to the cytoplasm and mitochondrial membrane; Involved in mitochondrial and peroxisomal division; Essential for mitochondrial fission. (Chan 2012)

MFF	Mitochondrial fission factor	Tail-anchored protein; Localized in the outer membrane; Best-established receptor for DRP1. (Otera et al. 2010)
MiD49	Mitochondrial elongation factor 2	Located in the outer membrane; Involved in the recruitment and regulation of DRP1; Precise roles unknown. (Chen et al. 2018)
MiD51	Mitochondrial elongation factor 1	

Table 1.3 Essential proteins involved in mitochondrial fusion and fission dynamic network. Mitofusin 1 (MFN1) and Mitofusin 2 (MFN2) take charge of fusion process of outer mitochondrial membrane (OMM) while OPA1 protein is essential for the fusion of inner mitochondrial membrane (IMM). Dynamin-related protein 1 (DRP1), oligomerized and recruited by OMM-localized receptors, assembles on mitochondrial tubules mediating constriction and scission on the mitochondrial membrane called fission.

1.3.2 Mitochondrial motility

Mitochondria are astonishingly dynamic organelles which are adaptable to alterations in cellular energy demand such as physiological stress or pathological conditions. In neurons, the mitochondrial population is distributed all the way down the processes of axons and dendrites to sustain ATP production and Ca^{2+} homeostasis, and is enriched in regions required high energy consumption, such as active growth cones and nodes of synaptic terminals (Chang and Reynolds 2006; Kann and Kovacs 2007; Mattson 2007). Mitochondrial transport is driven by the molecular motor proteins. There are three major motor protein families: microtubule-based kinesin and dynein motors are implicated in the long-distance transport of

mitochondria, in which kinesins carry cargos anterogradely from the cell body to the nerve endings while dynein motors move cargo in the opposite direction and back to the cell body; actin-based myosin motors are employed for the short-distance mitochondrial movements (Morris and Hollenbeck 1995). The complex formed by mitochondrial Rho (Miro) GTPase and the trafficking kinesin protein (TRAK) family adaptor proteins is one of the mechanisms for coupling mitochondria to motors (Brickley and Stephenson 2011). Importantly, mitochondria in neurites may switch status between motile and long-term stationary in a process called "docking", which can last longer than 10 min at a specific region with high energy requirements (Chang et al. 2006; Louie et al. 2008). Intracellular Ca^{2+} signaling has been reported to be an effective way to arrest microtubule-based mitochondrial transport temporarily at synaptic sites with the help of Miro proteins in neurons (Saotome et al. 2008). Additionally, Syntaphilin, a neuron specific protein, has also been demonstrated to be employed for docking mitochondria to the microtubule cytoskeleton (Kang et al. 2008).

1.3.3 Mitochondrial mitophagy and quality control

Mitophagy is a type of autophagy in which irreparably damaged mitochondria are selectively degraded by the lysosome (Ashrafi and Schwarz 2013). Since fragmented or dysfunctional mitochondria may produce excess ROS resulting in the damage to other cellular compartments and then cell death, mitophagy is the only way to eliminate the unhealthy mitochondria and maintain a healthy mitochondrial population, which is also called mitochondrial quality control (Twig and Shirihai 2011; Palikaras et al. 2016). In terms of mechanisms, mitophagy is Parkin-dependent mitochondrial autophagy, and mitochondrial dynamics, i.e. fusion and fission events, play a crucial role in mitophagy activity. Cellular stress (ischemia or reperfusion) or genetic mutations trigger fragmentation of the mitochondrial network, which has a close relationship with Drp1 and Fis1 (Smirnova et al. 2001; Yoon et al. 2003). Fragmentation is essential for mitophagy to occur (Twig et al. 2008; Tanaka et al. 2010). The dysfunctional mitochondria are eliminated through accumulation of PINK1 and Parkin

leading to sequestration into autophagosomes by interaction with LC3 or homologues, and eventually subjected to lysosomal fusion and degradation (Jin and Youle 2013; Eiyama and Okamoto 2015). Mfn1 and 2, which participate in OMM fusion, are ubiquitinated and targeted during mitophagy. Moreover, OPA1 protein, which is degraded during mitophagy, also shows a close interaction with mitophagy (McBride and Soubannier 2010; MacVicar and Lane 2014).

1.3.4 Mitochondrial biogenesis

Mitochondrial biogenesis acts in concert with mitophagy to maintain an adequate number of mitochondria within the cells, thus keep healthy cellular homeostasis. The structural and functional components of mitochondria are encoded by both nuclear and mitochondrial genes. The nuclear-encoded genes, which are responsible for the majority of mitochondrial proteins, are primarily controlled by the transcription cofactor peroxisome proliferator-activated receptor PGC-1α (Wu et al. 1999). PGC-1α is a master regulator of mitochondrial biogenesis, which controls the expression of nuclear respiratory factors 1 and 2, in return controlling the expression of mitochondrial transcription factor A (Tfam) (Virbasius and Scarpulla 1994). PGC-1α increased in RGCs as well as in retinal and optic nerve astrocytes in response to metabolic or oxidative stress (Noh et al. 2013; Guo et al. 2014).

There is a crucial interplay between mitophagy and mitochondrial biogenesis. Parkin-interacting substrate (PARIS) has been identified as a direct transcriptional repressor of PGC-1α (Shin et al. 2011). The activation of mitophagy increases Parkin expression and activity, leading to degradation of PARIS, which then relieves the transcriptional repression of PGC-1α, priming mitochondrial bioenergetics (Andres et al. 2015).

1.4 OPA1

1.4.1 *OPA1* gene and protein

The *OPA1* gene encodes a dynamin-related GTPase, an essential protein located in the intermembrane space (IMS) for mitochondrial inner membrane fusion and maintenance of mitochondrial cristae structure (Alexander et al. 2000; Delettre et al. 2000; Alavi and Fuhrmann 2013). OPA1 has distinct roles in regulating the process of apoptosis, mitochondrial energetic metabolism, as well as interacting with the oxidative phosphorylation complexes and mitochondrial membrane potential (Landes et al. 2010b; Patten et al. 2014; MacVicar and Langer 2016). The expression is ubiquitous in human. The gene has 30 exons, 3 of which (4, 4b and 5b) are alternatively spliced leading to 8 mRNA isoforms (Delettre et al. 2001; Lenaers et al. 2009). It is reported that the expression is quantitatively variable in different tissues. Retina, liver, brain, heart and pancreas present high OPA1 mRNA expression levels (Delettre et al. 2000; Delettre et al. 2001; Misaka et al. 2002). Of interest, the 8 spliced variable transcripts also seem to be tissue-specific (Alexander et al. 2000; Akepati et al. 2008). Different alternate splicing, including and excluding exon 4, 4b and 5b in the open reading frame, and the variability in the 3'end untranslated region (UTR), generate the 8 different OPA1 mRNA transcripts (Olichon et al. 2007a; Guillery et al. 2008). Exon 4 is evolutionarily conserved, and systematically appears in mouse OPA1 mRNAs, while in lower eukaryotes, no alternate splicing has been found in the open reading frame (Olichon et al. 2007a; Akepati et al. 2008). The 8 OPA1 mRNA variants encode proteins of 924-1014 amino acids, which belong to the GTPase dynamin family. OPA1 shares three conserved regions: a GTP effector domain (GED) containing a coiled-coil region (CC-II), a middle domain, and a GTPase domain. The amino-terminal region of OPA1, preceding the GTPase domain, displays a mitochondrial import sequence (MIS) followed by a predicted transmembrane domain (TM1), which is highly conserved in all homologs (Olichon et al. 2002). No remarkable feature is presented in exon 4 domain, while two specific encoded hydrophobic domains are present, TM2a and TM2b, corresponding to alternatively spliced exons 4b and 5b. Exon 5b also encodes a coiled coil

domain (CC-0) (Duvezin-Caubet et al. 2007; Olichon et al. 2007a). CC-I, another distinct coiled-coil domain, located downstream the alternatively spliced region. Both CC-I and CC-II could be responsible to form the homotypic complexes between distinct OPA1 proteins (Akepati et al. 2008).

There are two types of OPA1 protein isoforms: long and short. The 8 variable OPA1 mRNAs are translated into precursors and then targeted to mitochondria via MIS. The membrane-anchored long isoforms of the GTPase (l-OPA1) are generated by the cleavage of the MIS via the mitochondrial processing peptidase (MPP) (Satoh et al. 2003; Olichon et al. 2007a). Each l-OPA1 isoform might then be further processed at the S1 and S2 cleavage sites in the TM region, generating soluble short forms of GTPase (s-OPA1) (Song et al. 2007). Both long and short isoforms of OPA1 are associated with mitochondrial membranes, and it is reported that the l-Opa1 attach to the inner mitochondrial membrane (IMM), and the s-Opa1 localize to the intermembrane space (IMS) next to the outer mitochondrial membrane (OMM) (Fulop et al. 2013) (see Figure 1.5).

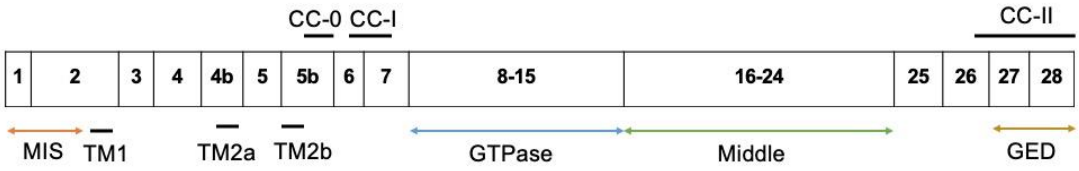

Figure 1.5 Schematic representation of human OPA1 structure. The *OPA1* gene is comprises 30 exons. 4, 4b and 5b are alternatively spliced leading to eight variants (isoforms 1-8). MIS, mitochondrial import sequence; TM, transmembrane domain; CC, coiled coil domain; GED, GTP effector domain.

1.4.2 OPA1, mitochondrial fusion

In humans and rodents, Opa1 protein regulates inner mitochondrial membrane (IMM) and cristae structure (Patten et al. 2014; Santarelli et al. 2015). Moreover, this protein contributes

to mitochondrial respiratory chain through ATP synthesis, and also plays an indispensable role in the cellular apoptosis pathway (Anand et al. 2014).

OPA1 is considered as a key factor in mitochondrial network dynamics, which shows a close collaboration with other GTPases involved in mitochondrial dynamics, such as Mitofusions, MFN1 and MFN2, and DRP1, a dominating pro-fission protein which also helps facilitate mitophagy and mitochondrial quality control (Meyer et al. 2017). Decreased function or loss of function of OPA1 through RNA interference or OPA1 gene knock-out causes healthy mitochondria to be fragmented, while overexpression of OPA1 protein causes elongation of the punctuated mitochondria (Cipolat et al. 2004; Griparic et al. 2004; Song et al. 2009), suggesting the alteration of OPA1 expression may disrupt the mitochondrial dynamic network and decrease the mitochondrial membrane potential, which leads to mitochondrial fragmentation. Interestingly, Misaka, T. et. al. found that exogenously introducing wide type mOPA1 resulted in fragmented mitochondria and accumulated ring-shaped mitochondrial fragments in the intermembrane space in COS-7 cells (Misaka et al. 2006), indicating *OPA1* overexpressed in healthy mitochondria may block its physiological pro-fusion ability. Spinazzi, M. et. al. found a novel deletion in the GTPase domain of OPA1 leads to defects in mitochondrial morphology and distribution, but the abnormalities did not affect respiration function, supporting the theory that OPA1 has a direct role in mitochondrial shape and distribution(Spinazzi et al. 2008).

1.4.3 OPA1, mitochondrial quality control

OPA1 is involved in fusion dynamics and also participates in mitochondrial quality control (MQC) and has a fundamental role in the maintenance of mitochondria (Alavi and Fuhrmann 2013). Mitochondria are reported to undergo frequent cycles of fusion and fission in the so-called ‘kiss and run’ pattern, which involves transient fusions between mitochondria. A study conducted by Twig, G. et. al. indicated mitochondria which were defective in OPA1 activity, with reduced membrane potential, were likely to have a reduced ability to ‘kiss and run’ and

move on to an active degradation by autophagy. One of the mechanisms is involved with the membrane potential dependent proteolytic cleavage of OPA1L isoforms and the research also concluded that the overexpression of OPA1 decreased mitochondrial autophagy (Twig et al. 2008; Youle and van der Bliek 2012). Another study showed that increased autophagy in optic nerve axons was likely to result from depolarized mitochondria in OPA1 mutant mouse model, which suggests that OPA1 mutation and fusion dysfunction may have a direct effect on mitochondrial autophagy (White et al. 2009). Moreover, Gomes, L. C. et. al. claim regulated changes in mitochondrial morphology such as mitochondria elongation, were able to prevent cells from autophagy and maintain the cell viability under starvation in mouse embryonic fibroblasts (MEFs) (Gomes et al. 2011). The Pink1/Parkin pathway plays an indispensable role in targeting mitochondria with reduced membrane potential to autophagosomes, and might decrease OPA1 and mitofusions, or increase DRP1 expression in order to promote fragmentation of mitochondria(Deng et al. 2008; Poole et al. 2008; Pilsl and Winklhofer 2012). Thus, subtle regulation of OPA1 pro-fusion ability may play a crucial role in mitochondrial network dynamics and quality control, which benefits long-term cell health, especially in some stress-vulnerable neurons like retinal ganglion cells (RGCs).

1.4.4 OPA1, cristae remodelling and apoptosis

OPA1 depletion is likely to be an important cause for spontaneous cellular apoptosis, which also supports the close connection between apoptosis and a mitochondrial dynamic network. Olichon, A. et. al. 2007 down-regulated OPA1 in Hela cells using RNA interfering technique and demonstrated fragmentation of mitochondria, decrease of membrane potential, disorganization of the cristae structure, release of cytochrome c and caspase-dependent apoptosis. Bcl-2 overexpression was shown to inhibit the OPA1 siRNA induced apoptosis in NIH-OVCAR-3 cells. It can be concluded that OPA1 not only plays a crucial role in organizing the mitochondrial inner membrane and maintenance of the cristae structure, but also is involved in the release of cytochrome c and could be one of the major targets for mitochondrial

apoptotic effectors (Olichon et al. 2003). Consistent with this, Zanna, C. and his colleagues claimed the a close relation between *OPA1* mutation and apoptosis by testing expression of apoptosis inducing factor (AIF) in fibroblasts derived from the skin of dominant optic atrophy (ADOA) patients (Zanna et al. 2008); Olichon, A. et al. 2007 also found that *OPA1* mutations resulted in a predisposition to apoptosis in fibroblasts from type-1 autosomal dominant optic atrophy (ADOA) individuals and Hela cells transfected with similar mutants through measuring the effects of pathogenic mutations of OPA1 on mitochondrial morphology and apoptosis (Olichon et al. 2007b). Moreover, the anti-apoptotic ability of OPA1 was reported as an independent function, which was induced through the mitochondrial pathway via inhibiting the release of cytochrome c, independent from the pro-fusion ability of OPA1.The mechanism was demonstrated to be related to the oligomerization of OPA1, regulating apoptosis through sustaining the tightness of cristae junctions (Frezza et al. 2006; Suen et al. 2008). Accordingly, ectopic OPA1 protein expression also showed protection to Mfn1 and Mfn2 double-knockout cells without attenuating the negative effects of fusion deficiency, suggesting that OPA1 may protect cells from apoptosis independently from mediating fusion network (Suen et al. 2008). The function of OPA1 in cristae remodelling maintains the normal cristae structure and is highly involved in anti-apoptotic potency (Olichon et al. 2003; Arnoult et al. 2005). OPA1 can form oligomeric interactions (long and short isoforms), which regulate the cristae integrity (i.e. tightness or apposition of cristae junctions) and also mitochondrial apoptosis through the regulation on the release of soluble cytochrome c within the cristae, see Figure 1.6 (Frezza et al. 2006). It has been demonstrated that the loss of OPA1 function or expression of *OPA1* pathogenic mutations plays an irreplaceable role in the disorganization of mitochondrial ultrastructure (Zanna et al. 2008; Zhang et al. 2017). There is a vicious cycle, with cytochrome c release rapidly and completely during apoptosis followed by the release of OPA1 soluble short forms. The mitochondrial leak of OPA1, causing disruption of OPA1 oligomerization at cristae junctions, results in the alterations of cristae structure and accelerates the continued release of cytochrome c into cytosol in a feed-forward method (Arnoult et al. 2005). Recently, it has been found that the short soluble isoforms of OPA1 alone could maintain the normal

mitochondrial cristae structure (Lee et al. 2017). Therefore, morphology alterations are proposed to modulate mitochondrial apoptosis precisely.

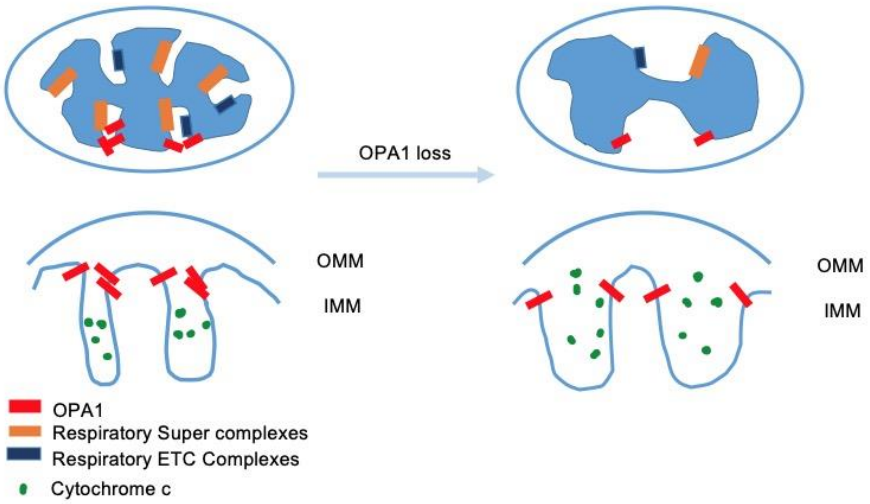

Figure 1.6 OPA1 mediates mitochondrial cristae remodelling. OPA1 situates at the cristae junctions to control the widening or constriction of cristae. The loss of OPA1 will cause excessively widened and dysfunctional cristae, and release of pro-apoptotic proteins including cytochrome c. OMM: outer mitochondrial membrane; IMM: inner mitochondrial membrane. (Diagram summarised from Baker et al. 2019).

Researchers have investigated the molecular mechanisms behind the anti-apoptotic function of OPA1. BNIP3 is a pro-apoptotic BH3-only protein of Bcl-2 family. The interaction between BNIP3 and OPA1 results in mitochondrial apoptosis by modulating the cristae structure, by the triggering of OPA1 complex disruption in a Bax- and/or Bak-dependent method and then leading to apoptosis (Landes et al. 2010a). Omi/HtrA2 is a serine protease which is thought to exert protective ability facing cellular stress (Dagda and Chu 2009). The loss of Omi/HtrA2 function resulted in the accumulation of reactive oxygen species (ROS), decreased mitochondrial membrane potential, elongated mitochondria with abnormal cristae structure and up-regulated soluble OPA1 protein. It suggested the direct interaction between Omi/HtrA2 and endogenous OPA1 is more likely to indicate a role of Omi/HtrA2 in the regulation of the

pro-fusion protein OPA1 under pathological cellular conditions (Kieper et al. 2010). Hypoxia-induced gene domain protein-1a (Higd-1a), which is a mitochondrial inner membrane protein, functions by specifically binding to OPA1 to prevent the cleavage and maintain the long isoforms of OPA1 in order to postpone the break-out of caspase-dependent apoptosis by inhibiting the release of cytochrome c (An et al. 2011; An et al. 2013). Another crucial effector related to OPA1 in the apoptotic pathway is presenilin-associated rhomboid-like (PARL), an inner mitochondrial membrane rhomboid protease. Both PARL and OPA1 are critical regulators of cristae remodeling, exerting an anti-apoptotic potency via close interaction (Gottlieb 2006; Pellegrini and Scorrano 2007). Additionally, there are 8 RNA transcript variants from alternative splicing of exons 4, 4b, and 5b (Akepati et al. 2008). The OPA1 transcripts splicing of exons 4 participates in mitochondrial fusion network, while those splicing of exons 4b or 5b are important for regulation of cytochrome c release (Olichon et al. 2007a).

1.4.5 OPA1, mtDNA maintenance

Mitochondria have their own genomes, called mitochondrial DNA (mtDNA), encoding 13 respiratory proteins, 22 transfer RNAs (tRNAs), and 2 ribosomal RNAs (Ishihara et al. 2015). Mutations of mtDNA are proposed to be associated with mitochondrial diseases such as neurodegeneration diseases presenting deficient mitochondrial respiratory capacity (Nunnari and Suomalainen 2012). Since mitochondria are highly mobile, fusing and dividing continually, it would be critical to allow mitochondria to exchange contents including mitochondrial DNA. Mitochondrial fusion shows a strict link with the maintenance of the mitochondrial genome, and pathological profiles would emerge in the absence of mitochondrial fusion, such as mtDNA depletion syndromes (Copeland 2008). There is emerging evidence that OPA1 is intimately linked to the mtDNA stability by stabilizing mtDNA copy number. Conversely, the deletion of *OPA1* may cause loss of the mtDNA nucleoids (Chen et al. 2007; Chen et al. 2010a). Accordingly, Amati-Bonneau and her colleagues collected 8 patients from 6 independent families with *OPA1* gene mutations, performing sequencing of mtDNA and analysis of mtDNA

deletions and copy number, finally demonstrating that certain *OPA1* mutations induce mtDNA multiple deletions and play a significant role in mtDNA instability (Amati-Bonneau et al. 2008). Furthermore, they also demonstrated that silencing of the *OPA1* variants containing exon 4b resulted in mtDNA depletion, inhibition of mtDNA replication and marked alteration of mtDNA distribution. A small hydrophobic 10-kDa peptide from cleavage of the exon 4b included isoform showed direct interaction with TFAM, POLV and mtDNA, suggesting exon 4b containing *OPA1* variants may exert a direct actor in the maintenance of mitochondrial genome integrity (Elachouri et al. 2011).

1.4.6 OPA1, bioenergetics metabolism

Mounting evidence suggests that increased levels of OPA1 could improve respiratory chain efficiency and reduce tissue damage, while OPA1 mutations may result in energetic defects. OPA1 is located in the inner mitochondrial membrane (IMM) and participates in the activation of the dynamin, indicating that it has an indispensable function in energy metabolism and Opa1 mutations could cause energetic defects (Carelli et al. 2007; Civiletto et al. 2015). Consistently, Kushnareva, Y. et al. 2016 found that partial OPA1 deficiency caused mitochondrial respiratory deficiency and a selective loss of respiratory Complex IV subunits using a heterozygous *OPA1* mutant mouse carrying a defective allele (Kushnareva et al. 2016). Furthermore, co-immunoprecipitation assays showed direct interactions between OPA1, apoptosis inducing factor (AIF) and subunits of complexes I, II and III in *OPA1* mutated fibroblasts (Zanna et al. 2008). Respiratory complex IV activity and the steady-state of subunits were also decreased due to *OPA1* mutations (Agier et al. 2012; Takahashi et al. 2017). They revealed that OPA1 had a direct function in the stabilization of the whole respiratory chain. Cogliati, S. and her colleagues investigated in the mouse model of *OPA1* conditional ablation and found the mitochondrial cristae shape determines the assembly and activity of the mitochondrial respiratory chain complexes, independently from changes to mitochondrial protein synthesis or the permeabilization of apoptotic OMM

permeabilization(Cogliati et al. 2013), indicating the significant link between membrane morphology and mitochondrial function. There are some new investigations indicates that OPA1 are likely to stabilize the respiratory chain complexes and convert energy during stochastic drops in mitochondrial membrane potential (Deltapsim) *via* a transient matrix alkalinisation renamed “mitopHflashes” (Santo-Domingo et al. 2013; Rosselin et al. 2017). Strikingly, Lee, H. and his colleagues found that short forms of OPA1 alone could maintain oxidative phosphorylation function by testing the growth in oxidative phosphorylation via measuring the respiration and levels of the respiratory complexes and hence concluded short forms of OPA1 may be fully competent for sustaining mitochondrial energetics (Lee et al. 2017).

1.5 Experimental models of ADOA

The pathophysiology of ADOA is associated with several mechanisms such as mitochondrial network disorganization, bioenergetic deficits and increased mitochondrial apoptosis. However, the exact mechanisms are still not clear, and their relative importance is uncertain. The creation of experimental models is important to provide insight and understanding of the pathophysiological mechanisms that lead to ADOA.

1.5.1 *OPA1* mutant mouse models

Because of the typical phylogenetic similarities and physiological similarities between mice and human, as well as the availability of the complete genome sequence of an experimental mouse stain, C57BL/6J, researchers developed numerous genetic mouse models to mimic the physiological and pathological process of human disorders (Perlman 2016). Although there are some anatomical differences between two species in the eye, such as fewer numbers and types of cone photoreceptors, lacking a foveal pit and a macular clustering of cones, mouse models are still playing a central role in replicate key features of human genetic conditions in the eye.

1.5.1.1 B6;C3-*Opa1*^{Q285STOP} mutant mouse model of ADOA

This mouse model of ADOA was utilized in the experimental work in this thesis. The model was generated by screening an ENU-mutagenized DNA archive from 10,000 C3H male mice for point mutations in *OPA1* exons 1, 8, 9, 10, 12 and 28. The exons were amplified using heteroduplex analysis by temperature gradient capillary electrophoresis (TGCE: Spectu Medix). By sequencing the positive fragments, 5 SNPs were found. A heterozygous nonsense mutation in exon 8, coding for a C-T transition at 1051 bp was selected. This mutation introduces a STP codon and is predicted to cause protein truncation (Gln 285 to Stop: Q285X) at the beginning of exon 8, which is also the start of the dynamin GTPase, a domain where a number of human disease -causing mutations locate. The mutant mouse line was established by using sperm to generate heterozygous hybrid *Opa1*$^{+/-}$ 'founders' (Davies et al. 2007).

The visual function in the *Opa1*^{Q285STOP} mutant mice has been reported at the age of 6, 12, 13 and 18 months using a rotating optokinetic drum with high (2°, 0.25 cycles/degree) to low (4° and 8°, 0.125 and 0.0625 cycles/degree) resolution gratings. The mean tracking frequencies were significantly decreased at both high and low spatial frequencies in the age of 12 and 13 months compared to C57Bl/6 controls, while the difference between the two groups was significant only for the low resolution (8°) grating but not for the high (2°) grating (Davies et al. 2007; Yu-Wai-Man et al. 2009a). Visual electrophysiological testing (ERGs and VEPs) has been performed *in vivo* at 11 to 13 months and showed functional deficits in electrophysiology (reduced PhNR) consistent with ganglion cell dysfunction, which may be correlated with the decrease in the dendritic arborisation of RGCs (Williams et al. 2010; Barnard et al. 2011). Neurological examination was also carried out on control and *Opa1* mutant groups by the primary SHIRPA screen for general health and neurological measures since OPA1 is ubiquitously expressed throughout the body not only in the retina but also in the neuromuscular tissue (Alexander et al. 2000). The SHIRA neurological testing revealed subtle systemic neurological and neuromuscular defects, including locomotor activity (Davies et al.

2007). Moreover, aged heterozygous *Opa1*$^{+/-}$ mice showed decreased fractional shortening, cardiac output and myocyte contraction compared to the wildtype littermates, coincided with the onset of blindness (Chen et al. 2012).

In terms of the retinal ganglion cell populations, in our lab Williams et al. 2010 and Davies et al. 2007 previously demonstrated that no apparent difference existed in RGC survival or morphology between WT and Opa1$^{+/-}$ mice before 10 months of age (including dendritic field area, total dendritic length, and dendritic complexity) (Davies et al. 2007; Williams et al. 2010). However, *Opa1*$^{+/-}$ mice began to show significant abnormalities in the myelin bundles and optic nerve fascicles after 9-month-old, such as whirls of myelin, watery and dark degeneration in the optic nerve axons. In addition, a significantly higher percentage of axons with disorganized myelin (clumping) were observed at 24-month-old compared to the controls by electron micrographs of optic nerve axons (Figure 1.7) (Davies et al. 2007; White et al. 2009). Selective dendropathy of RGCs occurs in the *Opa1* mutant mouse after 10 months. Progressive dendritic atrophy was localized to sublamina *b* of the inner plexiform layer in retinal ganglion cells of the *OPA1* mutant mice from as early as 10-month old without retinal ganglion cell loss, while no detectable changes in dendritic morphology were found in off-centre retinal ganglion cells. The reason might be the partially separated visual pathways for on- and off-centre RGCs with different stimulus and neurotransmitter requirements at the thalamic and cortical levels. It could also relate to the steep energy demand required by on-centre RGCs compare to the off-centre RGCs (Williams et al. 2010), suggesting the disturbance of mitochondrial fusion caused by OPA1 deficit may destroy the dendritic morphology of retinal ganglion cells in on-centre RGCs. Moreover, a significant reduction in the retinal ganglion cell synaptic connectivity was also detected, with decreased levels of postsynaptic density protein 95 (PSD95) in *OPA1* mutant mice, accompanied with a synaptic loss in the inner plexiform layer. OPA1 deficiency also caused reduction of glutamatergic but not GABAergic synaptic sites and elevation of synaptic vesicle number in bipolar cell terminal arbours, also indicating the selective dendropathy of on-centre RGCs caused by OPA1 haploinsufficiency (Williams et al. 2012b).

Mitochondrial morphology assessment (length, cristae to matrix ratio and dendritic

mitochondrial index) was carried out and shown a significant decrease in *Opa1*$^{+/-}$ RGCs compared with the wildtype controls (Williams et al. 2012b). Accordingly, Kushnareva et al. 2016 demonstrated a higher percentage of cells with fragmented morphology of mitochondria in the MEFs from *Opa1* mutant mice compared to the wild-type MEFs. Moreover, a significant bioenergetic deficiency and consistently a considerable decreased activity of mitochondrial complex IV were also found by detecting the per minute oxygen consumption rates (OCR) (Kushnareva et al. 2016). In addition, a significant increase in the number of autophagosomes in the RGC layer was observed in heterozygous mutant mice at 24 months, indicating increased autophagy and a critical sign of optic nerve degeneration (White et al. 2009). Further research on mitophagy in ADOA has been done on mouse embryonic fibroblasts (MEFs) as well as splenocytes isolated from *Opa1*^{Q285STOP}/RedMIT/GFP-LC3 mice and demonstrated increased mitophagy under OPA1 deficit (Diot et al. 2018). Reduced mtDNA copy number, decreased expression of nuclear antioxidant genes at were found in heterozygous Opa1+/- mice at 3 to 4 months and impaired cardiac mitochondrial function were demonstrated in aged heterozygous Opa1$^{+/-}$ mice (Chen et al. 2012).

Thus the B6;C3-*Opa1*^{Q285STOP} mutant mouse model of ADOA provides a direct means to investigate the cellular pathophysiology of ADOA, and it is also utilized in our project to illustrate the mitochondrial morphology and dynamics in RGCs under OPA1 deficit.

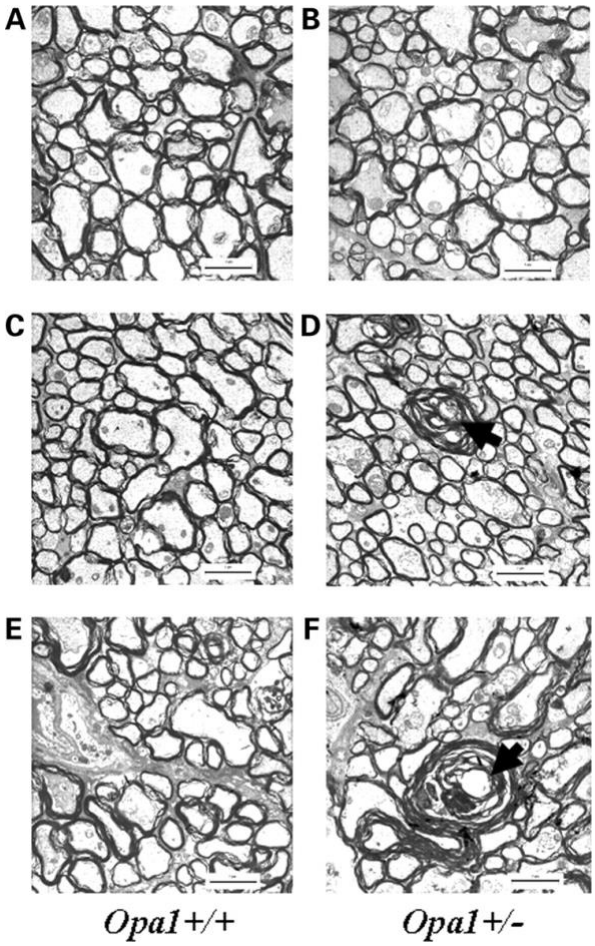

Figure 1.7 Transmission electron micrographs of optic nerve taken from B6;C3-*Opa1*^{Q285STOP} mutant mouse model of ADOA. (A, C, E) control groups; (B, D, F) Opa1$^{+/-}$ groups. The optic nerves appear comparable at 6 months old between genotypes (A, B); however, show evidence of anomalies in the optic nerve such as whirls of myelin (black arrows) by 9 months old (C, D), which continued to 18 months old (F). Scale bar = 2 μm (Image from Davies et al. 2007, copyright license #4927970479995).

1.5.1.2 Other mouse models of ADOA

B6; C3-*Opa1*$^{329\text{-}355del}$ mutant mouse model of ADOA

This mutant mouse model was also generated by gene-based screening an ENU-mutagenized DNA library of mouse DNA. The mutant mouse model was established *via* a mutant, carrying a heterozygous mutation in intron 10 (c.1065 +5 G $\rightarrow$ A) of *OPA1* gene,

rederived from the corresponding sperm archive by *in vitro* fertilization. The mutation causes skipping of exon 10 in the transcripts, which results in an in-frame deletion of 27 amino acid residues (p.329-355del) in the GTPase domain of OPA1. The heterozygous mutants (*Opa1*$^{enu/+}$) show a reduction in OPA1 protein levels to about 50% compared to the wildtype littermates (Alavi et al. 2007). Of interest, this mutant mouse model showed an age-dependent progressive loss of RGCs. The number of RGCs were reduced by approximately 50% compared to the control group at 13 months of age. Lately, it has been demonstrated that the functional properties of RGCs (spatial and temporal frequency tuning as well as sustainedness) are affected differently in Opa1$^{enu/+}$ and WT retinas at old age based on the data from multielectrode array recordings. This may be associated with the decreased RGC survival in mutant mice compared to the wild-type in this model (Gonzalez-Menendez et al. 2015). The differences between genetic models could be related to changes in the protein, haploinsufficiency, or genetic background differences.

Age	**Groups compared by unpaired *t*-test**	**Area**	**RGC (mm^2) ± SE**	***P*-value**
2 months	Control (*n* = 10)	Whole retina	3578 ± 113	
	Heterozygous (*n* = 12)		3022 ± 86	0.0007***
	Control	Central	4286 ± 138	
	Heterozygous		3730 ± 68	0.0029**
	Control	Mid-peripheral	3610 ± 134	
	Heterozygous		3111 ± 121	0.0119*
	Control	Peripheral	2840 ± 209	
	Heterozygous		2226 ± 47	0.0054**
9 months	Control (*n* = 4)	Whole retina	3204 ± 44	
	Heterozygous (*n* = 6)		2378 ± 71	0.0002***
	Control	Central	3896 ± 241	
	Heterozygous		3095 ± 237	0.0526

	Control	Mid-peripheral	3149 ± 151	
	Heterozygous		2424 ± 116	0.0047**
	Control	Peripheral	2388 ± 161	
	Heterozygous		1615 ± 114	0.00391**
13 months	Control (*n* = 2)	Whole retina	3063 ± 219	
	Heterozygous (*n* = 2)		1467 ± 31	0.0187*
	Control	Central	3539 ± 161	
	Heterozygous		1616 ± 199	0.0171*
	Control	Mid-peripheral	3173 ± 269	
	Heterozygous		1526 ± 225	0.0424*
	Control	Peripheral	2478 ± 228	
	Heterozygous		1260 ± 68	0.0359*

Table 1.4 Retinal ganglion cell survival in *Opa1*$^{enu/+}$ and littermate controls of different ages. To investigate changes within the different areas of the retina, results were subdivided into whole retina, central, mid-peripheral and peripheral sectors. Retinal ganglion cells were identified by retrograde labelling and counted in a semi-automatic fashion (cells/mm^2, means ± SEM). Statistical significance assessed by unpaired *t*-test: *p < 0.05, **p < 0.01, ***p < 0.001 vs controls. (Table from Alavi et al. 2007, copyright licence #4927990329777).

Alavi et al report that “there was a complete loss of large-calibre axons” (however, we cannot be sure that large axons were lost and can only assume that they saw a change in axon diameter profile), a disorganized structure, axonal swelling and distorted shapes of axons in *Opa1*$^{enu/+}$ mice, as well as membranous whorls and loss of myelin sheets under transmission electron microscopy. There was also an increased content of collagenous material and a decreased number of neurofibrils in the optic nerve. However, the mouse model showed no significant differences in the mitochondrial copy number or electroretinographic recordings between *Opa1*$^{enu/+}$ mice and control group. Also, the mutation in this mouse model showed no effect on the auditory system.

Opa1^{delTTAG} mouse model of ADOA

This is an *Opa1* knock-in mouse model carrying the recurrent *OPA1* c.2708_2711delTTAG mutation in exon 27 (Sarzi et al. 2012) which is found in 30% of patients of ADOA. Notably, the *OPA1*^{delTTAG} protein isoforms cannot be found in mutant tissues in those ADOA patients carrying this *OPA1* truncating mutation, substantiating a pathophysiological mechanism based on haploinsufficiency. Interestingly, the *OPA1*^{delTTAG} mutation is differentially expressed in mouse tissues, with a 25% reduction in the CNS tissues (brain, retina, optic nerve) and glycolytic fibres, whereas a 50% reduction in the oxidative fibres and heart. The mitochondrial DNA content is found upregulated in the CNS tissues but decreased in the oxidative tissues. Secondly, the *OPA1*^{delTTAG} mutation also leads to a common mitochondrial cytochrome oxidase defect in retina, optic nerve and glycolytic muscle fibres, but no difference in the brain, oxidative muscle and heart. Specifically, the deficiency of cytochrome oxidase activity in the optic nerve occurs until 11 months, indicating that the increased mtDNA in this tissue is likely to compensate the cytochrome oxidase activity in the RGC axons or glial cells along this nerve. Moreover, significant axonal autophagy and mitophagy were found in retinal ganglion cells and peripheral neurons, accordantly with the degenerated myelin. Structural and metabolic brain alterations were found in the *Opa1*$^{+/-}$ mutant mice by MRI and magnetic resonance spectroscopy analyses which might be related to the neuronal symptoms. Finally, the progressive deafness was also found in *Opa1*$^{+/-}$ mutant mice which develops with age and begins with the impairment of high-frequency perception. Thus, the *OPA1*^{delTTAG} mouse model mimics the multi-systemic degeneration which occurs in the ADOA “plus” and also supports the potential role of ageing involved in the development of clinical features and pathological process. In short, the *OPA1*^{delTTAG} mouse model plays a promising role in the further research on multi-systemic pathological development of ADOA as well as other neurodegenerative diseases (Sarzi et al. 2012).

1.5.2 Other animal models of ADOA

OPA1 mutant invertebrate models has also been established in *Caenorhabditis elegans* and *Drosophila*. In *Caenorhabditis elegans*, the mutation of *eat-3* gene, which is homologous to *OPA1*, was demonstrated to cause mitochondrial fragmentation consistent with the presentations of mutations in mammalian cells. Additionally, the inner membrane septa accumulated and divided the matrices of fragmented mitochondria, indicating a particular dysfunction in mitochondrial network. Moreover, the mutants are hypersensitive to oxidative stress stimulus and free radicals might get involved in the pathological process of *Caenorhabditis elegans eat-3* mutations (Kanazawa et al. 2008). Adult homozygous *Drosophila* mutants was generated by mutant *dOPA1* (CG8479), a ortholog of human *OPA1*. The *dOPA1* mutation resulted in an increase in production of reactive oxygen species (ROS) and mitochondrial fragmentation. Anti-oxidants were likely to reverse the pathological results caused by *dOPA1* mutation, thus ROS might play a crucial role in the pathologic process (Yarosh et al. 2008). Thus, both of the invertebrate models suggest the relative role of ROS involved in *OPA1* mutations, indicating the potential role of anti-oxidants in the treatment of ADOA.

1.5.3 Human induced pluripotent stem cells (hiPSCs) in modelling ADOA

Human induced pluripotent stem cells (hiPSCs), derived from skin or blood cells and then reprogrammed back into an embryonic-like pluripotent state, enable the differentiation into cells of all embryonic germ layers including ectoderm, mesoderm, and endoderm; and also provide an unlimited supply of patient-specific pluripotent stem cells (Lowry et al. 2008). Thus, the differentiation of hiPSCs into RGCs could serve as an ideal model for ADOA *in vitro* and provide tremendous potential for optic neuropathy research. Takahashi and Yamanaka 2006 first reprogrammed mouse embryonic and adult fibroblasts into a pluripotent state through four

transcription factors (*Oct3/4, Sox2, Klf4,* and *c-Myc*) related to the maintenance of pluripotency in embryonic stem cells (Takahashi and Yamanaka 2006). Afterwards, various modified protocols for hiPSCs were developed by researchers for its prospective role in the development of personalized treatment. Here listed are some protocols for transforming somatic cells to hiPSCs (Table 1.5) and differentiating hiPSCs to RGCs (Table 1.6) (Ji and Tang 2019).

Solutions are still required for the challenges existing in the present protocols. For example, the culture condition for the reprogramming procedure from somatic cells should be under feeder-free, xeno-free and integration-free conditions to get rid of the risk of graft rejection and genotoxicity. A highly efficient, robust and reproducible protocol is still required to be developed in order to better model disease to investigate the precise pathological mechanisms of ADOA and eventually personalized treatment.

Cell source	***Culture condition***	***Reprogramming factors***	***Delivery method***	***Time length (d)***
Human fibroblasts	Cell feeder	Oct4, Sox2, Nanog, Lin28	Lentivirus	15 (Yu et al. 2007)
Human fibroblasts	Cell feeder	Oct3/4, Sox2, Klf4, Sall4	Retrovirus	25 (Tsubooka et al. 2009)
Human blood mononuclear cells	Cell feeder	Oct4, Sox2, Klf4, C-myc, Lin28	Plasmid	14 (Chou et al. 2011)
Human keratinocytes	Cell feeder	Oct4, Sox2, Klf4, C-myc, Rem2	Retrovirus	12 (Edel et al. 2010)
Human fibroblasts	Xeno-free, feeder-free	Oct3/4, Sox2, C-myc, Klf4	Lentivirus	7-14 (Lu et al. 2014)

Table 1.5 Examples of protocol for reprogramming somatic cells to iPSCs (adapted from

Ji and Tang 2019).

Differentiation procedure	***Differentiation culture medium***	***Culture condition***	***Time length (d)***
EBs, neurosphere, RGCs	ES medium, DAPT	Gelatin pretreated, laminin coated	21 (Riazifar et al. 2014)
Neural, retina-like structures, RGCs	Proneural medium, FGF2, DAPT	Xeno-free, coating-free	21 (Reichman et al. 2014)
EBs, neurospheres, RGCs	NIM, FBS, RDM, BDNF	Coating-free	40 (Ohlemacher et al. 2016)
Neural aggregates, RGCs	mTeSR1 medium, NIM, RDM	Matrigel coated	15 (Li et al. 2017)
Neural rosettes, RGCs	Basal medium, Shh, FGF, DAPT, CNTF	PDL/Laminin matrigel coated	15 (Teotia et al. 2017)

Table 1.6 Examples of protocol for differentiating hiPSCs to RGCs (adapted from Ji and Tang 2019).

1.6 Hypothesis

OPA1 plays an important role in the pathophysiology of ADOA, causing visual dysfunction and even systemic disabilities. *OPA1* is also involved in the mitochondrial dynamic network and the *OPA1*^{Q285STOP} mutation has been demonstrated to cause mitochondrial dysfunctions in MEFs and fibroblasts in previous studies. Moreover, RGCs are preferentially affected in most ADOA patients. They have been demonstrated to be far more vulnerable to Opa1 dysfunction than other neuronal cell types.

There are many unanswered questions concerning the roles of mitochondrial dynamics in

retinal ganglion cell health and the progression of cell death. For example, how does OPA1 expression change RGC mitochondrial morphology? How does the imbalance of fusion and fission network precede the progress of RGC cell death?

Thus, we hypothesize that the alterations in mitochondrial dynamics during early asymptomatic stages of ADOA precede the neurodegeneration and consequent RGC cell death.

1.7 General aims

To explore the role of mitochondrial dynamics in retinal ganglion cell health by comparing the difference in mitochondrial morphology, dynamics and bioenergetics between RGCs cultured from B6; C3-*OPA1*^{Q285STOP} mutant and wild-type mice.

Chapter 2. General Materials and Methods

2.1 Reagents used

0.1 M Phosphate buffered saline pH 7.4 (1X PBS):

137 mM sodium chloride, 2.7 mM potassium chloride, 10 mM sodium phosphate dibasic, and 2 mM potassium phosphate was made up in 1 litre double distilled water. The pH was adjusted to 7.4 using PH meter (pH211, Hanna instruments, Italy). The solution was autoclaved at 121 °C for 20 minutes and then stored at room temperature. The working solution of 0.1 M phosphate buffered saline was obtained by diluting in double distilled water.

4% Paraformaldehyde pH 7.4:

800 ml of 1X PBS was added into a glass beaker on a stir plate in a ventilated hood and then heated to approximately 60 °C with care taken not to boil. 40 g of paraformaldehyde powder was added into the heated PBS solution. 1 N NaOH dropwise from a pipette was added into the solution to slowly raise the pH. The solution was cooled and filtered when the paraformaldehyde was thoroughly dissolved. 1X PBS was used to adjust the final volume of the solution to 1 litre. The pH of the solution was checked again and adjusted by small amounts of 1N HCL to approximately 6.9. The solution was dispensed into aliquots for storage at -20 °C.

BSA (4%)

8 g of BSA (SigmaAldrich A4161) powder was dissolved in 150 mL of D-PBS at 37˚C. Then pH was adjusted to 7.4 with 1N NaOH. Add D-PBS to bring the volume to 200 mL. The solution was filtered by a 0.22-µm filter (Starlab, UK) and stored at –20˚C.

DNase (0.4%)

12,500 units of DNase (Worthington LS002007) was dissolved in 1 mL of EBSS (Sigma-

Aldrich E6267). The solution was filtered and stored in 200-µL aliquots at –20˚C.

High-ovomucoid (high-ovo) stock solution (6×)

6 g of BSA and 6 g of Trypsin inhibitor (Worthington LS003086) was dissolved in 189 mL of D-PBS and then the pH was adjusted to 7.4 with 10N NaOH. The volume was brought to 200 mL with D-PBS. The solution was filtered and stored in aliquots at –20˚C.

Low-Ovomucoid (low-ovo) Stock Solution (10×)

3 g of BSA and 3 g of trypsin inhibitor was dissolved in 200mL of D-PBS. The pH was adjusted to 7.4 by 1 N NaOH. The solution was filtered and stored in aliquots at –20˚C.

Immunopanning purification reagents

Goat anti-mouse IgG + IgM (H + L) (Jackson ImmunoResearch 115-005-044)

Lectin from Bandeiraea simplicifolia (BSL-1; Vector Labs L-1100) (5 mg/mL)

Mouse anti-mouse Thy1.2 (CD90) IgM (Serotec MCA02R)

Insulin stock (0.5 mg/mL)

10 mg of insulin (Sigma-Aldrich I6634) and 20 mL of sterile water was mixed with 100 µL of 1.0 N HCl. The solution was filtered and stored at 4°C for 4–6 weeks.

Laminin (mouse) (Cultrex; R&D Systems 3400-010-01)

10-µL aliquots were made and stored at −80˚C.

Tris-HCl (50 mM, pH 9.5, sterile)

12.1 g of Trizma base was dissolved in 200 mL of sterile water. The pH was adjusted to 9.5 with HCl.

BDNF Stock (50 µg/mL)

50 µg of human brain-derived neurotrophic factor in powder form (BDNF; Peprotech 450-02) was resuspended in 50 µL of cold, sterile 0.2% BSA. Then the solution above was mixed with 950 µL of 0.2% BSA. and make aliquots. The solution was filtered , flash-freezed in liquid nitrogen and stored in 20-µL aliquots at –80˚C.

Ciliary Neurotrophic Factor (10 µg/mL)

Ciliary neurotrophic factor (CNTF; Peprotech 450-13) was diluted to 10 µg/mL in sterile 0.2% BSA. The solution was filtered , flash-freezed in liquid nitrogen and stored in 20-µL aliquots at –80˚C.

Forskolin Stock (4.2 mg/mL)

1 mL of sterile DMSO was added to a 50-mg bottle of forskolin (Sigma-Aldrich F6886) and then the solution was transferred to a 15mL conical tube and add an additional 11 mL of DMSO was added to achieve a final concentration of 4.2 mg/mL. The solution was filtered and stored in 20-µL aliquots at –20˚C.

NAC Stock (5 mg/mL)

50 mg of N-acetyl-L-cysteine (NAC) powder (Sigma-Aldrich A8199) was dissolved in 10 mL of Neurobasal Medium (Gibco). The solution was filtered and stored in 20- and 80-µL aliquots at –20˚C.

SATO Supplement (100×)

5 mg of progesterone (Sigma-Aldrich P8783) and 200 µL of ethanol were mixed to make a progesterone stock solution. 4 mg of sodium selenite (Sigma-Aldrich S5261) was mixed with 10 µL of 1 N NaOH in 10 mL of Dulbecco's modified Eagle's medium (DMEM; Gibco 11960-044). 2 g of BSA, 2g of Transferrin, 320mg of Putrescine (Sigma-Aldrich P5780), 50 µL of Progesterone stock solution and 2 mL of sodium selenite stock solution were combined together. The solution was mix gently and brought to a total volume of 200 mL in DMEM. The solution was filtered and stored in aliquots at –20˚C.

Thyroxine (T3) Stock (4 µg/mL)

3.2 mg of 3,3′,5-triiodo-L-thyronine sodium salt (T3; Sigma-Aldrich T6397) was dissolved in 400 µL of 0.1 N NaOH. 10 µL of T3 solution was added to 20 mL of Dulbecco's phosphatebuffered saline (D-PBS; Gibco 14287). Filter through a 0.22-µm filter, discarding the first 10 mL. The solution was filtered and the first 10 mL of the solution was discarded. Aliquots were stored at –20˚C.

RGC Growth Medium

The RGC growth medium was constituted by specific medium and nutrient factors as follows, the growth medium should be warmed up to 37°C prior to cell culture, which could be stored at 4°C for up to 3 days.

Reagents	Volume
Neurobasal medium	9.5 mL
DMEM medium	9.5 mL

Insulin stock (0.5 mg/mL)	10 µL
Sodium pyruvate 100mM	200 µL
SATO supplement100x	200 µL
T3 stock	200 µL
Glutamax (Gibco)	200 µL
NS21 (Gibco)	400 µL
NAC stock	20 µL
Forskolin stock	20 µL
BDNF stock	20 µL
Ciliary neurotrophic factor	20 µL

Table 2.1 The constitution of RGCs growth medium. The neurotrophic and growth factors were dissolved into prewarmed mixture of neurobasal and DMEM medium, i.e. Insulin, sodium pyruvate, L-glutamine, forskolin, NS21 supplement, bran-derived neurotrophic factor (BDNF) and ciliary neurotrophic factor (CNF) etc.

2.2 General methods

2.2.1 Breeding strategy

The heterozygous *Opa1* mutation B6; C3-*Opa1*^{Q285STOP} was generated as previously described (Davies et al. 2007). The founder generation mice were outcrossed to C57BL/6J (Charles River, UK) and the experiments were performed on the mice bred from generations 8 to 9. Mice were genotyped by *Opa1* allele-specific polymerase chain reaction (Davies et al. 2007). All animal procedures were performed under license (PPL 30/3268 held by PI M Votruba) in accordance with the UK Home Office Animals Scientific Procedures (Animals) Act (1986) and the ARVO Statement for the Use of Animals in Ophthalmic and Vision Research.

The Cardiff University Biological Standards Committee approved the experimental protocols, and the work was approved under a Home Office Personal Licence (PIL) for SS. We followed the guidelines of the Animal and Plant Health Agency for compliance with Regulation (EC) 1069/2009 and implementing Regulation (EC) 142/2011 for the transport, storage, use and disposal of animal by-products.

2.2.2 Genotyping

DNA extraction

Pups aged six to seven days were used for RGC culture. DNA was extracted from mouse tail tissue or ear clips. Mouse tissue was lysed at 95°C for 45 min with 75 µL of NaOH solution (25 mM NaOH + 2mM EDTA) followed by cooled down on ice for 10 minutes and neutralised with 75 µl of 40mM Tris-HCl solution per sample.

PCR reactions

Two reactions were carried out with two sets of primers for genotyping of *OPA1* mutant mice. The forward primer F1: 5′- TCTCTTCATGTATCTGTGGTCTTTG-3′ was identical for both reactions amplifying wild-type and mutant alleles. The two reverse primers: R1: 5′TTACCCGTGGTAGGTGATCATG-3′ and R2: 5′-TTACCCGTGGTAGGTGATCATA-3′ were designed to bind specifically to amplify the wild-type and mutant allele, respectively. Primers were designed using Primer3 software (Whitehead Institute for Biomedical Research, USA). For each reaction 2 µl of extracted DNA was amplified with 1 µl of forward and reverse primer respectively in a 15 µl reaction PCR mix (BioMix Red; Bioline, UK). PCR reactions were ran on TC-512 Techne Thermal Cycler (Techne Inc., US) and performed with initial denaturation for 5 minutes at 94°C followed by 35 cycles of denaturation (1 minute at 92°C), annealing (1 minute at 59°C) and elongation (1 minute at 72°C) after which a final elongation at 72 °C for 5 minutes.

Agarose gel electrophoresis

3g of agarose (Invitrogen) was dissolved in 197ml TBE buffer and then slightly heated in a microwave oven in order to be mixed thoroughly. Thereafter, the solution was cooled down by running water to room temperature. 10 µl of Ethidium bromide was added into 100ml TBE buffer. The solution was poured to the casting tray containing a sample comb and allowed to solidify at room temperature for approximately 1 hour. After that, the sample comb was removed and each well was loaded by 15 µl of PCR samples. Electrophoresis was run in the electrophoresis chamber with the gel completely covered with TBE buffer at 80 V for approximately 30 minutes. PCR products were separated by 1.5% agarose gel electrophoresis in TBE (Tris-borate-EDTA) buffer. 9 µl of 100 bp DNA ladder was added to a well for size determination. DNA fragments were visualized by UV light (UVITECH transilluminator).

2.2.3 Two-step immunopanning method for RGCs isolation

All procedures for RGCs culture were carried out on 6 to 7-day-old *Opa1*$^{+/-}$ and WT mouse pups using a two-step immunopanning protocol adapted from Winzeler and Wang (Winzeler and Wang 2013) with minor modifications. Briefly, the retina was dissected out from the mouse eye and dissociated and triturated into cell suspension. Afterwards, cells were purified by two negative panning plates coated with Lectin from Bandeiraea simplicifolia (BSL-1; Vector Laboratories Ltd., UK) to remove the contaminating cell types and RGCs were finally selected by one positive panning plate coated with Thy1.2 (CD90) IgM (Serotec MCA02R, Bio-Rad Laboratories, Inc.) for 45 min at room temperature (25 ˚C).

RGCs were collected and then seeded on glass coverslips (Academy Science Limited, UK) coated by Poly-D-lysine (Sigma-Aldrich Corp., St. Louis, MO, USA) and laminin (R&D systems, UK) with a seeding density of 50,000 RGCs per well in 24-well culture plates (Nunc™,

Thermofisher, UK). RGCs were cultured in a humidified atmosphere at 37 ˚C under 10% CO_2, in serum-free growth medium as previously described (Winzeler and Wang 2013). The two-step immunopanning method can yield RGCs with high purity (>80%) from rodents in published research (Barres 1988; Kamei et al. 2005; Gao et al. 2016; Hu et al. 2017). In our lab, the purity of cultured RGCs was identified by co-staining of anti-Thy 1.2 antibody and anti-RBPMS antibody (Abcam).

Steps	***Description***	***Time duration (min)***
1	Retinal dissection on 16-20 mouse pups	35-50
2	Papain dissociation	45
3	Trituration and low-ovo incubation	15-20
4	Spin in low-ovo and high-ovo medium	24-30
5	Negative panning in the plates coated with BSL-1	40-45
6	Positive panning in the plate coated with Thy 1.2 antibody	45
7	Trypsin digestion and RGCs collection	20-25
8	Count and plate cells	5-10
	Total time duration	Approximately 7 to 8 hours

Table 2.2 Major steps and time consumption of two-step immunopanning method. The retina was dissected out from the mouse eye and dissociated and triturated into cell suspension, followed by negative and positive panning process. The selected RGCs were then plated and cultured in the RGCs specific growth medium.

2.3 Mitochondrial staining with Mitotracker®Red CMXRos

2.3.1 Staining of cell cultures

Cells were grown on glass coverslips (Academy Science Limited, UK) in a 4-well culture plate (Nunc) in RGC growth medium. The growth medium was then removed and replaced by pre-

warmed (37 ˚C) staining solution containing 100nM MitoTracker®Red CMXRos (Molecular Probes, Invitrogen). After 30 min incubation at 37 ˚C, the cells were washed in fresh, pre-warmed 1XPBS and then cultured in fresh RGC growth medium for live cell staining.

2.3.2 Image analysis

Images were captured using a Zeiss LSM 880 confocal microscope and Zen Zeiss Blue 2.1 software under MtRed filters (Carl Zeiss, UK). A 63X oil magnification lens were used. All images were captured with the same gain, intensity and exposure time. Time-lapse imaging method was used to measure the morphology and motility of mitochondria.

2.4 Immunofluorescence

2.4.1 Staining of cell cultures

Cells were grown on 4-well slide chamber (Nunc) in RGC growth medium. The medium was then removed and replaced by 4% paraformaldehyde in PBS pH7.4 for 10 min at room temperature. The cells then washed thoroughly in ice-cold 1XPBS three times for 20 min. After that cells were incubated with 1XPBS containing 0.1%TritonX-100 followed by washed in 1XPBS three times for 10 min. Thereafter, cells were incubated with 1%BSA in PBST (containing 0.05% Tween 20) for 1 h at room temperature. The cells were then incubated with diluted antibodies (see Table 2.3 below) in 1%BSA in PBST in a humidified box overnight at 4 ˚C. The solution was then removed and cells were washed three times in PBST for 20 min. Then the cells were incubated with the secondary antibodies in 1% BSA in PBST for 1 h at room temperature in the dark. The secondary antibody solution was removed and the cells were then washed thoroughly with PBST three times for 20 min in the dark. Finally, the cells were stained with Hoechst 33342 diluted to 1:1000 in PBST for 10 min at room temperature before mounting coverslips using ProLong® Gold antifade Mountant (Thermo Fisher Scientific)

and sealing with nail polish.

Primary antibodies			
	Dilution	**Host Species**	**Brand**
RBPMS	1:100	Rabbit	Abcam
Thy-1	1:200	Rat	Abcam
Secondary antibodies			
	Dilution	**Target Species**	**Brand**
Alexa Fluor® 488	1:100	Rabbit	Invitrogen
Alexa Fluor® 488	1:200	Rat	Abcam

Table 2.3 Primary and secondary antibodies used for identifying retinal ganglion cells.

2.4.2 Image analysis

Images were captured using an upright fluorescence microscope (Leica WETZLAR DM6000B) with a FITC filter set, a TRITC filter set and a DAPI filter set. A 20X and 40X magnification lens were used respectively. All images were captured with the same gain, intensity and exposure time.

2.5 Statistical analysis

The data are presented as mean ± SD and mean ± SEM for different assays. All statistical analysis was performed in Graphpad Prism 8.0 (San Diego, CA, USA) and tested for normality with a Shapiro-Wilk test. Normally distributed data were analyzed by Student's t-test or one-way ANOVA (with Dunnett's multiple comparisons test). A value of $p < 0.05$ was defined to be statistically significant.

Chapter 3 Mitochondrial morphology, dynamics and function in RGCs from wild-type and *Opa1* mutant mice

3.1 Introduction

The nuclear Optic Atrophy 1 gene (*OPA1*) is responsible for most (ca. 75%), cases of autosomal dominant optic atrophy (ADOA) (Chun and Rizzo 2016). Over 250 *OPA1* mutations have been reported in patients and a reduction in the amount of OPA1 protein (haploinsufficiency) is believed to be the major pathogenic mechanism in many ADOA cases (Ferre et al. 2009; Chun and Rizzo 2017). OPA1 is ubiquitously expressed and plays a crucial role in the fusion process of inner mitochondrial membranes and in the maintenance of the normal architecture of mitochondrial cristae (Alavi and Fuhrmann 2013; Chun and Rizzo 2016). It is also involved in the maintenance of oxidative phosphorylation and membrane potential, as well as the control of apoptosis through anchoring cytochrome c. However, the cellular changes specific to retinal ganglion cell (RGC), the predominant cell type affected in ADOA (Kjer et al. 1983; Ito and Di Polo 2017), caused by OPA1 deficiency before the onset of pathology and their mechanisms remain unclear. Thus, we hypothesize that the alterations in mitochondrial dynamics during early asymptomatic stages of ADOA precede the neurodegeneration and consequent RGC cell death.

Mitochondrial transport along neurites, especially in axons, is vital for the development and maintenance of cellular health. It is also noteworthy that there is a close relationship between mitochondrial dynamics and transport. The outer membrane fusion proteins-mitofusins have been demonstrated to interact with motor linkers along the microtubules and participate in regulating the mitochondrial transport (Misko et al. 2010); the key fission protein DRP1 has also been implicated in regulating mitochondrial transport in Purkinje cells (Fukumitsu et al. 2016). It is therefore important to investigate whether haploinsufficiency of OPA1 would interrupt the balance of mitochondrial dynamics and consequently affect mitochondrial transport.

In our study, a heterozygous *Opa1* mutant mouse model (B6; C3-*Opa1*^{Q285STOP}) was used to model the pathophysiology of ADOA disease in mice. These mice carry a protein-truncating nonsense mutation in exon 8 immediately before the central dynamin-GTPase, leading to a ~50% reduction in Opa1 transcript and protein in retina and neural tissues (Davies et al. 2007).

The *in vitro* ADOA disease model utilised here was set up by utilising a two-step immunopanning strategy, in which the RGCs were selected using the surface RGC marker-Thy1.2 (CD90) antibody from wild-type and *Opa1* mutant dispersed mouse retinas. This chapter investigates how decreased expression of Opa1 protein affects mitochondrial health utilising panned RGCs from mutant mouse retina. Here we hypothesise that the Opa1 mutation would cause alterations in mitochondrial morphology, which could lead to disturbances in mitochondrial transport along the neurites and thus influence energy production in RGCs from the B6; C3-*Opa1*^{Q285STOP} mouse model.

3.2 Experimental design

RGCs were collected from dispersed mouse retinae by two-step immunopanning and then seeded on glass coverslips (Academy Science Limited, UK) coated by Poly-D-lysine (Sigma-Aldrich Corp., St. Louis, MO, USA) and laminin (R&D systems, UK) with a seeding density of 50,000 RGCs per well in 24-well culture plates (Nunc^{TM}, Thermofisher, UK). RGCs were cultured in a humidified atmosphere at 37 ˚C under 10% CO_2, in serum-free growth medium as previously described (Winzeler and Wang 2013). The purity of cultured RGCs was identified by co-staining of anti-Thy 1.2 antibody and anti-RBPMS antibody (Abcam).

3.2.1 Mitochondrial morphology assessment

In total 65 WT mouse pups and 60 *Opa1*$^{+/-}$ mouse pups were used for three independent experiments. Purified RGCs were extracted from approximately 20 WT or *Opa1*$^{+/-}$ mouse pups in each panning procedure, plated in 24-well plates in three replicates and then stained by the specific mitochondrial marker, MitoTracker®Red CMXRos (Molecular Probes, Invitrogen) at 37 ˚C for 30 min on the 8th day in *vitro*. Images were captured under a 63X oil magnification lens using Zeiss LSM 880 confocal microscope and Zen Zeiss software (Carl Zeiss). The length of each mitochondrial fragment was measured for morphological assessment by FIJI software (v1.52p, Wayne Rasband, National Institutes of Health, USA).

3.2.2 Measurement and classification of mitochondrial motility

Time-lapse imaging was used to record mitochondrial movements; images were captured every 5 seconds for 10 minutes from RGCs cultured from WT and *Opa1*$^{+/-}$ mouse pups (n=20 to 25 for each group) in three replicates on the 8th day *in vitro*. Three independent experiments were performed. Kymographs of mitochondrial movements were generated by KymoAnlyzer (Neumann et al. 2017) plugin in FIJI software (v1.52p, Wayne Rasband, National Institutes of Health, USA).

Depending on the kymographs generated from the 10-minute mitochondrial movement recordings, the mitochondria were classified as stationary (that moved no further than 5 μm), or motile (moved further than 5 μm). Lastly, a fluttering population of mitochondria was also defined as moved further than 2 μm with changed moving directions within the stationary population, for some mitochondria did short-distanced reversing but not categorised as motile population. The length of mitochondria was measured directly by FIJI software, and the mitochondrial coverage of neurite (100%) was measured as the total length of mitochondria within neurite account for each neurite length. The contact rate was calculated as the number of contacts between mitochondrial tracks divided by the total number of mitochondria per minute in each imaged region. The velocities of movements were calculated for motile mitochondria from the generated kymographs: the length of horizontal axis (the distance of movement) was divided by the length of vertical axis (the time of movement lasted) (μm/s).

3.2.3 Measurement of mitochondrial bioenergetics

The real-time measurement of oxygen consumption rate (OCR) was carried out by the Seahorse XF^{e} 96 Extracellular Flux Analyzer (Agilent Technologies, USA) using Seahorse XF Cell Mito Stress Test Kit (#103015-100, Agilent Technologies) according to the manufacturer's protocol. Briefly, cells were plated at the concentration of 20,000 cells/well in XF^{e} 96 microplates (Agilent Technologies) coated with Cell-Tak^{TM} (#354240, Corning, USA). OCR

was measured in Seahorse XF DMEM Medium containing 10 mM glucose, 1 mM pyruvate and 2 mM l-glutamine (#103575-100, #103577-100, #103578-100, #103579-100, Agilent Technologies) under basal conditions and in response to three serial injected compounds - oligomycin (1.0 μM), carbonylcyanide-4-(trifluoro- methoxy) phenylhydrazone (FCCP; 2.5 μM), and a mixture of rotenone and antimycin A (1.0 μM) to determine the values for the basal mitochondrial respiration, ATP-linked oxygen consumption rate, maximal respiration, and spare respiratory capacity. Each sample was plated in five replicates. After the assays, the cells were immediately fixed and stained with Hoechest 33342, and then the images of whole well were captured by IX71 inverted microscope (Olympus, Japan) to calculate the number of cells in each well using FIJI software (v1.52p, Wayne Rasband, National Institutes of Health, USA). OCR values were normalized to cell number. Three independent experiments were performed.

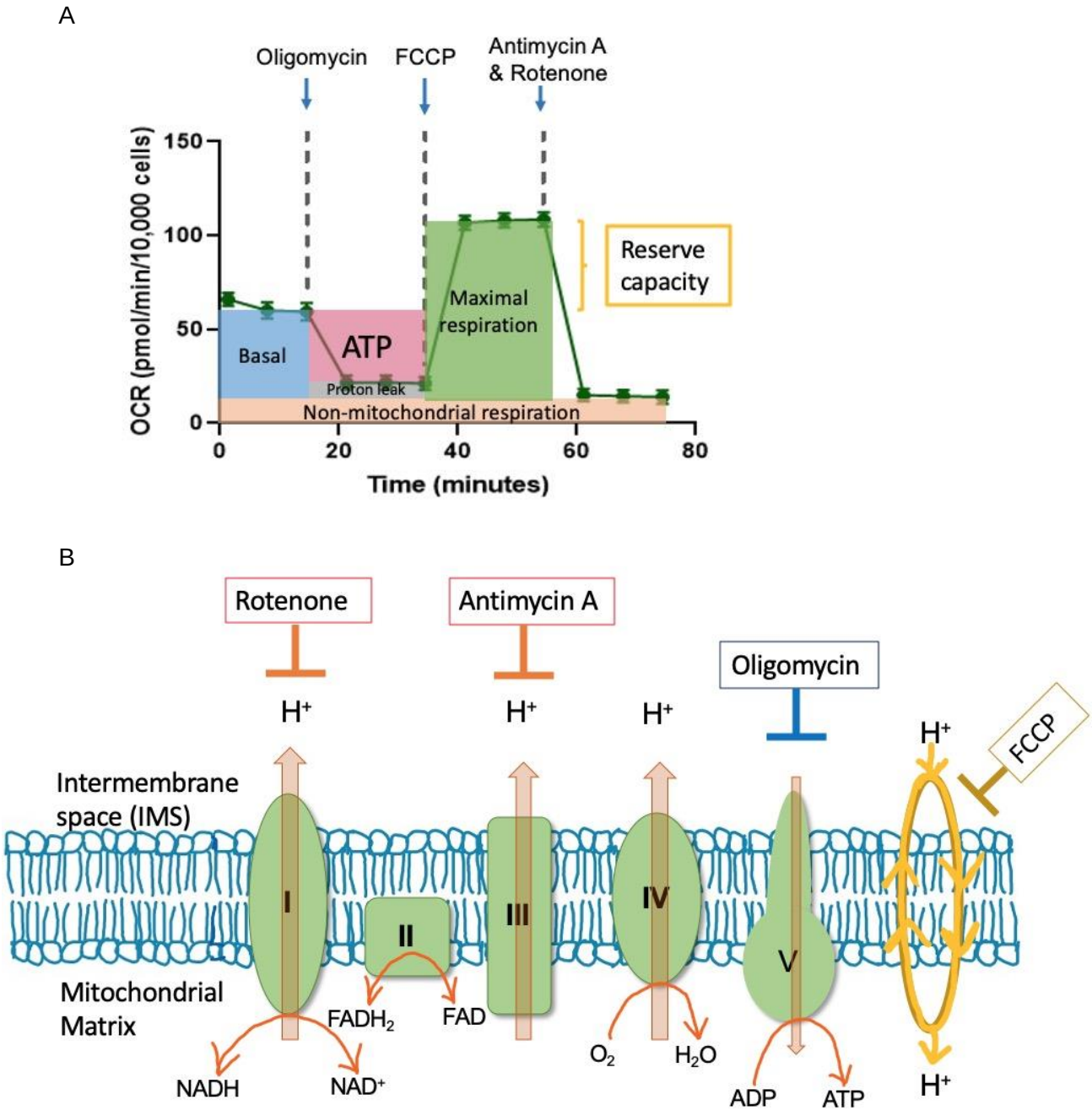

Figure 3.1 Principle of mitochondrial bioenergetic measurement. (A) Diagram of oxygen consumption rate (OCR) assay. (B) Targets of each compound injected during assay in the electron transport chain. In the electron transport chain, the electrons are transferred from complex I or II to complex III and IV and release energy/H^+ at the same time. Complex I, III and IV use the energy to pump H^+ to mitochondrial intermembrane space (MIS). So there is a electrochemical gradient established and the H^+ can flow down the gradient through complex

V (ATP synthase) to produce ATP. Oligomycin is an ATP synthase inhibitor, used to clarify the proportion of ATP-linked respiration in the basal respiration. FCCP is an uncoupling agent to collapse the proton gradient to claim Maximal respiration and reserve capacity. A mixture injection of rotenone and antimycin A can shut down the whole mitochondrial respiration.

3.3 Results

3.3.1 Identification of cultured RGCs

Approximately 23,000 to 27,000 RGCs were isolated from each mouse retina by two-step immunopanning. After two days in culture, RGCs were identified by their plump rounded cell bodies with characteristic long neurites (Figure 3.2A). Cell identity was also verified histologically by immunofluorescent co-staining of Thy1.2 and RBPMS (Figure 3.2B). The purity was approximately 85.22%, calculated as the ratio of double-stained Thy1.2 and RBPMS-positive cells to the total number of cells within imaged regions from 5 independent experiments.

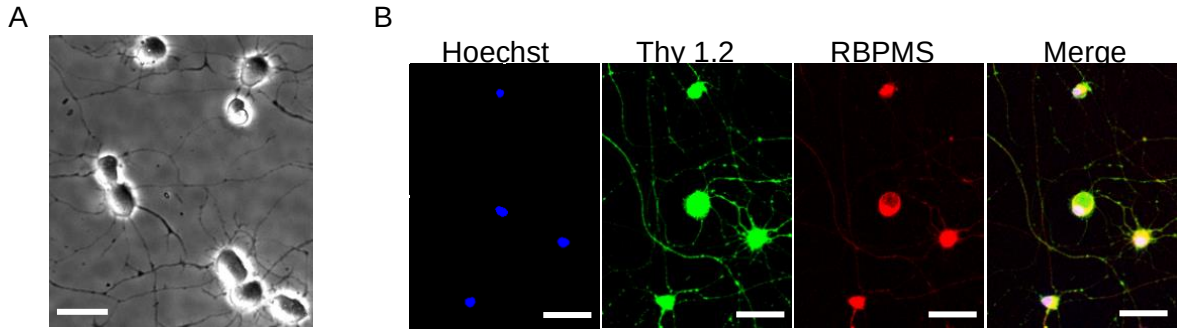

Figure 3.2 Identification of primary retinal ganglion cells (RGCs) isolated by two-step immunopanning after two days in culture. (A) Phase-contrast image showing the characteristic morphology of RGCs. (B) Immunofluorescent staining with Hoechst 33342 (blue), Thy1.2 (green), RBPMS (red) and merged image. Scale bar = 50 μm.

3.3.2 Opa1 deficiency leads to fragmented mitochondrial morphology in primary mouse RGCs *in vitro*

The length of each mitochondrion along the RGC neurites was measured and distribution of mitochondrial length was documented in μm using high-resolution confocal microscopy (See Figure 3.3). As the observation under the confocal microscopy for time-lapse imaging lasted for 10 minutes, it is also important to determine whether the laser scanning affect the mitochondrial length during the imaging. The length of mitochondria was measured at image frames 1, 30, 60, 90 and 120 (0 min, 2.5 min, 5 min, 7.5 min and 10 min). As shown in Figure 3.4, there's no significant difference was found on the length of mitochondria during the 10-minute time-lapse imaging under LSM880 confocal microscopy in WT and *Opa1*$^{+/-}$ cultures, respectively.

The length of mitochondria was then compared between WT and *Opa1*$^{+/-}$ cultures at image frames 1, 30, 60, 90 and 120 (0 min, 2.5 min, 5 min, 7.5 min and 10 min). The length of mitochondria during the laser scanning was 3.246 ± 0.5390 μm, 3.11 ± 0.22 μm, 3.34 ± 0.50 μm, 3.22 ± 0.48 μm and 3.11 ± 0.32 μm at each timepoint respectively. The length was significantly decreased in *Opa1*$^{+/-}$ RGCs, for the average length of mitochondria was 2.23 ±0.33 μm, 2.22 ± 0.43 μm, 2.17 ± 0.26 μm, 2.17 ± 0.05 μm and 2.21 ± 0.15 μm at 0 min, 2.5 min, 5 min, 7.5 min and 10 min, respectively (Figure 3.5). These results indicate the fragmented mitochondrial structure caused by Opa1 deficiency in RGCs *in vitro*.

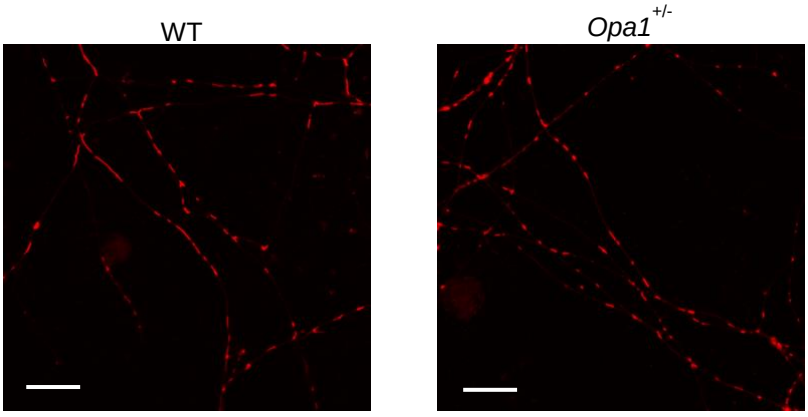

Figure 3.3 Representative confocal images of mitochondrial movements from WT and *Opa1*$^{+/-}$ RGC cultures. Mitochondria were stained by MitoTracker®Red CMXRos and captured under a Zeiss LSM 880 confocal microscope and Zen Zeiss software under the

MtRed filter with a 63X oil magnification lens (Carl Zeiss, UK), scale bar = 20 μm.

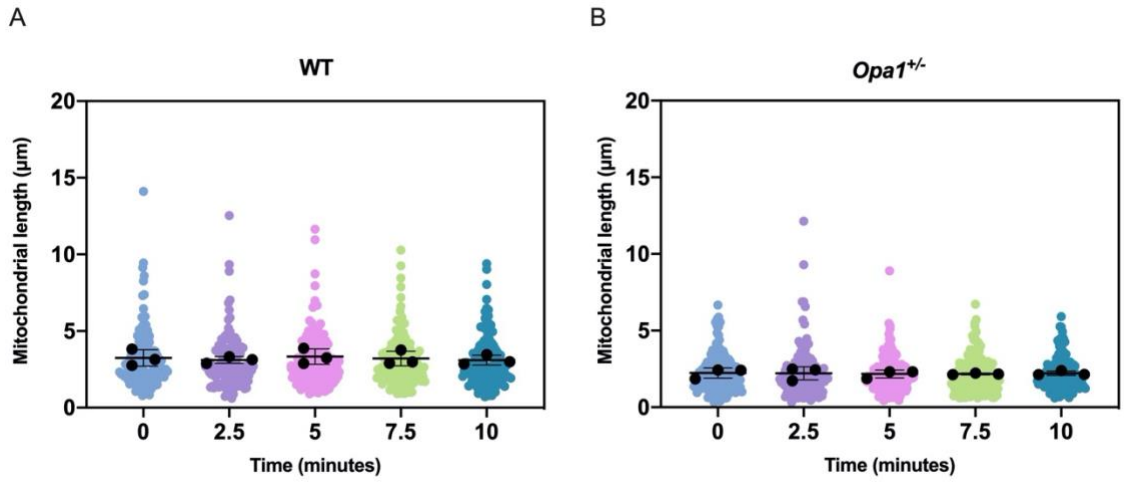

Figure 3.4 No significant change was found in mitochondrial length over time, as measured during 10-minute time-lapse imaging by confocal microscopy in WT and *Opa1*$^{+/-}$ cultures. Mitochondria were stained by the specific mitochondrial vital dye, MitoTracker®Red CMXRos and captured using a Zeiss LSM 880 confocal microscope by time-lapse imaging with 5-second intervals for 10 minutes. The length of mitochondria was measured manually by FIJI software at frames 1, 30, 60, 90 and 120 (0 min, 2.5 min, 5 min, 7.5 min and 10 min) in WT (A; n=665 mitochondria) and *Opa1*$^{+/-}$ (B; n=698 mitochondria) cultures respectively. All the results are from 3 independent cultures, data shown as mean ± SD, N=3.

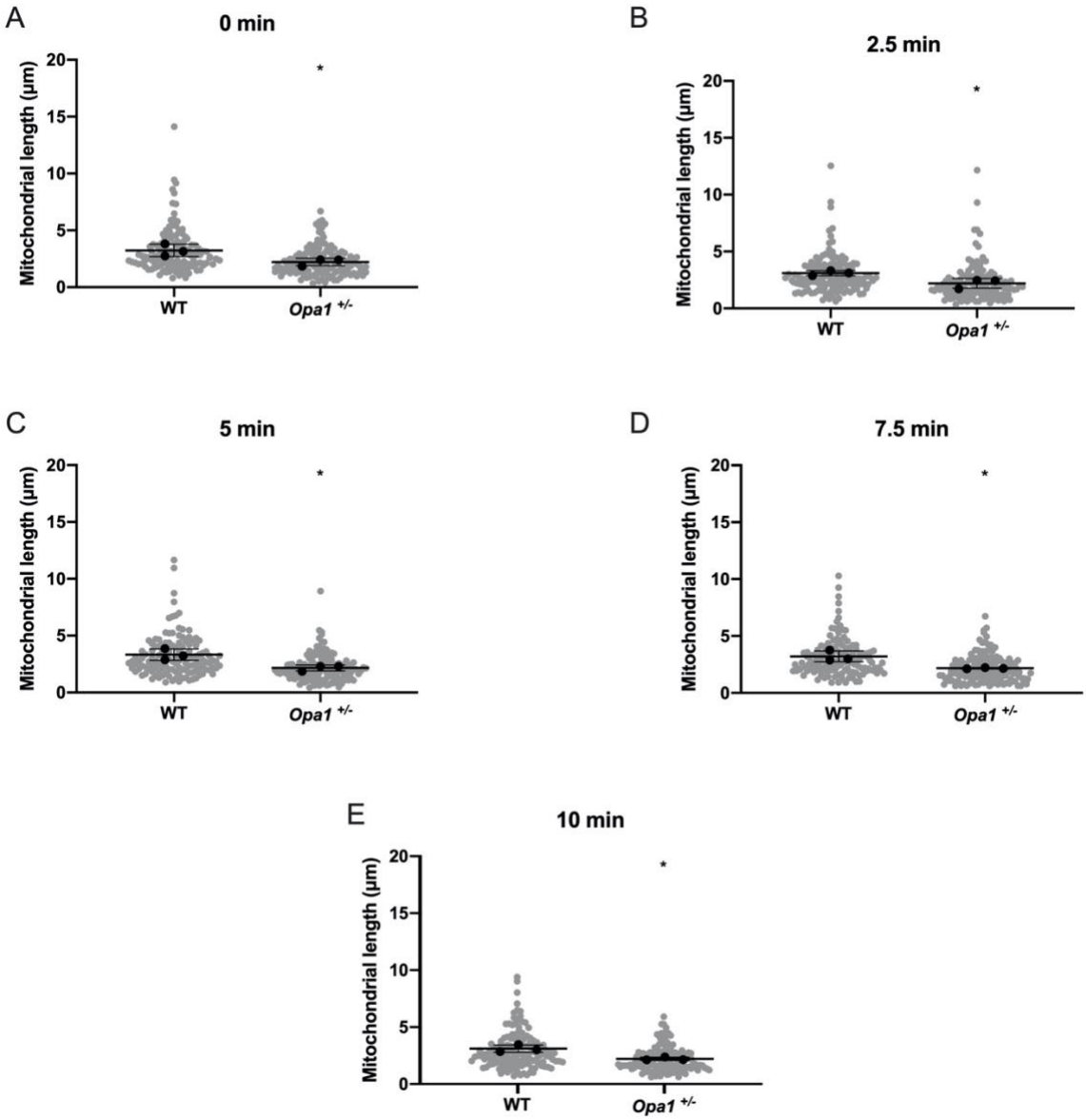

Figure 3.5 Opa1 deficiency decreases the length of mitochondria *in vitro*. The length of mitochondria was measured manually by FIJI software at frames 1, 30, 60, 90 and 120 (0 min, 2.5 min, 5 min, 7.5 min and 10 min). Statistically significant shorter mitochondria were observed in *Opa1*$^{+/-}$ cultures. (A) The length of mitochondria measured at frame 1 (0 min). n=130 mitochondria in WT group; n=140 mitochondria in *Opa1*$^{+/-}$ group. (B) The length of mitochondria measured at frame 30 (2.5 min). n=133 mitochondria in WT group; n=137 mitochondria in *Opa1*$^{+/-}$ group. (C) The length of mitochondria measured at frame 60 (5 min). n=130 mitochondria in WT group; n=143 mitochondria in *Opa1*$^{+/-}$ group. (D) The length of

mitochondria measured at frame 90 (7.5 min). n=136 mitochondria in WT group; n=141 mitochondria in *Opa1*$^{+/-}$ group. (E) The length of mitochondria measured at frame 120 (10 min). n=136 mitochondria in WT group; n=137 mitochondria in *Opa1*$^{+/-}$ group. Data analysed from 3 independent cultures. Data shown as mean ± SD, N=3. *p <0.05 vs WT.

3.3.3 Opa1 deficiency activates mitochondrial motility in primary mouse RGCs

To investigate how Opa1 deficiency influences the mitochondrial movement within neurites of RGCs from wild-type and *Opa1*$^{+/-}$ mice, time-lapse imaging of live mitochondrial movement was performed. Kymographs from 9 neurites in each of wild-type and *Opa1*$^{+/-}$ cultures was generated using FIJI software (representative kymographs shown in Figure 3.6. Whole sets of kymographs from wild-type and *Opa1*$^{+/-}$ cultures are shown in Appendix III Figure S31). The movement of each mitochondrion was manually tracked in kymographs and classified as stationary (including fluttering population) and motile categories.

In wild-type RGCs, 88.43% of mitochondria were stationary, and 12.57% of mitochondria moved further than 5 μm, and were thus identified as motile. The distribution of the mitochondrial population showed that there was a significant increase in the proportion of motile mitochondria in *Opa1*$^{+/-}$ RGCs compared to that in wild-type RGCs (motile mitochondria increased by 17.94%, $p < 0.01$, see Figure 3.7B). Also, the fluttering population within stationary category, which was defined as “short-distance reversing” was significantly increased in *Opa1*$^{+/-}$ RGCs (increased by 11.65%, $p < 0.01$, see Figure 3.7C). Consistently, the activated mitochondria in *Opa1*$^{+/-}$ RGCs also showed an elevated contact rate in the 10 minute scanning between mitochondria in RGC neurites (increased by 0.097 contact/mitochondrion/min, $p < 0.01$, see Figure 3.7D).

Figure 3.6 Representative kymographs from WT and *Opa1*$^{+/-}$ RGC cultures, n=9 neurites in each condition from 3 independent cultures. Scale bar = 20 µm. All kymographs are presented in the Appendix III Figure S31.

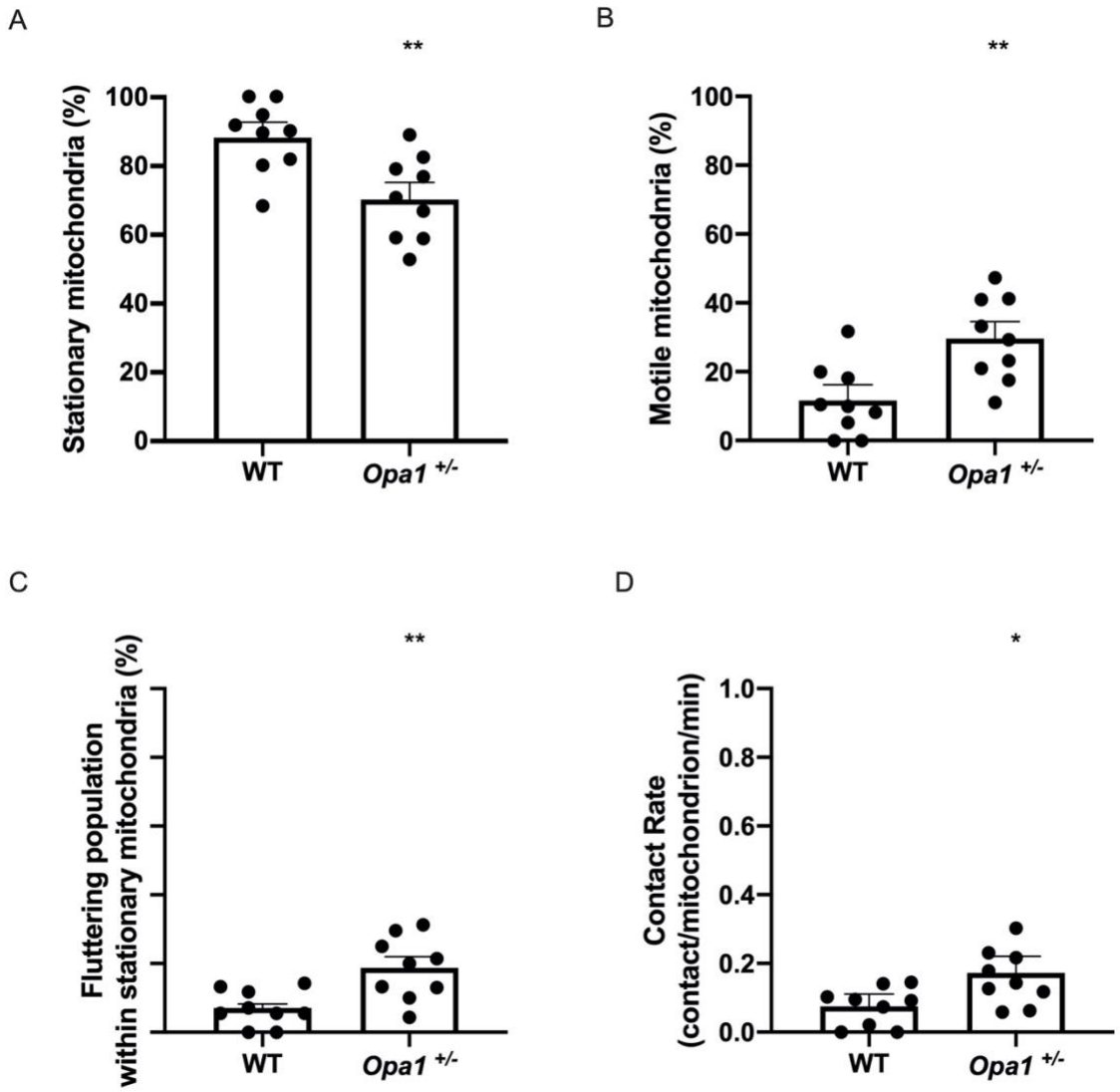

Figure 3.7 Opa1 deficiency increases mitochondrial motility. (A, B) Distribution of the

mitochondrial population classified as stationary and motile; n=9 neurites in both WT and *Opa1*$^{+/-}$ RGC cultures from 3 independent cultures. (C) Fluttering population within stationary mitochondria was defined as the number of mitochondria classified as stationary but which fluttered within a small distance (moving directions changed, maximum moving distance > 2 μm); n=9 neurites in WT and *Opa1*$^{+/-}$ RGC cultures from 3 independent cultures. (D) Contact rate calculated as the number of contacts between mitochondria per minute divided by the total number of mitochondria, n=9 neurites in WT and *Opa1*$^{+/-}$ RGC cultures from 3 independent cultures. Data shown as mean ± SD, N=3. *p <0.05, **p <0.01 vs WT.

3.3.4 Opa1 deficiency increases the velocity of mitochondria in primary mouse RGCs

Mitochondrial velocity is also an essential parameter of mitochondrial motility and dynamics; the velocity of motile mitochondria was also measured from kymographs. Remarkably, the motile mitochondria in *Opa1*$^{+/-}$ RGC neurites presented an increased velocity (0.39 ± 0.041 μm/s) compared to the wild-type (0.27 ± 0.035 μm/s): the velocity was increased by approximately 0.12 μm/s ($p < 0.05$, see Figure 3.8A). Furthermore, the mitochondrial length of the moving mitochondria were also measured, the average length was 2.951 μm and 1.770 μm in WT and *Opa1*$^{+/-}$ RGCs, no statistically difference was found (Figure 3.8B).

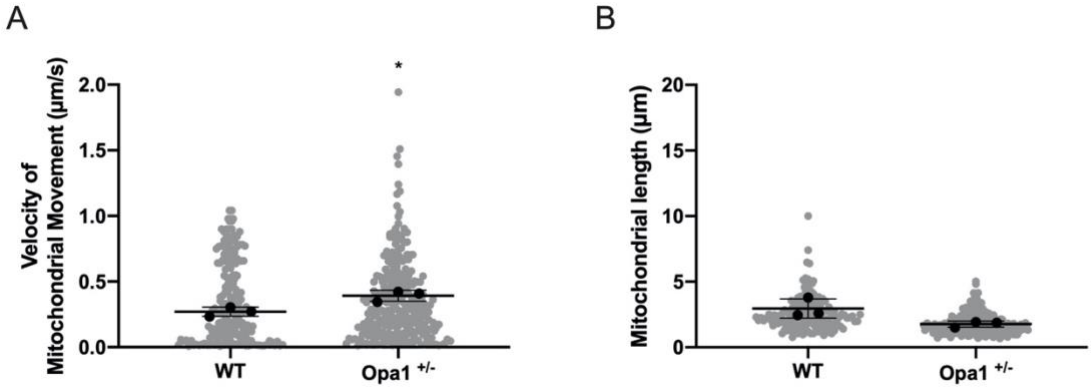

Figure 3.8 Opa1 deficiency increases the velocity of mitochondrial movement. No significant difference was found in mitochondrial length from RGC neurites between wild-type and *Opa1*$^{+/-}$ RGCs. (A) Velocities of mitochondria calculated from WT and *Opa1*$^{+/-}$

RGC neurites calculated from kymographs; n=147 mitochondria in WT group, n=267 mitochondria in *Opa1*$^{+/-}$ group from 3 independent cultures (N=3). (B) Each mitochondrial length of the moving mitochondria from WT and *Opa1*$^{+/-}$ RGC neurites in (A) was measured by FIJI software. Data shown as mean ± SD, N=3. *p <0.05 vs WT.

3.3.5 Relationship between mitochondrial velocity and length of moving mitochondria in both WT and *Opa1*$^{+/-}$ RGCs

In order to better understand the relationship between mitochondrial velocity and length of moving mitochondria in both WT and *Opa1*$^{+/-}$ RGCs, data were distributed in scatter plot (Figure 3.9A, 3.10A). As shown in the scatter plot and heatmap (Figure 3.9B), over 40% moving mitochondria in WT RGCs were moving slower than 0.25 μm/s with length between 1 μm to 3 μm. While over 55% moving mitochondria in *Opa1*$^{+/-}$ RGCs were moving in a higher speed (0-1 μm/s) with shorter length between 1 μm to 2 μm compared to the WT. Moreover, the mitochondria were classified as different length groups- <2 μm; 2-3 μm; >3 μm. The velocity of mitochondria was also compared between each group. The results showed no apparent changes on the velocity of mitochondria with the increase of the mitochondrial length in either WT or *Opa1*$^{+/-}$ RGCs (Figure 3.9C, 3.10C). The results indicated no apparent relationship between the mitochondrial length and velocity under the same condition.

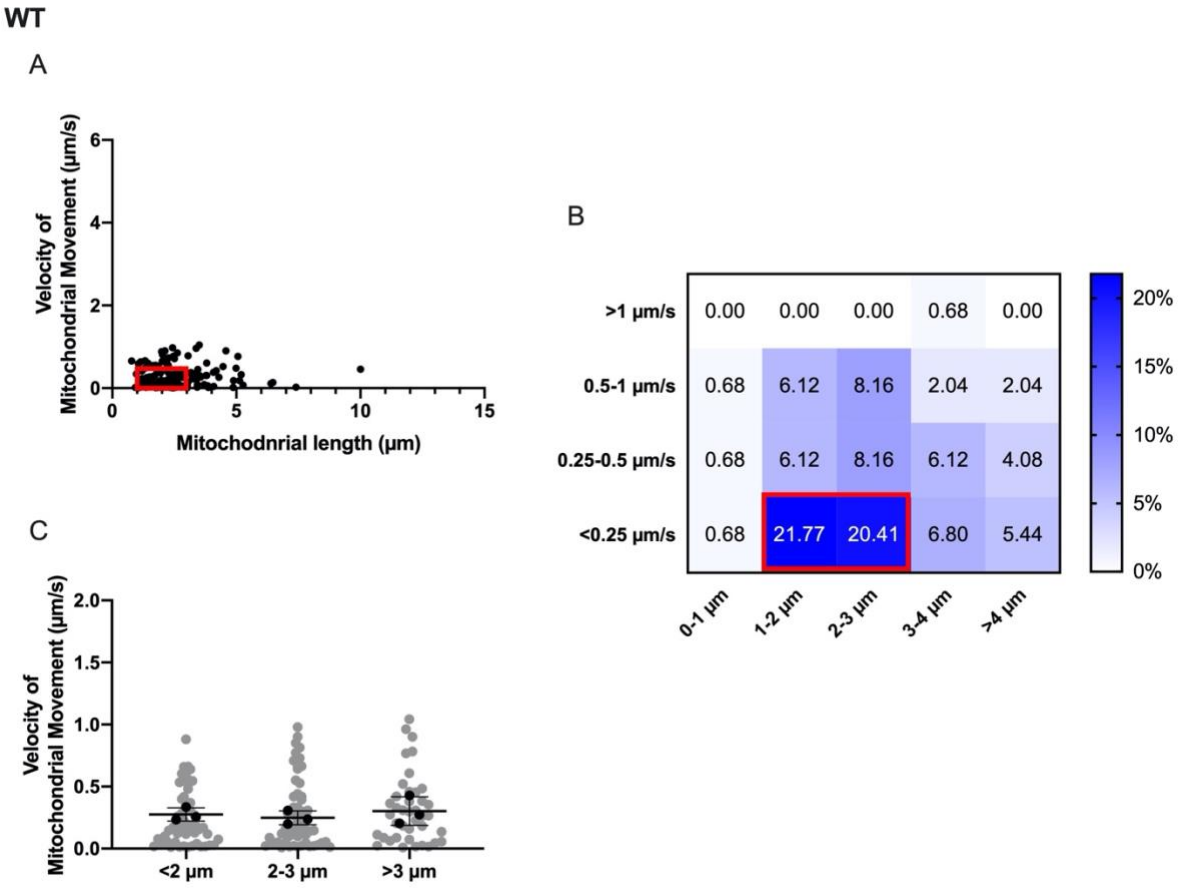

Figure 3.9 Distribution of mitochondrial velocity and length in WT RGCs. No significant difference was found in mitochondrial velocity with the increase of mitochondrial length in WT RGCs. (A) Distribution of mitochondrial velocity according to their length, n=147 mitochondrial from 3 independent cultures. Red line framed area=greatest mitochondrial concentration (based on the heatmap result from (B)). (B) Heatmap of distribution of mitochondrial velocity and length. Red line framed area=greatest mitochondrial concentration (percentage of distributed mitochondria in each square > 10%). (C) Mitochondria distributed by velocity with different ranges of length (<2 µm, 2-3 µm and >3 µm); n=53 mitochondria with length <2 µm; n=54 mitochondria with length between 2 and 3 µm; n=40 with length >3 µm from 3 independent cultures (N=3). Data shown as mean ± SD. Supplementary histograms characterizing the detailed distribution of mitochondrial velocity and length from WT RGCs have been added in Appendix III Figure S34.

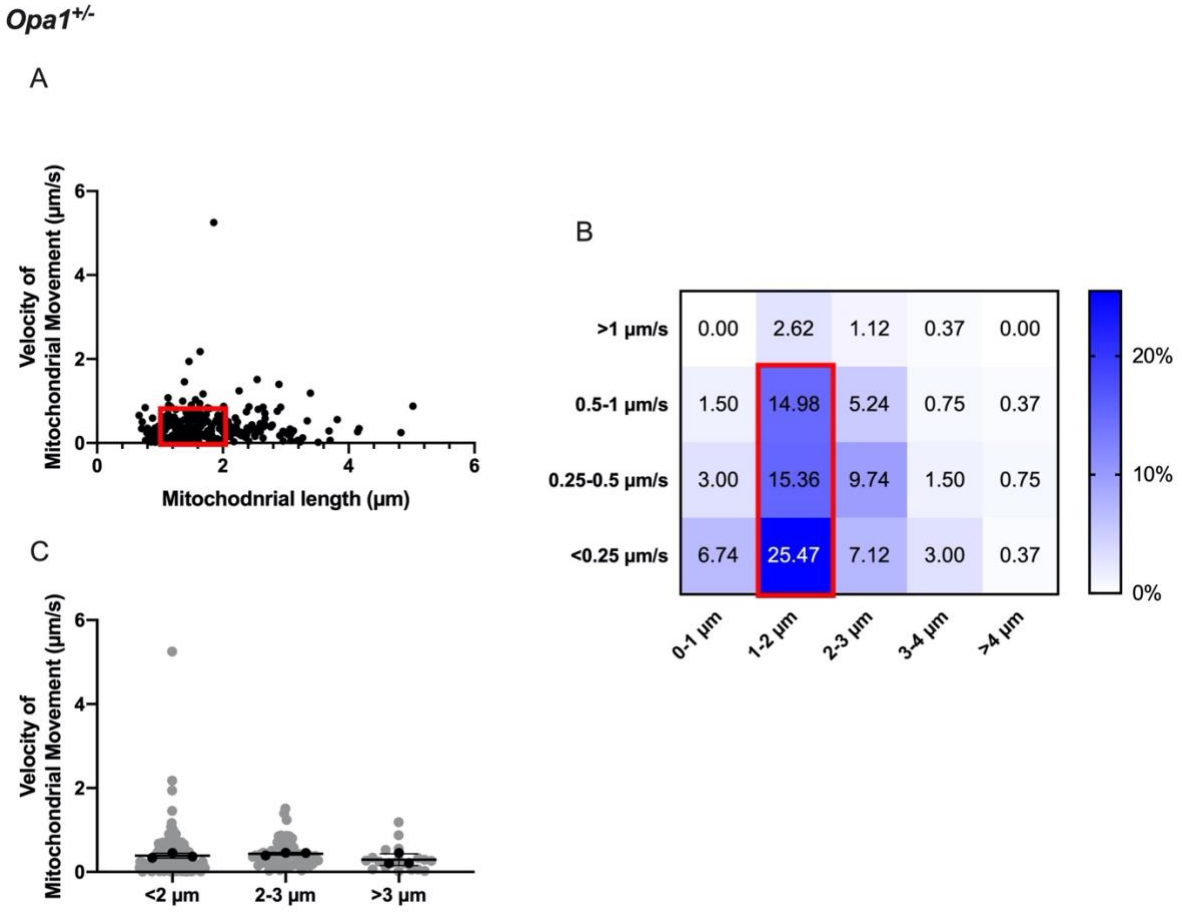

Figure 3.10 Distribution of mitochondrial velocity and length in *Opa1*$^{+/-}$ RGCs. No significant difference was found in mitochondrial velocity with the increase of mitochondrial length in *Opa1*$^{+/-}$ RGCs. (A) Distribution of mitochondrial velocity based on their length, n=267 mitochondrial from 3 independent cultures. Red line framed area=greatest mitochondrial concentration (based on the heatmap result from (B)). (B) Heatmap of distribution of mitochondrial velocity and length. Red line framed area=greatest mitochondrial concentration (percentage of distributed mitochondria in each square>10%). (C) Mitochondria distributed by velocity with different ranges of length (<2 µm, 2-3 µm and >3 µm); n=186 mitochondria with length <2 µm; n=62 mitochondria with length between 2 and 3 µm; n=19 with length >3 µm from 3 independent cultures (N=3). Data shown as mean ± SD. Supplementary histograms characterizing the detailed distribution of mitochondrial velocity and length from *Opa1*$^{+/-}$ RGCs have been added in Appendix III Figure S34.

3.3.6 Opa1 deficiency leads to impaired mitochondrial bioenergetics in primary mouse RGCs

To explore how Opa1 deficiency in the B6; C3-Opa1^{Q285STOP} mouse influences mitochondrial bioenergetics in mouse primary retinal ganglion cells, cellular oxygen consumption rates (OCR) were measured in real time using the Seahorse XF^{e} 96 Extracellular Flux Analyzer with sequential injection of mitochondrial respiration inhibitors. As shown in Figure 3.5B, Opa1 deficiency caused a significant decline in the basal respiration compared with the wild-type ($p < 0.05$) in the mouse primary retinal ganglion cells. The first compound injected in the assay was oligomycin, a complex V (ATP synthase) inhibitor, used to clarify the proportion of ATP-linked respiration in the basal respiration. The second injected compound was FCCP, an uncoupling agent for collapsing the proton gradient and disrupting the mitochondrial membrane potential, used to determine the maximal respiration. A combination treatment of antimycin A (complex III inhibitor) and rotenone (complex I inhibitor) was finally injected to shut down the whole mitochondrial respiration. A significant decline was observed in ATP-linked respiration, decreased by ~21.16 pmol/min per 10,000 cells ($p < 0.05$, see Figure 3.5C), and maximal respiration, decreased by ~51.09 pmol/min per 10,000 cells ($p <0.05$, see Figure 3.5D) respectively. Spare respiratory capacity, an indicator of cellular fitness which illustrates the capability of each cell to respond to an energetic demand *via* oxidative phosphorylation is calculated by subtracting maximal OCR from the basal OCR. The reserve capacity of mitochondrial respiration was shown to be significantly lower in *Opa1* +/- retinal ganglion cells compared to the wild-type (decreased by ~28.65 pmol/min per 10,000 cells, $p < 0.05$, see Figure 3.5E). Overall, these results from the OCR assay showed that Opa1 deficiency caused lower basal respiration, decreased ATP-linked oxygen consumption, diminished maximum value of oxidative phosphorylation, and depletion of the cellular capability for energy supply in mouse retinal ganglion cells.

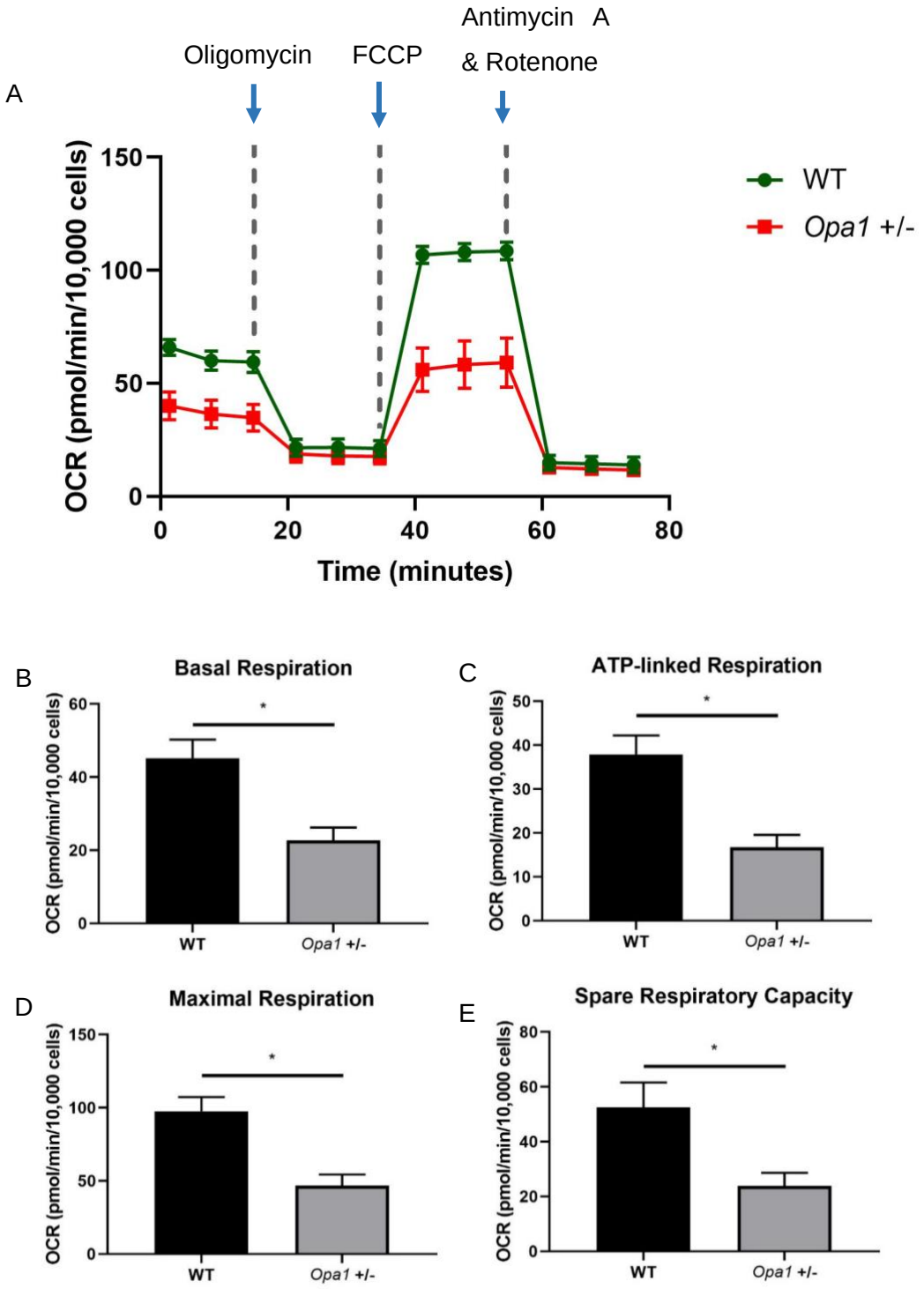

Figure 3.11 Comparative analysis of mitochondrial bioenergetics between wild-type and *Opa1*$^{+/-}$ mouse primary retinal ganglion cells. Cells were measured on the 3rd *in vitro*. (A) OCR profile plot. Oxygen consumption rate (OCR) was recorded by Seahorse Extracellular Flux Analyzer at baseline and after the sequential injections of oligomycin (1 μM), FCCP (2.5

μM), and a mixture of rotenone and antimycin (1 μM). (B) Basal respiration, (C) ATP-linked respiration, (D) maximal respiration, (E) spare respiratory capacity was calculated. Data are shown as the mean ± SEM of three independent experiments, each with five replicates. *p < 0.05 vs wild-type group.

3.4 Discussion

ADOA is an inherited optic neuropathy characterized by mitochondriopathy, which appears to result in selective RGC degeneration in the retina, followed by ascending optic atrophy. The exquisite vulnerability of RGCs to mitochondrial deficits caused by ADOA mutations may be associated with the acute energy demand along the neurites combined with their unique morphology (Ito and Di Polo 2017). Here we demonstrate for the first time that fragmented mitochondria caused by Opa1 deficiency showed an actively increased motility along RGC neurites in the presence of diminished mitochondrial bioenergetic function in RGCs isolated from B6; C3-*Opa1*^{Q285STOP} mouse model.

Mitochondrial morphology is the result of a balance between fusion and fission processes, and results in the existence of small fragments or elongated tubular structures based on the metabolic state of the cell. The defects in Opa1 in our primary RGCs firstly caused fragmentation of the tubular mitochondrial reticulum in RGCs, in which the lengths of mitochondria in *Opa1*$^{+/-}$ RGCs were decreased to nearly half of that in the wild-type. These results are consistent with the punctate pattern of mitochondria in mouse embryonic fibroblasts (MEFs) from *Opa1*^{Q285STOP} mouse model (Kushnareva et al. 2016), and in lymphoblastoid cell lines and fibroblasts derived from ADOA patients (Kao et al. 2015; Liao et al. 2017; Zhang et al. 2017). Mitochondria are actively transported along microtubule tracks from the soma to the RGC neurites, which is an energy-demanding process in mammals (Ito and Di Polo 2017). Interactions between polarized microtubules, motor proteins, adaptors that link motor proteins to mitochondria and anchors that arrest transport have been demonstrated to trigger the motility of mitochondria (Barnhart 2016). It has also been reported that the

activation of the energy biosensor AMP-activated protein kinase (AMPK) contributes to the detection of the energy deprivation in neurons which contributes to the recruitment of mitochondria to the energy-deficient area (Tao et al. 2014). The interplay in mitochondrial dynamics, including the morphology, motility and fusion-fission balance, are likely to be sophisticated and delicate. Previous studies demonstrated that augmented motility with a higher number of mitochondria in the neighbourhood could increase the likelihood of contacts between individual mitochondrion, which was consequently associated with the probability of fusion process. Further, increased fusion activity could then elongate the length of mitochondria in turn probably activating the machinery of fission process in order to inhibit a further elongation of mitochondrial length (Twig et al. 2010; Cagalinec et al. 2013). Additionally, it was shown that inhibited mitochondrial motility caused by nocodazol and vasopressin led to suppressed merging frequency in H9c2 cells (Liu et al. 2009). In our study, Opa1 deficiency caused shortened length of mitochondrial structures, an augmented number of motile mitochondria, with higher moving speed and was also accompanied by increased contact frequency between mitochondria. It may be speculated that shortened mitochondria were stimulated to increase motility in an attempt to increase the possibility of fusion activity, which may be a response to rescue the mitochondrial phenotype in RGCs suffering from Opa1 deficiency.

Apart from the promotion of the fusion process, OPA1 also works as a master regulator of cristae structure and remodelling, independently of its role in fusion (Meeusen et al. 2006; Cogliati et al. 2013). Since cristae are critical to the machinery of mitochondrial oxidative phosphorylation as the complexes of electron transport chain (ETC) are located within the large surface area of the cristae, OPA1 therefore plays an essential role in regulating mitochondrial respiratory efficiency by directly changing the control of cristae widening or constriction (Frezza et al. 2006; Pernas and Scorrano 2016; Wollweber et al. 2017). Additionally, elongated mitochondria also presented higher activity of energy production because of the larger area of cristae, higher levels of dimers of the ATPase as well as the escape from autophagic degradation (Gomes et al. 2011), emphasizing the vital character of

OPA1 in modulating mitochondrial bioenergetics and cell metabolism. However, the indicators of mitochondrial bioenergetics in samples from patients with ADOA mutations has revealed some controversial and sometimes conflicting results. Defective oxidative phosphorylation with remarkably reduced mitochondrial adenosine triphosphate production rate was observed in calf muscle *in vivo* from six patients (Lodi et al. 2004), consistent with the impaired ATP synthesis driven by complex I substrates in skin fibroblasts derived from ADOA patients (Zanna et al. 2008), and the reduced oxygen consumption as well as dysfunctional bioenergetics in lymphoblastoid cells obtained from four ADOA families (Kao et al. 2015). In contrast, no alterations in mitochondrial oxidative phosphorylation were observed in lymphoblastoid cells lines and fibroblasts derived from patients (Mayorov et al. 2008), which were not associated with the fragmented morphology (Spinazzi et al. 2008). These conflicting results may due to the distinct effects of *OPA1* mutations in different cell types, and might be associated with different bioenergetic profiles see with different *OPA1* mutations. Since the RGC is a cell type highly vulnerable to metabolic disturbances and is exquisitely affected in patients with ADOA, it is conceivable that the results of our mitochondrial measurements might be different in RGCs from other cell types. According to our study, mitochondrial bioenergetics in panned RGCs from the B6; C3-*Opa1*^{Q285STOP} mouse model revealed an impaired mitochondrial respiratory function with diminished reserve capacity in RGCs with Opa1 deficiency. Therefore, we propose, evidence that mitochondrial bioenergetics and energy production can be disrupted in RGCs due to OPA1 deficiency.

The critical role of mitochondria is central not only in ADOA, but also another classical optic neuropathy –Leber hereditary optic neuropathy (LHON), and even in some neurodegenerative diseases such as Alzheimer's, Parkinson's and Huntington's diseases in the central nervous system (CNS) (Yu-Wai-Man and Newman 2017). In ADOA, in addition to the clinical visual loss caused by the degeneration of optic nerves projected from about 1.2 million RGCs in the retina, some patients display a 'plus' phenotypes in a wider range of tissues including CNS and brain, indicating a broader link between mitochondrial dysfunction caused by OPA1 deficit and neurodegeneration within the CNS (Yu-Wai-Man et al. 2016). OPA1 exerts critical roles in

mitochondrial energy production through two independent pathways. Firstly, OPA1 protein directly affects cristae modelling by OPA1 to help regulate the mitochondrial energy production through oxidative phosphorylation. OPA1 also helps equilibrate the mitochondrial dynamic balance and enhances the fusion process, so that the elongated mitochondria with a larger area of cristae are more likely to consist of higher levels of dimers of the ATPase and escape from autophagic degradation, which also enhances mitochondrial bioenergetics. Thus in ADOA, we speculated that OPA1 deficit could cause impaired mitochondrial bioenergetics through fragmentation of mitochondrial morphology or direct damage of cristae structure. Surprisingly, with a larger number of mitochondria detected in the neurites of RGCs with higher motility, there would be higher probability of mitochondrial contact. As fusion activity could only occur when two mitochondria meet, the higher contact rate can then increase the possibility of fusion. Although only less than 10% contacts could result in fusion reported in cortical neurons (Cagalinec et al. 2013), the mitochondria with increased contact rates can also be benefit from mitochondrial 'kiss-and-run' interplays- transient fusions which could also be an alternative support for mitochondrial metabolism (Liu et al. 2009). In this pathway the mitochondrial bioenergetics can be also promoted consequently. Thus we infer that the activated motility under OPA1 deficit in RGC neurites could be a spontaneous compensation in an attempt to rescue the impaired fusion and fission balance as well as mitochondrial bioenergetics.

In terms of mechanism of mitochondrial transportation, mitochondria move along both microtubule and actin tracks in response to the physiological signals as well as pathological stress. Mitochondria moving along the microtubules for long-distances use fast axonal transport with the motor proteins of the kinesin superfamily in anterograde transport; and use the actin filaments with myosin motors for short-range movement (Hollenbeck 1996). The proteins involved in mitochondrial dynamics have a notable relationship with mitochondrial transport. The mitofusins (Mfn1/2) are outer mitochondrial membrane proteins that not only participate in mitochondrial fusion, but are also necessary for transport of mitochondria along axons by interacting with the Miro/Milto complex, which is a key linkage complex between

mitochondria and motor proteins (Misko et al. 2010). The fission protein-Drp1 has also been shown to modulate the dynein motor protein associated retrograde transport by interacting with the dynein-dynactin complex (Drerup et al. 2017). Drp1 was also shown to be critical for mitochondrial distribution in the nerve terminals of dopamine neurons, and a disruption in mitochondrial fission can result in the preferential death of nigrostriatal dopamine neurons (Berthet et al. 2014). The regulated equilibrium between fusion and fission proteins contributes to the healthy condition and integrity of mitochondria. The mitofusins are also critical to coordinate with Opa1 protein in maintaining the mitochondrial shape (Cipolat et al. 2004). Opa1 is the key fusion protein and also involved in the mitochondrial quality control by increasing the colocalization of mitochondria and autophagosomes (Liao et al. 2017). However, the expression levels of other dynamic proteins and motor factors related to mitochondrial transport under Opa1 haploinsufficiency are still unclear. It would therefore be interesting to further investigate whether Opa1 haploinsufficiency leads to alterations in the imbalanced expression of other dynamic proteins and thus result in the activation of mitochondrial transport. It would also be important to determine whether Opa1 haploinsufficiency results in changes of the levels of expression of motor proteins and linkage complexes associated with the mitochondrial transport.

Previous research has demonstrated that about a third of mitochondria are highly mobile before any branching patterns in dendrites are established. Mitochondria become largely stationary as they reach their positions at the synapses and branch points where energy is needed in mature RGC dendrites (Faits et al. 2016). Takihara et al. 2015 developed minimally invasive intravital multiphoton imaging to record the transportation of mitochondria in a single axon of RGCs *in vivo* and illustrated the dynamics in axonal transport of mitochondria during aging as well as the disturbances of mitochondrial transport in a mouse glaucoma model (Takihara et al. 2015). Previous studies also demonstrated that mitochondria were prominent in growth cones and preferentially recruited into distal axons where actively extending through the AMP-activated protein kinase (AMPK) energy-sensing pathway (Morris and Hollenbeck 1993; Ruthel and Hollenbeck 2003; Cunniff et al. 2016). Specifically, Steketee et al. 2012

demonstrated the critical role of mitochondrial fission in normal growth cone dynamics and axon extension by acutely inhibiting Drp1 function using mDivi-1 in rat retinal ganglion cell axons (Steketee et al. 2012). Moreover, numerous intrinsic and extrinsic factors that regulate the axonal growth also directly or indirectly effect the mitochondrial dynamics and function such as BDNF (Markham et al. 2004), NGF (Chada and Hollenbeck 2004), PTEN (Park et al. 2008), and Nogo (Goldberg and Barres 2000; Hu et al. 2002) in central neuron system (CNS). Notably, Kreymerman et al. 2019 found a novel mitochondrial fission protein- MTP18 which could regulate the mitochondrial size and also have a role in modulating neurite outgrowth in RGCs during development and injury conditions (Kreymerman et al. 2019). Additionally, melanopsin-containing RGCs (mRGCs), a special subset of RGCs constituting only 1% of the RGC population in humans, were reported to be resistant to mitochondrial dysfunction and maintain the non-image-forming light driven functions (La Morgia et al. 2010; Perganta et al. 2013) independently from melanopsin expression (Gonzalez-Menendez et al. 2015). The large cellular size of mRGCs with a high cellular content of mitochondria might be the possible factors protecting mRGCs from mitochondrial dysfunctions (La Morgia et al. 2010; Georg et al. 2017). Unlike primary cortical neurons cultured *in vitro* from fetal rodents which can establish synapse formation to mature status resembling that in the cerebral cortex *in vivo* (Ichikawa et al. 1993), purified RGCs cultured *in vitro* are unable to effectively form synapses without soluble astrocyte-derived signals (Ullian et al. 2001). Based on the findings in our current study from RGCs prior to the completion of synaptogenesis, we hypothesize that the increased motility of mitochondria could also possibly occur in mature RGCs with OPA1 deficit compared to normal RGCs *in vivo*. The generation of physiological relevant models, such as differentiated RGCs from induced pluripotent stem cells regenerated from patients' somatic cells, may assist in answering future questions.

Taken together, our results suggest that Opa1 haploinsufficiency leads to significant fragmentation of mitochondrial morphology, activation of mitochondrial motility and impaired respiratory function in retinal ganglion cells from the B6; C3-*Opa1*^{Q285STOP} mouse model. The increased motility of mitochondria is hypothesized to be a spontaneous compensatory

response which promotes fusion activity and facilitates energy production. More-in-depth studies are required to investigate the interplay between mitochondrial motility and bioenergetics and the precise mechanisms underlying the stimulated mitochondrial motility caused by Opa1 deficiency, which could be a new target for therapeutic intervention.

Chapter 4. Mitochondrial movement in RGCs from C57Bl6/J mice under hypertensive stress

4.1 Introduction

The axons of retinal ganglion cells connect the eye to the brain. Ocular hypertension is a major feature of most types of glaucoma, which is the leading cause of irreversible blindness in the world (Gupta and Chen 2016). Hypertensive stress could trigger the neurodegeneration and progressive death of RGCs by imposing compressive effects on the RGC axons. Multiple laboratories have suggested that the activation of several kinases such as p38 and JUN, as well as the recruitment of the BH3-only peptide families are involved in the early activation events after axonal damage. Following the BAX activation associated with mitochondrial dysfunction, later events are likely to include the activation of caspase 9 and probably endoplasmic reticulum (ER) stress. Furthermore, secondary degenerative events would be set in motion after RGCs begin to die due to the activation of macroglia and microglia, as well as the production of the inflammatory cytokine TNFα (Gordon et al. 2002; Howell et al. 2007; Nickells 2012). High intraocular pressure (IOP) and increasing age are the two critical features seen in glaucoma (Chrysostomou et al. 2010). Currently, most effective treatments for glaucoma are oriented towards lowering the elevated IOP (Heijl et al. 2002). However, the mechanisms regulating mitochondrial motility within RGC dendrites or axons associated with the glaucomatous neurodegeneration are still unclear.

As we know, mitochondrial motility contributes to transportation between the cell body and sites of high energy demand such as the synapses at the terminals of dendrites and axons in neurons (Vos et al. 2010). Mitochondrial dynamics and life-cycle, including fusion, fission, biogenesis, mitophagy and transportation, ensure a healthy population of mitochondria in neurons and help neurons adjust rapidly to the altered energy demands placed upon them.

There are a number of mouse models *in vivo* or *ex vivo* for experimental glaucoma research, such as genetic models (DBA/2J mouse model), and inducible models by laser photocoagulation or injection of obstructive substances (Dey et al. 2018). Here we set up a novel *in vitro* hypertension model using a half-closing culture system, in which RGCs were cultured under hypertensive stress induced by hydrostatic pressure for three days, in order to investigate the alterations of mitochondrial dynamics in RGCs directly exposed to

hypertensive stress.

4.2 Experimental design

RGCs were isolated from 7-day old C57BL/6 mouse pups using a two-step immunopanning method following the protocols from Winzeler and Wang (Winzeler and Wang 2013). RGCs were collected and then seeded on glass coverslips (Academy Science Limited, UK) coated by Poly-D-lysine (Sigma-Aldrich Corp., St. Louis, MO, USA) and laminin (R&D systems, UK) with a seeding density of 50,000 RGCs per well in 24-well culture plates (Nunc^{TM}, Thermofisher, UK). RGCs were cultured in a humidified atmosphere at 37 ˚C under 10% CO_2, in serum-free growth medium as previously described (Winzeler and Wang 2013). The RGC culture medium was changed every 3 days.

4.2.1 *In vitro* hypertension model setup

The hypertension model was set up using Quasi Vivo® QV600 cell culture system and consisted of two chambers connected by silicone connecting tubing Chamber B in the lower position was connected to a 10 mL syringe filled by RGC growth medium. The control chamber A was opened to the normal atmospheric pressure with a normal height of culture medium. So P_A is defined as normal pressure in the control or normal condition. Chamber B was fully closed by the matched lid and Chamber A was opened without a lid. All other tubing of Chamber A and B was fully sealed by Luer connectors. The pressure was formed by the liquid level difference *via* pushing the syringe plunger.

The added pressure in the chamber B was calculated by the formula of hydrostatic pressure: P_B-P_A=ρgh. The h is the difference of height between two samples (48.0 centimetre), as shown in Figure 4.1. The g is the acceleration of gravity 9.8 (m/s^2). The ρ (density) of culture medium is approximately 1000 kg/m^3. So the model provided a vertical pressure of approximately 35 mmHg to mimic a hypertensive condition *in vitro*. The conditions are the same between two groups except the hypertensive stress. RGCs were cultured on the Poly-D-lysine and laminin

coated glass coverslips in normal condition (24-well plates, Nunc, Thermofisher, UK) for seven days. Then one coverslip with attached RGCs, was carefully transferred to Chamber B by forceps for a period of three days culture under hypertensive stress and another coverslip (with RGCs) was transferred to Chamber A as the control group.

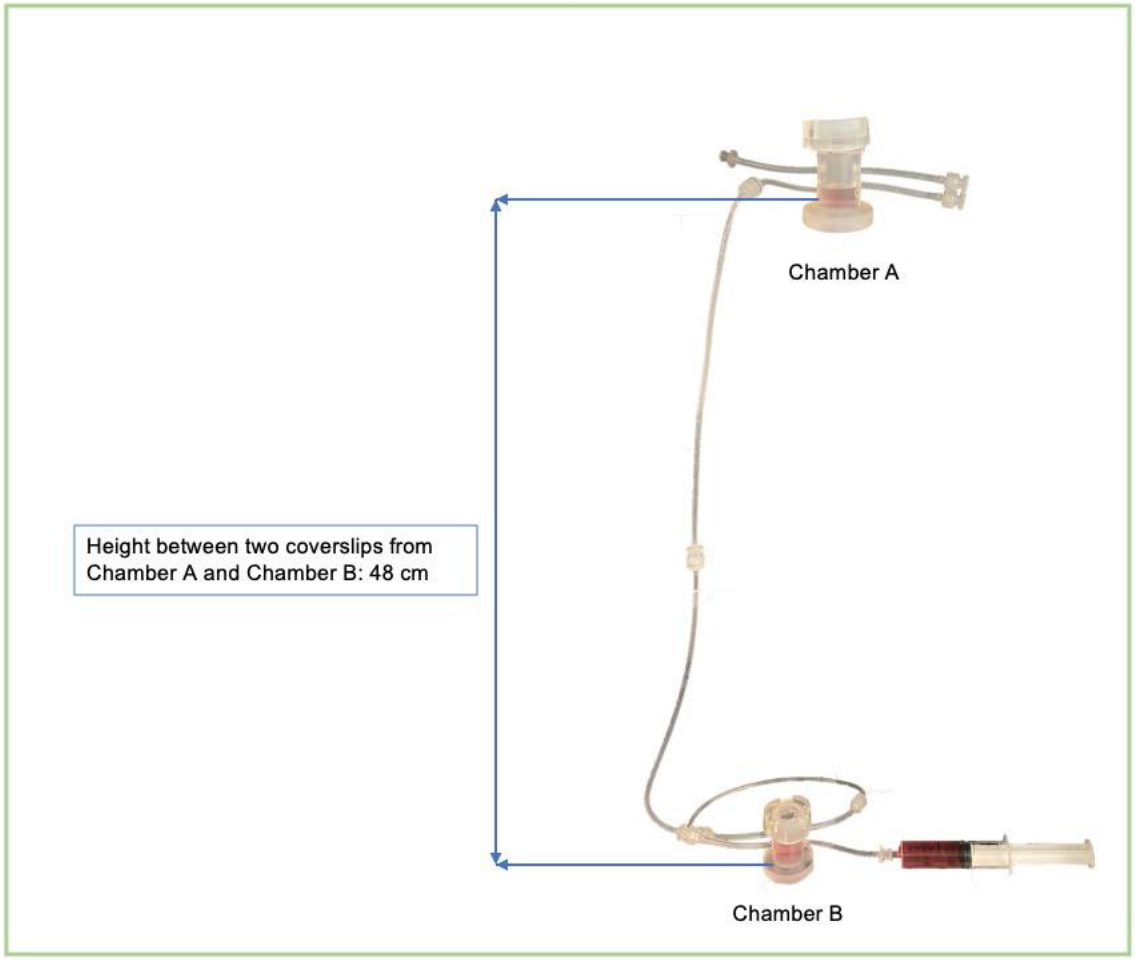

Figure 4.1 *In vitro* hypertension model setup.

4.2.2 Measurement and classification of mitochondrial motility

As described above, purified RGCs were firstly cultured in 24-well plates for seven days *in vitro*, and then the hypertension group was transferred into the chamber A of the hypertension model. Three days later, RGCs were stained by the specific mitochondrial marker, MitoTracker®Red CMXRos (Molecular Probes, Invitrogen) at 37 ˚C for 30 min. Images were captured under a 63X oil magnification lens using Zeiss LSM 880 confocal microscope and

Zen Zeiss software (Carl Zeiss). Time-lapse imaging was used to record mitochondrial movements; images were captured every 5 seconds for 10 minutes from RGCs cultured under normal pressure and hypertensive stress. Kymographs of mitochondrial movements were generated by KymoAnalyzer (Neumann et al. 2017) plugin in FIJI software (v1.52p, Wayne Rasband, National Institutes of Health, USA). Depending on the kymographs generated from the 10-minute mitochondrial movement recordings, the mitochondria were classified as stationary (those that moved no further than 5 μm), or motile (those that moved further than 5 μm). The fluttering population of mitochondria was defined as those that moved further than 2 μm with changed moving directions within the stationary population. This is because some mitochondria did short-distance reversing but could not be categorised as the motile population. The length of mitochondria was measured directly by FIJI software, and the mitochondrial coverage of neurite (100%) was measured as the total length of mitochondria within neurite account for each neurite length. The contact rate was calculated as the number of contacts between mitochondrial tracks divided by the total number of mitochondria per minute in each imaged region. The velocities of movements were calculated for motile mitochondria from the generated kymographs: the length of horizontal axis (the distance of movement) was divided by the length of vertical axis (the time of movement lasted) (μm/s).

4.3 Results

4.3.1 Hypertensive stress leads to fragmented mitochondrial morphology in primary mouse RGCs

As shown in Figure 4.2, the RGC cultures were stained with MitoTracker®Red and imaged under LSM880 confocal microscopy. The length of each mitochondrion along the RGC neurites under normal conditions and hypertensive stress was measured using by FIJI software. As in Chapter 3, the length of mitochondria was also measured at five image frames in the whole 120 frames from the 10 minutes time-lapse imaging in order to exclude damage from the laser scanning. The length of mitochondria was 3.09 ± 0.32 μm; 3.00 ± 0.34 μm; 3.11

± 0.13 μm; 3.09 ± 0.25 μm; 3.17 ± 0.08 μm in RGCs under normal conditions at image frames 1, 30, 60, 90, and 120 (0 min, 30 min, 60 min, 90 min and 120 min) respectively. There was no significant difference on the length of mitochondria among different images frames (Figure 4.3A). Similarly, the laser scanning did not affect the length of mitochondria in RGCs under hypertensive stress. The length of mitochondria at image frames 1, 30, 60, 90, and 120 (0 min, 30 min, 60 min, 90 min and 120 min) were 2.51 ± 0.15 μm; 2.45 ± 0.04 μm; 2.35 ± 0.17 μm; 2.48 ± 0.13 μm; 2.47 ± 0.26 μm, respectively (Figure 4.3B). However, there was an apparent decrease in the length of mitochondria in RGCs under hypertensive conditions compared to the control at timepoint 0 min (decreased by 0.58 μm, $p < 0.05$), 5 min (decreased by 0.77 μm, $p < 0.01$), 7.5 min (decreased by 0.61 μm, $p < 0.05$), 10 min (decreased by 0.70 μm, $p < 0.05$). At 2.5 min, the decrease of length caused by hypertensive stress was 0.56 μm compared to the control, the p value was 0.0502 by the Student's t test (Figure 4.4). Hence, he results indicate that hypertensive stress is likely to cause a fragmented structure of mitochondria.

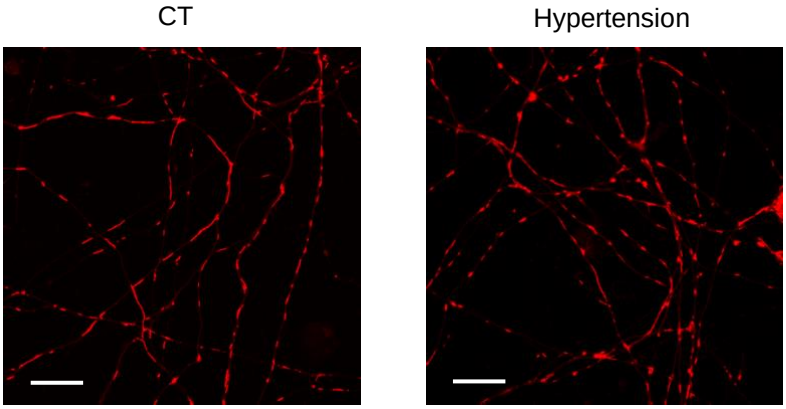

Figure 4.2 Representative confocal images of mitochondrial movements from control (CT) and hypertension cultures. RGC cultures were imaged after 10 days' culture and mitochondria were stained by MitoTracker®Red CMXRos and captured under a Zeiss LSM 880 confocal microscope and Zen Zeiss software under the MtRed filter with a 63X oil magnification lens (Carl Zeiss, UK), scale bar = 20 μm.

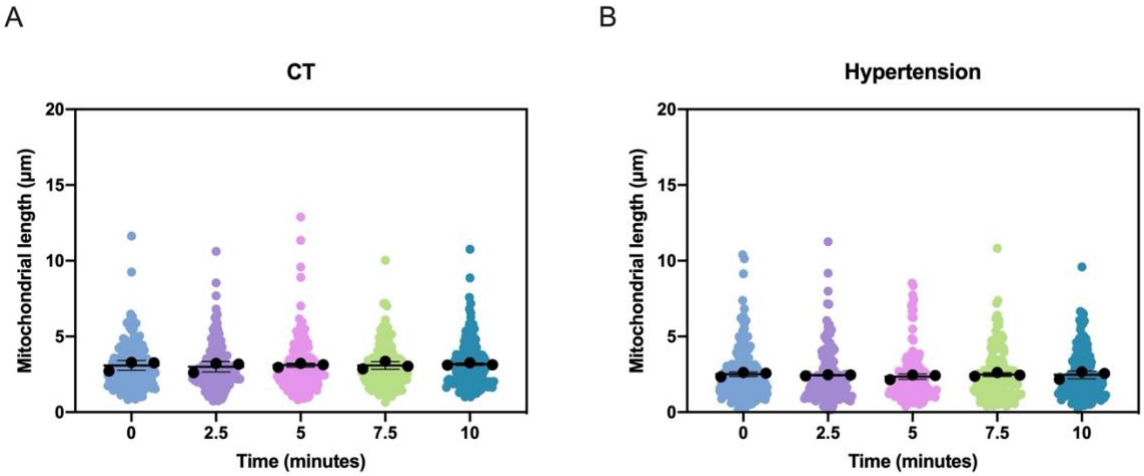

Figure 4.3 No significant difference was found in the mitochondrial length during 10-minute time-lapse imaging by confocal microscopy in control (CT) and hypertension cultures. The mitochondria were stained by the specific mitochondrial vital dye, MitoTracker®Red CMXRos and captured using a Zeiss LSM 880 confocal microscope by time-lapse imaging with 5-second intervals for 10 minutes. The length of mitochondria was measured manually by FIJI software at frames 1, 30, 60, 90 and 120 (0 min, 2.5 min, 5 min, 7.5 min and 10 min) in CT (A; n=778 mitochondria) and hypertension (B; n=755 mitochondria) cultures respectively. All the results are from 3 independent cultures, data shown as mean ± SD, N=3.

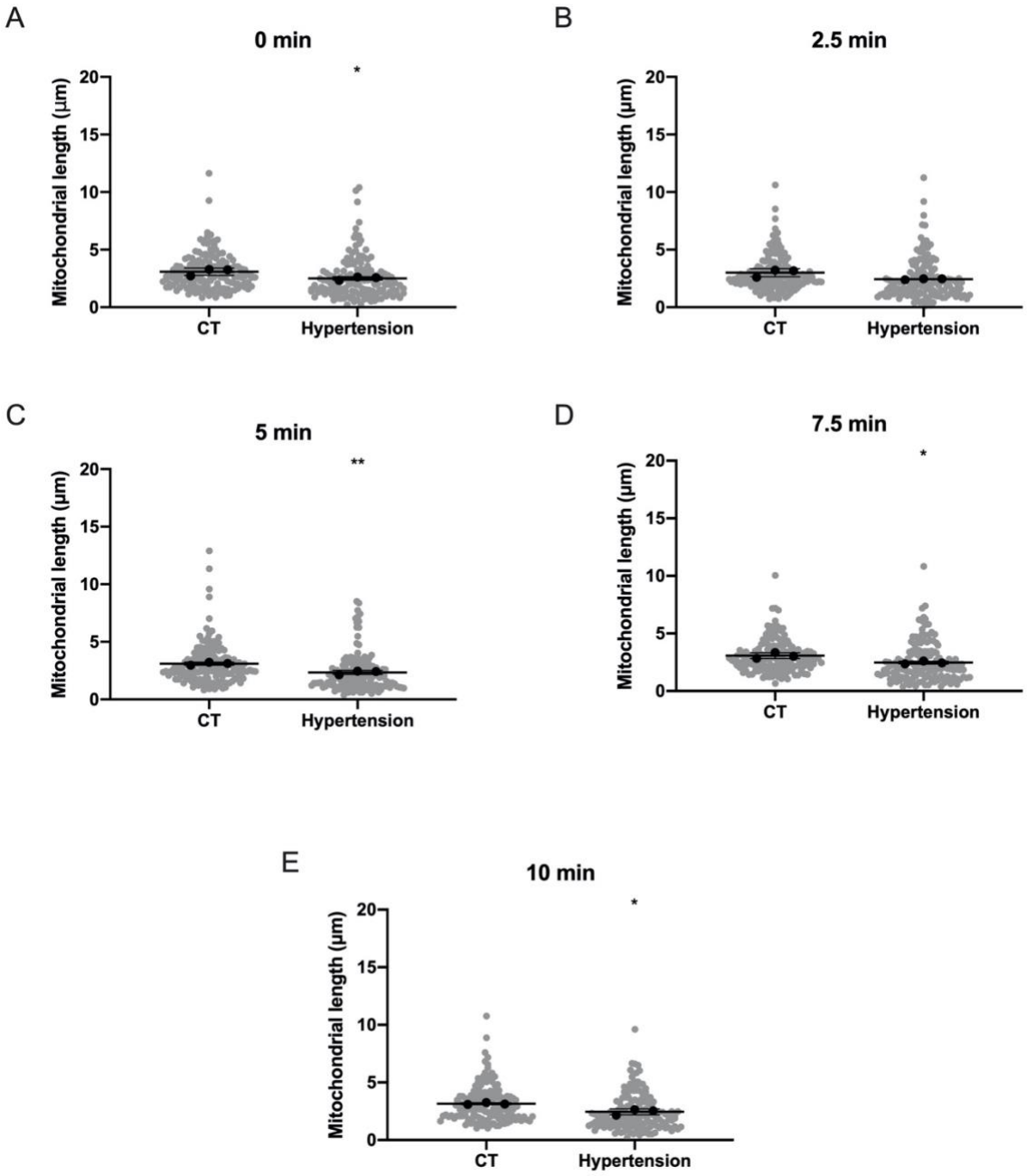

Figure 4.4 Hypertensive stress decreases the length of mitochondria *in vitro*. The length of mitochondria was measured manually by FIJI software at frames 1, 30, 60, 90 and 120 (0 min, 2.5 min, 5 min, 7.5 min and 10 min). Statistically significant shorter mitochondria were observed in hypertension cultures. (A) The length of mitochondria was measured at frame 1 (0 min). n=153 mitochondria in CT group; n=149 mitochondria in hypertension group. (B) The length of mitochondria was measured at frame 30 (2.5 min). n=165 mitochondria in CT group; n=148 mitochondria in hypertension group. (C) The length of mitochondria was measured at

frame 60 (5 min). n=158 mitochondria in CT group; n=154 mitochondria in hypertension group. (D) The length of mitochondria was measured at frame 90 (7.5 min). n=153 mitochondria in CT group; n=151 mitochondria in hypertension group. (E) The length of mitochondria was measured at frame 120 (10 min). n=149 mitochondria in CT group; n=153 mitochondria in hypertension group. Data analysed from 3 independent cultures. Data shown as mean ± SD, N=3. *p <0.05, **p <0.01 vs CT.

4.3.2 Hypertensive stress leads to increased percentage of motile mitochondria

The mitochondrial motility along the RGC neurites was measured using high-resolution confocal microscopy and tracing the tracks of each mitochondrion by FIJI software. 50,000 RGCs per well were seeded in 24-well plates. Approximately 18,000 ~ 20,000 RGCs were survived after 7-days' culture in each well. Thereafter, two groups of RGC cultures were treated under normal or hypertension condition for another 3 days respectively.

As shown in Figure 4.5, the kymographs were generated from RGC neurites with moving mitochondria using FIJI software. Totally 9 neurites from RGC cultures under normal and hypertensive stress conditions were assessed (all kymographs shown in Appendix IV S41). Approximately 87.45% mitochondria moved no further than 5 μm under normal condition; while 72.71% mitochondria moved further than 5 μm during the 10 minute's laser scanning under hypertensive stress (Figure 4.6A). Thus, there is an apparent increase of the motile mitochondrial population in RGCs under hypertension condition (increased by 14.74%, $p < 0.05$, Figure 4.6B). Specifically, 5.57% of the stationary mitochondria in RGCs under normal condition moved further than 2 μm and also changed their moving directions, which also defined as fluttering population within the stationary population. While approximately 10.33% of the stationary mitochondria were classified as fluttering population in RGCs under hypertensive stress, increased by 4.76%. The p value was 0.1943 by Student's t test, so no significant increase between the two fluttering populations (Figure 4.6C). Moreover, the contact rate between mitochondria during the movements was also calculated. However, no

apparent change was found on the number of contacts per minute from the RGCs under hypertensive stress compared to the control (Figure 4.6D).

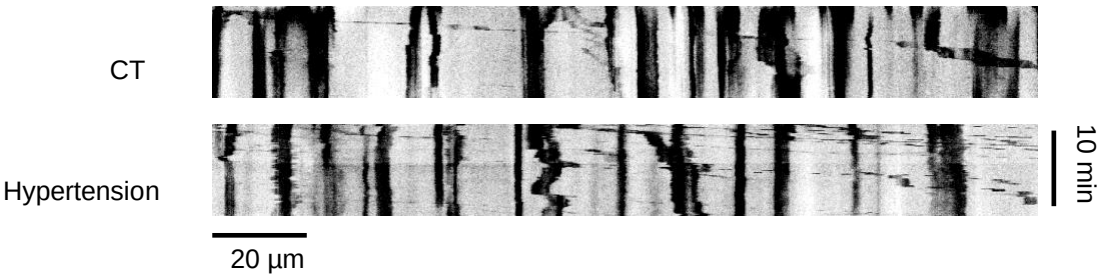

Figure 4.5 Representative kymographs from control (CT) and hypertension RGC cultures, n=9 neurites in both conditions from 3 independent cultures. Scale bar = 20 µm. All kymographs are presented in Appendix Figure S41.

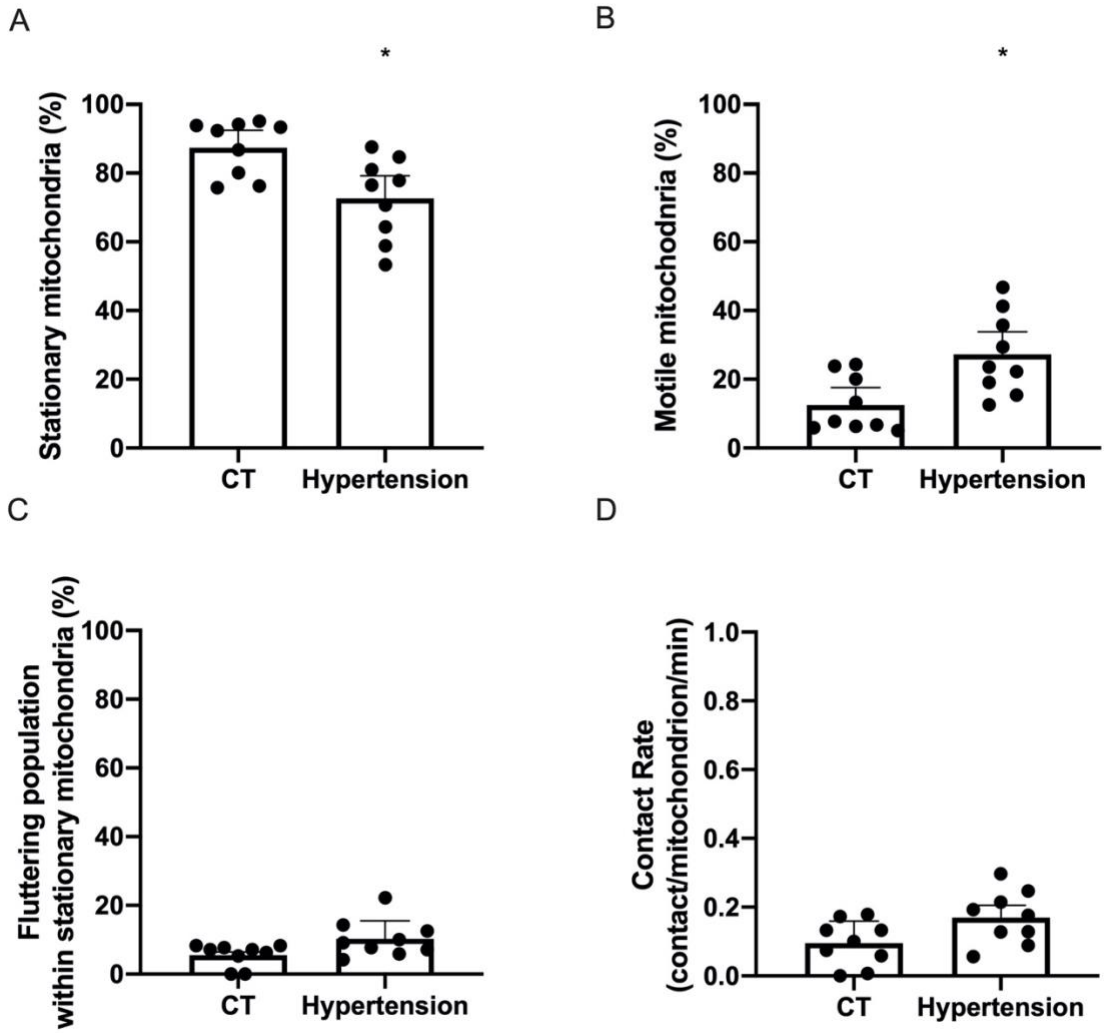

Figure 4.6 Hypertensive stress increases mitochondrial motility, but not contact rate. (A, B) Distribution of the mitochondrial population classified as stationary and motile; n=9 neurites in control (CT) and hypertension groups from 3 independent cultures. (C) The fluttering population within stationary mitochondria was defined as the mitochondria that had stationary status but fluttered within a small distance (moving directions changed, maximum moving distance > 2 μm); n=9 neurites in control and hypertension groups from 3 independent cultures. (D) The contact rate was calculated as the number of contacts between mitochondria per minute divided by the total number of mitochondria, n=9 neurites in in control and hypertension groups from 3 independent cultures. Data shown as mean ± SD, N=3. *p <0.05 vs CT.

4.3.3 No significant difference in mitochondrial velocity resulting from hypertensive stress

Mitochondrial velocity is an essential parameter of mitochondrial motility and dynamics; the velocity of motile mitochondria was also measured from kymographs. The velocity of motile mitochondria in RGC neurites under normal condition was 0.26 ± 0.074 μm/s), while the velocity of motile mitochondria in RGCs under hypertensive stress was 0.31 ± 0.13 μm/s). There was no significant difference caused by hypertensive condition compared to the normal groups, suggesting the stress produced by this hypertension model was not strong enough to change the velocity of mitochondrial movement. Furthermore, the length of each moving mitochondria was also measured by FIJI. The length of motile mitochondria under normal condition was 2.84 ± 0.31 μm, while the length under hypertensive stress was 2.45 ± 0.11 μm. No apparent difference between length of motile under normal and hypertension conditions.

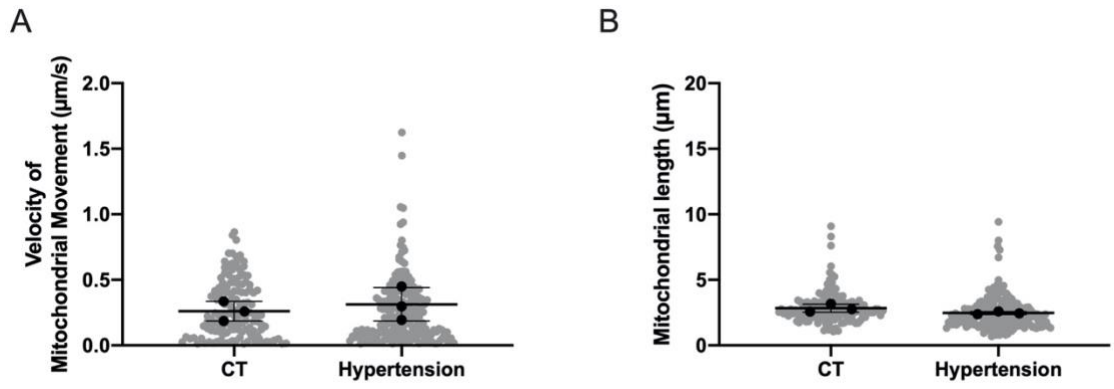

Figure 4.7 No apparent difference in the velocity of mitochondrial movement caused by hypertensive stress. (A) Velocities of mitochondria calculated from control (CT) and hypertension groups calculated from kymographs; n=137 mitochondria in CT group, n=195 mitochondria in hypertension group from 3 independent cultures (N=3). **No significant difference was found in mitochondrial length from RGC neurites between control and hypertension groups.** (B) Each mitochondrial length of the moving mitochondria from control and hypertension cultures in (A) was measured by FIJI software. Data shown as mean ± SD, N=3.

4.3.4 Relationship between mitochondrial velocity and length of moving mitochondria in RGCs under both control and hypertensive stress

As shown in Figure 4.8A and B, approximately 50% motile mitochondria (in red line framed, percentage of distributed mitochondria in each square>10%) were 3-4 μm with moving speed under 1 μm/s under normal condition, while over 60% motile mitochondria (in red line framed, percentage of distributed mitochondria in each square>10%) were moving in a slower velocity under 0.5 μm/s with shorter length between 1 μm and 2 μm under hypertensive stress shown in Figure 4.9A and B compared to the control. Furthermore, the velocity of mitochondria were measured in different groups: < 2 μm, 2-3 μm and >3 μm. In both normal and hypertension condition, no significant difference was found on the velocities with the increase of the mitochondrial length (Figure 4.8C, 4.9C).

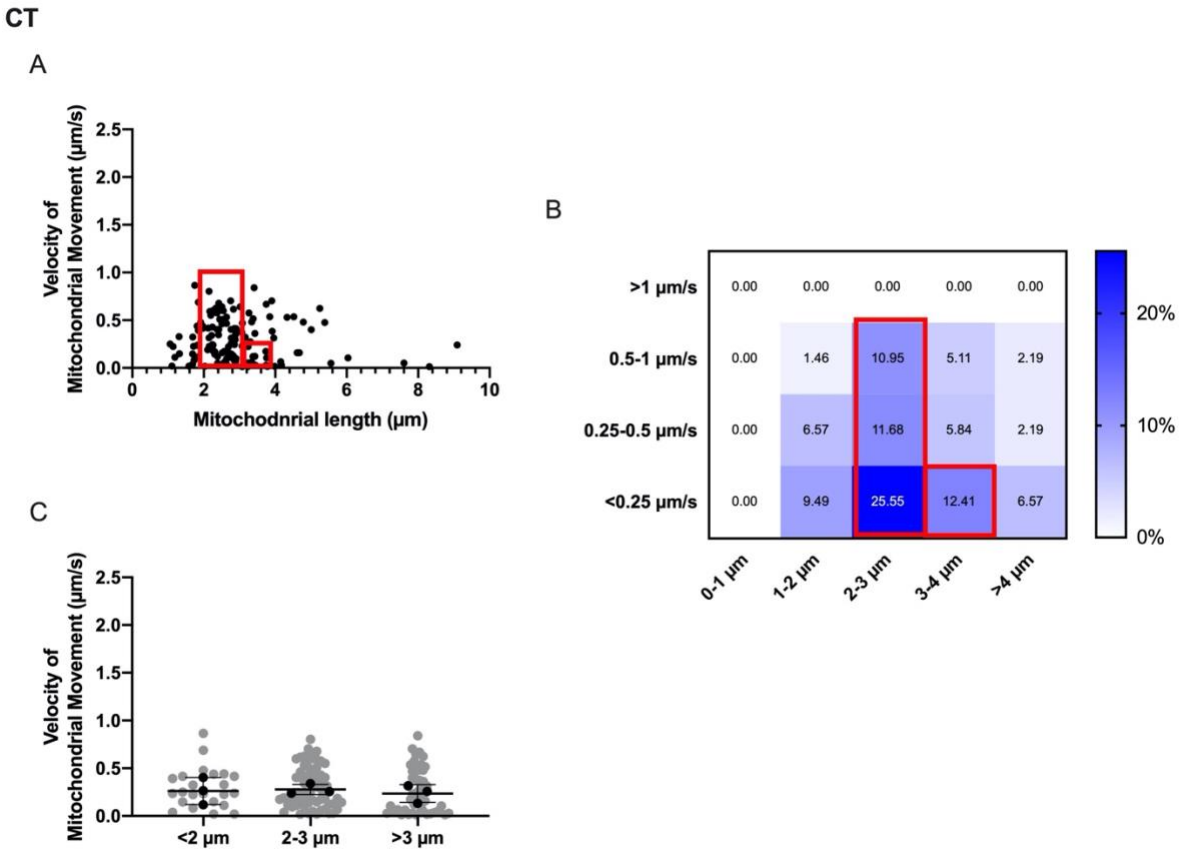

Figure 4.8 Distribution of mitochondrial velocity and length in control RGCs. No

significant difference was found on mitochondrial velocity with the increase of mitochondrial length in RGCs under normal condition. (A) Distribution of mitochondrial velocity according to their length, n=137 mitochondrial from 3 independent cultures. Red line framed area=greatest mitochondrial concentration (based on the heatmap result from (B)). (B) Heatmap of distribution of mitochondrial velocity and length. Red line framed area=greatest mitochondrial concentration (percentage of distributed mitochondria in each square>10%). (C) Mitochondria distributed by velocity with different ranges of length (<2 μm, 2-3 μm and >3 μm); n=24 mitochondria with length <2 μm; n=66 mitochondria with length between 2 and 3 μm; n=47 with length >3 μm from 3 independent cultures (N=3). Data shown as mean ± SD. The supplementary histograms characterized the detailed distribution of mitochondrial velocity and length from control RGCs has been added in Appendix Figure S44.

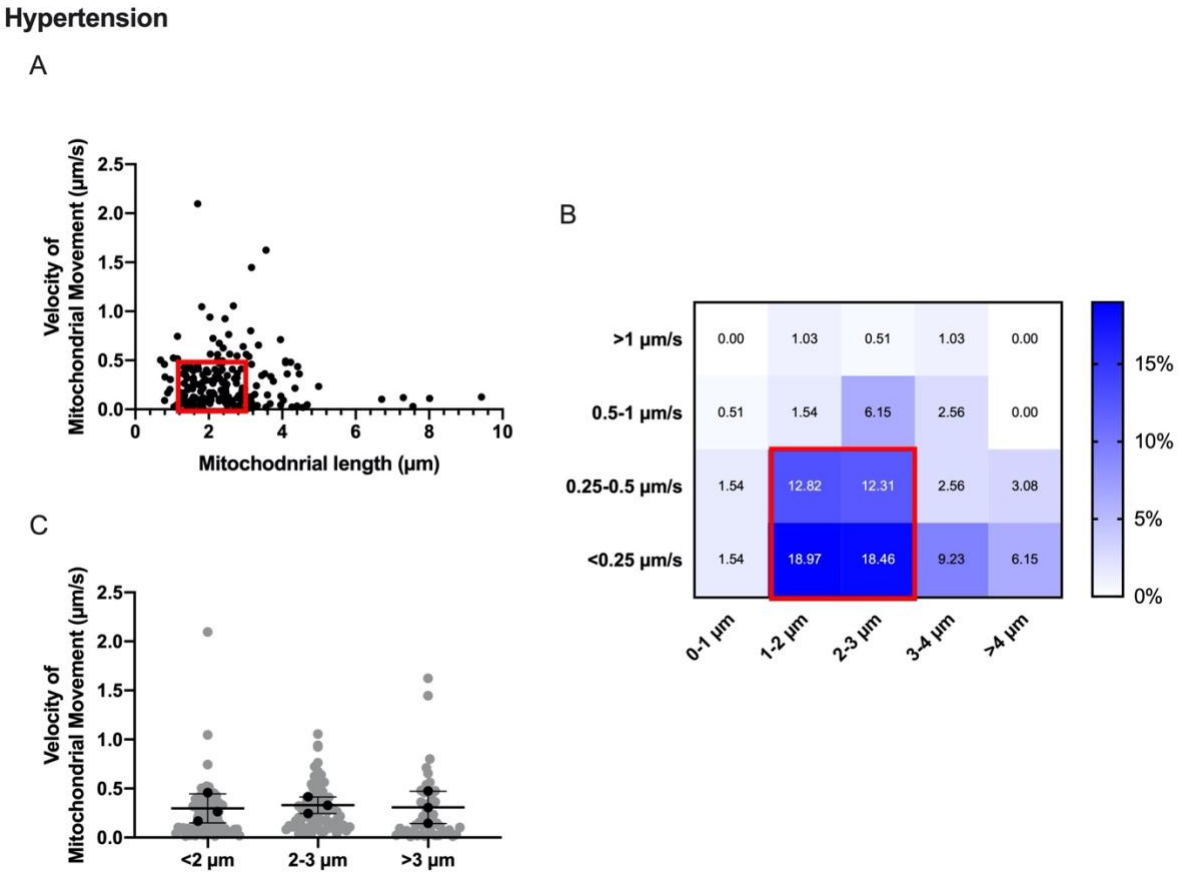

Figure 4.9 Distribution of mitochondrial velocity and length in RGCs under hypertensive stress. No significant difference was found on mitochondrial velocity with

the increase of mitochondrial length in RGCs under hypertensive stress. (A) Distribution of mitochondrial velocity based on their length, n=195 mitochondrial from 3 independent cultures. Red line framed area=greatest mitochondrial concentration (based on the heatmap result from (B)). (B) Heatmap of distribution of mitochondrial velocity and length. Red line framed area=greatest mitochondrial concentration (percentage of distributed mitochondria in each square>10%). (C) Mitochondria distributed by velocity with different ranges of length (<2 μm, 2-3 μm and >3 μm); n=74 mitochondria with length <2 μm; n=73 mitochondria with length between 2 and 3 μm; n=48 with length >3 μm from 3 independent cultures (N=3). Data shown as mean ± SD. The supplementary histograms characterized the detailed distribution of mitochondrial velocity and length from RGCs under hypertensive stress has been added in Appendix Figure S44.

4.4 Discussion

Glaucoma is an ocular disease frequently, if not always, associated with hypertensive stress, wherein there is selective and progressive death of RGCs. The typical age of onset of RGC loss in primary open angle glaucoma is much later than in patients with Leber's hereditary optic neuropathy (LHON) or autosomal dominant optic atrophy (ADOA). Elevated intraocular pressure can cause irreversible vision impairment by the selective death of RGCs and remodeling of the optic nerve head (Chrysostomou et al. 2010). Here, an easy *in vitro* hypertension model was created and the results suggest that hypertensive stress caused shortened length of mitochondrial structures accompanied with increased mitochondrial motility. However, there was no difference in the velocity of mitochondrial movements between control and hypertension groups.

However, the limitation is also obvious that only one pressure value was created by the vertical pressure of 35 mmHg in our simple hypertension model. Due to the Covid-19 lockdown, the plan was suspended to repeat mitochondrial measurement under different pressure by changing the vertical height between the chambers in our model. Thus there was also a lack

of pressure gradient to fully describe a dose response curve and thoroughly illustrate the relationship between pressure and mitochondrial dynamics. However, it is a pity that no time available to repeat experiments on various different pressure to obtain a dose-related curve due to the suspended lab work during Covid-19 lockdown from March 21st 2020 for approximately 5 months.

Mitochondria can appear as small individual membranes or elongated networks, mainly depending on the metabolic state of the cell. Neurons sustain a healthy population of mitochondria by achieving a delicate balance between fusion and fission through a delicate dynamic quality control system (Youle and van der Bliek 2012). Mitochondrial fission, regulated by the dynamin-1-like protein (Drp1), is essential in the quality control of the mitochondrial cohort by enhancing mitophagy, the selective degradation process of defective mitochondria followed by any internal damage or external stress. Previous research has documented that mitochondria became smaller and fragmented in RGC soma and axons observed from DBA/2J glaucoma mice (Coughlin et al. 2015), implying increased fission activity or imbalanced mitochondrial dynamics under hypertensive stress. Furthermore, fragmented mitochondria with decreased mitochondrial surface area, were shown to be less energy productive and deficient in autophagosomal degradation, indicating the deteriorating mitochondria were not able to be efficiently recycled through mitophagy in the hypertensive condition (Coughlin et al. 2015). Additionally, the inhibition of DRP1 expression or overexpression of OPA1 protein is likely to promote the RGC soma and axon survival under hypertensive condition (Ju et al. 2008; Kim et al. 2015). In our study, the length of mitochondria in neurites was moderately shortened after three days of hypertensive insult compared to the control.

The average eye pressure in human is approximately 15 mm Hg with a range between 10 and 21 mm Hg. In research, different mouse or rat models were used to mimic the condition of hypertensive stress. The DBA/2J (D2) mouse is a typical inherent glaucomatous model developing a progressive form of pigmentary angle-closure glaucoma (Anderson et al. 2002), which exhibits sustained elevations in IOP that are comparable to those observed in glaucoma

patients (23 mm Hg to 35 mm Hg) (Inman et al. 2006; Ju et al. 2008; Coughlin et al. 2015). The “glaucoma bead model” is a common method to elevate IOP in rats or mice by injecting microbeads into the anterior chamber of the eye to obtain a sustained increase in IOP around 40 mm Hg (Bunker et al. 2015). Thus, in our research, we chose 35 mm Hg as our experimental level to explore the alterations under hypertensive stress. Interestingly, Kimball et al. 2018 used the method of microbead injection and showed that the mitochondria in axons were significantly smaller after 3-hours’ or 3-days’ IOP elevation, but no significant difference after 4-days’ IOP elevation, implying the response to the elevated pressure that is attributed to fission might not be a continued feature in the long term. Thus, not only the levels of pressure, but also the time course of pressure is likely to be an important factor in hypertension models, and both of them could be our next research focuses based on our *in vitro* model.

Mitochondrial motility or transportation is a complex process involving interactions between polarized microtubes, motor proteins, adaptors that link motors to mitochondria and anchors that arrest transportation (Barnhart 2016). Elevated ocular pressure was demonstrated as a highly specific factor altering the extracellular matrix composition of the optic nerve head (Morrison et al. 1990). It is also known that the movement of mitochondria and other organelles along the axon is interrupted within the optic nerve head, but the precise mechanisms are still not thoroughly understood. By using our simple hypertension device, the fragmented mitochondria along the neurites caused by the elevated pressure showed a moderate increase in the proportion of motile mitochondria- defined as movement further than 5 um. Furthermore, hypertensive stress did not change the velocity of mitochondrial movement in our hypertension model. Few researchers have developed *in vivo* or *ex vivo* explant methods to image the transportation of mitochondria under hypertensive stress. Takihara et al. 2015 also demonstrated decreased mitochondrial length and unchanged transport velocity/distance in RGC axons caused by hypertensive stress by intravital imaging, which was consistent with the results from our *in vitro* model. Our result of mitochondrial coverage of neurites showed no significant difference in RGC neurites under control and hypertensive conditions *in vitro*. However, Takihara showed that significantly fewer mitochondria were transported in both

retrograde and anterograde direction and more mitochondria-free areas were observed in RGC axons in the hypertensive condition compared to the control. They also indicated that the disturbances of mitochondrial transport in the glaucoma model *in vivo* was likely to be linked with the decreased biogenesis (Takihara et al. 2015). The advanced intravital imaging without opening of the sclera or changes in the intraocular humour that Takihara used offers benefits over *in vitro* or *ex vivo* imaging. Aaxonal transport of mitochondria is quite sensitive to changes in the living environment, and the dissection of retina and purification of RGCs from explanted retina could affect their transport (Germain et al. 2006). Kimball et al. 2018 documented a significantly smaller size of mitochondria after 3 days of chronic IOP elevation in the glaucoma eyes in their pilot trial, which is consistent with the results from Takihara et al. 2015, and with the data presented here. Similarly, there was no significant alteration in mitochondrial moving speed in 4-month-old adult mice but ageing was noted to decrease the moving speed in the elderly. Interestingly, there was no statistically significant difference in the size of mitochondria after 4 days IOP elevation (Kimball et al. 2018), indicating the time duration of exposure to elevated IOP was also likely to alter the mitochondrial morphology. However, Kimball et al. 2018 also reported that mitochondrial movement was decreased with exposure to elevated IOP in a murine ocular explant model compared with the control group (Kimball et al. 2018), conflicting with our results *in vitro*.

There could be three reasons for the different results with respect to the proportion of motile numbers of mitochondria. Firstly, as described above, Takihara et al. 2015 and Kimball et al. 2018, etc. observed axons *in vivo* or *ex vivo*, but the observations presented here are on mitochondria in all neuritis, including axons and dendrites, in purified RGCs *in vitro*. So we would plan to identify the axon among the neurites in RGCs in future experiments and explore the axonal profile of mitochondrial dynamics. The sensitive mitochondrial dynamics in neurites could be changed due to the invasive way of isolating the RGCs from mice. Secondly, the *in vitro* hypertension model presented here might involve other stimulating factors associated with the hypertensive condition, such as the disturbance of pH level in the RGC culture medium due to significant reduction of the exchange between CO_2 and carbonic acid in the

semi-closed hypertension *in vitro* model. Though there has been no evidence published relating explicitly to mitochondrial motility and the level of carbonic acid, an elevated CO_2 level was reported to cause mitochondrial dysfunction in human lung fibroblasts (Vohwinkel et al. 2011). Thus, the disturbance of the molecular environment in the RGC culture system in the hypertension model could alter the mitochondrial motility. Finally, there are some common mathematical methods to define “motile cargo” within neurites- either defined by the velocity of movement (≥ a μm/s) (Takihara et al. 2015); or defined by the distance of movement within time of observation (≥ b μm) (Neumann et al. 2017); or even defined visibly (Kimball et al. 2018). The parameter “a” and “b” as thresholds were usually set by the user subjectively after original observation. Moreover, the interval and whole time duration of time-lapse imaging are also likely to be factors that may influence the result. For example, in our study, the mitochondrial movement was measured for 10 minutes with 5 second intervals, which was much longer than that in the protocols employed by Takihara et al. 2015 and Kimball et al. 2018 (2 min with 4s intervals; 3 min with 3s intervals respectively). It is possible that some mitochondria with very low moving speed were transported further than 5 μm in a much longer period (10 min) and were identified as “motile” in our study, which would be identified as “stationary” using other definition of groups. Thus, it will be interesting to perform further studies to set up standard criteria for mitochondrial motility and also explore a more physiological hypertension model *in vitro* to illustrate the movement of mitochondria in RGCs.

Elevated intraocular pressure is a critical risk factor for optic nerve damage and RGCs death in glaucoma. Hypertensive stress was demonstrated to result in a reduction in expression of cytochrome c oxidase and Opa1 protein, and an increase of Drp1 gene expression in a glaucomatous mouse model (Ju et al. 2008). Loss of Opa1 protein reduces bioenergetic function in axonal mitochondria, and leads to significant deficits in maintaining the normal ATP production and synaptic vesicle cycling (Landes et al. 2010b). The expression of mitofusin (Mfn1 and 2) proteins was also shown to decline in primary optic nerve head astrocytes under hypertensive stress (Ju et al. 2019). Thus, these evidences indicate that the balance between fusion and fission dynamics within mitochondria was disturbed by increasing excessive

mitochondrial fission due to hypertensive stress. Oxidative stress has been recognised as playing an important role in the pathological envelopment of glaucoma by generating excessive ROS, decreasing the activity of respiratory complex I and consequently ATP production (Tezel 2006). Specifically, Van Bergen et al. 2015 documented that lymphoblasts derived from glaucoma patients have impaired complex I and milder disease development in mitochondrial oxidative phosphorylation compared with that from LHON patients (Abu-Amero et al. 2006; Van Bergen et al. 2015). Moreover, Williams et al. 2017, demonstrated that the mitochondrial dysfunction and alterations in oxidative phosphorylation pathways is an early feature of neuronal dysfunction, occurring before detectable degeneration, which is also associated with age-dependent decline in retinal NAD^+ and glutathione in DBA/2J mice (Williams et al. 2017). Intriguingly, not only could hypertensive stress-induced oxidative stress trigger excessive fission activity, but the fission process itself could also enhance the oxidative stress-mediated mitochondrial dysfunction in RGCs and further degeneration of their axons. Kim et al. 2015 using the genetic glaucoma mouse model (DBA/2J) as well as an *in vitro* RGC culture system, demonstrated an important vicious circle relevant to glaucomatous neurodegeneration, which starts with increased intraocular pressure producing oxidative stress, and is then followed by increased mitochondrial fission and oxidative stress-mediated mitochondrial dysfunction that generates further oxidative stress, thus perpetuating the cycle (Kim et al. 2015). Glutathione s-transferase (GST) enzymes may also be declined by oxidative stress under hypertensive stress, which then contributes to exacerbate the negative effects of oxidative stress in the region of optic nerve head and consequently result in glaucomatous neurodegeneration (Lascaratos et al. 2012). Hypertensive stress was also shown to upregulate the Tumour necrosis factor alpha (TNFα), a multifunctional pro-inflammatory cytokine, to impair the mitochondrial biogenesis and functions by down-regulating eNOS expression and disturbing the mitochondrial dynamics (Chen et al. 2010b). The upregulated expression of TNFα has been implicated to induce RGC apoptosis in animal models and human glaucomatous optic nerve degeneration (Nakazawa et al. 2006; Tezel 2008). Recently, cyclic adenosine 3′,5′-monophosphate (cAMP)/protein kinase A (PKA) signaling pathway was

demonstrated to be involved in the pathological process of hypertensive stress in optic nerve head, which is a critical pathway in a variety of cellular functions including cell survival and death (Corredor et al. 2012). It was found that inhibition of cAMP/PKA pathway would activate Akt/Bax phosphorylation and promote Mfn1/2 oligomerization so as to inhibit the caspase-3 activation-mediated cell death (Ju et al. 2019). On the other hand, aging is another risk factor for increased mitochondrial dysfunction in ocular hypertension models and samples from glaucoma patients (Rochtchina et al. 2002; Bratic and Larsson 2013). Patients with primary angle closure glaucoma had a high frequency of mtDNA transversion mutations with a decrease of mitochondrial mean respiratory activity (Abu-Amero et al. 2007). The mtDNA mutations have been shown to accumulated with age (Wei 1992) by diminishing the activity of cellular autophagy (Terman 1995), which contributes to the mitochondrial dysfunction under ocular hypertension (Jeoung et al. 2014).

Therefore, the alterations of mitochondrial dynamics and/or oxidative stress resulting from elevated intraocular pressure are likely to be a major cause for RGC neurodegeneration under hypertensive stress. However, there may be other factors at play in our *in vitro* hypertension model that do not fully mimic the pathological condition of elevated IOP. Thus other physiologically relevant animal models would be required to explore the precise mechanism linking mitochondrial dynamics with the early onset and progression of RGC death under ocular hypertension.

Chapter 5. Effect of nicotinamide on mitochondrial dynamics in RGCs from C57Bl6/J mice

5.1 Introduction

RGCs are extremely vulnerable to mitochondrial deficits resulting from internal (mutations in genes) or external (elevated pressure, persistent light exposure) insults due to their unique axonal morphology, distribution of mitochondria and steep energy requirement for the maintenance of complex dendritic structure with millions of synapses (Wang et al. 2003; Vos et al. 2010).

Nicotinamide, a water-soluble form of vitamin B3 or niacin, is synthesized naturally in the body by eating niacin-rich foods such as fish, poultry, nuts, eggs, legumes, and cereal grains. Vitamin B3 is an essential nutrient and the body cannot create it, so that humans must obtain it from the above food. Nicotinamide supplement can also be used to prevent and treat skin conditions and niacin deficiencies such as pellagra. Nicotinamide helps the body convert food (carbohydrates) into energy . Nicotinamide adenine dinucleotide (NAD^+/NADH) and nicotinamide adenine dinucleotide (NADP) are two coenzyme derivatives from nicotinamide. The ratio of NAD+/NADH performs a critical role in varieties of enzymatic oxidation-reduction reactions in glycolysis, pyruvate oxidation, citric acid (Krebs) cycle and oxidative phosphorylation (Belenky et al. 2007). Specifically, high NADH/NAD+ levels activate the transfer of electrons to complex I, and sequentially accelerate the activity of the electron transport chain (ETC), as well as ATP production. Furthermore, the activities of the sirtuin family (SIRT1-7) are tightly regulated by the levels of NAD+, in which SIRT1 and SIRT3 are critically associated with mitochondrial biogenesis and mitophagy (Brenmoehl and Hoeflich 2013; Hwang and Hwang 2017). Thus NAD+ plays a critical role in the cellular energy metabolism and mitochondrial quality control by regulating the oxidative phosphorylation and sirtuin protein activities. Oral supplementation of NAM (vitamin B3) has been successfully used to correct the disturbances in NAD+ metabolism in two mouse models of pre-eclampsia, which benefited both mothers and pups (Li et al. 2016). Nicotinamide has been recognized to be associated with neuronal development, survival and function in the central nervous system (CNS). Recently, nicotinamide was demonstrated as an essential neuroprotective agent for ocular hypertension, which caused an age-dependent decrease in the retinal level of NAD^+ (a

key molecule in energy and redox metabolism) and glutathione (Williams et al. 2017). However, the molecular mechanisms underlying how nicotinamide alters mitochondrial dynamics, and thus facilitates a neuroprotective effect on neurons or RGCs, are not fully understood.

Thus, in our study, we aimed to explore the effect of nicotinamide on mitochondrial dynamics in RGCs purified from C57BL/6 mouse pups by applying nicotinamide directly into the RGC culture medium *in vitro* with different concentrations for 24 hours. Here we provide a novel insight into the effect of nicotinamide on mitochondrial motility in RGCs *in vitro*.

5.2 Experimental design

All procedures for RGC culture were carried out on 7-day old C57BL/6 mouse pup retina using a two-step immunopanning method, adapted from and following the protocols from Winzeler and Wang (Winzeler and Wang 2013). RGCs were collected and then seeded onto glass coverslips (Academy Science Limited, UK) coated by Poly-D-lysine (Sigma-Aldrich Corp., St. Louis, MO, USA) and laminin (R&D systems, UK) with a seeding density of 50,000 RGCs per well in 24-well culture plates (Nunc^{TM}, Thermofisher, UK). RGCs were cultured in a humidified atmosphere at 37 ˚C under 10% CO_2, in serum-free growth medium, as previously described (Winzeler and Wang 2013). After 7-days of culture, RGCs were then cultured with nicotinamide for 24 h. Different concentrations (500 mM, 250 mM, 100 mM, 10 mM and 1 mM) of nicotinamide were administrated on RGC cultures in 24-well plates as a pilot trial. RGCs were dead and floated in the culture medium within 6 hours under concentrations of nicotinamide at 500 mM, 250 mM and 100 mM. The cell bodies of RGCs were shrunk and neurites were significantly fragmented under contrast microscopy with administration of 10 mM, indicating that 10 mM of nicotinamide was too toxic for RGCs in 24-well plates *in vitro*. As shown in Fig 5.1(A), RGCs survived with a healthy status by applying 1 mM of nicotinamide. It was thus e decided to use 1 mM, 500 μM, 100 μM and 50 μM nicotinamiode administrated on the RGCs culture to observe the effect of nicotinamide on mitochondrial motility in RGCs.

Mitochondria were stained using the specific mitochondrial vital dye, MitoTracker®Red

CMXRos (Molecular Probes, Invitrogen) at 37 ˚C in the incubator for 30 min. Mitochondrial motility measurement was performed by time-lapse imaging using a Zeiss LSM 880 confocal microscope and Zen Zeiss software under the MtRed filter (Carl Zeiss, UK). A 63X oil magnification lens was used. Time-lapse imaging was used to record mitochondrial movements; images were captured every 5 seconds for 10 minutes from RGCs cultured from control and nicotinamide-treated groups. Kymographs of mitochondrial movements were generated by KymoAnlyzer (Neumann et al. 2017) plugin in FIJI software (v1.52p, Wayne Rasband, National Institutes of Health, USA). Depending on the kymographs generated from the 10-minute mitochondrial movement recordings, the mitochondria were classified as stationary (that moved no further than 5 μm), or motile (moved further than 5 μm).Finally, the fluttering population of mitochondria was also defined as moved further than 2 μm with changed moving directions within the stationary population, for some mitochondria did short-distanced reversing but not categorised as motile population. The length of mitochondria was measured directly by FIJI software, and the mitochondrial coverage of neurite (100%) was measured as the total length of mitochondria within neurite account for each neurite length. The contact rate was calculated as the number of contacts between mitochondrial tracks divided by the total number of mitochondria per minute in each imaged region. The velocities of movements were calculated for motile mitochondria from the generated kymographs: the length of horizontal axis (the distance of movement) was divided by the length of vertical axis (the time of movement lasted) (μm/s).

5.3 Results

5.3.1 Nicotinamide treatment increases the length of mitochondria

Approximately 18,000 ~ 20,000 RGCs survived in each well before imaging. As shown in Figure 5.1, the mitochondrial movement was stained with MitoTracker®Red and captured under LSM880 confocal microscopy. The length of mitochondria was firstly measured at five timepoints (0 min, 2.5 min, 5 min, 7.5 min and 10 min) to determine whether the laser scanning

from microscopy affected the mitochondrial health, and no significant difference was found on the mitochondrial length during the 10 minutes' scanning (data shown in Appendix V S52).

Also, the length of mitochondrial at five timepoints from each of the nicotinamide-treated cultures was compared to the control. Specifically, the average length of mitochondria in control RGCs was 3.04 μm, 2.79 μm, 2.99 μm, 2.90 μm, 2.90 μm at each time points from 0 min to 10 min, respectively. And 3.15 μm, 3.32 μm, 3.32 μm, 3.23 μm and 3.23 μm in 50 μM nicotinamide-treated RGCs; 3.38 μm, 3.23 μm, 3.37 μm, 3.51 μm, 3.50 μm in 100 μM nicotinamide-treated RGCs; 3.48 μm, 3.29 μm, 3.49 μm, 3.03 μm, 3.62 μm in 500 μM nicotinamide-treated RGCs; 3.50 μm, 3.50 μm, 3.62 μm, 3.48 μm, 3.62 μm in 1 mM nicotinamide-treated RGCs. At timepoint 0 min, 7.5 min and 10 min, the length of mitochondria in 1 mM nicotinamide-treated RGCs was significantly longer compared to the control. Furthermore, the mitochondrial coverage of neurite (100%) was also measured. A higher coverage was found in 100 μM and 1 mM nicotinamide-treated RGCs at timepoints 0 min, 2.5 min and 7.5 min. These results indicated that the length of mitochondria always changed overtime for the dynamic network, and high concentration of nicotinamide would promote the fusion process and obtain longer mitochondrial structure.

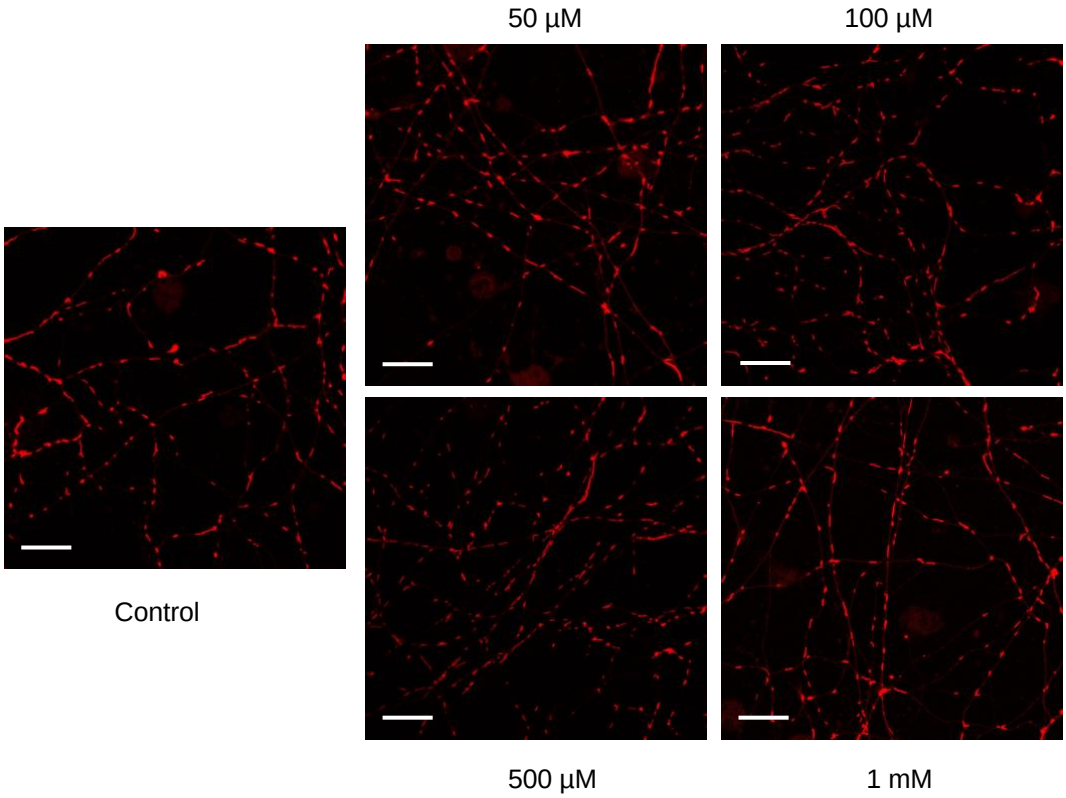

Figure 5.1 Representative confocal images of mitochondrial movements from control and nicotinamide-treated (50 µM, 100 µM, 500 µM and 1 mM) groups. Mitochondria were stained by MitoTracker®Red CMXRos and captured under a Zeiss LSM 880 confocal microscope and Zen Zeiss software under the MtRed filter with a 63X oil magnification lens (Carl Zeiss, UK), scale bar = 20 µm.

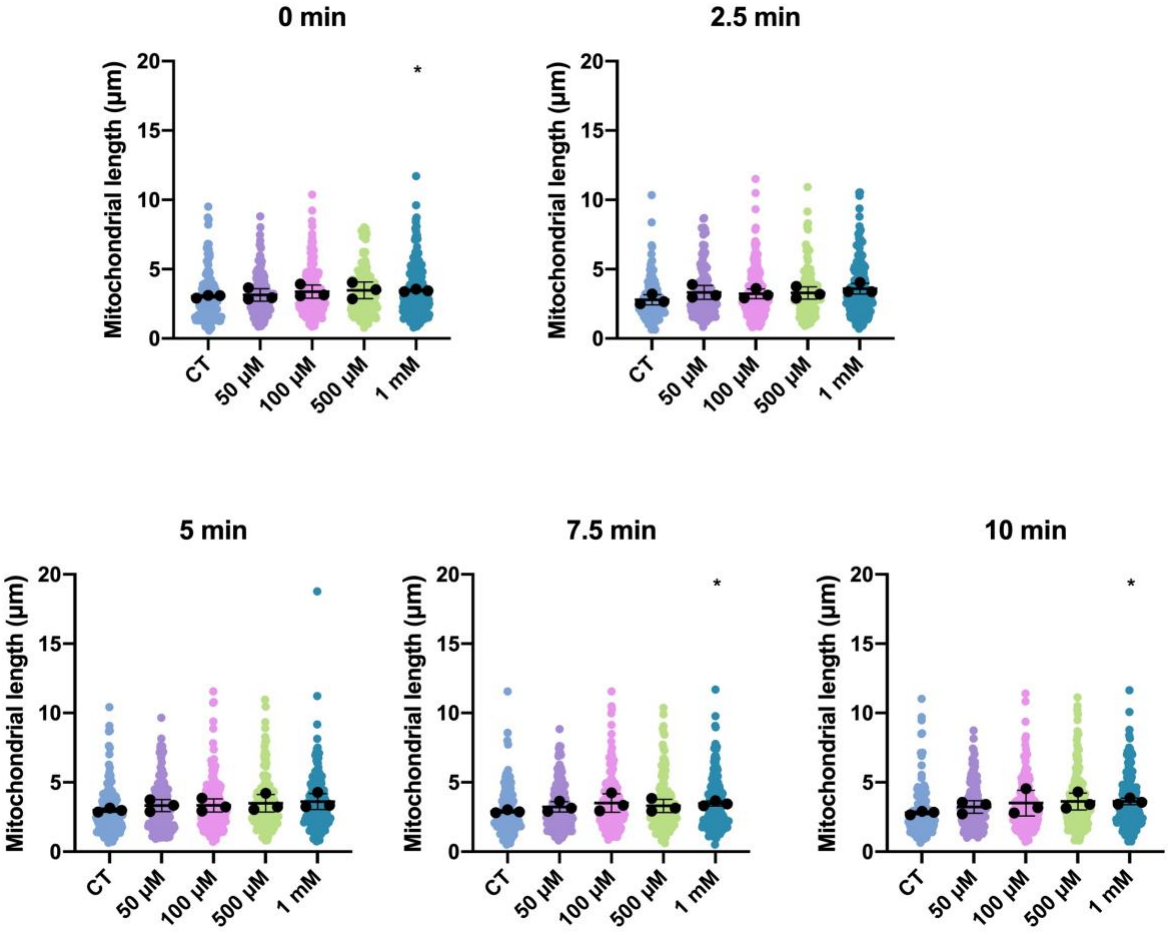

Figure 5.2 The length of mitochondria was increased in 1 mM nicotinamide-treated RGCs at 0 min, 7.5 min and 10 min compared to the control. The length of mitochondria was stained by specific mitochondrial vital dye, MitoTracker®Red CMXRos and captured using a Zeiss LSM 880 confocal microscope by time-lapse imaging with 5-seconds' interval for 10 minutes. The length of mitochondria were measured manually by FIJI software at frames 1, 30, 60, 90 and 120 (0 min, 2.5 min, 5 min, 7.5 min and 10 min). (A) The length of mitochondria was measured at frame 1 (0 min). n=127 mitochondria in control group; n=171 mitochondria in 50 μM nicotinamide-treated group; n=209 mitochondria in 100 μM nicotinamide-treated group; n=159 mitochondria in 500 μM nicotinamide-treated group; n=203 mitochondria in 1 mM nicotinamide-treated group. (B) The length of mitochondria was measured at frame 30 (2.5 min). n=127 mitochondria in control group; n=161 mitochondria in 50 μM nicotinamide-treated group; n=219 mitochondria in 100 μM nicotinamide-treated group; n=174 mitochondria in 500 μM nicotinamide-treated group; n=193 mitochondria in 1 mM

nicotinamide-treated group. (C) The length of mitochondria was measured at frame 60 (5 min). n=137 mitochondria in control group; n=154 mitochondria in 50 μM nicotinamide-treated group; n=212 mitochondria in 100 μM nicotinamide-treated group; n=167 mitochondria in 500 μM nicotinamide-treated group; n=194 mitochondria in 1 mM nicotinamide-treated group. (D) The length of mitochondria was measured at frame 90 (7.5 min). n=137 mitochondria in control group; n=160 mitochondria in 50 μM nicotinamide-treated group; n=202 mitochondria in 100 μM nicotinamide-treated group; n=174 mitochondria in 500 μM nicotinamide-treated group; n=197 mitochondria in 1 mM nicotinamide-treated group. (E) The length of mitochondria was measured at frame 120 (10 min). n=137 mitochondria in control group; n=158 mitochondria in 50 μM nicotinamide-treated group; n=193 mitochondria in 100 μM nicotinamide-treated group; n=168 mitochondria in 500 μM nicotinamide-treated group; n=186 mitochondria in 1 mM nicotinamide-treated group. Data shown as mean ± SD, N=3.

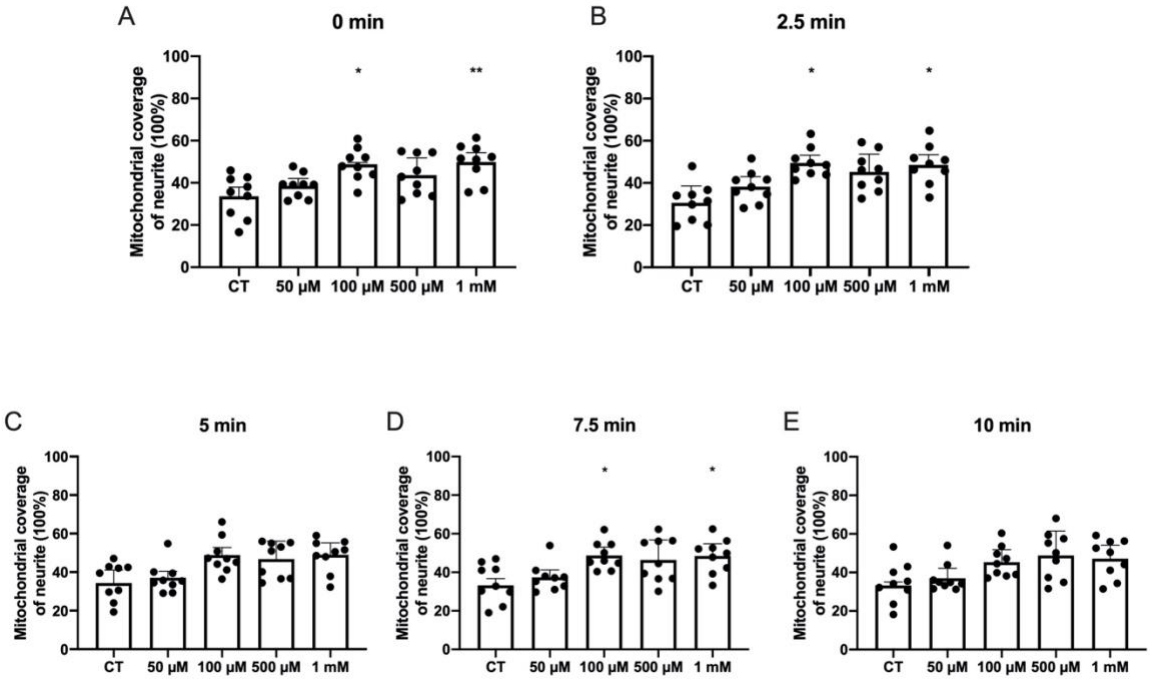

Figure 5.3 Nicotinamide treatment increases mitochondrial coverage in RGC neurites *in vitro* observed at 0 min, 2.5 min and 7.5 min. The mitochondrial coverage in the neurite was calculated as the percentage of total mitochondrial length along the neurite divided by the

length of neurite, n=9 neurites from each of control and nicotinamide-treated groups from 3 independent cultures. The mitochondrial coverage in the neurite was statistically increased by nicotinamide at concentrations of 100μM and 1mM at timepoints 0 min, 2.5 min and 7.5 min compared to the control group. No significant difference was found on the mitochondrial coverage of neurite during the 10-minute time-lapse imaging through confocal microscope in each of control and nicotinamide-treated groups (see Appendix V Figure S53). (A, B, C, D, E) The percentage of mitochondrial coverage of neurite calculated from 9 neurites in control and nicotinamide-treated cultures at frames 1, 30, 60, 90 and 120 (0 min, 2.5 min, 5 min, 7.5 min and 10 min). Data shown as mean ± SD, N=3. *p <0.05, **p <0.01 vs control.

5.3.2 Nicotinamide treatment increases the motility of mitochondrial movement

The kymographs were generated from 9 neurites in each of the control and nicotinamide-treated RGC cultures. Representative images are shown as Figure 5.4. All kymographs from each of the control and nicotinamide-treated cultures are shown in Appendix V S51. As shown in Figure 5.5A and B, nicotinamide treatment increased the motile population of mitochondria. The average motile population in control RGCs was 14.48%, whilst it was 29.07%, 30.05%, 34.91% and 30.37% in 50 μM, 100 μM, 500 μM and 1mM of nicotinamide-treated RGC cultures, respectively. However, the short-distance reversing population, which also defined as the “fluttering population” within the stationary population, was not apparently observed to change after nicotinamide treatment (Figure 5.5C). However, the contact rate of mitochondrial entities was also increased by nicotinamide treatment ($p < 0.05$, Figure 5.5D).

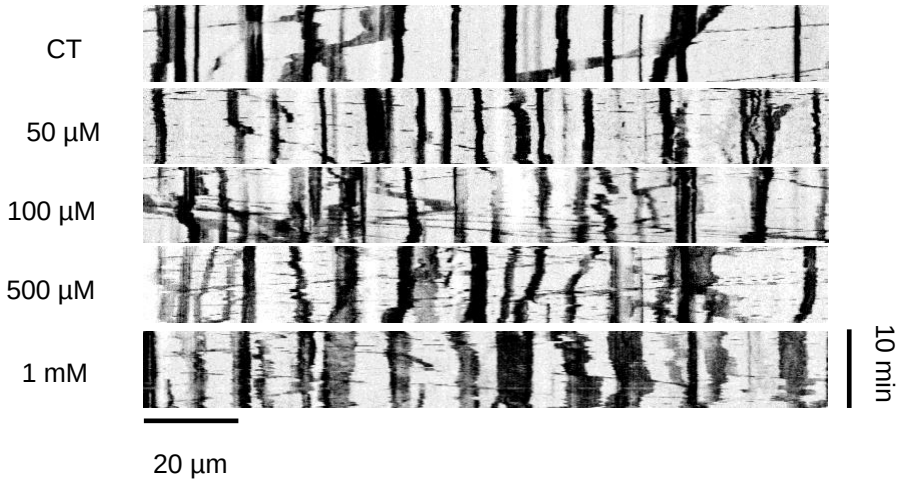

Figure 5.4 Representative Kymographs from control and nicotinamide-treated groups (50 µM, 100, 500, 1 mM), n=9 neurites treated with each concentration from 3 independent cultures. All kymographs are presented in the Appendix V Figure S51.

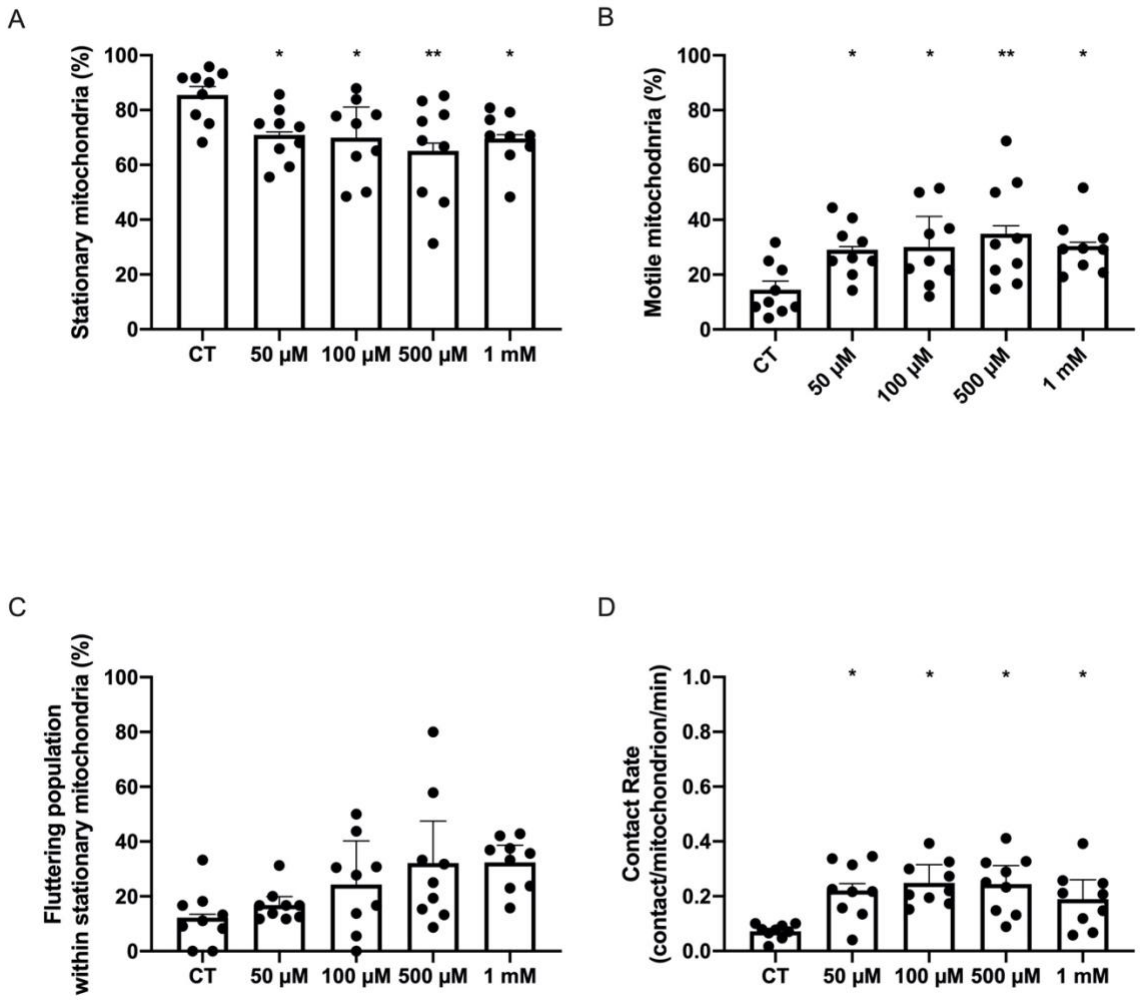

Figure 5.5 Nicotinamide treatment increases mitochondrial motility. (A, B) Distribution of the mitochondrial population classified as stationary and motile; n=9 neurites in each condition from 3 independent cultures. (C) Fluttering population within stationary mitochondria was defined as the mitochondria classified as stationary status but fluttered within a small distance (moving directions changed, maximum moving distance > 2 μm); n=9 neurites in each condition from 3 independent cultures. (D) Contact rate calculated as the number of contacts between mitochondria per minute divided by the total number of mitochondria, n=9 neurites in each condition from 3 independent cultures. Data shown as mean ± SD, N=3. *p <0.05, **p <0.01 vs control.

5.3.3 Nicotinamide treatment increases the velocity of mitochondrial movement

Mitochondrial velocity is also essential for the assessment of mitochondrial motility and dynamics. The velocity of mitochondria in untreated RGCs throughout 10 minutes of imaging was 0.24 ± 0.038 μm/s, while the velocities of mitochondria in RGCs treated with 50 μM, 100 μM, 500 μM and 1 mM nicotinamide were 0.50 ± 0.08 μm/s, 0.51 ± 0.06 μm/s, 0.56 ± 0.06 μm/s and 0.61 ± 0.04 μm/s respectively. The velocities of mitochondria in RGCs treated with nicotinamide were significantly higher than those of the untreated group (Figure 5.6A), indicating that the nicotinamide was able to raise the velocity of mitochondrial movement in RGCs, potentially to activate the transportation of mitochondria along neurites within RGCs *in vitro*. However, no significant difference in the velocity of mitochondrial movement was observed between the doses of nicotinamide at 50 μM, 100 μM, 500 μM or 1 mM. In order to further investigate whether there was any difference on the length of moving mitochondria by treatment with nicotinamide in RGCs, the mitochondrial length was measured in RGCs from each of the control and nicotinamide-treated cultures shown as Figure 5.6B. However, the length of motile mitochondria in each group showed no apparent difference. The average mitochondrial length was 2.91 μm, 3.08 μm, 2.85 μm, 2.87 μm, and 3.02 μm in RGCs from control and four doses of nicotinamide-treatment cultures (50 μM, 100 μM, 500 μM and 1 mM), respectively.

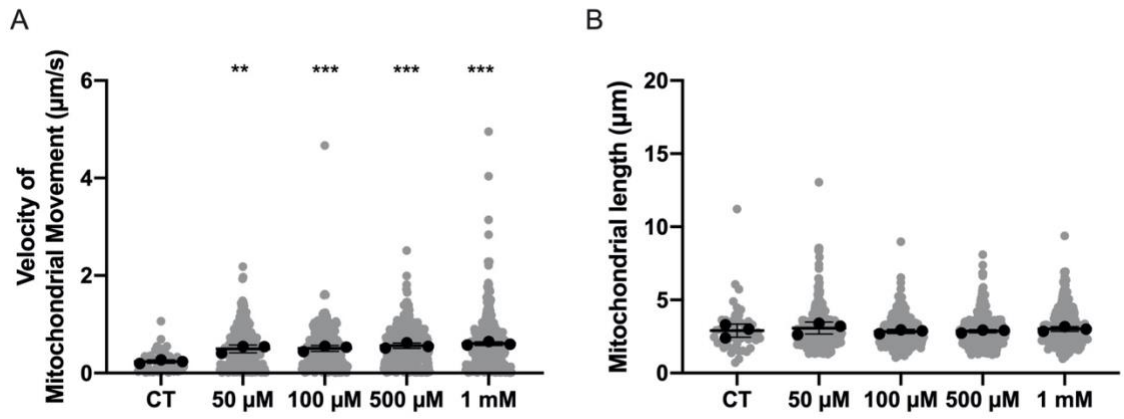

Figure 5.6 Nicotinamide treatment increases the velocity of mitochondrial movement.

No significant difference was found on mitochondrial length between control and nicotinamide-treated groups. (A) Velocities of mitochondria calculated from control and nicotinamide treated groups; n=52 mitochondria in control group, n=356 mitochondria in 50 μM nicotinamide-treated group, n=249 mitochondria in 100 μM nicotinamide-treated group, n=324 mitochondria in 500 μM nicotinamide-treated group, n=292 mitochondria in 1 mM nicotinamide-treated group from 3 independent cultures (N=3). (B) Each mitochondrial length of the moving mitochondria from each condition in (A) was measured by FIJI software. Data shown as mean ± SD, N=3. *p <0.05, **p <0.01, ***p <0.001 vs control.

5.3.4 The relationship between mitochondrial length and velocity in each of the control and nicotinamide-treated cultures.

To further illustrate the relationship between velocity of mitochondrial movement and the length of the moving mitochondria, a scatter plot and heatmap were made as shown in A and B (Figure 5.7, 5.8, 5.9, 5.10, 5.11). Notably, the highest concentrated squares (>10%) in scatter plots and heatmaps (darkest blue) were all located at 2-3 μm of X axis, indicated that the moving mitochondria were more likely to be around 2-3 μm of length. It is also observed that the highest concentrated squares were located at 0.5-1 μm/s of Y axis in the nicotinamide-treated groups; while the moving mitochondria with 2-3 μm of length were more likely to show lower velocity (< 0.5 μm/s). The distributions based on both mitochondrial length and velocity from control and nicotinamide-treated groups also support the result in Figure 5.6, nicotinamide treatment leads to a significant increase in the velocity of mitochondrial movement, but not to the length of moving mitochondria. Furthermore, mitochondria were classified by length as < 2 μm, 2-3 μm and > 3 μm, and the velocity of each category was compared between each other. The statistical data showed no significant changes on velocities with the increase of mitochondrial length in each of the control and nicotinamide-treated groups (Figure 5.7C, 5.8C, 5.9C, 5.10C and 5.11C). Thus, there was no observed relationship between mitochondrial length and velocity within the same culture condition.

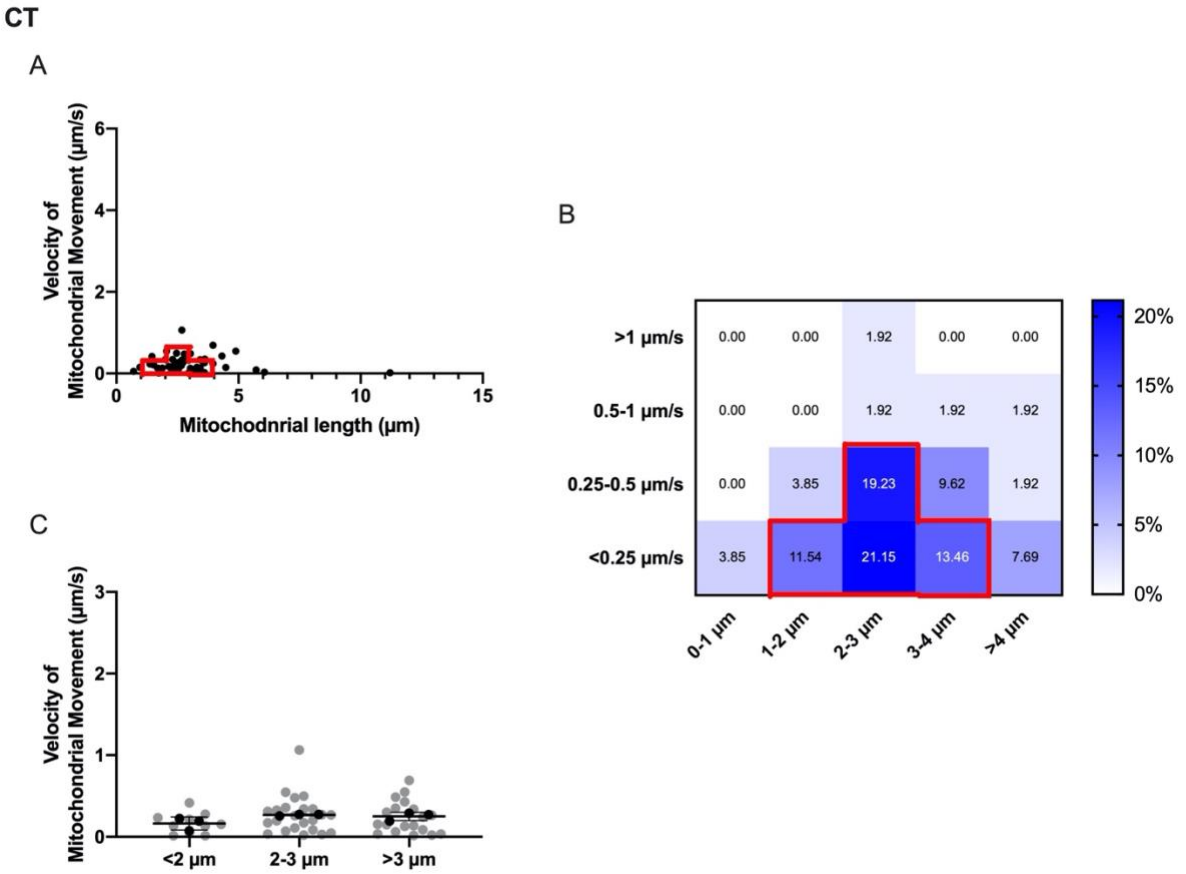

Figure 5.7 Distribution of mitochondrial velocity and length in control RGCs. No significant difference was found on mitochondrial velocity with the increase of mitochondrial length in control RGCs. (A) Distribution of mitochondrial velocity according to their length, n=52 mitochondrial from 3 independent cultures. Red line framed area=highly concentrated area of mitochondrial distribution (based on the data from (B)). (B) Heatmap of distribution of mitochondrial velocity and length. Red line framed area = mitochondrial distribution >10% in each square. (C) Mitochondria distributed by velocity with different ranges of length (<2 μm, 2-3 μm and >3 μm); n=10 mitochondria with length <2 μm; n=23 mitochondria with length between 2 and 3 μm; n=19 with length >3 μm from 3 independent cultures (N=3). Data shown as mean ± SD. The supplementary histograms characterized the detailed distribution of mitochondrial velocity and length from control RGCs has been added in Appendix V Figure S54.

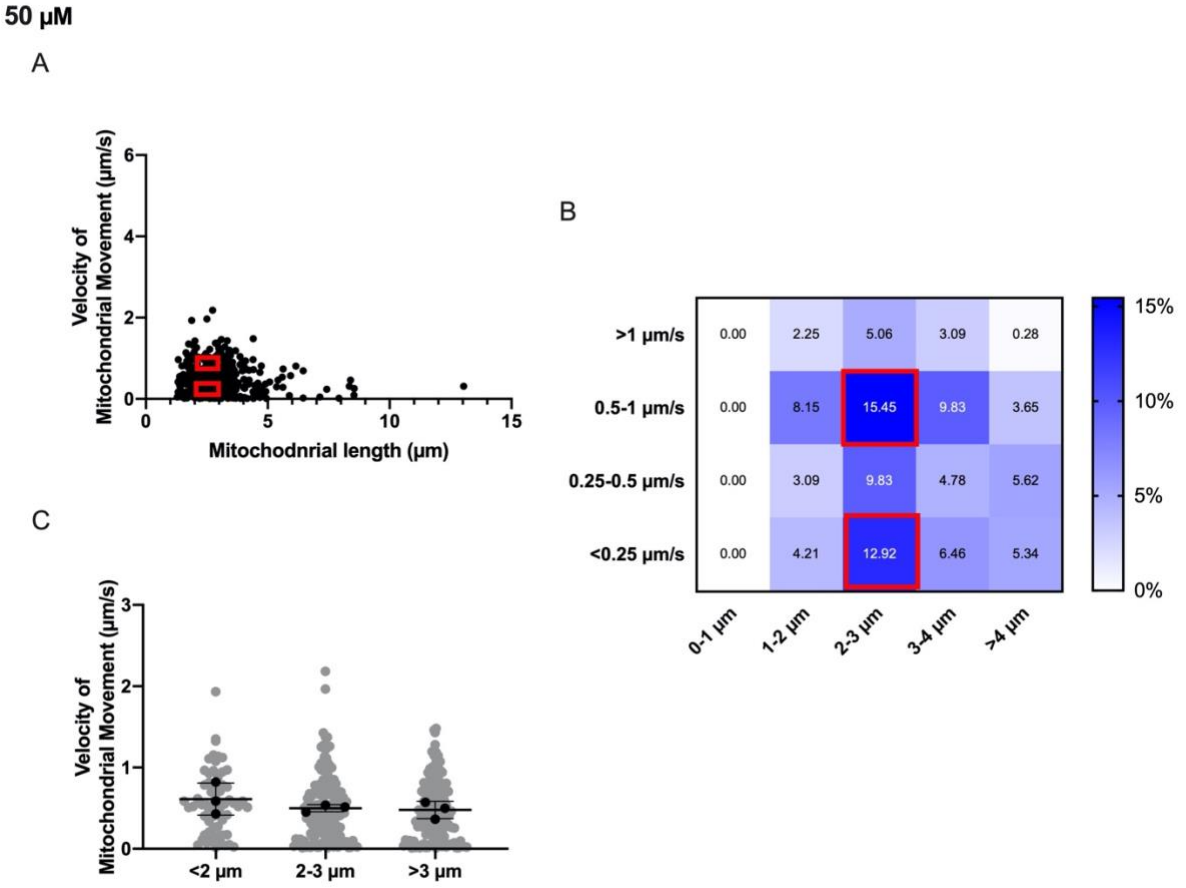

Figure 5.8 Distribution of mitochondrial velocity and length in 50 µM nicotinamide-treated RGCs. No significant difference was found on mitochondrial velocity with the increase of mitochondrial length in 50 µM nicotinamide-treated RGCs. (A) Distribution of mitochondrial velocity according to their length, n=356 mitochondrial from 3 independent cultures. Red line framed area=highly concentrated area of mitochondrial distribution (based on the data from (B)). (B) Heatmap of distribution of mitochondrial velocity and length. Red line framed area = mitochondrial distribution >10% in each square. (C) Mitochondria distributed by velocity with different ranges of length (<2 µm, 2-3 µm and >3 µm); n=63 mitochondria with length <2 µm; n=154 mitochondria with length between 2 and 3 µm; n=139 with length >3 µm from 3 independent cultures (N=3). Data shown as mean ± SD. The supplementary histograms characterized the detailed distribution of mitochondrial velocity and length from 50 µM nicotinamide-treated RGCs has been added in Appendix V Figure S54.

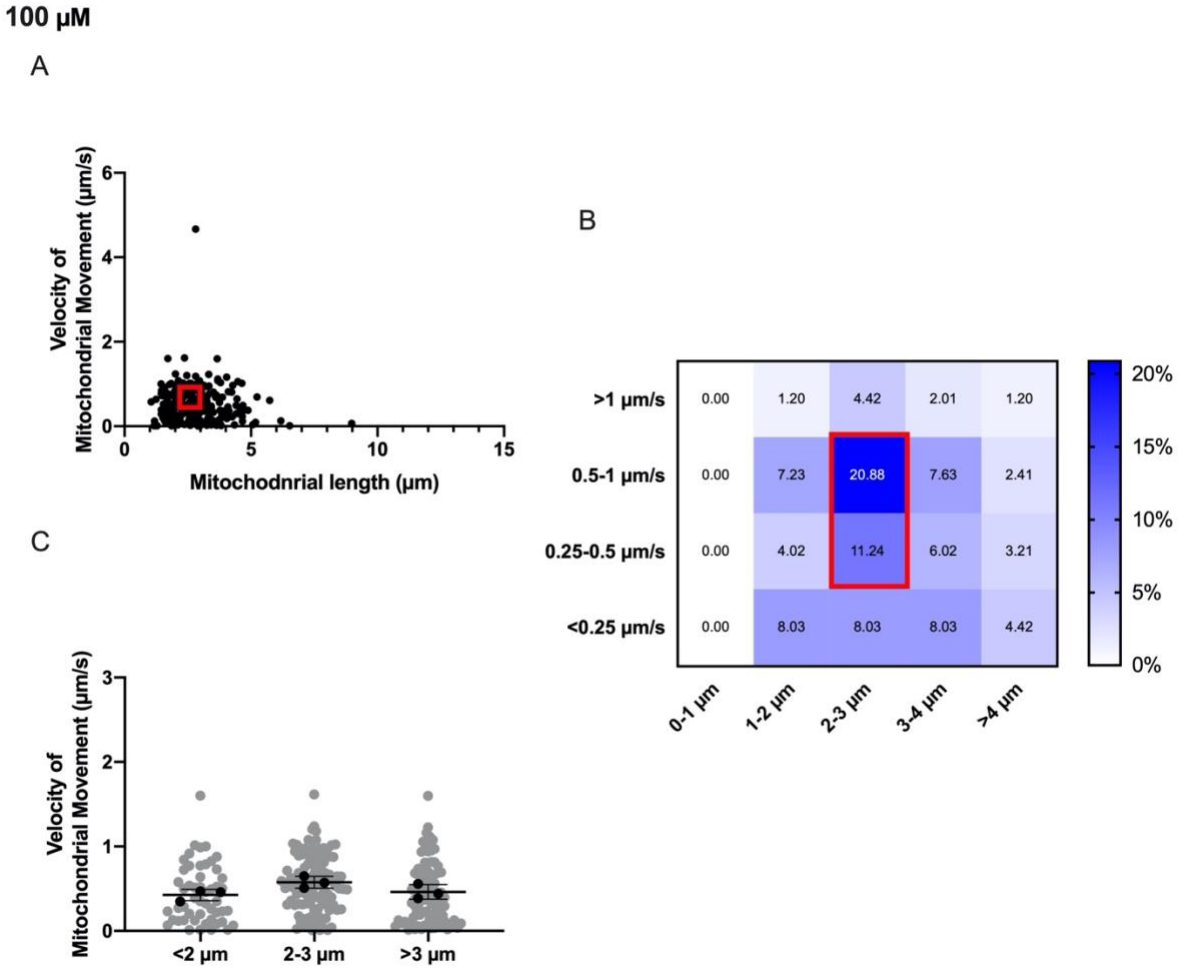

Figure 5.9 Distribution of mitochondrial velocity and length in 100 μM nicotinamide-treated RGCs. No significant difference was found on mitochondrial velocity with the increase of mitochondrial length in 100 μM nicotinamide-treated RGCs. (A) Distribution of mitochondrial velocity according to their length, n=249 mitochondrial from 3 independent cultures. Red line framed area=highly concentrated area of mitochondrial distribution (based on the data from (B)). (B) Heatmap of distribution of mitochondrial velocity and length. Red line framed area = mitochondrial distribution >10% in each square. (C) Mitochondria distributed by velocity with different ranges of length (<2 μm, 2-3 μm and >3 μm); n=51 mitochondria with length <2 μm; n=111 mitochondria with length between 2 and 3 μm; n=87 with length >3 μm from 3 independent cultures (N=3). Data shown as mean ± SD. The supplementary histograms characterized the detailed distribution of mitochondrial velocity and length from 100 μM nicotinamide-treated RGCs has been added in Appendix V Figure S54.

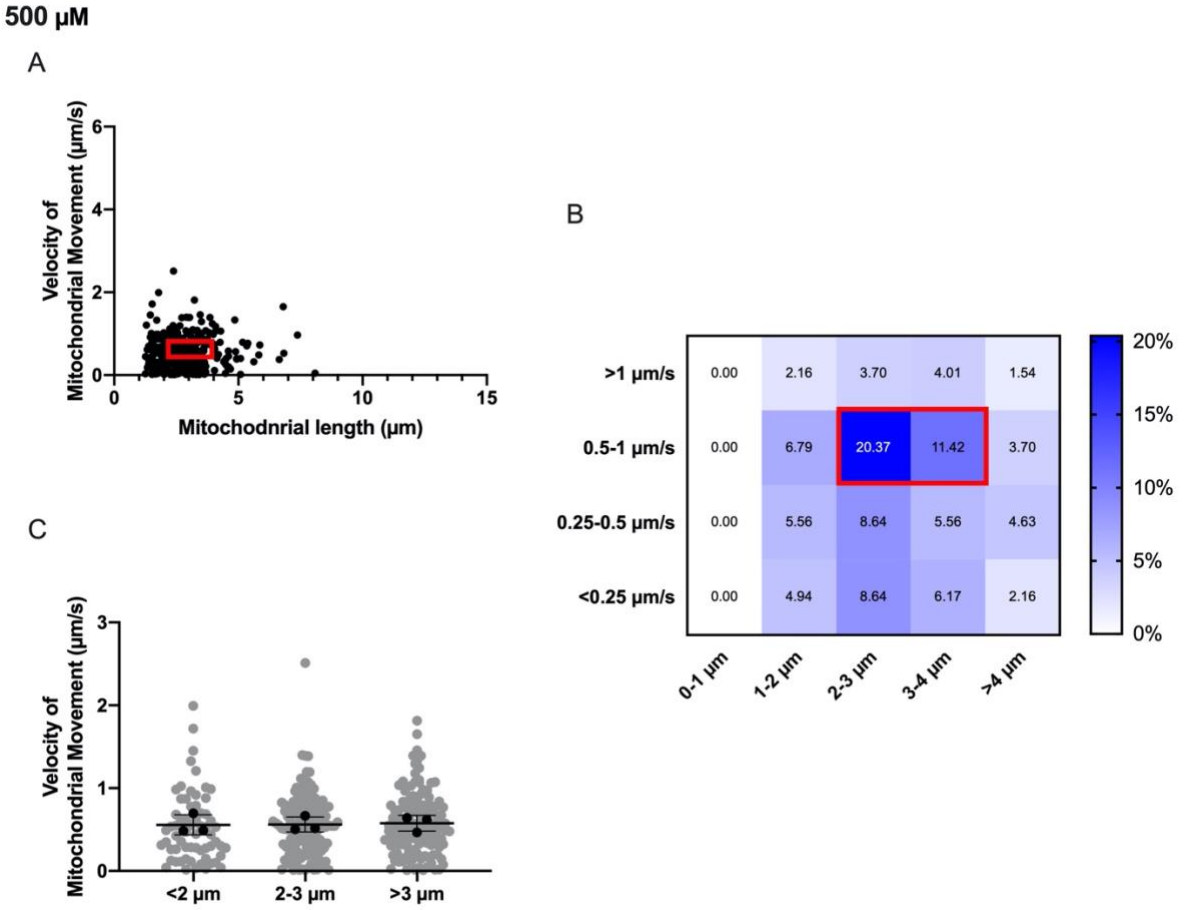

Figure 5.10 Distribution of mitochondrial velocity and length in 500 μM nicotinamide-treated RGCs. No significant difference was found on mitochondrial velocity with the increase of mitochondrial length in 500 μM nicotinamide-treated RGCs. (A) Distribution of mitochondrial velocity according to their length, n=324 mitochondrial from 3 independent cultures. Red line framed area=highly concentrated area of mitochondrial distribution (based on the data from (B)). (B) Heatmap of distribution of mitochondrial velocity and length. Red line framed area = mitochondrial distribution >10% in each square. (C) Mitochondria distributed by velocity with different ranges of length (<2 μm, 2-3 μm and >3 μm); n=63 mitochondria with length <2 μm; n=134 mitochondria with length between 2 and 3 μm; n=127 with length >3 μm from 3 independent cultures (N=3). Data shown as mean ± SD. The supplementary histograms characterized the detailed distribution of mitochondrial velocity and length from 500 μM nicotinamide-treated RGCs has been added in Appendix V Figure S54.

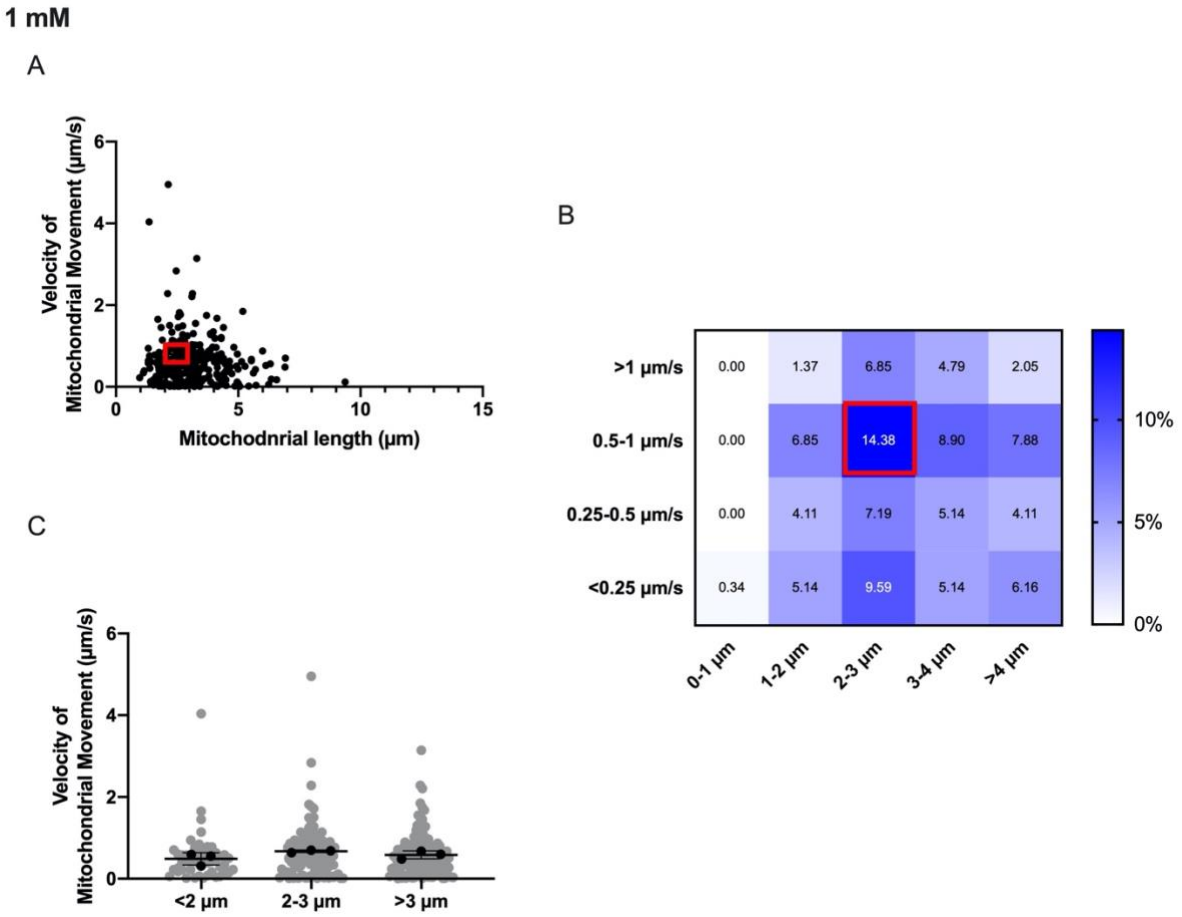

Figure 5.11 Distribution of mitochondrial velocity and length in 1 mM nicotinamide-treated RGCs. No significant difference was found on mitochondrial velocity with the increase of mitochondrial length in 1 mM nicotinamide-treated RGCs. (A) Distribution of mitochondrial velocity according to their length, n=292 mitochondrial from 3 independent cultures. Red line framed area=highly concentrated area of mitochondrial distribution (based on the data from (B)). (B) Heatmap of distribution of mitochondrial velocity and length. Red line framed area = mitochondrial distribution >10% in each square. (C) Mitochondria distributed by velocity with different ranges of length (<2 μm, 2-3 μm and >3 μm); n=52 mitochondria with length <2 μm; n=111 mitochondria with length between 2 and 3 μm; n=129 with length >3 μm from 3 independent cultures (N=3). Data shown as mean ± SD. The supplementary histograms characterized the detailed distribution of mitochondrial velocity and length from 1 mM nicotinamide-treated RGCs has been added in Appendix V Figure S54.

5.4 Discussion

Vitamins were defined as biologically active organic compounds necessary for the maintenance of body health and growth. There are currently 13 classes of vitamins recognized and grouped by the biological and chemical activity performing biochemical functions such as mineral metabolism, cellular growth and differentiation regulation etc., whose deficiencies will cause disorders involving multiple systems such as pellagra, scurvy, beriberi, and xerophthalmia (Kraemer et al. 2012; Semba 2012).

Nicotinamide, the water-soluble amide form of vitamin B_3 and key component of metabolic pathway involved in the production of NAD^+, has been reported to be neuroprotective by readily entering the brain and is increasingly recognized to show a critical role in neuroprotection in traumatic injury, ischaemia, stroke and neurodegenerative diseases - Alzheimer's, Parkinson's and Huntington's diseases (Fricker 2017). Liu et al. 2013 reported that nicotinamide could improve brain bioenergetics by preserving the mitochondrial integrity, and enhance the autophagy function through autophagy-lysosome pathway, as well as reduce the neuronal vulnerability to oxidative or metabolic insults in a mouse model of Alzheimer's disease (AD) (Liu et al. 2013). Moreover, nicotinamide also reversed the behavioural impairments and provided neuroprotection in 3-nitropropionic acid induced animal model of Huntington's disease (HD) by performing antioxidant properties to slow the progression of clinical HD and improve the motor functions in HD patients (Sidhu et al. 2018). Nicotinamide exerts neuroprotection by preventing axonal degeneration in neurodegenerative diseases through increasing the activity of the NAD-dependent deacetylase (SIRT1) and then inducing the expression of genes involved in neuroprotection (Araki et al. 2004; Bedalov and Simon 2004). Levels of NAD^+ and SIRT1 activity also decline with ageing. NAD+ and sirtuin supplementations have been demonstrated to be promising for extending the lifespan in humans (Bonkowski and Sinclair 2016). However, the adverse effects of nicotinamide were also found in high-dose treatments. Nicotinamide at the concentration of 10 mM significantly promoted neuronal differentiation, while high levels of nicotinamide (20 mM) induced

cytotoxicity and cell death in mouse embryonic stem cells (Griffin et al. 2013). In animal studies, the lethal dose (50 percent kill) for oral administration in mice was 2.5 g/kg and that in rats was 3.5 g/kg (Hwang and Song 2020). For human, approximately 1 g to 3 g of daily intake of nicotinamide, for short-term or long-term administration, was demonstrated to be safe in many studies. The lowest published toxic dose is 35.7 mg/kg for oral administration (Knip et al. 2000; Hwang and Song 2020).

Nicotinamide has also been proposed to have a key role in optic neuropathy within the eye. Nicotinamide mononucleotide adenylyltransferase (Nmnat1) is one of three mammalian NAD synthase isoforms, which convert nicotinamide mononucleotide (NMN) to NAD^+. Findings from Zhu's research show that Nmnat1 overexpression in the cytoplasm could afford pan-cellular protection of RGCs against both acute and chronic retinal injury paradigms, indicating a promising therapeutic strategy for protecting both the axon and soma of RGCs even other CNS neurons (Zhu et al. 2013). Subsequently and further validating this, Williams et al. 2017, also showed that dietary supplementation with a single molecule (nicotinamide) or *Nmnat1* gene therapy would significantly prevent both retinal ganglion cell soma loss and thinning of the retinal nerve fibre layer, which decreased the vulnerability of RGCs to elevated ocular pressure by supporting the mitochondrial health and metabolism in an aged mouse *in vivo* glaucoma model (Williams et al. 2017). Specifically, findings from Williams et al. 2017 showed an increased neuroprotective effect accompanied with decreased degree of IOP elevation with a higher dose of nicotinamide (2000 mg/kg of body weight per day) compared to the low dose of nicotinamide (550 mg/kilogram per day) *in vivo*, indicating the neuroprotective effect of nicotinamide might be enhanced by the increase of dosage. However, in our study, we found that significantly higher concentration of NAD+ (>10mM) resulted in cell death within in 6 hours in RGCs culture after nicotinamide administration, which was consistent with previous studies that overdosage of nicotinamide administration are possibly neurotoxic towards neurons (Williams and Ramsden 2005; Wakade et al. 2015). But there was no significant dose dependence in the percentage of motile mitochondrion population or the velocity of mitochondrial movement for doses of nicotinamide at 50 μM, 100 μM, 500 μM or 1 mM,

contrasting with the result showed in Williams et al. 2017. As there are fewer RGCs treated with nicotinamide in *in vitro* cultures (18,000 ~ 20,000 RGCs per 24-well) compared with those *in vivo*, the effect of nicotinamide on RGCs might be more delicate based on dosage. So we suggest that more values of dosage should be tested between 1 mM (by which RGCs were positively affected) and 10 mM (by which RGCs were extensively dead in culture). Also, Williams et al. 2017 only tested two dosages of nicotinamide treatment on RGCs in vivo; no research has illustrated a full curve of nicotinamide effects on RGCs based on dosage but some have raised a concern over neurotoxic effects by overdosage of nicotinamide (Williams and Ramsden 2005; Wakade et al. 2015). It will require further research to fully explore how RGCs are affected by increasing dosages of nicotinamide in order to thoroughly describe the neuroprotective and neurotoxic role of nicotinamide on RGCs. Additionally, nicotinamide-regulated pathways are also a promising avenue for therapeutics to combat age-related macular degeneration (AMD), in which nicotinamide could ameliorate the disease-related phenotypes in RPE cells by inhibiting drusen proteins and inflammatory and complement factors and upregulating nucleosome, ribosome as well as chromatin-modifying genes from pluripotent stem cell lines derived from AMD patients (Saini et al. 2017).

Some mechanisms associated with the neuroprotective property of nicotinamide have been proposed recently. Nicotinamide was shown not only as an essential cellular nutrient for cellular growth and maintenance, but also supportive for DNA stability, maintaining membrane integrity and preventing cellular inflammation as well as phagocytosis (Maiese and Chong 2003). Specifically, nicotinamide was shown to protect cells from oxidative stress apoptosis and necrosis by inhibiting the activity of poly(ADP-ribose) polymerase (PARP), thereby preserving the levels of NAD^+ and ATP (Williams et al. 2012a). Nicotinamide also provides cytoprotection through the Akt pathway (activation of protein kinase B) to inhibit the depolarization of mitochondrial membrane and downstream caspase cascade (Maiese and Chong 2003). Anderson et al. 2008, also presented a broad neuroprotective profile of nicotinamide in 1-methyl-4-phenyl-1,2,3,6-tetrahydropyridine (MPTP)-induced PD models through the restoration of intracellular NAD^+ and ATP levels (Anderson et al. 2008).

Additionally, calcium signalling performs a vital role in neuronal processes especially in axon elongation and responding to external stimuli and would probably be a target for neuroprotection (Wang et al. 2012; Fairless et al. 2014). Nicotinamide has been proposed to prevent neurodegeneration through inhibiting cyclic ADP-ribose-mediated calcium signalling in sea urchin eggs (Sethi et al. 1996). Nicotinamide has also been proposed to offer neuroprotection by altering the levels of silent information regulator 1 (SIRT1), which is expressed predominantly within the nucleus of neurons throughout the CNS (Araki et al. 2004; Donmez 2012).

In this study, we measured the mitochondrial motility and velocity of movement for 10 minutes with 5 seconds interval and concluded that nicotinamide increased the percentage of motile mitochondria in neurites of RGCs as well as the velocities of mitochondrial movement. We also measured the length of mitochondria at five different time points during the time-lapse imaging from control and four concentrations of nicotinamide-treated cultures. The results indicated a fusion-fission change in mitochondrial structure and an increased trend of mitochondrial length and coverage of each neurite in the nicotinamide-treated RGCs. The relationship between mitochondrial length and velocity of the moving mitochondria was also assessed in the experiment. The results in Figure 5.6 showed the average length of motile mitochondria from control and 50 μM, 100 μM, 500 μM and 1 mM nicotinamide-treated cultures were 2.91 μm, 3.08 μm, 2.85 μm, 2.87 μm, and 3.02 μm. The mitochondria with increased velocity in nicotinamide-treated RGCs were not significantly longer than that in the control condition. However, the length of the total mitochondria (motile and stationary) in 1 mM was 3.50 μm, 3.50 μm, 3.62 μm, 3.48 μm and 3.62 μm at five time points, and was statically significantly longer than that in control at 0 min, 7.5 min and 10 min during the laser scanning. The above results indicated no apparent statistically significance difference on the length of motile mitochondria between control and nicotinamide-treated RGCs, and the elongated mitochondria were likely to be the mitochondria moving no further than 5 μm. This raised a new question: why were the elongated mitochondria not transported along the neurite? Why did they stay at a relatively fixed position with theoretically elevated energy-capacity? It is also

worthy to deeply explore how nicotinamide elongated the length of mitochondria at high concentration; how nicotinamide elevated the moving speed along the neurite; whether nicotinamide was involved in oxidative phosphorylation in RGCs, which is also associated with the alterations of mitochondrial structure and motility. As mentioned before, more investigations could probably further focus on Sirtuins protein family (esp. SIRT1, SIRT2), which can be activated by nicotinamide. Adenosine monophosphate-activated protein kinase (AMPK) and target of rapamycin (TOR) are also critical metabolic sensors closely associated with Sirtuins, which regulate downstream activities such as mitochondrial biogenesis and function, mitophagy and stress resistance. Moreover, we saw no dose-response effect, with increased concentrations of nicotinamide between the dosage of 50 μM and 1 mM added into the culture medium. Previous research and our pilot trial demonstrate, that nicotinamide over 5 mM would present adverse effects in cells *in vitro*. More concentrations should be studied from 1 mM (our study) to 5 mM to further illustrate the cumulative effect of nicotinamide on RGCs by continuously adding dosages of nicotinamide *in vitro*. To date, the nicotinamide treatment in mitochondria of RGC neurites here in Chapter 5 is a pilot investigation of the effect and mechanisms of nicotinamide in RGCs survival. More in-depth research is required to explore the specific pathways involved in mitochondrial changes caused by administration of nicotinamide in RGC cultures.

Chapter 6. General Discussion

6.1 Discussion

Autosomal dominant optic atrophy (ADOA), a common hereditary cause of progressive bilateral vision loss, is also considered to be a mitochondrial optic neuropathy. The retinal ganglion cell (RGC) is the major cell type affected in the pathological process of mitochondrial optic neuropathies. This is presumed to be due to its sensitivity to the disturbances in the supply of energy sources. The peculiar anatomical structure of the optic nerve plays a critical role in the pathological consequences of the genetic defect associated with mutation in the OPA1 gene. Specifically, the pre-laminar unmyelinated region of RGC axons is postulated to require greater energetic input to achieve equally efficient generation and propagation of action potentials by recruiting a higher number of mitochondria compared with that in the myelinated region of RGC axons (Morgan 2004; Yu-Wai-Man et al. 2011b). In addition, dysfunction of the mitochondrial network can influence cellular processes such as axonal transport in the relatively long RGC axons, in which the mitochondria provide energy for the energy-dependent transportation through mitochondrial-cytoskeletal interactions. Thus, the distribution or localisation of mitochondria along whatever pre- or post-laminar segment of RGCs delicately affects the energy supply along the long RGC axons, which also contributes to the vulnerability of RGCs towards genetic defects or external stimuli (Yu-Wai-Man et al. 2011b). Moreover, the mitochondria located in the pre-laminar region of RGC axons are directly exposed to light, in which the blue component of visible light has the shortest wavelength with the greatest potential for producing reactive oxygen species (ROS) (Ouyang et al. 2020). The cumulative mitochondrial toxicity during ageing is likely to increase the susceptibility of RGCs to cellular insults which then affects the RGC survival in the pathological process of diseases (Eells 2019).

In this thesis, mouse RGCs were purified from wild-type and *Opa1*$^{+/-}$ mouse retina with a high purity of 85.22%. The mitochondrial morphology, motility and bioenergetics were assesed and it was concluded that Opa1 haploinsufficiency may lead to significant fragmentation of mitochondrial morphology, activation of mitochondrial motility and impaired respiratory function in retinal ganglion cells in the B6; C3-*Opa1*^{Q285STOP} mouse model. The results illustrate

the alterations in mitochondrial dynamics during early asymptomatic stages of ADOA, which are likely to precede the neurodegeneration and consequent RGC cell death. Additionally, OPA1 is also reported as an important protein involved in glaucomatous damage. The *OPA1* gene is also likely to be a disease-susceptibility gene in the pathological process of glaucoma (Mabuchi et al. 2007; Yu-Wai-Man et al. 2010b). The upregulated expression of Opa1 protein was reported to protect against RGC loss by improving mitochondrial health in glaucomatous rodent models (Ju et al. 2010; Hu et al. 2018). In Chapter 4, a novel *in vitro* hypertension model using a culture system, in which RGCs were cultured under hypertensive stress induced by hydrostatic pressure for three days, was evaluated up to investigate the alterations of mitochondrial dynamics in RGCs directly exposed to hypertensive stress. Hypertensive stress was shown to cause the shortened length of mitochondrial structures accompanied by increased mitochondrial motility.

However, the purified RGC culture that was used for modelling ADOA or glaucoma *in vitro* has some limitations. For example, purified RGC cultures are unable to effectively form synapses to perfectly mimic the physiological living conditions of the RGCs in the retina *in vivo*. Takihara et al. 2015 and Faits et al. 2016 developed advanced methods to image the movement of mitochondria in RGC axons, using live retinal tissue incubated in neuronal medium bubbled with carbon dioxide under appropriate temperature to closely mimic the living conditions of the retina *in vivo*, which might be something to draw lessons from in future research (Takihara et al. 2015; Faits et al. 2016). Although there are typical phylogenetic similarities and physiological similarities between mice and human, limitations still exist when applied to the treatment of optic nerve diseases due to the anatomical differences in the retina between the two species. The application of human-induced pluripotent stem cells (hiPSCs) derived from patients can broaden the outlook of biomedical research. The hiPSC technology could not only serve as an ideal candidate for disease modelling to investigate the precise mechanism, but also provide the future of personalized medicine using iPSC-based drug screening to conduct drug testing and toxicity studies (Sayed et al. 2016). In Chapter 5, the effect of nicotinamide on mitochondrial motility in RGC neurites was explored by applying nicotinamide

at varied concentration, to RGC cultures (derived by two-step immunopanning). However, two-step immunopanning is not efficient, with a small number of RGCs isolated from one retina, and thus unable to test multiple drugs with multiple concentrations at the same time. Libraries of disease-specific cells can be generated by creating allele-specific patient iPSC lines for drug screening. Those cells show the genetic backgrounds of specific patients with more precise disease-specific phenotypes and pathophysiology compared with those isolated from the rodent models (Farkhondeh et al. 2019). Although the optimisation of an efficient, robust and reproducible technique for differentiating RGCs from iPSCs is still required to be developed, utilizing the current protocol to differentiate RGCs from iPSCs is a promising research technique for the further investigation of the precise pathological mechanisms of ADOA or other optic nerve diseases.

Ageing plays a critical role in the development of optic nerve diseases. Age-dependent thinning of the retinal nerve fibre layer (RNFL) is observed in normal human eyes between 18 to 80 years old, with a smaller number of RGCs and axons and a compensating increase of non-neuronal tissue in the elderly group (Harwerth and Wheat 2008). The ageing process includes multiple complex biological phenomena, in which the decline in mitochondrial turnover is likely to be a critical factor due to impaired mitochondrial function and quality control (Terman et al. 2010). Mitochondria are highly dynamic structures which could quickly adapt their morphology and function in response to various metabolic needs under internal and external stimuli. In the retina, mitochondria are critical to the function and survival of retinal cells for their central role in cell metabolisms, such as oxidative phosphorylation, calcium homeostasis and the regulation of neuronal excitability (Country 2017). However, during the ageing process, the homeostatic regulation of mitochondrial biogenesis, dynamics and quality control are unable to efficiently maintain a healthy mitochondrial population for normal bioenergetically demanding cellular activities. Specifically, the toxic reactive oxygen species (ROS) generated and accumulated during normal biological activity could gradually impair the cellular mitochondrial homeostatic and sequentially trigger caspase-dependent apoptosis, and ultimately result in cellular senescence (Seo et al. 2010). The balance between fusion and

fission is the major determinant of mitochondrial dynamics, which is critical for maintaining mitochondrial morphology, distribution and function and provides the capacity for energy disturbances. Moreover, the fusion-fission balance also participates in controlling mitochondrial quality, closely associated with mitophagy (MacVicar and Langer 2016). Furthermore, Cao et al. 2017 demonstrated that impairing fission-fusion balance but not mitophagy in neurons significantly accelerated ageing in *Drosophila*, indicating the pivotal role of fusion-fission cycle in maintaining axonal integrity during ageing rather than mitophagy (Cao et al. 2017). Bevan et al. 2020 also demonstrated that heterozygous loss of *Opa1* led to premature age-related loss of spines in hippocampal neurons and a reduction in synaptic density in the hippocampus in *Opa1* mutant mouse model (B6; C3-*Opa1*^{Q285STOP}), indicating that Opa1 deficiency may accelerate hippocampal synaptic remodelling and age-related deficits, and thus emphasizing the critical role of Opa1 in maintaining mitochondrial homeostasis and neuronal health during ageing (Bevan et al. 2020).

The onset of vision loss in most ADOA patients occurs quite early between 0 and 9 years old (Ham et al. 2019), but patients are usually asymptomatic in the early stages and not identified until testing due to family diagnosis or history of ADOA (Pilz et al. 2017). The progressive clinical symptoms which manifest later during adult life are caused by the loss of RGC axons in the optic nerve (Yu-Wai-Man et al. 2011a). By using the B6; C3-*Opa1*^{Q285STOP} mutant mouse model of ADOA, our lab has previously demonstrated that functional deficits in visual and neurological examination, and significant abnormalities in the morphology and function of mitochondria or RGCs, were observed in the *Opa1* mutant group compared with the control littermates at an elder age, supporting the view that Opa1 deficiency may accelerate the age-related degeneration in neurons (Davies et al. 2007; White et al. 2009; Williams et al. 2010). Thus, additional studies are therefore warranted to investigate the mitochondrial dynamics and RGC health using a more physiologically relevant model such as live tissue culture and iPSCs derived from patients (as discussed above), to better illustrate the molecular mechanism of optic nerve diseases with the consideration of ageing as a factor.

In the thesis, the number of contacts between mitochondria happened on each mitochondrion

per minute was defined as the contact rate to roughly describe the fusion rate. Fusion can only take place when two mitochondria meet (Cagalinec et al. 2013). So a good way to measure fusion activity is to count the exact number of fusions happening in observed neurites. Kikume Green-Red protein (KikGR) is a photoconvertible fluorescent protein, originally from the stony coral Favia favus (Tsutsui et al. 2005). Cells can be transfected with the photoconvertible mitochondrially targeted construct mito-Kikume-Green. The selected mitochondria are irradiated by a 405-nm laser line and rapidly converted to mito-Kikume-Red. After fusion events between mito-Kikume-Green and mito-Kikume-Red mitochondria, the merged mitochondria become yellow as shown in Figure 6.1. In terms of the live cell imaging, the purified RGCs in culture can be scanned under the confocal microscopy with a temperature control of 37°C. However, the limitation for the in vitro imaging is that the purified RGCs obtained through two-step immunopanning were unable to contact other retinal cells to effectively form synapses without soluble astrocyte-derived signals (Ullian et al. 2001). In order to better mimic the physiological condition of RGCs, an alternative way is to conduct live mitochondrial imaging ex vivo. In the ex vivo method, the retinae need to be dissected from eye cups and prepared as flat mounts. The retinal explants can be labelled by biolistic transfection and imaged under confocal microscopy in a heated platform (37°C) (Faits et al. 2016). To keep the explant alive and healthy, the tissue requires constant perfusion of O2 or 95% O2 / 5% CO2. In the ex vivo retinal explant, RGCs can live in a better physiological environment compared to in vitro culture. Additionally, some researchers developed advanced intravital imaging of mitochondrial axonal transport in a minimally invasive manner. They anesthetized the animal on a heating pad, then kept the sclera exposed for time-lapse imaging using a Multiphoton Microscope without bleeding (Takihara et al. 2015). The in vivo method of mitochondrial imaging allows true observations in the alive animal with physiological oxygen levels and metabolism, and also minimises the disturbances of axonal environment for mitochondrial transport.

Recently, there are some new commercial imaging instruments which provide non-invasive in vivo live cell imaging such as Photon Imager from Biospace Lab. The Photon Imager system

includes gas anesthesia input and heating plate for optimal physiological conditions of animals and was designed with a view to make whole body in vivo acquisitions easy and powerful. However, the application of Photon Imager is still limited by the spatial resolution of images and also the lack of optimized probe sets. Although there are still many technological fortresses to be breached, the live cell imaging is a promising way for exploring the molecular dynamics and biological mechanism.

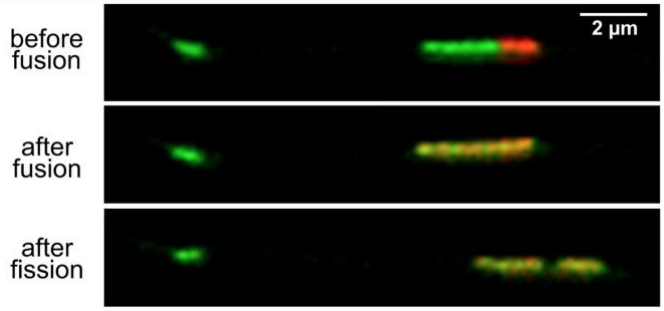

Figure 6.1 Primary cortical neurons were transfected with mito-Kikume-Green. Selected mitochondria were irradiated using a 405-nm laser line and mito-Kikume-Green was converted into mito-Kikume-Red. Fusion events can be observed when green and red fluorescent mitochondria merged as yellow (Cagalinec et al. 2016).

In conclusion, the findings in the thesis demonstrate that mitochondrial morphology, motility and respiratory function are affected by Opa1 deficiency, hypertensive stress and nicotinamide administration, indicating the intricate interplay between mitochondrial morphology, motility, and energy production underlying genetic or external factors in RGCs *in vitro*. However, more in-depth studies are required to investigate the precise mechanisms underlying the pathological or protective process using advanced disease modelling, to find out new therapeutic targets for the vulnerability of RGCs.

6.2 Future plans

6.2.1 Testing the expression of Mitofusins, Drp1, and motor proteins related to mitochondrial transport

The findings from Chapter 3 indicate that Opa1 haploinsufficiency leads to significant fragmentation of mitochondrial morphology, activation of mitochondrial motility and impaired respiratory function in retinal ganglion cells from the B6; C3-*Opa1*^{Q285STOP} mouse model. However, the exact mechanisms related to the alterations in mitochondria caused by Opa1 haploinsufficiency are still unrevealed so far. So the future plan should be focused on testing the levels of expression of motor proteins (kinesin superfamily and dynein family) as well as key linkage complexes (Miro and Milton) under the deficit of Opa1. Moreover, previous research demonstrated the critical role of Mitofusins (Mfn1/2) and Drp1 proteins in not only mitochondrial structure, but also transport of mitochondria along the axons (Misko et al. 2010; Fukumitsu et al. 2016). So, it is also interesting to determine the levels of expression of Mfn1, Mfn2 and Drp1 under Opa1 deficiency, to find out whether Opa1 deficiency causes alterations in the imbalanced fusion-fission network and then resulted in the activated mitochondrial transport.

6.2.2 RGC cultured under hypertension *in vitro*

The observations on mitochondrial morphology and movement in Chapter 4 were under 35 mmHg of pressure by hydrostatic pressure *in vitro*. Due to the Covid-19 lockdown in 2020, we only tried one pressure in the model. The normal eye pressure ranges from 10-21 mmHg and ocular hypertension is usually defined as an eye pressure of greater than 21 mmHg in humans. So for the next step, it would be interesting to culture RGCs under a range of pressures (20 mmHg, 25 mmHg and 30 mmHg) by modifying the elevated height from Chamber A to Chamber B.

6.2.3 Testing the expressions of mitochondrial respiratory complexes (Complex I, Complex IV) in RGCs under hypertensive stress

Complex I, also known as NADH dehydrogenase, is the first enzyme of the mitochondrial electron transport chain (ETC). Complex I translocates four protons across the inner membrane per molecule of oxidized NADH to help build the electrochemical potential difference for ATP production (Galkin et al. 2006). Complex IV (cytochrome c oxidase), transfers electrons from cytochrome c to oxygen and in the process of forming water, and also helps generates a proton gradient. It is the last and rate limiting step in the respiratory electron transport chain, which represents the regulatory center of oxygen phosphorylation (Kadenbach 2020). From previous studies, it was found that the activity of Complex I was significantly decreased by ocular hypertension, and consequently there was an impaired capacity of mitochondrial respiration due to hypertensive stress in patient lymphoblasts *in vitro* (Lee et al. 2012; Van Bergen et al. 2015). However, how mitochondrial respiration is impaired by hypertensive stress in RGCs is still unknown. It would be interesting to figure out the dysfunction of mitochondrial bioenergetics by measuring the levels of expressions of Complex I and IV in RGCs under different hypertensive stress *in vitro*, to better understand the cumulative effect of hypertension on the health of RGCs *in vitro*.

6.2.4 Identify axons among the neurites in RGCs culture *in vitro*

The findings of mitochondrial morphology and transport were all measured in neurites in this thesis. This needs to be delineated in axons and dendrites for better understanding. As showed in Chapter 3, the neurites became long and overlapping after culture for three days. We plan to coculture the RGCs with other retinal cells, especially bipolar and amacrine cells, which contact with the dendrites of RGCs, and also utilise immunofluorescence on RGCs by double staining Tuj1 (class III beta-tubulin) and microtubule-associated protein-2 (MAP2) antibody. The axons will be detected by Tuj1 positivity but MAP2 negativity (MAP2 only detects dendrites).

6.2.5 Investigating the alterations in SIRT1 pathway after nicotinamide treatment in

RGCs

In Chapter 5, nicotinamide dramatically increased the motility of mitochondria with elongated length in RGCs. However, the mechanisms of how nicotinamide activated the mitochondrial movement in RGC neurites are not yet elucidated. Nicotinamide is endogenously found at low quantities in mammalian cells. Nicotinamide could also serve as a supplement in therapeutic doses, where it would be rapidly converted to NAD+ through a salvage pathway (Revollo et al. 2004). In cell culture, increased NAD+ can lead to an increased ratio of NAD+/NADH, which directly participates in oxidative phosphorylation and plays a key role in cellular redox homeostasis (Sun et al. 2017). Moreover, NAD+ is a substrate for a number of enzymes such as the poly (ADP-ribose) polymerase family proteins (PARPs) and the sirtuin family proteins (SIRT1-7) for further regulation of energy metabolism and cellular homeostasis (Kane and Sinclair 2018). Sirtuin 1 (SIRT1), a member of the sirtuin family, is a nicotinamide adenine dinucleotide (NAD+)-dependent deacetylases. SIRT1 acts as an intracellular regulatory protein involving energy homeostasis. For example, SIRT1 is involved in regulating the glycolysis process through activating the peroxisome proliferator-activated receptor γ coactivator 1-alpha (PGC1α) and suppressing the transcription factor HIFα (Houtkooper et al. 2012). Furthermore, PGC1α, which is a transcriptional coregulator and could govern the mitochondrial biogenesis and activity, could also activate and induce the downstream pathways in mitochondrial gene expression (Rodgers et al. 2005). Recently, nicotinamide has been recognized to promote tissue regeneration by significantly upregulating the NAD+-dependent decetylase of SIRT1 (Wan et al. 2019). So, it would be very interesting to look at the protein and gene expression levels of Sirt1 in both control and nicotinamide-treated RGCs *in vitro*. As discussed in the Chapter 5, a larger range of dosages of nicotinamide should also be considered to further clear the cumulative effect of nicotinamide in mitochondrial morphology and motility in RGCs *in vitro*. Therefore, he next step for investigating the effect of nicotinamide in RGCs will be to further determine the expression levels of Sirt1 and associated factors such as PGC1α in RGCs treated with a larger range of dosages (100 μM to 5 mM).

References

Abu-Amero, K. K. et al. 2006. Mitochondrial abnormalities in patients with primary open-angle glaucoma. *Invest Ophthalmol Vis Sci* 47(6), pp. 2533-2541. doi: 10.1167/iovs.05-1639

Abu-Amero, K. K. et al. 2007. Nuclear and mitochondrial analysis of patients with primary angle-closure glaucoma. *Invest Ophthalmol Vis Sci* 48(12), pp. 5591-5596. doi: 10.1167/iovs.07-0780

Agier, V. et al. 2012. Defective mitochondrial fusion, altered respiratory function, and distorted cristae structure in skin fibroblasts with heterozygous OPA1 mutations. *Biochim Biophys Acta* 1822(10), pp. 1570-1580. doi: 10.1016/j.bbadis.2012.07.002

Ainbinder, A. et al. 2015. Role of Mitofusin-2 in mitochondrial localization and calcium uptake in skeletal muscle. *Cell Calcium* 57(1), pp. 14-24. doi: 10.1016/j.ceca.2014.11.002

Akepati, V. R. et al. 2008. Characterization of OPA1 isoforms isolated from mouse tissues. *J Neurochem* 106(1), pp. 372-383. doi: 10.1111/j.1471-4159.2008.05401.x

Alavi, M. V. et al. 2007. A splice site mutation in the murine Opa1 gene features pathology of autosomal dominant optic atrophy. *Brain* 130(Pt 4), pp. 1029-1042. doi: 10.1093/brain/awm005

Alavi, M. V. and Fuhrmann, N. 2013. Dominant optic atrophy, OPA1, and mitochondrial quality control: understanding mitochondrial network dynamics. *Mol Neurodegener* 8, p. 32. doi: 10.1186/1750-1326-8-32

Alexander, C. et al. 2000. OPA1, encoding a dynamin-related GTPase, is mutated in autosomal dominant optic atrophy linked to chromosome 3q28. *Nat Genet* 26(2), pp. 211-215. doi: 10.1038/79944

Almind, G. J. et al. 2012. Dominant optic atrophy in Denmark - report of 15 novel mutations in OPA1, using a strategy with a detection rate of 90%. *BMC Med Genet* 13, p. 65. doi: 10.1186/1471-2350-13-65

Amati-Bonneau, P. et al. 2009. OPA1-associated disorders: phenotypes and pathophysiology. *Int J Biochem Cell Biol* 41(10), pp. 1855-1865. doi: 10.1016/j.biocel.2009.04.012

Amati-Bonneau, P. et al. 2008. OPA1 mutations induce mitochondrial DNA instability and optic atrophy 'plus' phenotypes. *Brain* 131(Pt 2), pp. 338-351. doi: 10.1093/brain/awm298

An, H. J. et al. 2013. Higd-1a interacts with Opa1 and is required for the morphological and functional integrity of mitochondria. *Proc Natl Acad Sci U S A* 110(32), pp. 13014-13019. doi: 10.1073/pnas.1307170110

An, H. J. et al. 2011. The survival effect of mitochondrial Higd-1a is associated with suppression of cytochrome C release and prevention of caspase activation. *Biochim Biophys Acta* 1813(12), pp. 2088-2098. doi: 10.1016/j.bbamcr.2011.07.017

Anand, R. et al. 2014. The i-AAA protease YME1L and OMA1 cleave OPA1 to balance mitochondrial fusion and fission. *J Cell Biol* 204(6), pp. 919-929. doi: 10.1083/jcb.201308006

Anderson, D. W. et al. 2008. Broad neuroprotective profile of nicotinamide in different mouse models of MPTP-induced parkinsonism. *Eur J Neurosci* 28(3), pp. 610-617. doi: 10.1111/j.1460-9568.2008.06356.x

Anderson, M. G. et al. 2002. Mutations in genes encoding melanosomal proteins cause pigmentary glaucoma in DBA/2J mice. *Nat Genet* 30(1), pp. 81-85. doi: 10.1038/ng794

Andres, A. M. et al. 2015. A time to reap, a time to sow: mitophagy and biogenesis in cardiac pathophysiology. *J Mol Cell Cardiol* 78, pp. 62-72. doi: 10.1016/j.yjmcc.2014.10.003

Araki, T. et al. 2004. Increased nuclear NAD biosynthesis and SIRT1 activation prevent axonal degeneration. *Science* 305(5686), pp. 1010-1013. doi: 10.1126/science.1098014

Arnoult, D. et al. 2005. Release of OPA1 during apoptosis participates in the rapid and complete release of cytochrome c and subsequent mitochondrial fragmentation. *J Biol Chem* 280(42), pp. 35742-35750. doi: 10.1074/jbc.M505970200

Ashrafi, G. and Schwarz, T. L. 2013. The pathways of mitophagy for quality control and clearance of mitochondria. *Cell Death Differ* 20(1), pp. 31-42. doi: 10.1038/cdd.2012.81

Aung, T. et al. 2002. A major marker for normal tension glaucoma: association with polymorphisms in the OPA1 gene. *Hum Genet* 110(1), pp. 52-56. doi: 10.1007/s00439-001-0645-7

Barboni, P. et al. 2014. Early macular retinal ganglion cell loss in dominant optic atrophy: genotype-phenotype correlation. *Am J Ophthalmol* 158(3), pp. 628-636 e623. doi: 10.1016/j.ajo.2014.05.034

Barnard, A. R. et al. 2011. Specific deficits in visual electrophysiology in a mouse model of dominant optic atrophy. *Exp Eye Res* 93(5), pp. 771-777. doi: 10.1016/j.exer.2011.07.004

Barnhart, E. L. 2016. Mechanics of mitochondrial motility in neurons. *Curr Opin Cell Biol* 38, pp. 90-99. doi: 10.1016/j.ceb.2016.02.022

Barres, B. A. 1988. Immunological, Morphological, and Electrophysiological Variation among Retinal Ganglion Cells Purified by Panning.

Barron, M. J. et al. 2004. The distributions of mitochondria and sodium channels reflect the specific energy requirements and conduction properties of the human optic nerve head. *Br J Ophthalmol* 88(2), pp. 286-290.

Batten, B. 1896. A family suffering from hereditary optic atrophy. *Trans Ophthalmol Soc UK* 16, p. 125.

Bedalov, A. and Simon, J. A. 2004. Neuroscience. NAD to the rescue. *Science* 305(5686), pp. 954-955. doi: 10.1126/science.1102497

Belenky, P. et al. 2007. NAD+ metabolism in health and disease. *Trends Biochem Sci* 32(1), pp. 12-19. doi: 10.1016/j.tibs.2006.11.006

Berthet, A. et al. 2014. Loss of mitochondrial fission depletes axonal mitochondria in midbrain dopamine neurons. *J Neurosci* 34(43), pp. 14304-14317. doi: 10.1523/JNEUROSCI.0930-14.2014

Bevan, R. J. et al. 2020. OPA1 deficiency accelerates hippocampal synaptic remodelling and age-related deficits in learning and memory. *Brain Communications* 2(2), doi: 10.1093/braincomms/fcaa101

Bonkowski, M. S. and Sinclair, D. A. 2016. Slowing ageing by design: the rise of NAD(+) and sirtuin-activating compounds. *Nat Rev Mol Cell Biol* 17(11), pp. 679-690. doi: 10.1038/nrm.2016.93

Bratic, A. and Larsson, N. G. 2013. The role of mitochondria in aging. *J Clin Invest* 123(3), pp. 951-957. doi: 10.1172/JCI64125

Bremner, F. D. et al. 2001. The pupil in dominant optic atrophy. *Invest Ophthalmol Vis Sci* 42(3), pp. 675-678.

Brenmoehl, J. and Hoeflich, A. 2013. Dual control of mitochondrial biogenesis by sirtuin 1 and sirtuin 3. *Mitochondrion* 13(6), pp. 755-761. doi: 10.1016/j.mito.2013.04.002

Brickley, K. and Stephenson, F. A. 2011. Trafficking kinesin protein (TRAK)-mediated transport of mitochondria in axons of hippocampal neurons. *J Biol Chem* 286(20), pp. 18079-18092. doi: 10.1074/jbc.M111.236018

Bunker, S. et al. 2015. Experimental glaucoma induced by ocular injection of magnetic microspheres. *J Vis Exp* (96), doi: 10.3791/52400

Cagalinec, M. et al. 2016. Role of Mitochondrial Dynamics in Neuronal Development: Mechanism for Wolfram Syndrome. *PLoS Biol* 14(7), p. e1002511. doi: 10.1371/journal.pbio.1002511

Cagalinec, M. et al. 2013. Principles of the mitochondrial fusion and fission cycle in neurons. *J Cell Sci* 126(Pt 10), pp. 2187-2197. doi: 10.1242/jcs.118844

Cao, X. et al. 2017. In vivo imaging reveals mitophagy independence in the maintenance of axonal mitochondria during normal aging. *Aging Cell* 16(5), pp. 1180-1190. doi: 10.1111/acel.12654

Carelli, V. et al. 2007. Mitochondrial optic neuropathies: how two genomes may kill the same cell type? *Biosci Rep* 27(1-3), pp. 173-184. doi: 10.1007/s10540-007-9045-0

Carelli, V. et al. 2013. Mitochondrial dysfunction in optic neuropathies: animal models and therapeutic options. *Curr Opin Neurol* 26(1), pp. 52-58. doi: 10.1097/WCO.0b013e32835c5f0b

Carelli, V. et al. 2009. Retinal ganglion cell neurodegeneration in mitochondrial inherited disorders. *Biochim Biophys Acta* 1787(5), pp. 518-528. doi: 10.1016/j.bbabio.2009.02.024

Chada, S. R. and Hollenbeck, P. J. 2004. Nerve growth factor signaling regulates motility and docking of axonal mitochondria. *Curr Biol* 14(14), pp. 1272-1276. doi:

10.1016/j.cub.2004.07.027

Chan, D. C. 2012. Fusion and fission: interlinked processes critical for mitochondrial health. *Annu Rev Genet* 46, pp. 265-287. doi: 10.1146/annurev-genet-110410-132529

Chang, D. T. et al. 2006. Mitochondrial trafficking to synapses in cultured primary cortical neurons. *J Neurosci* 26(26), pp. 7035-7045. doi: 10.1523/JNEUROSCI.1012-06.2006

Chang, D. T. and Reynolds, I. J. 2006. Mitochondrial trafficking and morphology in healthy and injured neurons. *Prog Neurobiol* 80(5), pp. 241-268. doi: 10.1016/j.pneurobio.2006.09.003

Chen, A. T. et al. 2019. An evaluation of genetic causes and environmental risks for bilateral optic atrophy. *PLoS One* 14(11), p. e0225656. doi: 10.1371/journal.pone.0225656

Chen, H. et al. 2003. Mitofusins Mfn1 and Mfn2 coordinately regulate mitochondrial fusion and are essential for embryonic development. *J Cell Biol* 160(2), pp. 189-200. doi: 10.1083/jcb.200211046

Chen, H. et al. 2007. Mitochondrial fusion protects against neurodegeneration in the cerebellum. *Cell* 130(3), pp. 548-562. doi: 10.1016/j.cell.2007.06.026

Chen, H. et al. 2010a. Mitochondrial fusion is required for mtDNA stability in skeletal muscle and tolerance of mtDNA mutations. *Cell* 141(2), pp. 280-289. doi: 10.1016/j.cell.2010.02.026

Chen, K. H. et al. 2018. Epigenetic Dysregulation of the Drp1 Binding Partners MiD49 and MiD51 Increases Mitotic Mitochondrial Fission and Promotes Pulmonary Arterial Hypertension: Mechanistic and Therapeutic Implications. *Circulation*, doi: 10.1161/CIRCULATIONAHA.117.031258

Chen, L. et al. 2012. OPA1 mutation and late-onset cardiomyopathy: mitochondrial dysfunction and mtDNA instability. *J Am Heart Assoc* 1(5), p. e003012. doi: 10.1161/JAHA.112.003012

Chen, X. H. et al. 2010b. TNF-alpha induces mitochondrial dysfunction in 3T3-L1 adipocytes. *Mol Cell Endocrinol* 328(1-2), pp. 63-69. doi: 10.1016/j.mce.2010.07.005

Chou, B. K. et al. 2011. Efficient human iPS cell derivation by a non-integrating plasmid from blood cells with unique epigenetic and gene expression signatures. *Cell Res* 21(3), pp. 518-

529. doi: 10.1038/cr.2011.12

Chrysostomou, V. et al. 2010. Mechanisms of retinal ganglion cell injury in aging and glaucoma. *Ophthalmic Res* 44(3), pp. 173-178. doi: 10.1159/000316478

Chun, B. Y. and Rizzo, J. F., 3rd. 2016. Dominant optic atrophy: updates on the pathophysiology and clinical manifestations of the optic atrophy 1 mutation. *Curr Opin Ophthalmol* 27(6), pp. 475-480. doi: 10.1097/ICU.0000000000000314

Chun, B. Y. and Rizzo, J. F., 3rd. 2017. Dominant Optic Atrophy and Leber's Hereditary Optic Neuropathy: Update on Clinical Features and Current Therapeutic Approaches. *Semin Pediatr Neurol* 24(2), pp. 129-134. doi: 10.1016/j.spen.2017.06.001

Cipolat, S. et al. 2004. OPA1 requires mitofusin 1 to promote mitochondrial fusion. *Proc Natl Acad Sci U S A* 101(45), pp. 15927-15932. doi: 10.1073/pnas.0407043101

Civiletto, G. et al. 2015. Opa1 overexpression ameliorates the phenotype of two mitochondrial disease mouse models. *Cell Metab* 21(6), pp. 845-854. doi: 10.1016/j.cmet.2015.04.016

Cogliati, S. et al. 2013. Mitochondrial cristae shape determines respiratory chain supercomplexes assembly and respiratory efficiency. *Cell* 155(1), pp. 160-171. doi: 10.1016/j.cell.2013.08.032

Cohn, A. C. et al. 2007. Autosomal dominant optic atrophy: penetrance and expressivity in patients with OPA1 mutations. *Am J Ophthalmol* 143(4), pp. 656-662. doi: 10.1016/j.ajo.2006.12.038

Copeland, W. C. 2008. Inherited mitochondrial diseases of DNA replication. *Annu Rev Med* 59, pp. 131-146. doi: 10.1146/annurev.med.59.053006.104646

Corredor, R. G. et al. 2012. Soluble adenylyl cyclase activity is necessary for retinal ganglion cell survival and axon growth. *J Neurosci* 32(22), pp. 7734-7744. doi: 10.1523/JNEUROSCI.5288-11.2012

Coughlin, L. et al. 2015. Mitochondrial morphology differences and mitophagy deficit in murine glaucomatous optic nerve. *Invest Ophthalmol Vis Sci* 56(3), pp. 1437-1446. doi: 10.1167/iovs.14-16126

Country, M. W. 2017. Retinal metabolism: A comparative look at energetics in the retina. *Brain Res* 1672, pp. 50-57. doi: 10.1016/j.brainres.2017.07.025

Cunniff, B. et al. 2016. AMPK activity regulates trafficking of mitochondria to the leading edge during cell migration and matrix invasion. *Mol Biol Cell* 27(17), pp. 2662-2674. doi: 10.1091/mbc.E16-05-0286

Dagda, R. K. and Chu, C. T. 2009. Mitochondrial quality control: insights on how Parkinson's disease related genes PINK1, parkin, and Omi/HtrA2 interact to maintain mitochondrial homeostasis. *J Bioenerg Biomembr* 41(6), pp. 473-479. doi: 10.1007/s10863-009-9255-1

Davies, V. J. et al. 2007. Opa1 deficiency in a mouse model of autosomal dominant optic atrophy impairs mitochondrial morphology, optic nerve structure and visual function. *Hum Mol Genet* 16(11), pp. 1307-1318. doi: 10.1093/hmg/ddm079

Delettre, C. et al. 2001. Mutation spectrum and splicing variants in the OPA1 gene. *Hum Genet* 109(6), pp. 584-591. doi: 10.1007/s00439-001-0633-y

Delettre, C. et al. 2000. Nuclear gene OPA1, encoding a mitochondrial dynamin-related protein, is mutated in dominant optic atrophy. *Nat Genet* 26(2), pp. 207-210. doi: 10.1038/79936

Deng, H. et al. 2008. The Parkinson's disease genes pink1 and parkin promote mitochondrial fission and/or inhibit fusion in Drosophila. *Proc Natl Acad Sci U S A* 105(38), pp. 14503-14508. doi: 10.1073/pnas.0803998105

Dey, A. et al. 2018. Methods to Induce Chronic Ocular Hypertension: Reliable Rodent Models as a Platform for Cell Transplantation and Other Therapies. *Cell Transplant* 27(2), pp. 213-229. doi: 10.1177/0963689717724793

Diot, A. et al. 2018. Validating the RedMIT/GFP-LC3 Mouse Model by Studying Mitophagy in Autosomal Dominant Optic Atrophy Due to the OPA1Q285STOP Mutation. *Front Cell Dev Biol* 6, p. 103. doi: 10.3389/fcell.2018.00103

Donmez, G. 2012. The neurobiology of sirtuins and their role in neurodegeneration. *Trends Pharmacol Sci* 33(9), pp. 494-501. doi: 10.1016/j.tips.2012.05.007

Drerup, C. M. et al. 2017. Regulation of mitochondria-dynactin interaction and mitochondrial retrograde transport in axons. *Elife* 6, doi: 10.7554/eLife.22234

Duvezin-Caubet, S. et al. 2007. OPA1 processing reconstituted in yeast depends on the subunit composition of the m-AAA protease in mitochondria. *Mol Biol Cell* 18(9), pp. 3582-3590. doi: 10.1091/mbc.E07-02-0164

Edel, M. J. et al. 2010. Rem2 GTPase maintains survival of human embryonic stem cells as well as enhancing reprogramming by regulating p53 and cyclin D1. *Genes Dev* 24(6), pp. 561-573. doi: 10.1101/gad.1876710

Eells, J. T. 2019. Mitochondrial Dysfunction in the Aging Retina. *Biology (Basel)* 8(2), doi: 10.3390/biology8020031

Eiyama, A. and Okamoto, K. 2015. PINK1/Parkin-mediated mitophagy in mammalian cells. *Curr Opin Cell Biol* 33, pp. 95-101. doi: 10.1016/j.ceb.2015.01.002

Elachouri, G. et al. 2011. OPA1 links human mitochondrial genome maintenance to mtDNA replication and distribution. *Genome Res* 21(1), pp. 12-20. doi: 10.1101/gr.108696.110

Erskine, L. and Herrera, E. 2014. Connecting the retina to the brain. *ASN Neuro* 6(6), doi: 10.1177/1759091414562107

Fairless, R. et al. 2014. Dysfunction of neuronal calcium signalling in neuroinflammation and neurodegeneration. *Cell Tissue Res* 357(2), pp. 455-462. doi: 10.1007/s00441-013-1758-8

Faits, M. C. et al. 2016. Dendritic mitochondria reach stable positions during circuit development. *Elife* 5, p. e11583. doi: 10.7554/eLife.11583

Farkhondeh, A. et al. 2019. Induced pluripotent stem cells for neural drug discovery. *Drug Discov Today* 24(4), pp. 992-999. doi: 10.1016/j.drudis.2019.01.007

Ferre, M. et al. 2009. Molecular screening of 980 cases of suspected hereditary optic neuropathy with a report on 77 novel OPA1 mutations. *Hum Mutat* 30(7), pp. E692-705. doi: 10.1002/humu.21025

Frezza, C. et al. 2006. OPA1 controls apoptotic cristae remodeling independently from mitochondrial fusion. *Cell* 126(1), pp. 177-189. doi: 10.1016/j.cell.2006.06.025

Fricker, R. 2017. The Influence of Nicotinamide on Health and Disease in the Central Nervous

System.

Fukumitsu, K. et al. 2016. Mitochondrial fission protein Drp1 regulates mitochondrial transport and dendritic arborization in cerebellar Purkinje cells. *Mol Cell Neurosci* 71, pp. 56-65. doi: 10.1016/j.mcn.2015.12.006

Fulop, L. et al. 2013. Extramitochondrial OPA1 and adrenocortical function. *Mol Cell Endocrinol* 381(1-2), pp. 70-79. doi: 10.1016/j.mce.2013.07.021

Galkin, A. et al. 2006. The proton pumping stoichiometry of purified mitochondrial complex I reconstituted into proteoliposomes. *Biochim Biophys Acta* 1757(12), pp. 1575-1581. doi: 10.1016/j.bbabio.2006.10.001

Gao, F. et al. 2016. Comparative analysis of three purification protocols for retinal ganglion cells from rat. *Mol Vis* 22, pp. 387-400.

Georg, B. et al. 2017. Melanopsin-expressing retinal ganglion cells are resistant to cell injury, but not always. *Mitochondrion* 36, pp. 77-84. doi: 10.1016/j.mito.2017.04.003

Germain, R. N. et al. 2006. Dynamic imaging of the immune system: progress, pitfalls and promise. *Nat Rev Immunol* 6(7), pp. 497-507. doi: 10.1038/nri1884

Goldberg, J. L. and Barres, B. A. 2000. Nogo in nerve regeneration. *Nature* 403(6768), pp. 369-370. doi: 10.1038/35000309

Gomes, L. C. et al. 2011. During autophagy mitochondria elongate, are spared from degradation and sustain cell viability. *Nat Cell Biol* 13(5), pp. 589-598. doi: 10.1038/ncb2220

Gonzalez-Menendez, I. et al. 2015. Influence of Opa1 Mutation on Survival and Function of Retinal Ganglion Cells. *Invest Ophthalmol Vis Sci* 56(8), pp. 4835-4845. doi: 10.1167/iovs.15-16743

Gordon, M. O. et al. 2002. The Ocular Hypertension Treatment Study: baseline factors that predict the onset of primary open-angle glaucoma. *Arch Ophthalmol* 120(6), pp. 714-720; discussion 829-730. doi: 10.1001/archopht.120.6.714

Gottlieb, E. 2006. OPA1 and PARL keep a lid on apoptosis. *Cell* 126(1), pp. 27-29. doi: 10.1016/j.cell.2006.06.030

Griffin, S. M. et al. 2013. Nicotinamide promotes neuronal differentiation of mouse embryonic stem cells in vitro. *Neuroreport* 24(18), pp. 1041-1046. doi: 10.1097/WNR.0000000000000071

Griparic, L. et al. 2004. Loss of the intermembrane space protein Mgm1/OPA1 induces swelling and localized constrictions along the lengths of mitochondria. *J Biol Chem* 279(18), pp. 18792-18798. doi: 10.1074/jbc.M400920200

Guillery, O. et al. 2008. Metalloprotease-mediated OPA1 processing is modulated by the mitochondrial membrane potential. *Biol Cell* 100(5), pp. 315-325. doi: 10.1042/BC20070110

Guo, X. et al. 2014. PGC-1alpha signaling coordinates susceptibility to metabolic and oxidative injury in the inner retina. *Am J Pathol* 184(4), pp. 1017-1029. doi: 10.1016/j.ajpath.2013.12.012

Gupta, D. and Chen, P. P. 2016. Glaucoma. *Am Fam Physician* 93(8), pp. 668-674.

Ham, M. et al. 2019. Meta-analysis of genotype-phenotype analysis of OPA1 mutations in autosomal dominant optic atrophy. *Mitochondrion* 46, pp. 262-269. doi: 10.1016/j.mito.2018.07.006

Harwerth, R. S. and Wheat, J. L. 2008. Modeling the effects of aging on retinal ganglion cell density and nerve fiber layer thickness. *Graefes Arch Clin Exp Ophthalmol* 246(2), pp. 305-314. doi: 10.1007/s00417-007-0691-5

Heijl, A. et al. 2002. Reduction of intraocular pressure and glaucoma progression: results from the Early Manifest Glaucoma Trial. *Arch Ophthalmol* 120(10), pp. 1268-1279. doi: 10.1001/archopht.120.10.1268

Hollenbeck, P. J. 1996. The pattern and mechanism of mitochondrial transport in axons. *Front Biosci* 1, pp. d91-102. doi: 10.2741/a118

Houtkooper, R. H. et al. 2012. Sirtuins as regulators of metabolism and healthspan. *Nat Rev Mol Cell Biol* 13(4), pp. 225-238. doi: 10.1038/nrm3293

Howell, G. R. et al. 2007. Axons of retinal ganglion cells are insulted in the optic nerve early in DBA/2J glaucoma. *J Cell Biol* 179(7), pp. 1523-1537. doi: 10.1083/jcb.200706181

Hu, W. H. et al. 2002. Identification and characterization of a novel Nogo-interacting mitochondrial protein (NIMP). *J Neurochem* 81(1), pp. 36-45. doi: 10.1046/j.1471-4159.2002.00788.x

Hu, X. et al. 2017. Parkin overexpression protects retinal ganglion cells against glutamate excitotoxicity. *Mol Vis* 23, pp. 447-456.

Hu, X. et al. 2018. Overexpression of Optic Atrophy Type 1 Protects Retinal Ganglion Cells and Upregulates Parkin Expression in Experimental Glaucoma. *Front Mol Neurosci* 11, p. 350. doi: 10.3389/fnmol.2018.00350

Hudson, G. et al. 2008. Mutation of OPA1 causes dominant optic atrophy with external ophthalmoplegia, ataxia, deafness and multiple mitochondrial DNA deletions: a novel disorder of mtDNA maintenance. *Brain* 131(Pt 2), pp. 329-337. doi: 10.1093/brain/awm272

Hwang, E. S. and Hwang, S. Y. 2017. Cellular NAD+Level: A Key Determinant of Mitochondrial Quality and Health. *Annals of Geriatric Medicine and Research* 21(4), pp. 149-157. doi: 10.4235/agmr.2017.21.4.149

Hwang, E. S. and Song, S. B. 2020. Possible Adverse Effects of High-Dose Nicotinamide: Mechanisms and Safety Assessment. *Biomolecules* 10(5), doi: 10.3390/biom10050687

Ichikawa, M. et al. 1993. Formation and maturation of synapses in primary cultures of rat cerebral cortical cells: an electron microscopic study. *Neurosci Res* 16(2), pp. 95-103. doi: 10.1016/0168-0102(93)90076-3

Inman, D. M. et al. 2006. Quantitative correlation of optic nerve pathology with ocular pressure and corneal thickness in the DBA/2 mouse model of glaucoma. *Invest Ophthalmol Vis Sci* 47(3), pp. 986-996. doi: 10.1167/iovs.05-0925

Ishihara, T. et al. 2015. Physiological roles of mitochondrial fission in cultured cells and mouse development. *Ann N Y Acad Sci* 1350, pp. 77-81. doi: 10.1111/nyas.12848

Ito, Y. A. and Di Polo, A. 2017. Mitochondrial dynamics, transport, and quality control: A bottleneck for retinal ganglion cell viability in optic neuropathies. *Mitochondrion* 36, pp. 186-192. doi: 10.1016/j.mito.2017.08.014

Jeoung, J. W. et al. 2014. Mitochondrial DNA variant discovery in normal-tension glaucoma

patients by next-generation sequencing. *Invest Ophthalmol Vis Sci* 55(2), pp. 986-992. doi: 10.1167/iovs.13-12968

Ji, S. L. and Tang, S. B. 2019. Differentiation of retinal ganglion cells from induced pluripotent stem cells: a review. *Int J Ophthalmol* 12(1), pp. 152-160. doi: 10.18240/ijo.2019.01.22

Jin, S. M. and Youle, R. J. 2013. The accumulation of misfolded proteins in the mitochondrial matrix is sensed by PINK1 to induce PARK2/Parkin-mediated mitophagy of polarized mitochondria. *Autophagy* 9(11), pp. 1750-1757. doi: 10.4161/auto.26122

Ju, W. K. et al. 2010. Increased optic atrophy type 1 expression protects retinal ganglion cells in a mouse model of glaucoma. *Mol Vis* 16, pp. 1331-1342.

Ju, W. K. et al. 2008. Intraocular pressure elevation induces mitochondrial fission and triggers OPA1 release in glaucomatous optic nerve. *Invest Ophthalmol Vis Sci* 49(11), pp. 4903-4911. doi: 10.1167/iovs.07-1661

Ju, W. K. et al. 2019. Inhibition of cAMP/PKA Pathway Protects Optic Nerve Head Astrocytes against Oxidative Stress by Akt/Bax Phosphorylation-Mediated Mfn1/2 Oligomerization. *Oxid Med Cell Longev* 2019, p. 8060962. doi: 10.1155/2019/8060962

Kadenbach, B. 2020. Complex IV - The regulatory center of mitochondrial oxidative phosphorylation. *Mitochondrion*, doi: 10.1016/j.mito.2020.10.004

Kamei, S. et al. 2005. Expression of the Opa1 mitochondrial protein in retinal ganglion cells: its downregulation causes aggregation of the mitochondrial network. *Invest Ophthalmol Vis Sci* 46(11), pp. 4288-4294. doi: 10.1167/iovs.03-1407

Kanazawa, T. et al. 2008. The C. elegans Opa1 homologue EAT-3 is essential for resistance to free radicals. *PLoS Genet* 4(2), p. e1000022. doi: 10.1371/journal.pgen.1000022

Kane, A. E. and Sinclair, D. A. 2018. Sirtuins and NAD(+) in the Development and Treatment of Metabolic and Cardiovascular Diseases. *Circ Res* 123(7), pp. 868-885. doi: 10.1161/CIRCRESAHA.118.312498

Kang, J. S. et al. 2008. Docking of axonal mitochondria by syntaphilin controls their mobility and affects short-term facilitation. *Cell* 132(1), pp. 137-148. doi: 10.1016/j.cell.2007.11.024

Kann, O. and Kovacs, R. 2007. Mitochondria and neuronal activity. *Am J Physiol Cell Physiol* 292(2), pp. C641-657. doi: 10.1152/ajpcell.00222.2006

Kao, S. H. et al. 2015. Changes in Mitochondrial Morphology and Bioenergetics in Human Lymphoblastoid Cells With Four Novel OPA1 Mutations. *Invest Ophthalmol Vis Sci* 56(4), pp. 2269-2278. doi: 10.1167/iovs.14-16288

Kieper, N. et al. 2010. Modulation of mitochondrial function and morphology by interaction of Omi/HtrA2 with the mitochondrial fusion factor OPA1. *Exp Cell Res* 316(7), pp. 1213-1224. doi: 10.1016/j.yexcr.2010.01.005

Kim, K. Y. et al. 2015. DRP1 inhibition rescues retinal ganglion cells and their axons by preserving mitochondrial integrity in a mouse model of glaucoma. *Cell Death Dis* 6, p. e1839. doi: 10.1038/cddis.2015.180

Kimball, E. C. et al. 2018. The effects of age on mitochondria, axonal transport, and axonal degeneration after chronic IOP elevation using a murine ocular explant model. *Exp Eye Res* 172, pp. 78-85. doi: 10.1016/j.exer.2018.04.001

Kjer, P. 1959. Infantile optic atrophy with dominant mode of inheritance: a clinical and genetic study of 19 Danish families. *Acta Ophthalmol Suppl* 164(Supp 54), pp. 1-147.

Kjer, P. et al. 1983. Histopathology of eye, optic nerve and brain in a case of dominant optic atrophy. *Acta Ophthalmol (Copenh)* 61(2), pp. 300-312. doi: 10.1111/j.1755-3768.1983.tb01424.x

Knip, M. et al. 2000. Safety of high-dose nicotinamide: a review. *Diabetologia* 43(11), pp. 1337-1345. doi: 10.1007/s001250051536

Kraemer, K. et al. 2012. Introduction: the diverse and essential biological functions of vitamins. *Ann Nutr Metab* 61(3), pp. 185-191. doi: 10.1159/000343103

Kreymerman, A. et al. 2019. MTP18 is a Novel Regulator of Mitochondrial Fission in CNS Neuron Development, Axonal Growth, and Injury Responses. *Sci Rep* 9(1), p. 10669. doi: 10.1038/s41598-019-46956-5

Kushnareva, Y. et al. 2016. Mitochondrial dysfunction in an Opa1(Q285STOP) mouse model of dominant optic atrophy results from Opa1 haploinsufficiency. *Cell Death Dis* 7, p. e2309. doi: 10.1038/cddis.2016.160

La Morgia, C. et al. 2010. Melanopsin retinal ganglion cells are resistant to neurodegeneration in mitochondrial optic neuropathies. *Brain* 133(Pt 8), pp. 2426-2438. doi: 10.1093/brain/awq155

Labbe, K. et al. 2014. Determinants and functions of mitochondrial behavior. *Annu Rev Cell Dev Biol* 30, pp. 357-391. doi: 10.1146/annurev-cellbio-101011-155756

Landes, T. et al. 2010a. The BH3-only Bnip3 binds to the dynamin Opa1 to promote mitochondrial fragmentation and apoptosis by distinct mechanisms. *EMBO Rep* 11(6), pp. 459-465. doi: 10.1038/embor.2010.50

Landes, T. et al. 2010b. OPA1 (dys)functions. *Semin Cell Dev Biol* 21(6), pp. 593-598. doi: 10.1016/j.semcdb.2009.12.012

Lascaratos, G. et al. 2012. Mitochondrial dysfunction in glaucoma: understanding genetic influences. *Mitochondrion* 12(2), pp. 202-212. doi: 10.1016/j.mito.2011.11.004

Lascaratos, G. et al. 2007. Visible light affects mitochondrial function and induces neuronal death in retinal cell cultures. *Vision Res* 47(9), pp. 1191-1201. doi: 10.1016/j.visres.2006.12.014

Lee, H. et al. 2017. The short variant of the mitochondrial dynamin OPA1 maintains mitochondrial energetics and cristae structure. *J Biol Chem* 292(17), pp. 7115-7130. doi: 10.1074/jbc.M116.762567

Lee, S. et al. 2012. Impaired complex-I-linked respiration and ATP synthesis in primary open-angle glaucoma patient lymphoblasts. *Invest Ophthalmol Vis Sci* 53(4), pp. 2431-2437. doi: 10.1167/iovs.12-9596

Lee, Y. J. et al. 2004. Roles of the mammalian mitochondrial fission and fusion mediators Fis1, Drp1, and Opa1 in apoptosis. *Mol Biol Cell* 15(11), pp. 5001-5011. doi: 10.1091/mbc.E04-04-0294

Lenaers, G. et al. 2012. Dominant optic atrophy. *Orphanet J Rare Dis* 7, p. 46. doi: 10.1186/1750-1172-7-46

Lenaers, G. et al. 2009. OPA1 functions in mitochondria and dysfunctions in optic nerve. *Int J Biochem Cell Biol* 41(10), pp. 1866-1874. doi: 10.1016/j.biocel.2009.04.013

Li, F. et al. 2016. Nicotinamide benefits both mothers and pups in two contrasting mouse models of preeclampsia. *Proc Natl Acad Sci U S A* 113(47), pp. 13450-13455. doi: 10.1073/pnas.1614947113

Li, G. Y. and Osborne, N. N. 2008. Oxidative-induced apoptosis to an immortalized ganglion cell line is caspase independent but involves the activation of poly(ADP-ribose)polymerase and apoptosis-inducing factor. *Brain Res* 1188, pp. 35-43. doi: 10.1016/j.brainres.2007.10.073

Li, K. et al. 2017. HiPSC-derived retinal ganglion cells grow dendritic arbors and functional axons on a tissue-engineered scaffold. *Acta Biomater* 54, pp. 117-127. doi: 10.1016/j.actbio.2017.02.032

Liao, C. et al. 2017. Dysregulated mitophagy and mitochondrial organization in optic atrophy due to OPA1 mutations. *Neurology* 88(2), pp. 131-142. doi: 10.1212/WNL.0000000000003491

Liu, D. et al. 2013. Nicotinamide forestalls pathology and cognitive decline in Alzheimer mice: evidence for improved neuronal bioenergetics and autophagy procession. *Neurobiol Aging* 34(6), pp. 1564-1580. doi: 10.1016/j.neurobiolaging.2012.11.020

Liu, X. et al. 2009. Mitochondrial 'kiss-and-run': interplay between mitochondrial motility and fusion-fission dynamics. *EMBO J* 28(20), pp. 3074-3089. doi: 10.1038/emboj.2009.255

Lodi, R. et al. 2004. Deficit of in vivo mitochondrial ATP production in OPA1-related dominant optic atrophy. *Ann Neurol* 56(5), pp. 719-723. doi: 10.1002/ana.20278

Louie, K. et al. 2008. Effects of imaging conditions on mitochondrial transport and length in larval motor axons of Drosophila. *Comp Biochem Physiol A Mol Integr Physiol* 151(2), pp. 159-172. doi: 10.1016/j.cbpa.2008.06.023

Lowry, W. E. et al. 2008. Generation of human induced pluripotent stem cells from dermal fibroblasts. *Proc Natl Acad Sci U S A* 105(8), pp. 2883-2888. doi: 10.1073/pnas.0711983105

Lu, H. F. et al. 2014. A defined xeno-free and feeder-free culture system for the derivation, expansion and direct differentiation of transgene-free patient-specific induced pluripotent stem cells. *Biomaterials* 35(9), pp. 2816-2826. doi: 10.1016/j.biomaterials.2013.12.050

Mabuchi, F. et al. 2007. The OPA1 gene polymorphism is associated with normal tension and high tension glaucoma. *Am J Ophthalmol* 143(1), pp. 125-130. doi: 10.1016/j.ajo.2006.09.028

MacVicar, T. and Langer, T. 2016. OPA1 processing in cell death and disease - the long and short of it. *J Cell Sci* 129(12), pp. 2297-2306. doi: 10.1242/jcs.159186

MacVicar, T. D. and Lane, J. D. 2014. Impaired OMA1-dependent cleavage of OPA1 and reduced DRP1 fission activity combine to prevent mitophagy in cells that are dependent on oxidative phosphorylation. *J Cell Sci* 127(Pt 10), pp. 2313-2325. doi: 10.1242/jcs.144337

Maiese, K. and Chong, Z. Z. 2003. Nicotinamide: necessary nutrient emerges as a novel cytoprotectant for the brain. *Trends Pharmacol Sci* 24(5), pp. 228-232. doi: 10.1016/S0165-6147(03)00078-6

Marchbank, N. J. et al. 2002. Deletion of the OPA1 gene in a dominant optic atrophy family: evidence that haploinsufficiency is the cause of disease. *J Med Genet* 39(8), p. e47. doi: 10.1136/jmg.39.8.e47

Markham, A. et al. 2004. BDNF increases rat brain mitochondrial respiratory coupling at complex I, but not complex II. *Eur J Neurosci* 20(5), pp. 1189-1196. doi: 10.1111/j.1460-9568.2004.03578.x

Mattson, M. P. 2007. Mitochondrial regulation of neuronal plasticity. *Neurochem Res* 32(4-5), pp. 707-715. doi: 10.1007/s11064-006-9170-3

Mayorov, V. I. et al. 2008. Mitochondrial oxidative phosphorylation in autosomal dominant optic atrophy. *BMC Biochem* 9, p. 22. doi: 10.1186/1471-2091-9-22

McBride, H. and Soubannier, V. 2010. Mitochondrial function: OMA1 and OPA1, the grandmasters of mitochondrial health. *Curr Biol* 20(6), pp. R274-276. doi: 10.1016/j.cub.2010.02.011

Meeusen, S. et al. 2006. Mitochondrial inner-membrane fusion and crista maintenance requires the dynamin-related GTPase Mgm1. *Cell* 127(2), pp. 383-395. doi: 10.1016/j.cell.2006.09.021

Meyer, J. N. et al. 2017. Mitochondrial fusion, fission, and mitochondrial toxicity. *Toxicology* 391, pp. 42-53. doi: 10.1016/j.tox.2017.07.019

Misaka, T. et al. 2002. Primary structure of a dynamin-related mouse mitochondrial GTPase and its distribution in brain, subcellular localization, and effect on mitochondrial morphology. *J*

Biol Chem 277(18), pp. 15834-15842. doi: 10.1074/jbc.M109260200

Misaka, T. et al. 2006. The dynamin-related mouse mitochondrial GTPase OPA1 alters the structure of the mitochondrial inner membrane when exogenously introduced into COS-7 cells. *Neurosci Res* 55(2), pp. 123-133. doi: 10.1016/j.neures.2006.02.010

Misko, A. et al. 2010. Mitofusin 2 is necessary for transport of axonal mitochondria and interacts with the Miro/Milton complex. *J Neurosci* 30(12), pp. 4232-4240. doi: 10.1523/JNEUROSCI.6248-09.2010

Morgan, J. E. 2004. Circulation and axonal transport in the optic nerve. *Eye (Lond)* 18(11), pp. 1089-1095. doi: 10.1038/sj.eye.6701574

Morris, R. L. and Hollenbeck, P. J. 1993. The regulation of bidirectional mitochondrial transport is coordinated with axonal outgrowth. *J Cell Sci* 104 (Pt 3), pp. 917-927.

Morris, R. L. and Hollenbeck, P. J. 1995. Axonal transport of mitochondria along microtubules and F-actin in living vertebrate neurons. *J Cell Biol* 131(5), pp. 1315-1326. doi: 10.1083/jcb.131.5.1315

Morrison, J. C. et al. 1990. Optic nerve head extracellular matrix in primary optic atrophy and experimental glaucoma. *Arch Ophthalmol* 108(7), pp. 1020-1024. doi: 10.1001/archopht.1990.01070090122053

Nakazawa, T. et al. 2006. Tumor necrosis factor-alpha mediates oligodendrocyte death and delayed retinal ganglion cell loss in a mouse model of glaucoma. *J Neurosci* 26(49), pp. 12633-12641. doi: 10.1523/JNEUROSCI.2801-06.2006

Neumann, S. et al. 2017. KymoAnalyzer: a software tool for the quantitative analysis of intracellular transport in neurons. *Traffic* 18(1), pp. 71-88. doi: 10.1111/tra.12456

Nickells, R. W. 2012. The cell and molecular biology of glaucoma: mechanisms of retinal ganglion cell death. *Invest Ophthalmol Vis Sci* 53(5), pp. 2476-2481. doi: 10.1167/iovs.12-9483h

Noh, Y. H. et al. 2013. Inhibition of oxidative stress by coenzyme Q10 increases mitochondrial mass and improves bioenergetic function in optic nerve head astrocytes. *Cell Death Dis* 4, p. e820. doi: 10.1038/cddis.2013.341

Nunnari, J. and Suomalainen, A. 2012. Mitochondria: in sickness and in health. *Cell* 148(6), pp. 1145-1159. doi: 10.1016/j.cell.2012.02.035

Nusbaum, D. M. et al. 2015. Elevated intracranial pressure causes optic nerve and retinal ganglion cell degeneration in mice. *Exp Eye Res* 136, pp. 38-44. doi: 10.1016/j.exer.2015.04.014

Ohlemacher, S. K. et al. 2016. Stepwise Differentiation of Retinal Ganglion Cells from Human Pluripotent Stem Cells Enables Analysis of Glaucomatous Neurodegeneration. *Stem Cells* 34(6), pp. 1553-1562. doi: 10.1002/stem.2356

Olichon, A. et al. 2003. Loss of OPA1 perturbates the mitochondrial inner membrane structure and integrity, leading to cytochrome c release and apoptosis. *J Biol Chem* 278(10), pp. 7743-7746. doi: 10.1074/jbc.C200677200

Olichon, A. et al. 2007a. OPA1 alternate splicing uncouples an evolutionary conserved function in mitochondrial fusion from a vertebrate restricted function in apoptosis. *Cell Death Differ* 14(4), pp. 682-692. doi: 10.1038/sj.cdd.4402048

Olichon, A. et al. 2002. The human dynamin-related protein OPA1 is anchored to the mitochondrial inner membrane facing the inter-membrane space. *FEBS Lett* 523(1-3), pp. 171-176.

Olichon, A. et al. 2007b. Effects of OPA1 mutations on mitochondrial morphology and apoptosis: relevance to ADOA pathogenesis. *J Cell Physiol* 211(2), pp. 423-430. doi: 10.1002/jcp.20950

Osborne, N. N. et al. 2008. Light affects mitochondria to cause apoptosis to cultured cells: possible relevance to ganglion cell death in certain optic neuropathies. *J Neurochem* 105(5), pp. 2013-2028. doi: 10.1111/j.1471-4159.2008.05320.x

Otera, H. et al. 2010. Mff is an essential factor for mitochondrial recruitment of Drp1 during mitochondrial fission in mammalian cells. *J Cell Biol* 191(6), pp. 1141-1158. doi: 10.1083/jcb.201007152

Ouyang, X. et al. 2020. Mechanisms of blue light-induced eye hazard and protective measures: a review. *Biomed Pharmacother* 130, p. 110577. doi: 10.1016/j.biopha.2020.110577

Palikaras, K. et al. 2016. Mitophagy: In sickness and in health. *Mol Cell Oncol* 3(1), p. e1056332. doi: 10.1080/23723556.2015.1056332

Park, K. K. et al. 2008. Promoting axon regeneration in the adult CNS by modulation of the PTEN/mTOR pathway. *Science* 322(5903), pp. 963-966. doi: 10.1126/science.1161566

Patten, D. A. et al. 2014. OPA1-dependent cristae modulation is essential for cellular adaptation to metabolic demand. *EMBO J* 33(22), pp. 2676-2691. doi: 10.15252/embj.201488349

Pellegrini, L. and Scorrano, L. 2007. A cut short to death: Parl and Opa1 in the regulation of mitochondrial morphology and apoptosis. *Cell Death Differ* 14(7), pp. 1275-1284. doi: 10.1038/sj.cdd.4402145

Perganta, G. et al. 2013. Non-image-forming light driven functions are preserved in a mouse model of autosomal dominant optic atrophy. *PLoS One* 8(2), p. e56350. doi: 10.1371/journal.pone.0056350

Perlman, R. L. 2016. Mouse models of human disease: An evolutionary perspective. *Evol Med Public Health* 2016(1), pp. 170-176. doi: 10.1093/emph/eow014

Pernas, L. and Scorrano, L. 2016. Mito-Morphosis: Mitochondrial Fusion, Fission, and Cristae Remodeling as Key Mediators of Cellular Function. *Annu Rev Physiol* 78, pp. 505-531. doi: 10.1146/annurev-physiol-021115-105011

Pilsl, A. and Winklhofer, K. F. 2012. Parkin, PINK1 and mitochondrial integrity: emerging concepts of mitochondrial dysfunction in Parkinson's disease. *Acta Neuropathol* 123(2), pp. 173-188. doi: 10.1007/s00401-011-0902-3

Pilz, Y. L. et al. 2017. A Review of Mitochondrial Optic Neuropathies: From Inherited to Acquired Forms. *J Optom* 10(4), pp. 205-214. doi: 10.1016/j.optom.2016.09.003

Poole, A. C. et al. 2008. The PINK1/Parkin pathway regulates mitochondrial morphology. *Proc Natl Acad Sci U S A* 105(5), pp. 1638-1643. doi: 10.1073/pnas.0709336105

Puomila, A. et al. 2005. Dominant optic atrophy: correlation between clinical and molecular genetic studies. *Acta Ophthalmol Scand* 83(3), pp. 337-346. doi: 10.1111/j.1600-0420.2005.00448.x

Quigley, H. A. et al. 1981. Optic nerve damage in human glaucoma. II. The site of injury and susceptibility to damage. *Arch Ophthalmol* 99(4), pp. 635-649. doi: 10.1001/archopht.1981.03930010635009

Quigley, H. A. et al. 2000. Retrograde axonal transport of BDNF in retinal ganglion cells is blocked by acute IOP elevation in rats. *Invest Ophthalmol Vis Sci* 41(11), pp. 3460-3466.

Reichman, S. et al. 2014. From confluent human iPS cells to self-forming neural retina and retinal pigmented epithelium. *Proc Natl Acad Sci U S A* 111(23), pp. 8518-8523. doi: 10.1073/pnas.1324212111

Revollo, J. R. et al. 2004. The NAD biosynthesis pathway mediated by nicotinamide phosphoribosyltransferase regulates Sir2 activity in mammalian cells. *J Biol Chem* 279(49), pp. 50754-50763. doi: 10.1074/jbc.M408388200

Riazifar, H. et al. 2014. Chemically induced specification of retinal ganglion cells from human embryonic and induced pluripotent stem cells. *Stem Cells Transl Med* 3(4), pp. 424-432. doi: 10.5966/sctm.2013-0147

Rochtchina, E. et al. 2002. Relationship between age and intraocular pressure: the Blue Mountains Eye Study. *Clin Exp Ophthalmol* 30(3), pp. 173-175. doi: 10.1046/j.1442-9071.2002.00519.x

Rodgers, J. T. et al. 2005. Nutrient control of glucose homeostasis through a complex of PGC-1alpha and SIRT1. *Nature* 434(7029), pp. 113-118. doi: 10.1038/nature03354

Rosselin, M. et al. 2017. L-OPA1 regulates mitoflash biogenesis independently from membrane fusion. *EMBO Rep* 18(3), pp. 451-463. doi: 10.15252/embr.201642931

Ruthel, G. and Hollenbeck, P. J. 2003. Response of mitochondrial traffic to axon determination and differential branch growth. *J Neurosci* 23(24), pp. 8618-8624.

Ryu, S. W. et al. 2015. The mitochondrial fusion-related proteins Mfn2 and OPA1 are transcriptionally induced during differentiation of bone marrow progenitors to immature dendritic cells. *Mol Cells* 38(1), pp. 89-94. doi: 10.14348/molcells.2015.2285

Saini, J. S. et al. 2017. Nicotinamide Ameliorates Disease Phenotypes in a Human iPSC Model of Age-Related Macular Degeneration. *Cell Stem Cell* 20(5), pp. 635-647 e637. doi:

10.1016/j.stem.2016.12.015

Saita, S. et al. 2016. Distinct types of protease systems are involved in homeostasis regulation of mitochondrial morphology via balanced fusion and fission. *Genes Cells* 21(5), pp. 408-424. doi: 10.1111/gtc.12351

Santarelli, R. et al. 2015. OPA1-related auditory neuropathy: site of lesion and outcome of cochlear implantation. *Brain* 138(Pt 3), pp. 563-576. doi: 10.1093/brain/awu378

Santo-Domingo, J. et al. 2013. OPA1 promotes pH flashes that spread between contiguous mitochondria without matrix protein exchange. *EMBO J* 32(13), pp. 1927-1940. doi: 10.1038/emboj.2013.124

Saotome, M. et al. 2008. Bidirectional Ca2+-dependent control of mitochondrial dynamics by the Miro GTPase. *Proc Natl Acad Sci U S A* 105(52), pp. 20728-20733. doi: 10.1073/pnas.0808953105

Sarzi, E. et al. 2012. The human OPA1delTTAG mutation induces premature age-related systemic neurodegeneration in mouse. *Brain* 135(Pt 12), pp. 3599-3613. doi: 10.1093/brain/aws303

Satoh, M. et al. 2003. Differential sublocalization of the dynamin-related protein OPA1 isoforms in mitochondria. *Biochem Biophys Res Commun* 300(2), pp. 482-493.

Sayed, N. et al. 2016. Translation of Human-Induced Pluripotent Stem Cells: From Clinical Trial in a Dish to Precision Medicine. *J Am Coll Cardiol* 67(18), pp. 2161-2176. doi: 10.1016/j.jacc.2016.01.083

Semba, R. D. 2012. The discovery of the vitamins. *Int J Vitam Nutr Res* 82(5), pp. 310-315. doi: 10.1024/0300-9831/a000124

Seo, A. Y. et al. 2010. New insights into the role of mitochondria in aging: mitochondrial dynamics and more. *J Cell Sci* 123(Pt 15), pp. 2533-2542. doi: 10.1242/jcs.070490

Sethi, J. K. et al. 1996. Nicotinamide inhibits cyclic ADP-ribose-mediated calcium signalling in sea urchin eggs. *Biochem J* 319 (Pt 2), pp. 613-617. doi: 10.1042/bj3190613

Shin, J. H. et al. 2011. PARIS (ZNF746) repression of PGC-1alpha contributes to

neurodegeneration in Parkinson's disease. *Cell* 144(5), pp. 689-702. doi: 10.1016/j.cell.2011.02.010

Sidhu, A. et al. 2018. Nicotinamide reverses behavioral impairments and provides neuroprotection in 3-nitropropionic acid induced animal model ofHuntington's disease: implication of oxidative stress- poly(ADP- ribose) polymerase pathway. *Metab Brain Dis* 33(6), pp. 1911-1921. doi: 10.1007/s11011-018-0297-0

Skidd, P. M. et al. 2013. Autosomal dominant hereditary optic neuropathy (ADOA): a review of the genetics and clinical manifestations of ADOA and ADOA+. *Semin Ophthalmol* 28(5-6), pp. 422-426. doi: 10.3109/08820538.2013.825296

Smirnova, E. et al. 2001. Dynamin-related protein Drp1 is required for mitochondrial division in mammalian cells. *Mol Biol Cell* 12(8), pp. 2245-2256.

Song, Z. et al. 2007. OPA1 processing controls mitochondrial fusion and is regulated by mRNA splicing, membrane potential, and Yme1L. *J Cell Biol* 178(5), pp. 749-755. doi: 10.1083/jcb.200704110

Song, Z. et al. 2009. Mitofusins and OPA1 mediate sequential steps in mitochondrial membrane fusion. *Mol Biol Cell* 20(15), pp. 3525-3532. doi: 10.1091/mbc.E09-03-0252

Spinazzi, M. et al. 2008. A novel deletion in the GTPase domain of OPA1 causes defects in mitochondrial morphology and distribution, but not in function. *Hum Mol Genet* 17(21), pp. 3291-3302. doi: 10.1093/hmg/ddn225

Steketee, M. B. et al. 2012. Mitochondrial dynamics regulate growth cone motility, guidance, and neurite growth rate in perinatal retinal ganglion cells in vitro. *Invest Ophthalmol Vis Sci* 53(11), pp. 7402-7411. doi: 10.1167/iovs.12-10298

Suen, D. F. et al. 2008. Mitochondrial dynamics and apoptosis. *Genes Dev* 22(12), pp. 1577-1590. doi: 10.1101/gad.1658508

Sun, S. et al. 2017. Cannabidiol attenuates OGD/R-induced damage by enhancing mitochondrial bioenergetics and modulating glucose metabolism via pentose-phosphate pathway in hippocampal neurons. *Redox Biol* 11, pp. 577-585. doi: 10.1016/j.redox.2016.12.029

Tagaya, M. and Arasaki, K. 2017. Regulation of Mitochondrial Dynamics and Autophagy by

the Mitochondria-Associated Membrane. *Adv Exp Med Biol* 997, pp. 33-47. doi: 10.1007/978-981-10-4567-7_3

Takahashi, K. et al. 2017. Optic atrophy 1 mediates coenzyme Q-responsive regulation of respiratory complex IV activity in brain mitochondria. *Exp Gerontol* 98, pp. 217-223. doi: 10.1016/j.exger.2017.09.002

Takahashi, K. and Yamanaka, S. 2006. Induction of pluripotent stem cells from mouse embryonic and adult fibroblast cultures by defined factors. *Cell* 126(4), pp. 663-676. doi: 10.1016/j.cell.2006.07.024

Takihara, Y. et al. 2015. In vivo imaging of axonal transport of mitochondria in the diseased and aged mammalian CNS. *Proc Natl Acad Sci U S A* 112(33), pp. 10515-10520. doi: 10.1073/pnas.1509879112

Tanaka, A. et al. 2010. Proteasome and p97 mediate mitophagy and degradation of mitofusins induced by Parkin. *J Cell Biol* 191(7), pp. 1367-1380. doi: 10.1083/jcb.201007013

Tao, K. et al. 2014. AMP-activated protein kinase mediates activity-dependent axon branching by recruiting mitochondria to axon. *Dev Neurobiol* 74(6), pp. 557-573. doi: 10.1002/dneu.22149

Teotia, P. et al. 2017. Generation of Functional Human Retinal Ganglion Cells with Target Specificity from Pluripotent Stem Cells by Chemically Defined Recapitulation of Developmental Mechanism. *Stem Cells* 35(3), pp. 572-585. doi: 10.1002/stem.2513

Terman, A. 1995. The effect of age on formation and elimination of autophagic vacuoles in mouse hepatocytes. *Gerontology* 41 Suppl 2, pp. 319-326. doi: 10.1159/000213753

Terman, A. et al. 2010. Mitochondrial turnover and aging of long-lived postmitotic cells: the mitochondrial-lysosomal axis theory of aging. *Antioxid Redox Signal* 12(4), pp. 503-535. doi: 10.1089/ars.2009.2598

Tezel, G. 2006. Oxidative stress in glaucomatous neurodegeneration: mechanisms and consequences. *Prog Retin Eye Res* 25(5), pp. 490-513. doi: 10.1016/j.preteyeres.2006.07.003

Tezel, G. 2008. TNF-alpha signaling in glaucomatous neurodegeneration. *Prog Brain Res* 173, pp. 409-421. doi: 10.1016/S0079-6123(08)01128-X

Tsubooka, N. et al. 2009. Roles of Sall4 in the generation of pluripotent stem cells from blastocysts and fibroblasts. *Genes Cells* 14(6), pp. 683-694. doi: 10.1111/j.1365-2443.2009.01301.x

Tsutsui, H. et al. 2005. Semi-rational engineering of a coral fluorescent protein into an efficient highlighter. *EMBO Rep* 6(3), pp. 233-238. doi: 10.1038/sj.embor.7400361

Twig, G. et al. 2008. Fission and selective fusion govern mitochondrial segregation and elimination by autophagy. *EMBO J* 27(2), pp. 433-446. doi: 10.1038/sj.emboj.7601963

Twig, G. et al. 2010. Biophysical properties of mitochondrial fusion events in pancreatic beta-cells and cardiac cells unravel potential control mechanisms of its selectivity. *Am J Physiol Cell Physiol* 299(2), pp. C477-487. doi: 10.1152/ajpcell.00427.2009

Twig, G. and Shirihai, O. S. 2011. The interplay between mitochondrial dynamics and mitophagy. *Antioxid Redox Signal* 14(10), pp. 1939-1951. doi: 10.1089/ars.2010.3779

Ullian, E. M. et al. 2001. Control of synapse number by glia. *Science* 291(5504), pp. 657-661. doi: 10.1126/science.291.5504.657

Van Bergen, N. J. et al. 2015. Measurement of Systemic Mitochondrial Function in Advanced Primary Open-Angle Glaucoma and Leber Hereditary Optic Neuropathy. *PLoS One* 10(10), p. e0140919. doi: 10.1371/journal.pone.0140919

Verhoeven, K. et al. 2006. MFN2 mutation distribution and genotype/phenotype correlation in Charcot-Marie-Tooth type 2. *Brain* 129(Pt 8), pp. 2093-2102. doi: 10.1093/brain/awl126

Virbasius, J. V. and Scarpulla, R. C. 1994. Activation of the human mitochondrial transcription factor A gene by nuclear respiratory factors: a potential regulatory link between nuclear and mitochondrial gene expression in organelle biogenesis. *Proc Natl Acad Sci U S A* 91(4), pp. 1309-1313.

Vohwinkel, C. U. et al. 2011. Elevated CO(2) levels cause mitochondrial dysfunction and impair cell proliferation. *J Biol Chem* 286(43), pp. 37067-37076. doi: 10.1074/jbc.M111.290056

Vos, M. et al. 2010. Synaptic mitochondria in synaptic transmission and organization of vesicle pools in health and disease. *Front Synaptic Neurosci* 2, p. 139. doi: 10.3389/fnsyn.2010.00139

Wakade, C. et al. 2015. Low-dose niacin supplementation modulates GPR109A, niacin index and ameliorates Parkinson's disease symptoms without side effects. *Clin Case Rep* 3(7), pp. 635-637. doi: 10.1002/ccr3.232

Wan, H. F. et al. 2019. Nicotinamide induces liver regeneration and improves liver function by activating SIRT1. *Mol Med Rep* 19(1), pp. 555-562. doi: 10.3892/mmr.2018.9688

Wang, B. et al. 2017. In-vivo effects of intraocular and intracranial pressures on the lamina cribrosa microstructure. *PLoS One* 12(11), p. e0188302. doi: 10.1371/journal.pone.0188302

Wang, J. T. et al. 2012. Axon degeneration: molecular mechanisms of a self-destruction pathway. *J Cell Biol* 196(1), pp. 7-18. doi: 10.1083/jcb.201108111

Wang, L. et al. 2003. Varicosities of intraretinal ganglion cell axons in human and nonhuman primates. *Invest Ophthalmol Vis Sci* 44(1), pp. 2-9.

Watson, A. B. 2014. A formula for human retinal ganglion cell receptive field density as a function of visual field location. *J Vis* 14(7), doi: 10.1167/14.7.15

Wei, Y. H. 1992. Mitochondrial DNA alterations as ageing-associated molecular events. *Mutat Res* 275(3-6), pp. 145-155. doi: 10.1016/0921-8734(92)90019-l

White, K. E. et al. 2009. OPA1 deficiency associated with increased autophagy in retinal ganglion cells in a murine model of dominant optic atrophy. *Invest Ophthalmol Vis Sci* 50(6), pp. 2567-2571. doi: 10.1167/iovs.08-2913

Williams, A. and Ramsden, D. 2005. Nicotinamide: a double edged sword. *Parkinsonism Relat Disord* 11(7), pp. 413-420. doi: 10.1016/j.parkreldis.2005.05.011

Williams, A. C. et al. 2012a. Nicotinamide, NAD(P)(H), and Methyl-Group Homeostasis Evolved and Became a Determinant of Ageing Diseases: Hypotheses and Lessons from Pellagra. *Curr Gerontol Geriatr Res* 2012, p. 302875. doi: 10.1155/2012/302875

Williams, P. A. et al. 2017. Vitamin B3 modulates mitochondrial vulnerability and prevents glaucoma in aged mice. *Science* 355(6326), pp. 756-760. doi: 10.1126/science.aal0092

Williams, P. A. et al. 2010. Opa1 deficiency in a mouse model of dominant optic atrophy leads

to retinal ganglion cell dendropathy. *Brain* 133(10), pp. 2942-2951. doi: 10.1093/brain/awq218

Williams, P. A. et al. 2012b. Opa1 is essential for retinal ganglion cell synaptic architecture and connectivity. *Brain* 135(Pt 2), pp. 493-505. doi: 10.1093/brain/awr330

Winzeler, A. and Wang, J. T. 2013. Purification and culture of retinal ganglion cells from rodents. *Cold Spring Harb Protoc* 2013(7), pp. 643-652. doi: 10.1101/pdb.prot074906

Wollweber, F. et al. 2017. Mitochondrial contact site and cristae organizing system: A central player in membrane shaping and crosstalk. *Biochim Biophys Acta Mol Cell Res* 1864(9), pp. 1481-1489. doi: 10.1016/j.bbamcr.2017.05.004

Wu, Z. et al. 1999. Transcriptional activation of adipogenesis. *Curr Opin Cell Biol* 11(6), pp. 689-694.

Yarosh, W. et al. 2008. The molecular mechanisms of OPA1-mediated optic atrophy in Drosophila model and prospects for antioxidant treatment. *PLoS Genet* 4(1), p. e6. doi: 10.1371/journal.pgen.0040006

Yoon, Y. et al. 2003. The mitochondrial protein hFis1 regulates mitochondrial fission in mammalian cells through an interaction with the dynamin-like protein DLP1. *Mol Cell Biol* 23(15), pp. 5409-5420.

Youle, R. J. and van der Bliek, A. M. 2012. Mitochondrial fission, fusion, and stress. *Science* 337(6098), pp. 1062-1065. doi: 10.1126/science.1219855

Yu, D.-Y. et al. 2014. Retinal energetics: its critical role in retinal physiology and pathology. *Expert Review of Ophthalmology* 6(4), pp. 395-399. doi: 10.1586/eop.11.44

Yu, J. et al. 2007. Induced pluripotent stem cell lines derived from human somatic cells. *Science* 318(5858), pp. 1917-1920. doi: 10.1126/science.1151526

Yu-Wai-Man, P. et al. 2011a. Pattern of retinal ganglion cell loss in dominant optic atrophy due to OPA1 mutations. *Eye (Lond)* 25(5), pp. 596-602. doi: 10.1038/eye.2011.2

Yu-Wai-Man, P. et al. 2009a. Secondary mtDNA defects do not cause optic nerve dysfunction in a mouse model of dominant optic atrophy. *Invest Ophthalmol Vis Sci* 50(10), pp. 4561-4566. doi: 10.1167/iovs.09-3634

Yu-Wai-Man, P. et al. 2010a. The prevalence and natural history of dominant optic atrophy due to OPA1 mutations. *Ophthalmology* 117(8), pp. 1538-1546, 1546 e1531. doi: 10.1016/j.ophtha.2009.12.038

Yu-Wai-Man, P. et al. 2011b. Mitochondrial optic neuropathies - disease mechanisms and therapeutic strategies. *Prog Retin Eye Res* 30(2), pp. 81-114. doi: 10.1016/j.preteyeres.2010.11.002

Yu-Wai-Man, P. et al. 2009b. Inherited mitochondrial optic neuropathies. *J Med Genet* 46(3), pp. 145-158. doi: 10.1136/jmg.2007.054270

Yu-Wai-Man, P. and Newman, N. J. 2017. Inherited eye-related disorders due to mitochondrial dysfunction. *Hum Mol Genet* 26(R1), pp. R12-R20. doi: 10.1093/hmg/ddx182

Yu-Wai-Man, P. et al. 2010b. OPA1 increases the risk of normal but not high tension glaucoma. *J Med Genet* 47(2), pp. 120-125. doi: 10.1136/jmg.2009.067512

Yu-Wai-Man, P. et al. 2016. A neurodegenerative perspective on mitochondrial optic neuropathies. *Acta Neuropathol* 132(6), pp. 789-806. doi: 10.1007/s00401-016-1625-2

Yu-Wai-Man, P. et al. 2014. Treatment strategies for inherited optic neuropathies: past, present and future. *Eye (Lond)* 28(5), pp. 521-537. doi: 10.1038/eye.2014.37

Zanna, C. et al. 2008. OPA1 mutations associated with dominant optic atrophy impair oxidative phosphorylation and mitochondrial fusion. *Brain* 131(Pt 2), pp. 352-367. doi: 10.1093/brain/awm335

Zhang, J. et al. 2017. A novel ADOA-associated OPA1 mutation alters the mitochondrial function, membrane potential, ROS production and apoptosis. *Sci Rep* 7(1), p. 5704. doi: 10.1038/s41598-017-05571-y

Zhao, N. et al. 2015. Mfn2 Affects Embryo Development via Mitochondrial Dysfunction and Apoptosis. *PLoS One* 10(5), p. e0125680. doi: 10.1371/journal.pone.0125680

Zhu, Y. et al. 2013. Protection of mouse retinal ganglion cell axons and soma from glaucomatous and ischemic injury by cytoplasmic overexpression of Nmnat1. *Invest Ophthalmol Vis Sci* 54(1), pp. 25-36. doi: 10.1167/iovs.12-10861

Appendix I

Major retinal cell types and a selection of the antibodies used to visualize them

Cell Type	***Layer***	***Antigen***	***Description of antigen***	***Antibody (Example)***
Glial cells: 1). **Muller Cells** (90% of glial cells in retina) 2). **Astrocytes** (Microglia, oligodendrocytes)	Muller cell bodies – inner nuclear layer (INL), across the entire retina. Astrocytes – originate in the optic nerve head and subsequently migrate to nerve fibre layer (NFL) & GCL.	Vimentin	An intermediate filament protein, A cytoskeleton marker.	Rabbit Anti-Vimentin Antibody (Abcam, ab92547)
		GFAP (glial fibrillary acidic protein)	An intermediate filament protein, widely used, expressed in both Muller cells and astrocytes.	Rabbit Anti-GFAP Antibody (Abcam, ab7260)
		GS (glutamine synthetase)	An enzyme involved in glutamate metabolism, selectively to Muller cells.	Rabbit Anti-Glutamine Synthetase Antibody Abcam, Ab49873)
RGC	GCL	Thy-1	Surface glycoprotein.	Rat Anti-CD90/Thy1 antibody (Abcam, ab3105)
		Brn3a	Transcription factor, a specific nuclear epitope.	Mouse Anti-Brn-3a Antibody (Santa Cruz, sc8429)
		RBPMS	a conserved RNA binding protein with a single RNA recognition motif (RRM) – abundantly expressed in both nucleus and cytoplasm	Rabbit Anti-RBPMS Antibody (Abcam, ab194213)
		b-III tubulin	Involved in forming microtubule of cytoskeleton.	Rabbit Anti-Beta III Tubulin Antibody (Abcam, ab18207)
Amacrine cells	INL; displaced in GCL	Syntaxin-1 (HPC-1, an integral membrane protein)	Enriched in the membrane of amacrine cells.	Mouse Anti-Syntaxin 1 Antibody (Santa Cruz, Sc-12736)
Bipolar cells	INL	Chx10 (Pan-bipolar cell marker)	Expressed in the somas and terminals of bipolar cells.	Sheep Anti-CHX10 Antibody (Abcam, ab16141)

		PKCα (Protein kinase Cα, rod bipolar cell marker)	A protein kinase expressed in the somas, dendrites and axon terminals of rod bipolar cells.	Rabbit anti-PKCα Antibody (Abcam, ab32376)
Horizontal cells	INL	Calbindin	Expressed in the entire cell: soma, processes, and endings. Calbindin also labels a subset of bipolar cells.	Mouse monoclonal Antibody against calbindin-28K (Sigma, C9848)
Photoreceptors (mouse retina: rod-dominated, cones constitute 1-3%)	ONL & photoreceptor layer	Recoverin (cones and rods)	General photoreceptor marker.	Rabbit Anti-Recoverin Antibody (Merck Millipore, AB5585)
		Rhodopsin (rods)	Enriched in the rod cell body membrane, specific rod-OS marker	Mouse Anti-Rhodopsin Antibody (Abcam, ab5417)
		CAR (cones, cone arrestin)	Enriched in cone photoreceptor inner segments and somata.	Rabbit anti-Cone Arrestin Antibody (Merk Millipore, AB15282
		RXRγ (cones,retinoid X receptor gamma)	A nulear receptor, expressed specifically in cone nuclei.	Mouse RXRγ Antibody (G-6) (Santa Cruz, Sc-5141434)

(Table summarised from Lorber et al. 2002; Quina et al. 2005; Tian and Yang 2006; Kwong et al. 2010; Lakowski et al. 2010; Hirano et al. 2011; Szabadfi et al. 2015; Gao et al. 2016; Reinehr et al. 2018)

Appendix II Dissociated retinal cell culture from mice

Dissociated retinal cell culture was performed as a pilot trial for retinal cells culture from adult mice (two to four months old, one retina per well of 4-well slide chamber in culture) before two-step immunopanning based on the protocol from Ann Logan's lab, University of Birmingham (Lorber et al. 2005; Suggate et al. 2009) using Papain dissociation kit (Worthington Biochemical, USA).

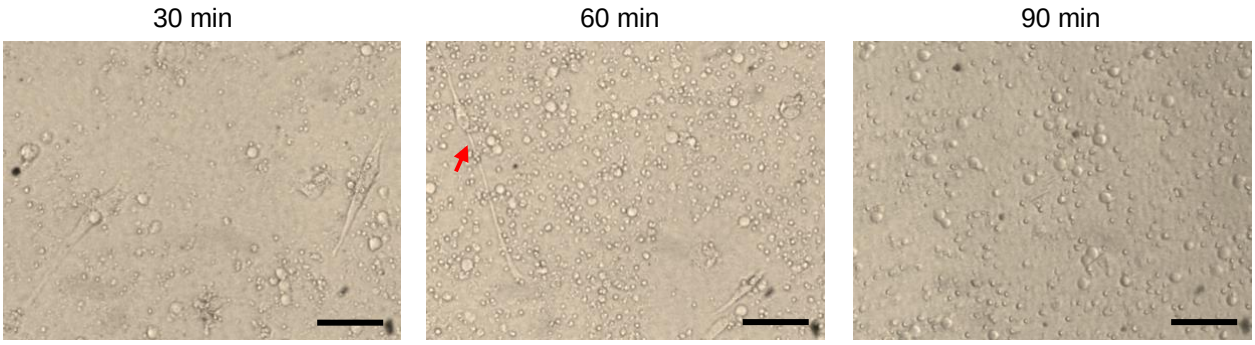

Figure x1 Dissociated retinal cell suspension by papain after two days in culture. Three different time durations of retina incubation with papain were tried for cell suspension: 30 minutes, 60 minutes and 90 minutes. In conditions of 30 minutes' and 60 minutes' papain incubation, the average numbers of cells with processes counted from 5 randomly chosen areas were 1.4 ± 0.55 and 2.2 ± 0.84 (shown as mean ± SD) respectively under a phase contrast microscope. No cells with processes under the condition of 90 minutes' incubation was observed. The culture with 60-minutes' papain incubation, showed dissociated cells with longest processes (red arrow), was chosen for RBPMS staining (a specific RGC marker). Scale bar = 50 μm.

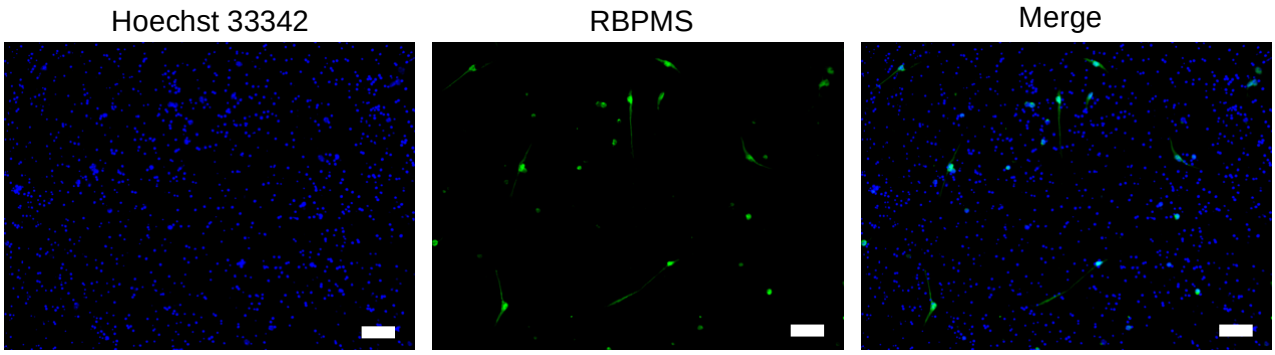

Figure x2 Harvest of RBPMS-positive cells from dissociated retinal cell culture after seven days in culture. The harvest was shown as a percentage of RBPMS-positive cells compared to the total number of cells counted from five randomly chosen fields. Three independent experiments were performed. One retina was dissociated in one well of 4-well chamber slide (1.7 cm^2). The harvest of RGCs from one retina was 2.48%, 1.65% and 2.01% respectively from three independent dissociation. Scale bar = 50 μm.

Appendix III

Supplementary data for Chapter 3

1. Supplementary kymograghs from 10 minutes of mitochondrial time-lapse imaging from WT and *Opa1*$^{+/-}$ RGC cultures.

WT:

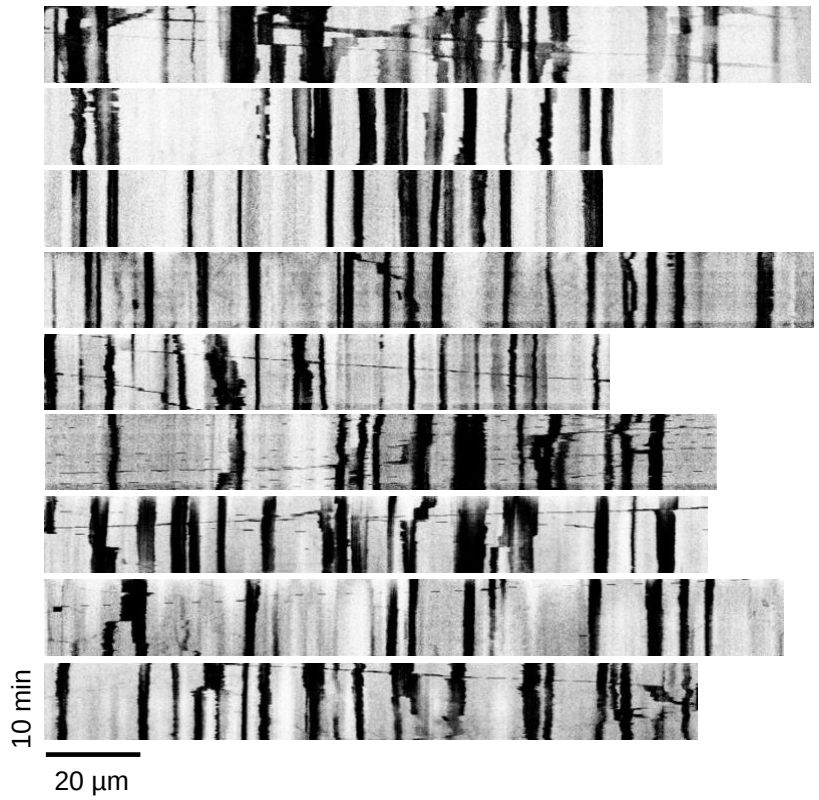

Opa1$^{+/-}$:

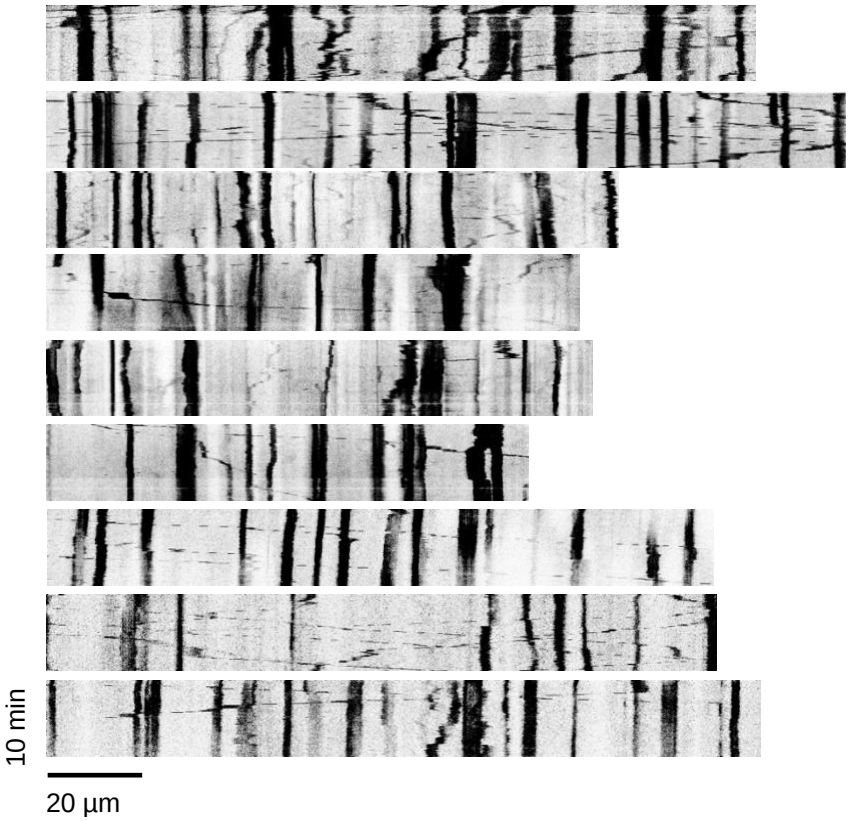

Figure S31 Kymographs from WT and *Opa1*$^{+/-}$ RGC cultures, n=9 neurites in both conditions from 3 independent cultures. Scale bar = 20 µm.

2. The mitochondrial coverage of neurites (100%) was calculated as the percentage of total mitochondrial length along the neurite divided by the length of the neurite, as measured at frames 1, 30, 60, 90 and 120 (0 min, 2.5 min, 5 min, 7.5 min and 10 min) to determine whether laser scanning through LSM880 confocal microscopy damaged the mitochondria within the 10-minute time-lapse imaging.

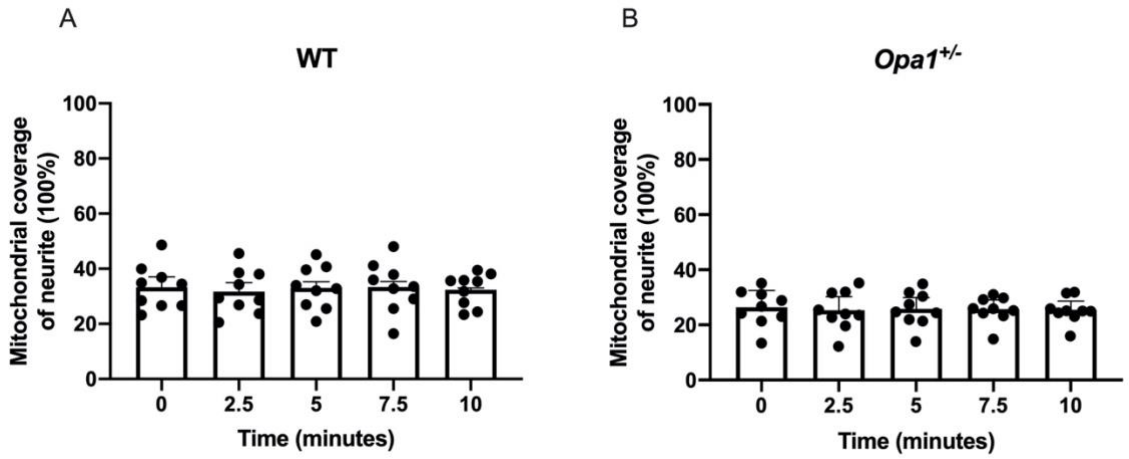

Figure S32 No significant difference was found in the mitochondrial coverage of neurites during the 10-minute time-lapse imaging through confocal microscopy in WT and *Opa1*$^{+/-}$ cultures. The mitochondrial coverage in the neurite was calculated as the percentage of total mitochondrial length along the neurite divided by the length of neurite from 3 independent cultures, n=9 neurites from WT (A) and *Opa1*$^{+/-}$ cultures (B) at image frames 1, 30, 60, 90 and 120 (0 min, 2.5 min, 5 min, 7.5 min and 10 min). All the results are from 3 independent cultures, data shown as mean ± SD, N=3.

3. The mitochondrial coverage of neurites (100%) from WT and *Opa1*$^{+/-}$ cultures were also compared at frames 1, 30, 60, 90 and 120 (0 min, 2.5 min, 5 min, 7.5 min and 10 min), respectively.

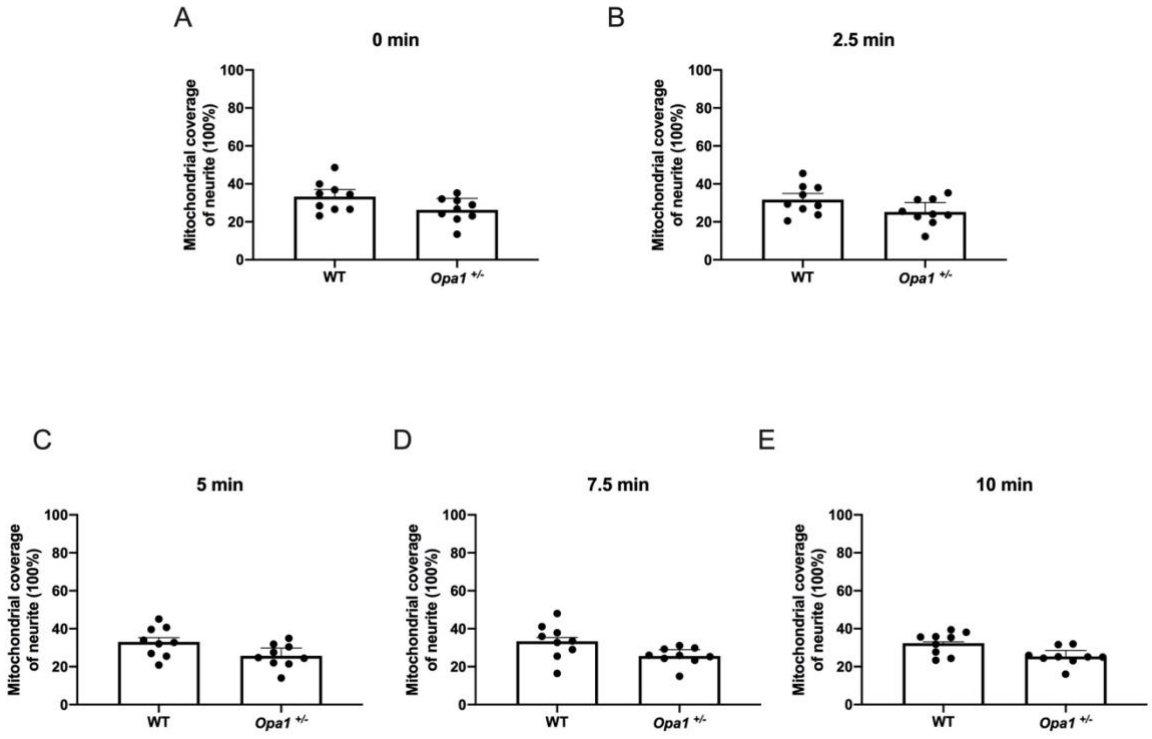

Figure S33 No significant difference was found on mitochondrial coverage of neurite (100%) between WT and *Opa1*$^{+/-}$ cultures. (A, B, C, D, E) n=9 neurites in WT and *Opa1*$^{+/-}$ RGCs at image frames 1, 30, 60, 90 and 120 (0 min, 2.5 min, 5 min, 7.5 min and 10 min), respectively. All the results are from 3 independent cultures, data shown as mean ± SD, N=3.

4. Supplementary data of mitochondrial velocity and length in WT and *Opa1*$^{+/-}$ RGC cultures.

WT

A

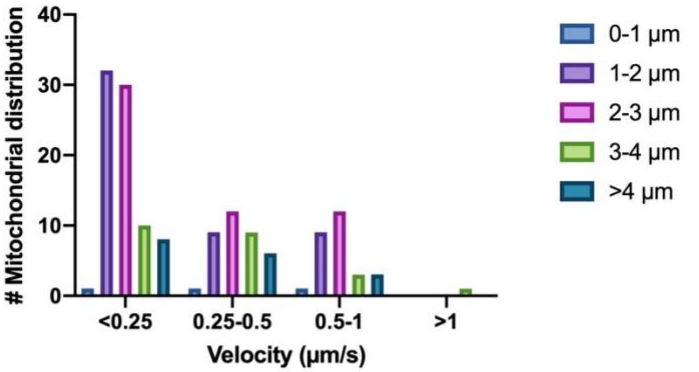
Mitochondrial distribution
40
30
20
10
0
<0.25
0.25-0.5
0.5-1
>1
Velocity (µm/s)
0-1 µm
1-2 µm
2-3 µm
3-4 µm
>4 µm

B

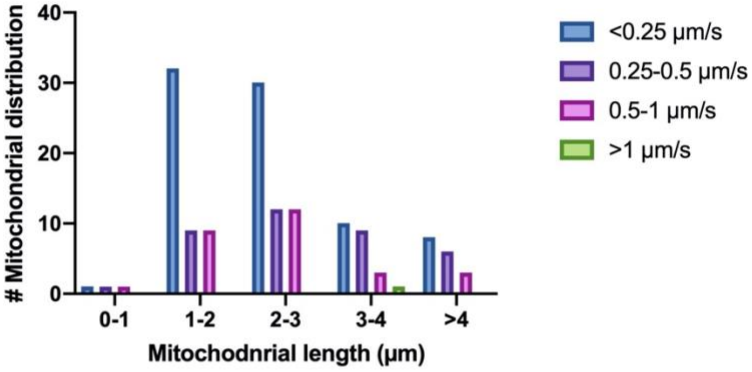
Mitochondrial distribution
40
30
20
10
0
0-1
1-2
2-3
3-4
>4
Mitochodnrial length (µm)
<0.25 µm/s
0.25-0.5 µm/s
0.5-1 µm/s
>1 µm/s

***Opa1*$^{+/-}$**

C

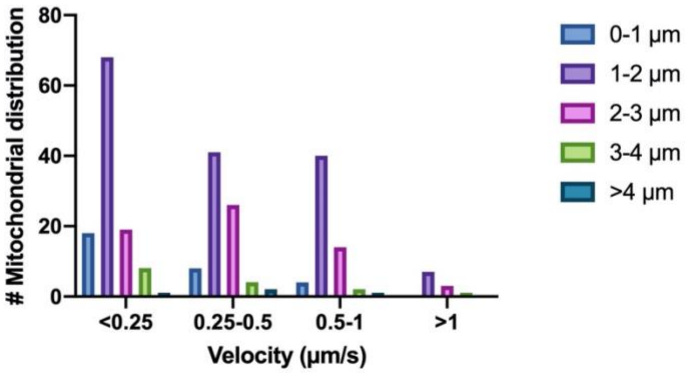
Mitochondrial distribution
80
60
40
20
0
<0.25
0.25-0.5
0.5-1
>1
Velocity (µm/s)
0-1 µm
1-2 µm
2-3 µm
3-4 µm
>4 µm

D

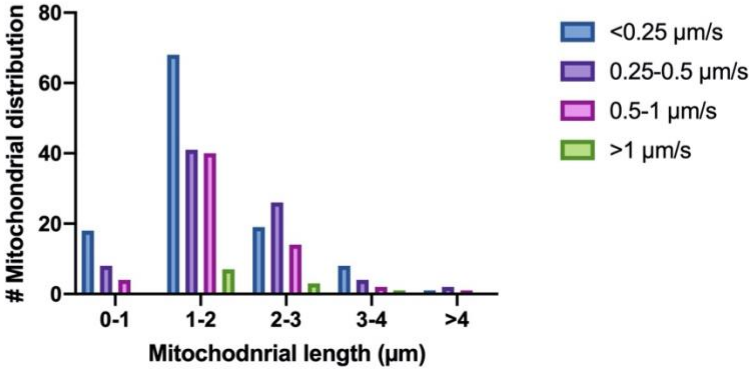
Mitochondrial distribution
80
60
40
20
0
0-1
1-2
2-3
3-4
>4
Mitochodnrial length (µm)
<0.25 µm/s
0.25-0.5 µm/s
0.5-1 µm/s
>1 µm/s

Figure S34 Supplementary histograms of distribution of mitochondrial velocity and length in WT and *Opa1*$^{+/-}$ cultures. (A) Distribution of mitochondrial velocity with length ranged between 0-1 µm (n=4), 1-2 µm (n=50), 2-3 µm (n=54), 3-4 µm (n=23), and >4 µm (n=17) in WT RGCs from 3 independent cultures. (B) Distribution of mitochondrial length with velocity ranged between 0-0.25 µm/s (n=81), 0.25-0.5 µm/s (n=37), 0.5-1 µm/s (n=28) and >1 µm/s (n=1) in WT RGCs from 3 independent cultures. (C) Distribution of mitochondrial velocity with length ranged between 0-1 µm (n=30), 1-2 µm (n=156), 2-3 µm (n=62), 3-4 µm (n=15), and >4 µm (n=4) in *Opa1*$^{+/-}$ RGCs from 3 independent culture. (D) Distribution of mitochondrial length with velocity ranged between 0-0.25 µm/s (n=114), 0.25-0.5 µm/s (n=81), 0.5-1 µm/s (n=61) and >1 µm/s (n=11) in *Opa1*$^{+/-}$ RGCs from 3 independent cultures.

Appendix IV

Supplementary data for Chapter 4

1. Supplementary kymograghs from 10 minutes of mitochondrial time-lapse imaging from Control (CT) and hypertension cultures.

CT:

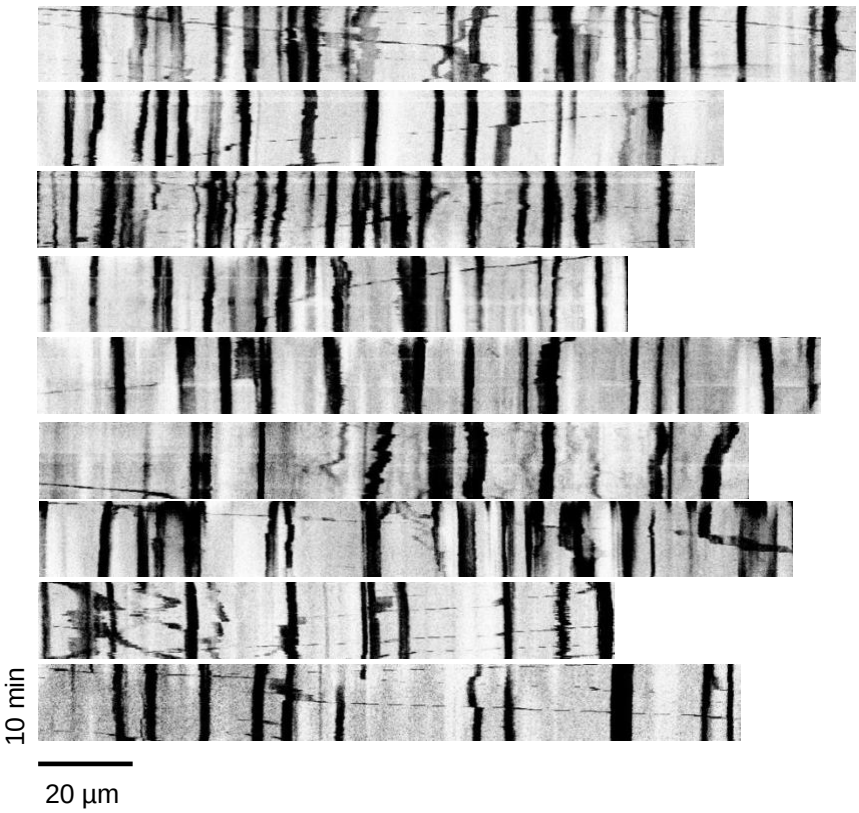

Hypertension:

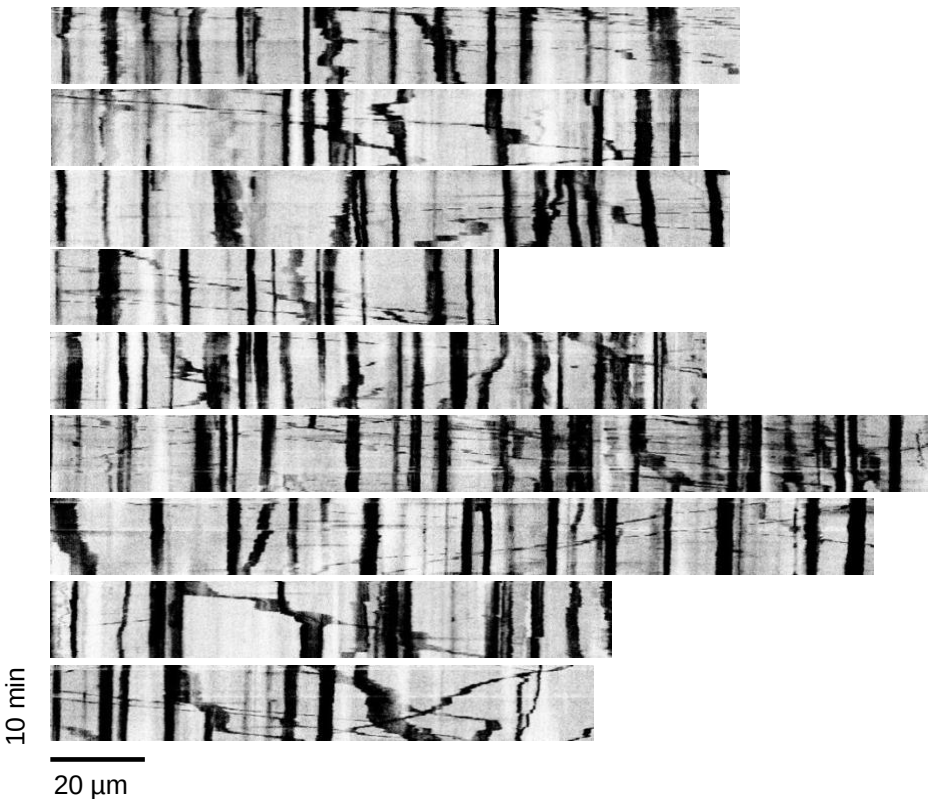

Figure S41 Kymographs from CT and hypertension RGC cultures, n=9 neurites in both conditions from 3 independent cultures. Scale bar = 20 µm.

2. The mitochondrial coverage of neurites (100%) was measured as the percentage of total mitochondrial length along the neurite divided by the length of the neurite at frames 1, 30, 60, 90 and 120 (0 min, 2.5 min, 5 min, 7.5 min and 10 min) to determine whether laser scanning through LSM880 confocal microscopy damaged the mitochondria within in the 10-minute time-lapse imaging.

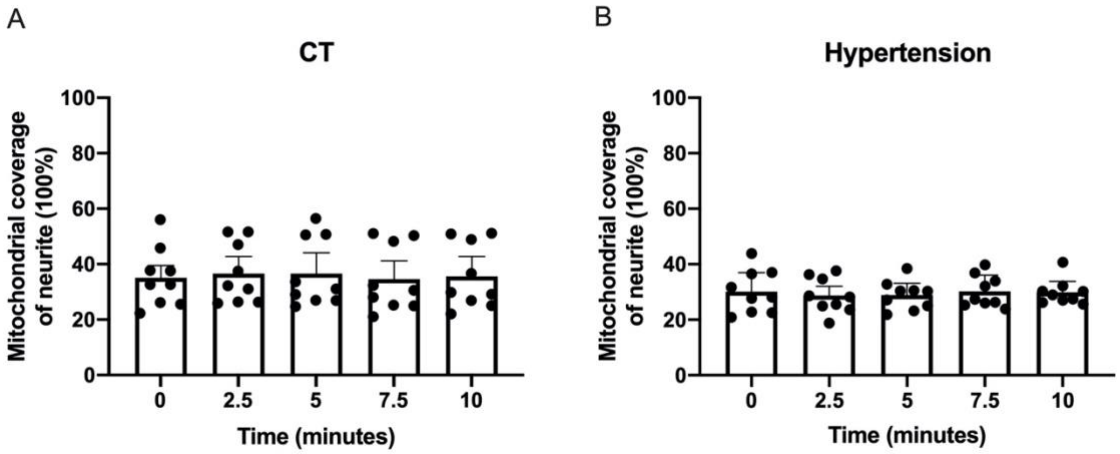

Figure S42 No significant difference was found in the mitochondrial coverage of neurites during the 10-minute time-lapse imaging through confocal microscope in control (CT) and hypertension cultures. The mitochondrial coverage in the neurite was calculated as the percentage of total mitochondrial length along the neurite divided by the length of neurite from 3 independent cultures, n=9 neurites from CT (A) and hypertension cultures (B) at image frames 1, 30, 60, 90 and 120 (0 min, 2.5 min, 5 min, 7.5 min and 10 min). All the results are from 3 independent cultures, data shown as mean ± SD, N=3.

3. The mitochondrial coverage of neurites (100%) from control and hypertension cultures were also compared at frames 1, 30, 60, 90 and 120 (0 min, 2.5 min, 5 min, 7.5 min and 10 min), respectively.

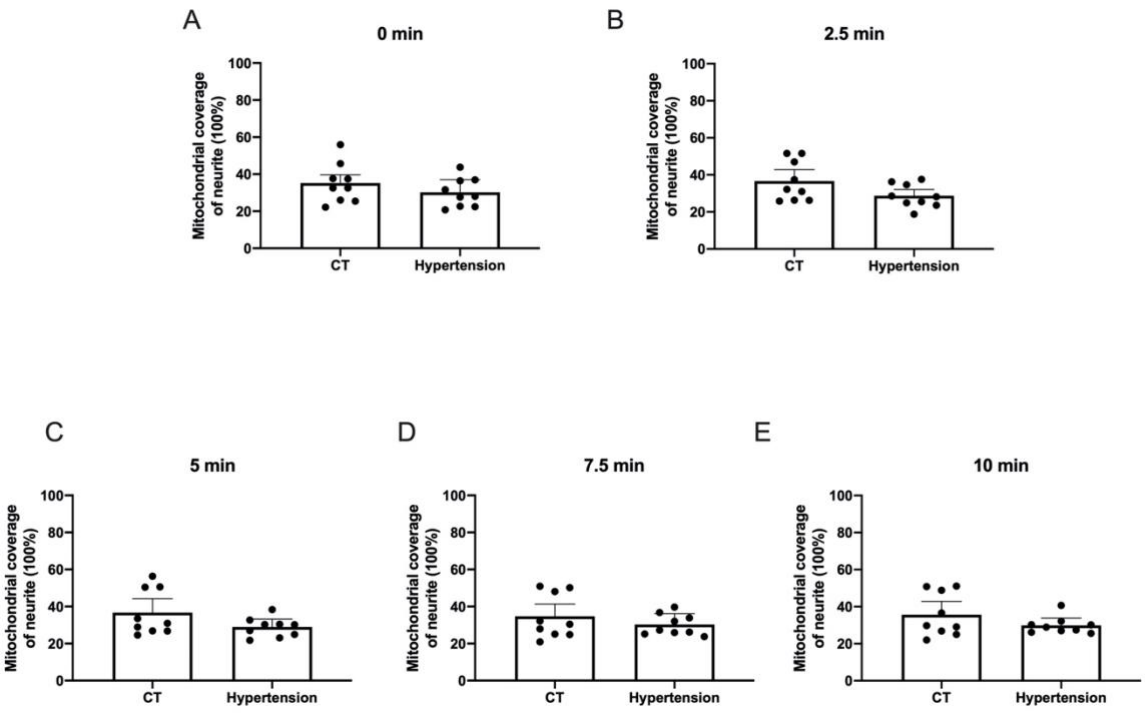

Figure S43 No significant difference was found on the mitochondrial coverage of neurite (100%) between CT and hypertension cultures. (A, B, C, D, E) n=9 neurites in CT and hypertension cultures at image frames 1, 30, 60, 90 and 120 (0 min, 2.5 min, 5 min, 7.5 min and 10 min), respectively. All the results are from 3 independent cultures, data shown as mean ± SD, N=3.

4. Supplementary data of mitochondrial velocity and length in cultures under normal and hypertensive stress.

CT

A

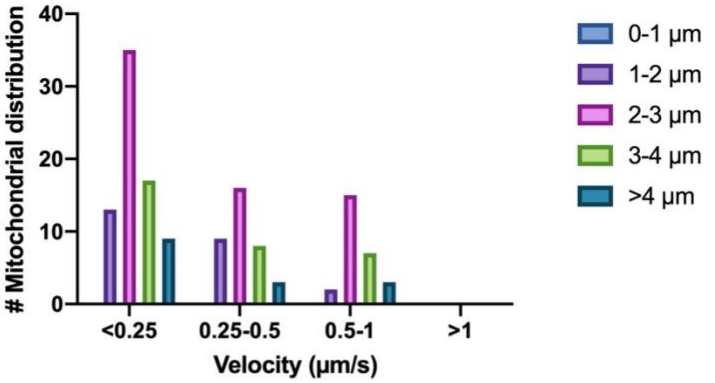

B

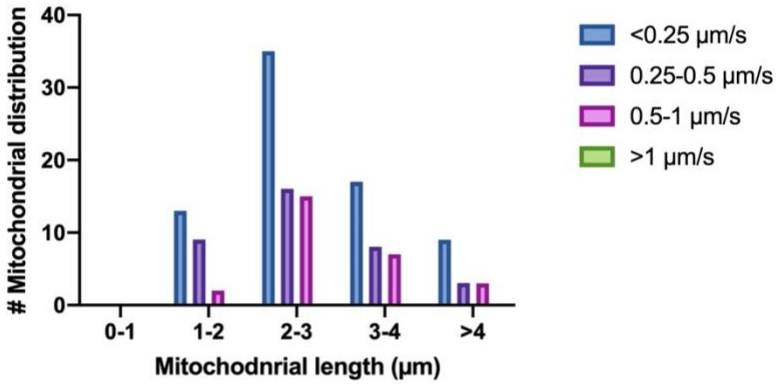

Hypertension

C

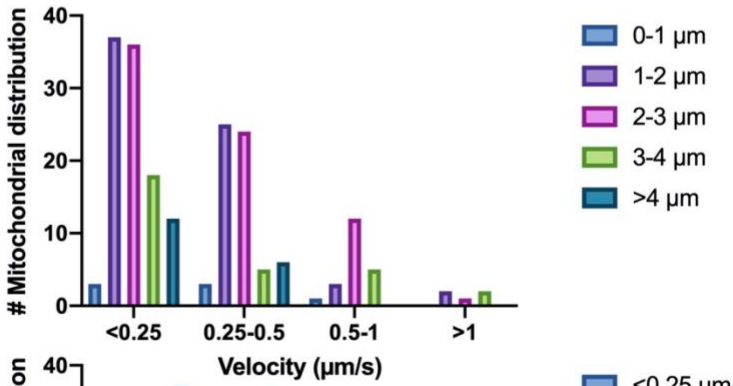

D

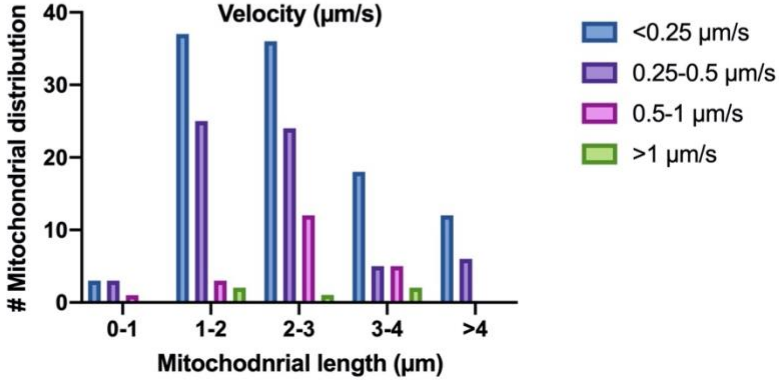

Figure S44 Supplementary histograms of distribution of mitochondrial velocity and length in RGCs under control and hypertensive conditions. (A) Distribution of mitochondrial velocity with length ranged between 0-1 µm (n=0), 1-2 µm (n=24), 2-3 µm (n=66), 3-4 µm (n=32), and >4 µm (n=15) in RGCs under normal condition from 3 independent cultures. (B) Distribution of mitochondrial length with velocity ranged between 0-0.25 µm/s (n=74), 0.25-0.5 µm/s (n=36), 0.5-1 µm/s (n=27) and >1 µm/s (n=0) in RGCs under normal condition from 3 independent cultures. (C) Distribution of mitochondrial velocity with length ranged between 0-1 µm (n=7), 1-2 µm (n=67), 2-3 µm (n=73), 3-4 µm (n=30), and >4 µm (n=18) in RGCs under hypertensive stress from 3 independent cultures. (D) Distribution of mitochondrial length with velocity ranged between 0-0.25 µm/s (n=106), 0.25-0.5 µm/s (n=63), 0.5-1 µm/s (n=21) and >1 µm/s (n=5) in RGCs under hypertensive stress from 3 independent cultures.

Appendix V

Supplementary data for Chapter 5

1. Kymograghs from mitochondrial time-lapse imaging from control and nicotinamide-treated conditions. N=9 neurites in each condition from 3 independent cultures.

Control:

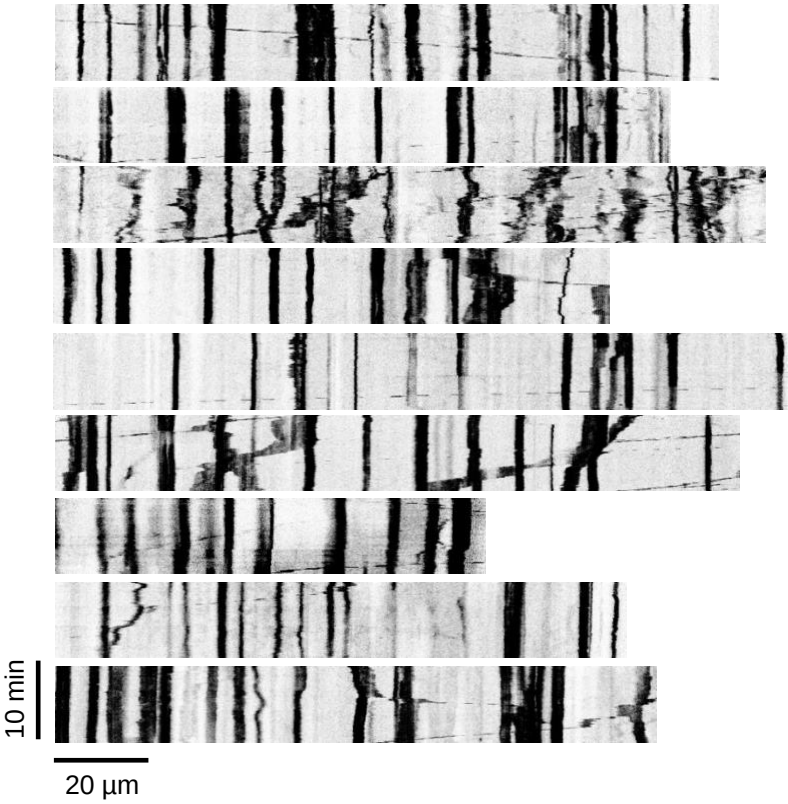

50 µM nicotinamide:

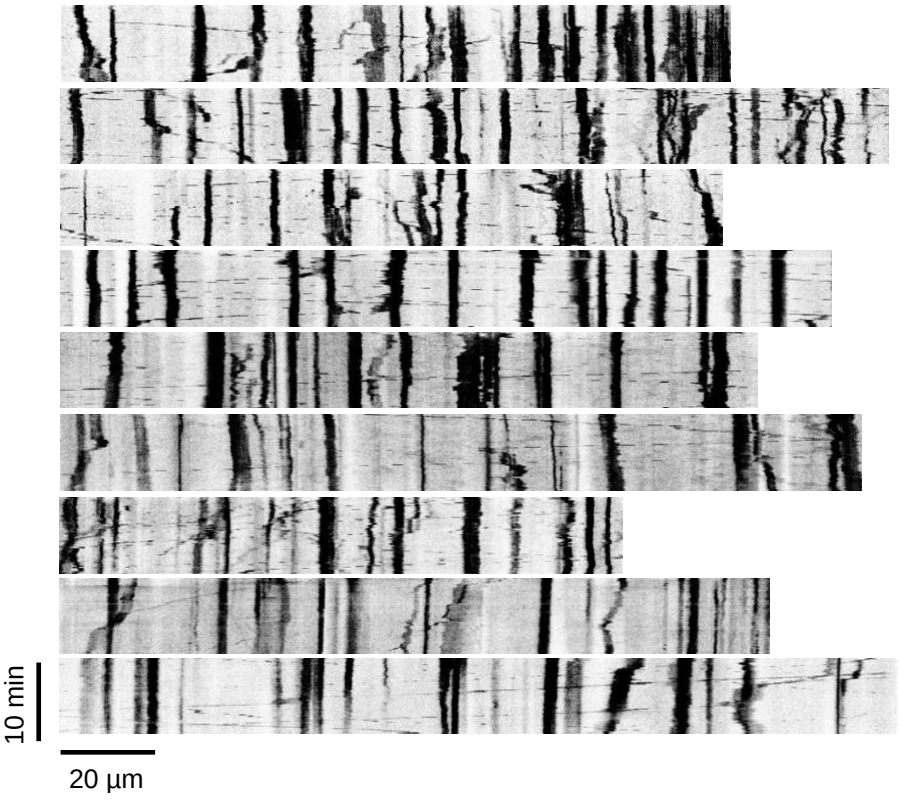

100 µM nicotinamide:

500 µM nicotinamide:

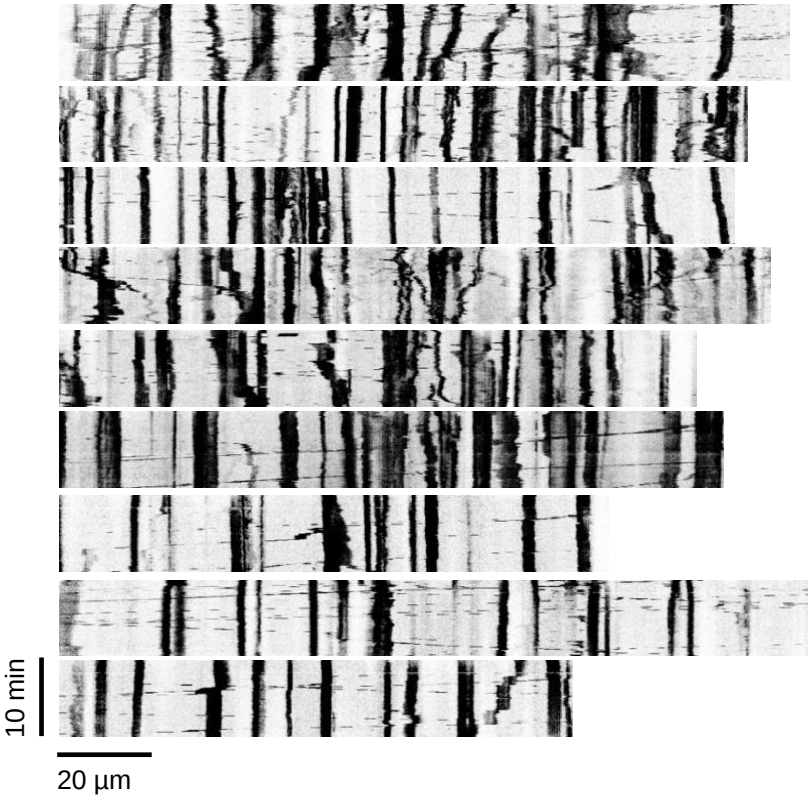

1 mM nicotinamide:

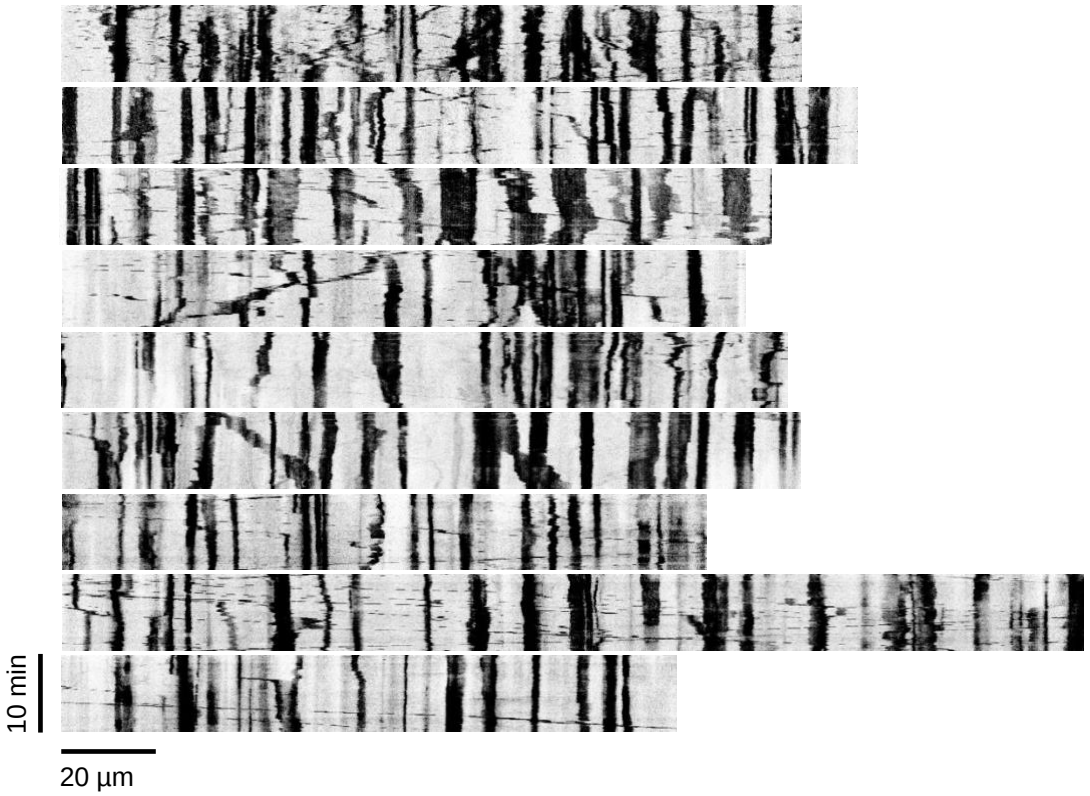

Figure S51 Kymographs from control and nicotinamide-treated groups (50 µM, 100, 500, 1 mM), n=9 neurites treated with each concentration from 3 independent cultures. Scale bar=20 µm.

2. In order to determine whether the laser scanning through LSM880 confocal microscopy affect the mitochondrial length within in 10-minute time-lapse imaging, the length of mitochondria was measured at image frames 1, 30, 60, 90 and 120 (0 min, 2.5 min, 5 min, 7.5 min and 10 min).

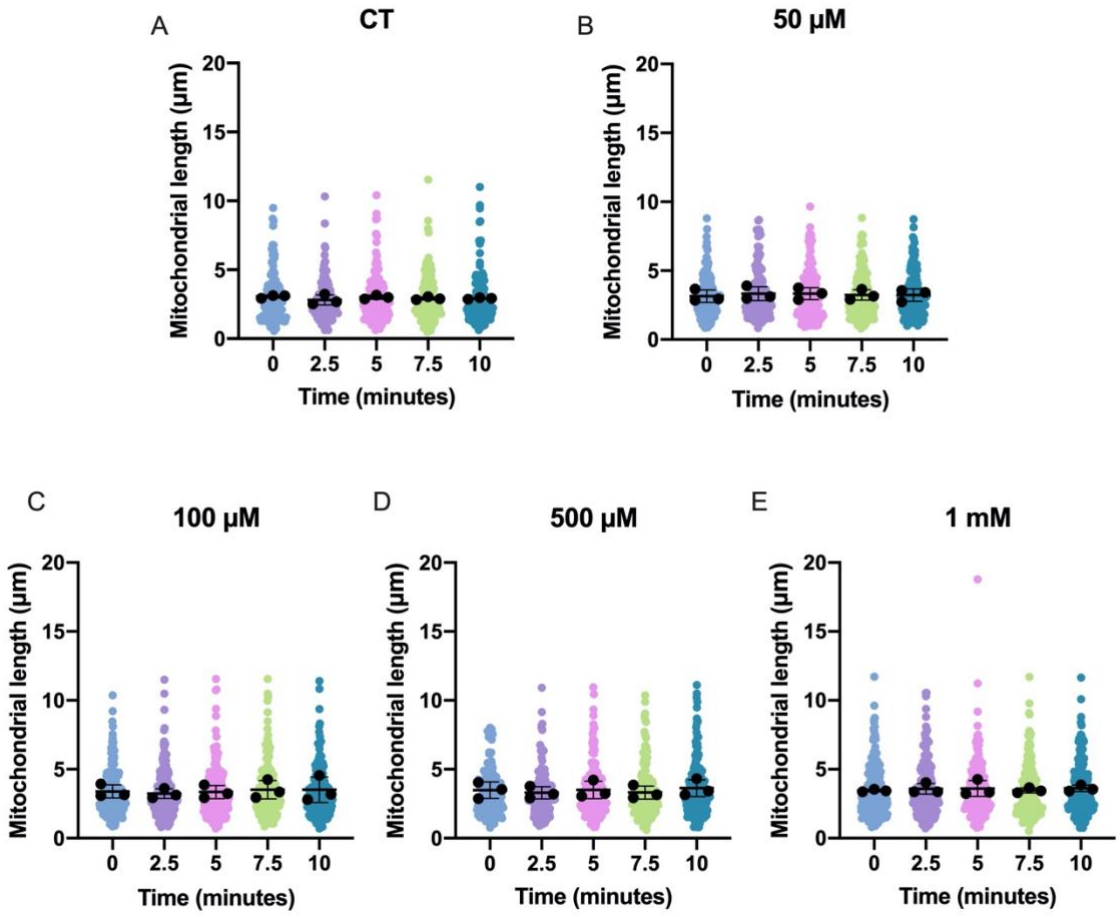

Figure S52 No significant difference was found on the length of mitochondria during the 10-minute time-lapse imaging through confocal microscope. The length of mitochondria was captured using a Zeiss LSM 880 confocal microscope by time-lapse imaging with 5-seconds' interval for 10 minutes. The length of mitochondria were measured manually by FIJI software at frames 1, 30, 60, 90 and 120 (0 min, 2.5 min, 5 min, 7.5 min and 10 min). (A; n=665 mitochondria in control group. B; n=804 mitochondria in 50 µM nicotinamide-treated group. C; n=1035 mitochondria in 100 µM nicotinamide-treated group. D; n=842 mitochondria in 500 µM nicotinamide-treated group. E; n=973 mitochondria in 1 mM nicotinamide-treated group from 3 independent cultures for all conditions). Data shown as mean ± SD, N=3.

3. The mitochondrial coverage of neurite (100%) was also calculated at frames 1, 30, 60, 90 and 120 (0 min, 2.5 min, 5 min, 7.5 min and 10 min) to determine whether the laser scanning through LSM880 confocal microscopy damage the mitochondria within in 10-minute time-lapse imaging.

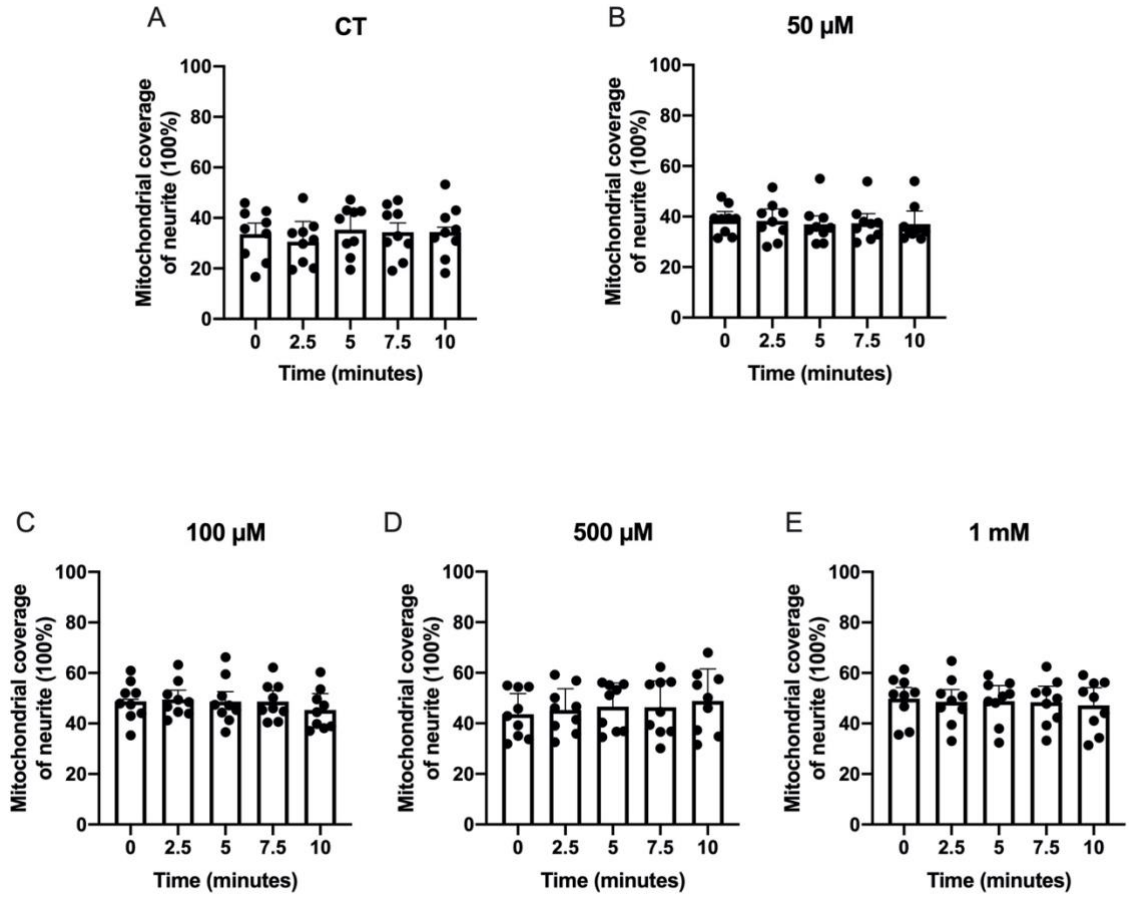

Figure S53 No significant difference was found on the mitochondrial coverage of neurite during the 10-minute time-lapse imaging through confocal microscope in each of control and nicotinamide-treated groups. The mitochondrial coverage in the neurite was calculated as the percentage of total mitochondrial length along the neurite divided by the length of neurite from 3 independent cultures, n=9 neurites from each of control (A) and nicotinamide-treated groups (B; 50 µM nicotinamide. C; 100 µM nicotinamide. D; 500 µM nicotinamide. E; 1 mM nicotinamide) at image frames 1, 30, 60, 90 and 120 (0 min, 2.5 min, 5 min, 7.5 min and 10 min). Data shown as mean ± SD, N=3.

4. Supplementary data of mitochondrial velocity and length in each of the control and nicotinamide-treated RGC cultures.

CT

A

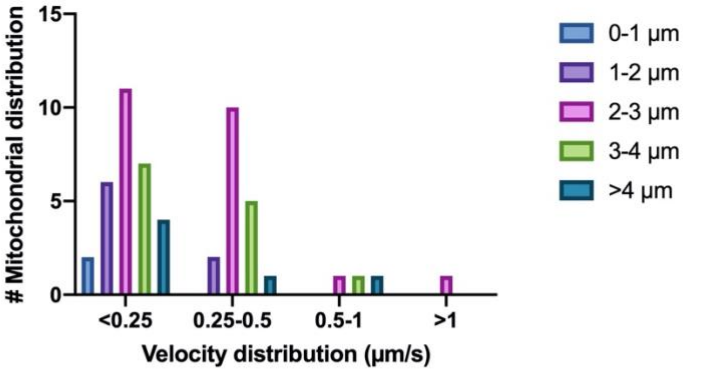
Mitochondrial distribution
15
10
5
0
<0.25
0.25-0.5
0.5-1
>1
Velocity distribution (µm/s)
0-1 µm
1-2 µm
2-3 µm
3-4 µm
>4 µm

B

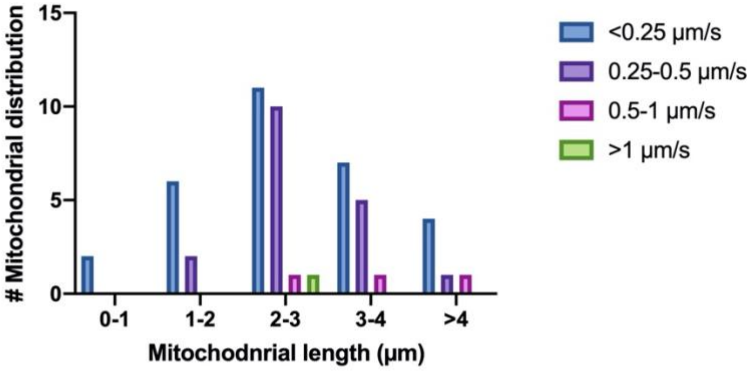
Mitochondrial distribution
15
10
5
0
0-1
1-2
2-3
3-4
>4
Mitochodnrial length (µm)
<0.25 µm/s
0.25-0.5 µm/s
0.5-1 µm/s
>1 µm/s

50 µM

C

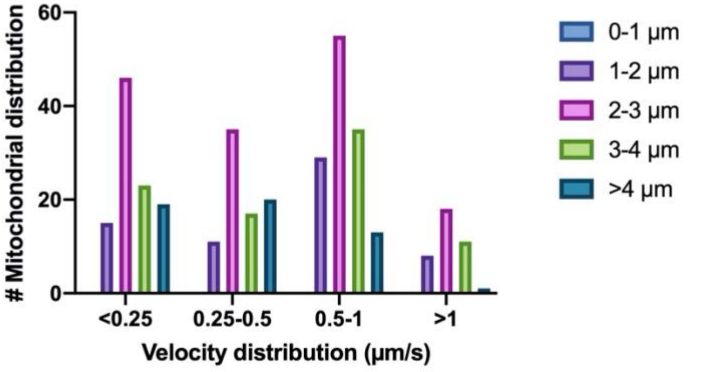
Mitochondrial distribution
60
40
20
0
<0.25
0.25-0.5
0.5-1
>1
Velocity distribution (µm/s)
0-1 µm
1-2 µm
2-3 µm
3-4 µm
>4 µm

D

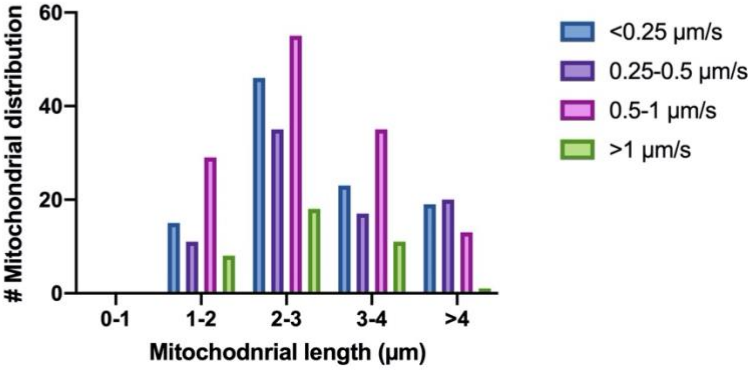
Mitochondrial distribution
60
40
20
0
0-1
1-2
2-3
3-4
>4
Mitochodnrial length (µm)
<0.25 µm/s
0.25-0.5 µm/s
0.5-1 µm/s
>1 µm/s

100 µM

E

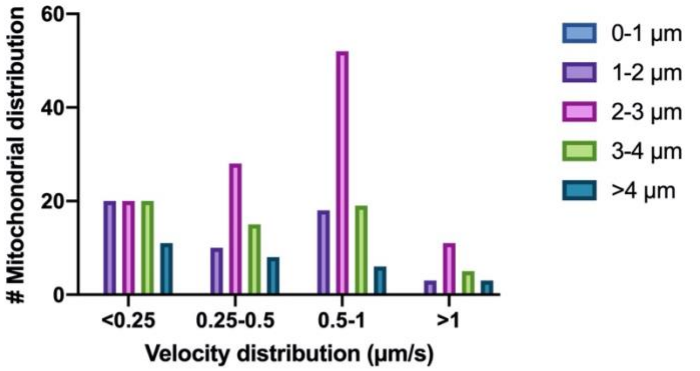

F

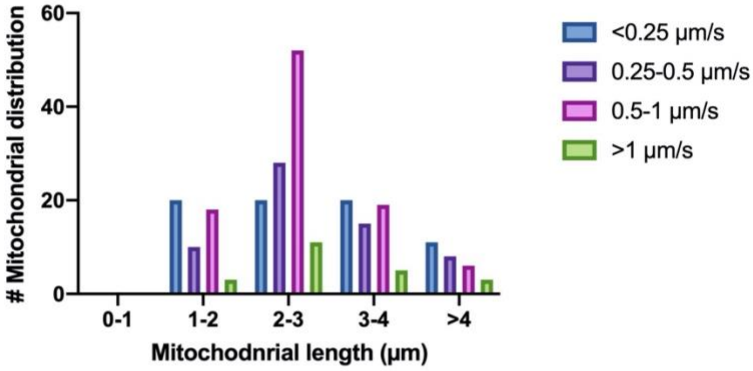

500 µM

G

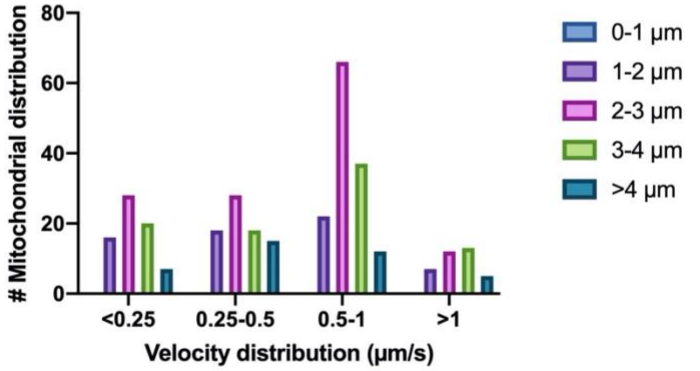

H

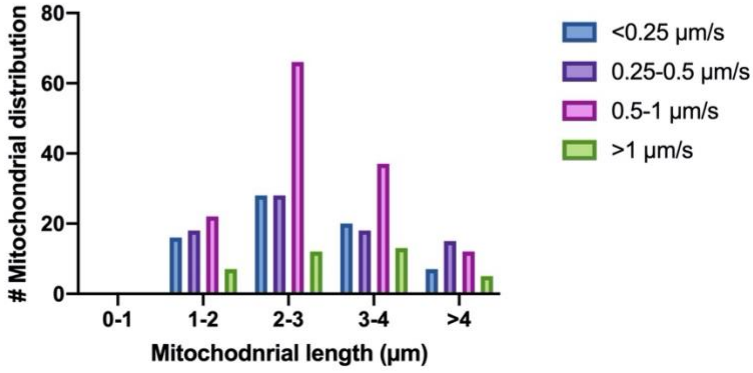

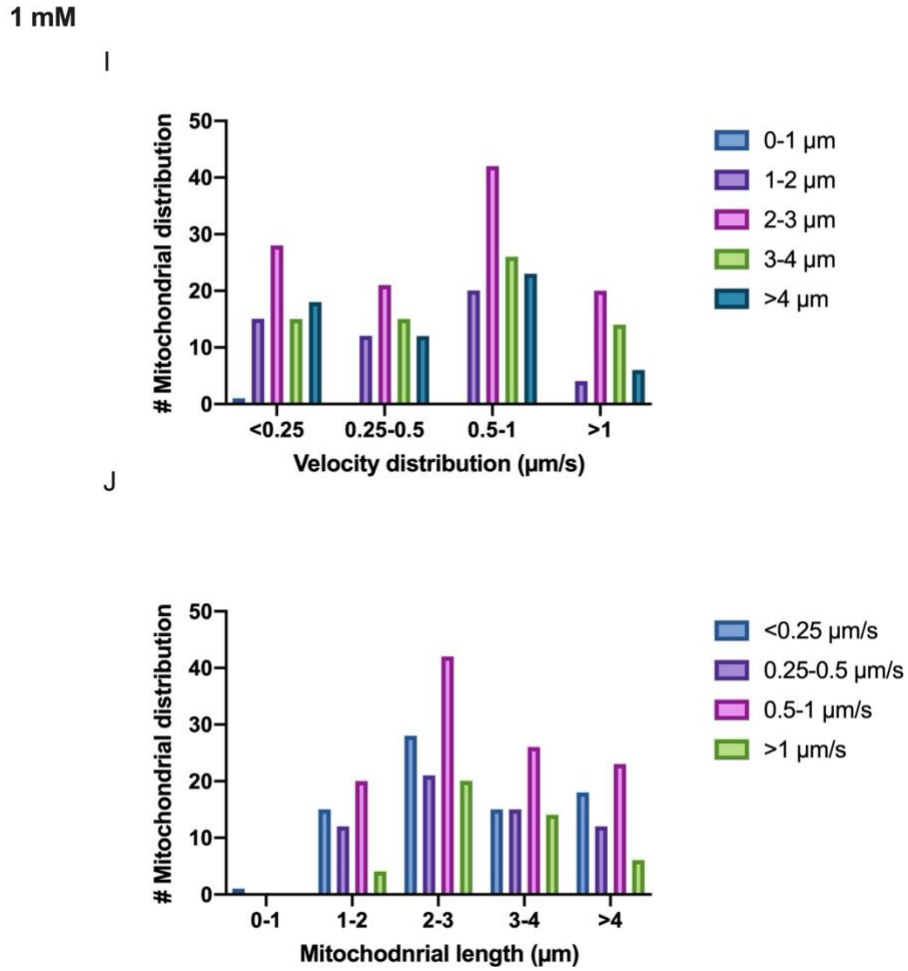

Figure S54 Supplementary histograms of mitochondrial velocity and length in control and nicotinamide-treated RGC cultures. (A) Distribution of mitochondrial velocity with length ranged between 0-1 µm (n=2), 1-2 µm (n=6), 2-3 µm (n=11), 3-4 µm (n=7), and >4 µm (n=4) in control culture from 3 independent cultures. (B) Distribution of mitochondrial length with velocity ranged between 0-0.25 µm/s (n=30), 0.25-0.5 µm/s (n=18), 0.5-1 µm/s (n=3) and >1 µm/s (n=1) in control RGCs from 3 independent cultures. (C) Distribution of mitochondrial velocity with length ranged between 0-1 µm (n=0), 1-2 µm (n=63), 2-3 µm (n=154), 3-4 µm (n=86), and >4 µm (n=53) in 50 µM nicotinamide-treated culture from 3 independent cultures. (D) Distribution of mitochondrial length with velocity ranged between 0-0.25 µm/s (n=103), 0.25-0.5 µm/s (n=83), 0.5-1 µm/s (n=132) and >1 µm/s (n=38) in 50 µM nicotinamide-treated culture from 3 independent cultures. (E) Distribution of mitochondrial velocity with length ranged between 0-1 µm (n=0), 1-2 µm (n=51), 2-3 µm (n=111), 3-4 µm (n=59), and >4 µm (n=28) in 100 µM nicotinamide-treated culture from 3 independent cultures. (F) Distribution of mitochondrial length with velocity ranged between 0-0.25 µm/s (n=71), 0.25-0.5 µm/s (n=61), 0.5-1 µm/s (n=95) and >1 µm/s (n=22) in 100 µM nicotinamide-treated culture from 3 independent cultures. (G) Distribution of mitochondrial velocity with length ranged between 0-1 µm (n=0), 1-2 µm (n=63), 2-3 µm (n=134), 3-4 µm (n=88), and >4 µm (n=39) in

500 µM nicotinamide-treated culture from 3 independent cultures. (H) Distribution of mitochondrial length with velocity ranged between 0-0.25 µm/s (n=71), 0.25-0.5 µm/s (n=79), 0.5-1 µm/s (n=137) and >1 µm/s (n=37) in 500 µM nicotinamide-treated culture from 3 independent cultures. (I) Distribution of mitochondrial velocity with length ranged between 0-1 µm (n=1), 1-2 µm (n=51), 2-3 µm (n=111), 3-4 µm (n=70), and >4 µm (n=59) in 1 mM nicotinamide-treated culture from 3 independent cultures. (J) Distribution of mitochondrial length with velocity ranged between 0-0.25 µm/s (n=77), 0.25-0.5 µm/s (n=60), 0.5-1 µm/s (n=111) and >1 µm/s (n=44) in 1 mM nicotinamide-treated culture from 3 independent cultures.

References

Gao, F. J. et al. 2016. Expression and Distribution of Mesencephalic Astrocyte-Derived Neurotrophic Factor in the Retina and Optic Nerve. Front Hum Neurosci 10, p. 686. doi: 10.3389/fnhum.2016.00686

Hirano, A. A. et al. 2011. SNAP25 expression in mammalian retinal horizontal cells. J Comp Neurol 519(5), pp. 972-988. doi: 10.1002/cne.22562

Kwong, J. M. et al. 2010. RNA binding protein with multiple splicing: a new marker for retinal ganglion cells. Invest Ophthalmol Vis Sci 51(2), pp. 1052-1058. doi: 10.1167/iovs.09-4098

Lakowski, J. et al. 2010. Cone and rod photoreceptor transplantation in models of the childhood retinopathy Leber congenital amaurosis using flow-sorted Crx-positive donor cells. Hum Mol Genet 19(23), pp. 4545-4559. doi: 10.1093/hmg/ddq378

Lorber, B. et al. 2005. Lens injury stimulates adult mouse retinal ganglion cell axon regeneration via both macrophage- and lens-derived factors. Eur J Neurosci 21(7), pp. 2029-2034. doi: 10.1111/j.1460-9568.2005.04034.x

Lorber, B. et al. 2002. Effect of lens lesion on neurite outgrowth of retinal ganglion cells in vitro. Mol Cell Neurosci 21(2), pp. 301-311.

Quina, L. A. et al. 2005. Brn3a-expressing retinal ganglion cells project specifically to thalamocortical and collicular visual pathways. J Neurosci 25(50), pp. 11595-11604. doi: 10.1523/JNEUROSCI.2837-05.2005

Reinehr, S. et al. 2018. HSP27 immunization reinforces AII amacrine cell and synapse damage induced by S100 in an autoimmune glaucoma model. Cell Tissue Res 371(2), pp. 237-249. doi: 10.1007/s00441-017-2710-0

Suggate, E. L. et al. 2009. Optimisation of siRNA-mediated RhoA silencing in neuronal cultures. Mol Cell Neurosci 40(4), pp. 451-462.

Szabadfi, K. et al. 2015. Retinal aging in the diurnal Chilean rodent (Octodon degus): histological, ultrastructural and neurochemical alterations of the vertical information processing pathway. Front Cell Neurosci 9, p. 126. doi: 10.3389/fncel.2015.00126

Tian, M. and Yang, X. L. 2006. C-type natriuretic peptide modulates glutamate receptors on cultured rat retinal amacrine cells. Neuroscience 139(4), pp. 1211-1220. doi: 10.1016/j.neuroscience.2006.02.069